

https://dspace.org/

Integrated geophysical methods for near-surface site characterization in South Africa

Onyebueke, Emmanuel Onyebuchi

2020

https://hdl.handle.net/10539/31605

Downloaded from a DSpace repository. https://dspace.org/

INTEGRATED GEOPHYSICAL METHODS FOR NEAR-SURFACE SITE CHARACTERIZATION IN SOUTH AFRICA

By

ONYEBUEKE Emmanuel Onyebuchi

Student No: 868683

ORCID No: 0000-0002-9089-2270



UNIVERSITY OF THE WITWATERSRAND, JOHANNESBURG

A thesis submitted to the Faculty of Science, University of the Witwatersrand, Johannesburg, in fulfilment of the requirements for the degree of Doctor of Philosophy.

April 2020

Declaration

I declare that this thesis is my own, unaided work. It is being submitted in fulfilment of the requirements for the Degree of Doctor of Philosophy in the University of the Witwatersrand, Johannesburg. It has not been submitted before for any degree or examination in any other University.



___ _____

E. O. Onyebueke

____16_____ day of __April__ 2020.

Abstract

The aim of this research is to integrate reflection seismics with other geophysical methods (such as first-arrival traveltime refraction tomography (RT) and electrical resistivity tomography (ERT), multichannel analysis of surface waves (MASW), horizontal-to-vertical spectral ratio (HVSR) and magnetic field methods) for site investigation. The results will assist the environmental planners, infrastructural engineers, geologists and hydrologists to plan and conduct comprehensive site characterization investigation in the study area. Where possible, the geophysical datasets were constrained by borehole and surface geological map information. This research work was carried out by way of four different case studies, which are discussed in this thesis.

Chapter 2 is a brief review of seismic theory and its applications, and basic principles of electrical resistivity and magnetic methods. **Chapter 3** presents the integration of high-resolution reflection seismics with RT, ERT and MASW for hydrogeological investigation in the Nylsvley Nature Reserve, South Africa. The integrated data were used to image near-surface geology. The interface between the unsaturated sand and saturated sand-gravel was interpreted as the water table, while the undulating bedrock erosional surface with associated weathered/fractured system was interpreted to play a role with respect to the underground water movement and storage in the survey area. In **Chapter 4**, a similar geophysical approach was adopted. High-resolution reflection seismic, RT and ERT were combined to investigate the historic shallow narrow-reef and bulk open-pit mining at the Lancaster gold mine, Krugersdorp, South Africa. The reflection seismic data produced images that were used to delineate stopes and the geological boundaries, while the refraction and resistivity tomograms, on the other hand, generated detailed images of the top 20-30 m of the subsurface. Together they were used to map the shallow geometry of the fluid migration path, mined-out areas, weak zones and boundaries between bedrock and overburden.

Chapter 5 presents the integration of legacy 2D reflection seismic and magnetic data acquired within the Transvaal Basin to investigate and characterize the subsurface architecture, and insights into hydrogeological prospecting and

engineering applications were emphasized. The study area is dominated by agricultural activities, biosphere reserves, mining sites and residential houses. The major Rustenburg Fault (RF) was mapped, as well with other several secondary faults, heterogenous fracture systems, slumps and palaeo-karst features. The fault and fractured structures were interpreted as brittle shear-type deformation. The interpreted fault structures were shown to provide a flow path for fluid migration, while fractured zones were regarded as potential fluid storage regions. Moreover, the intrusive structures were observed to provide several paleo-compartments which could increase groundwater storage within the confined zones.

Chapter 6 focuses on the stability and reliability of the microtremor signal characteristics (predominant frequency and H/V spectral ratio) for site effect assessment of the seismological stations spread across South Africa using the HVSR technique. The results show that the fundamental natural frequency of the near-surface low-velocity-layer (LVL) was essentially the same in all the analyzed time windows, irrespective of the time-of-day or season, while the amplification amplitude varied slightly with the recording duration. The estimated predominant frequency was deemed to be reliable and stable as a representation of the natural fundamental resonance frequency of the ground motion at the site location. Furthermore, the estimated values were used to approximate the thickness of the LVL and the vulnerability index for liquefaction potential at the stations that satisfied the criteria for a clear H/V peak.

In conclusion, the research methodologies and results in this thesis provide a set of case studies of the use of seismic methods integrated with an appropriate geophysical method, to investigate the near-surface as a part of a comprehensive site characterization in South Africa.

Dedication

This project is dedicated to Almighty God (Chukwuokike Abiama), to Whom and through Him all things were made possible, and the entire Onyebueke family and loved ones.

Supervisors & Examination Committee

Supervisor

Professor Raymond Durrheim
School of Geosciences, Department of Geophysics
University of the Witwatersrand

Co-supervisor

Professor Musa Manzi
School of Geosciences, Department of Geophysics
University of the Witwatersrand

List of papers and research contributions

These following papers are based on the thesis, which are referred to in the text by their respective chapters.

Chapter 3 Onyebueke, E.O., Manzi, M.S.D. and Durrheim, R.J., 2018. High-resolution shallow reflection seismic integrated with other geophysical methods for hydrogeological prospecting in the Nylsvley Nature Reserve, South Africa. *Journal of Geophysics and Engineering*, *15*(6), pp.2658-2673.

Chapter 4 Onyebueke E.O., Durrheim R.J., Manzi M.S.D., Sebothoma S., Zhang S and Stettler E., 2020. High-resolution reflection seismic and electrical resistivity survey for environmental purpose: A case study at the Lancaster Gold Mine, Krugersdorp, South Africa. *Pure and Applied Geophysics*. (under revision: PAAG_19_00528R1).

Chapter 5 Onyebueke E.O., Manzi M.D.S., Raymond D.J and Nwaila G., 2020. Geophysical site investigation of the Archaean-Palaeoproterozoic Transvaal Basin Architecture near Boons-Magaliesburg-Hekpoort area, South Africa. *Journal of Applied Geophysics* (under review with submission number: APPGEO_2020_62).

Chapter 6 Onyebueke E.O., Durrheim R.J., Manzi M.S.D., Raveloson A., I. Saunders and Mulabisana T., Assessment of the site effect at South African National Seismograph Network stations using the HVSR technique. *South Africa Journal of Geology* (under review)

Other conference contributions during my PhD study include.

I. Onyebueke, E.O., Durrheim, R.J and Manzi M.S.D., 2017. High-Resolution Shallow Seismic Imaging for Hydrogeological Investigation in an Area Characterized by High Source-Generated Noise. 12th Annual AfricaArray Workshop, p. 27.
II. Onyebueke, E.O., Durrheim, R.J and Manzi M.S.D., 2017. Assessment of Site effect at the seismological Stations in South Africa using the HVSR Technique. Extended Abstracts - 15th SAGA Biennial Conference & Exhibition.

III. Onyebueke, E.O., Durrheim, R.J and Manzi M.S.D., 2018. Near-Surface Site Characterization in South Africa using Different Geophysical Methods. GeoCongress 18 – 20 July, bringing the Geosciences together at University of Johannesburg, South Africa.

IV. Onyebueke, E.O., Durrheim, R.J., Manzi M.S.D and Simon Sebothoma., 2018. Integrated geophysical survey for investigation of the subsurface architecture in a shallow gold mine: A case study, 13th Annual AfricaArray Workshop, p. 22.

V. Onyebueke, E.O., Manzi, M.S.D and Durrheim, R., 2018, September. High-resolution shallow seismic integrated with electrical resistivity method for hydrogeological prospecting. Extended abstract - In 24th European Meeting of Environmental and Engineering Geophysics, Portugal.

VI. Onyebueke, E.O., Durrheim, R.J., Musa M.S.D and Nwaila, G., 2019. Integration of seismic and other geophysical methods for site investigation in South Africa: A case studies. 55th International Conference and Exhibition, Nigerian Mining and Geosciences Society, NMGS, Coal city 2019.

VII. Onyebueke, E.O., Durrheim, R.J., Musa M.S.D and Nwaila, G., 2019. Geophysical investigation of the Transvaal Basin in the Boons-Magaliesburg-Hekpoort area, South Africa: 14th Annual AfricaArray Workshop, p. 23.

VIII. Onyebueke, E.O., Durrheim, R.J., Musa M.S.D and Nwaila, G., 2019. Geophysical investigation of the Transvaal Basin in the Boons-Magaliesburg-Hekpoort area, South Africa: Extended Abstracts - 16th SAGA Biennial Conference & Exhibition, Durban, South Africa.

Acknowledgment

Firstly, I will like to thank my supervisors, Professor Raymond Durrheim and Musa Manzi, for having confidence in my capability to conduct this Ph.D. research project under their immense supervision. They gave me this privilege and honour to be a Ph.D. student at this prestigious University of the Witwatersrand, with all their listening ears to my worries, complaints and numerous questions. I really appreciate all the financial assistance, help, lunch, dinner and patience on me. I am most honoured and privileged to be one of your students. I thank the former HoS, Prof. Roger Gibson for his great student support and counselling and the HoS, Prof. Gillian Drennan for her immense support.

I am most thankful to the entire Onyebueke families for their enduring innumerable love and financial support, most especially Onyebueke Marius (O' Martec Nig. Ltd) and Onyebueke Chinedu, the Julian Baring Scholarship Fund and Allied Drilling Company Nig. Ltd for their magnanimous financial support that enable me to complete this Ph.D. research. Without these financial assistances, this project might not have been completed.

I'm thankful to Dr. Steve Zhang, Dr. Ranto Raveloson, Dr. Stephanie Enslin-Scheiber, Dr. Glen Nwaila, Dr. Isiaka Ahmed, Thifhelimbilu Mulabisana and Prof. Susan Webb for their technical assistance and intensive knowledge sharing. I am thankful to my Geophysics department colleagues for the assistance in the fieldwork and cheer-up conversations; Dr. E.F.S.T. Andriampenomanana Ny Ony, Tochukwu Nwachukwu, Sikelela Gomo, Wesley Harrison, Lebogang Sehoole, Nkimo Moleleki, and Simon Sebothoma, and so many others who were there to discuss, advise, help, talk, drink beer, dance, sports, student fieldworks, camping and other trips. Although, it'll be very difficult to enumerate all the good things that came across. From Geophysics department, I thank Prof. Gordon Cooper, Dr. Mike Jones, Tsiriandrimanana Rakotondraibe, Michael Westgate, Julius von Ketelhodt, Tamara Makhateng, Zamaswazi Nkozi, Siyanda Mngadi, Abigail Ayikwei, Ofentse Sebidi, Kutlwanu Pascal, Vuyolwethu Mahlalela, Buhle Donga and Seeiso Moshoeshoe. I also thank School of Geoscience administrative staff;

Lenah Mtiyane, Jamila Dias, Lungelwa Ndevu, Lesego Mookapele and Nicholas Chokoe for their administrative support.

I’m grateful to the Nylsvley Nature Reserve and Prof. Edger Stettler for giving me the permission to conduct my research in their properties. I thank Anglo Gold Ashanti for providing the 2D seismic data, the Council for Geosciences South Africa for providing access to the MASW software, magnetic data, borehole logs, surface geological map and microtremor data from the network stations (Dr. Ian Saunders), and Council for Science and Industrial Research (CSIR) for granting access to the ReflexW seismic processing software, DUG INSIGHT for donating the seismic interpretation software used for the seismic analysis, visualisation and interpretation (Dug-Insight software), SESAME Research Group for the free access software (Geopsy), AfricaArray for providing microtremor data. Thanks to Michael Westgate and Julius von Ketlhodt for giving me access to their MATLAB codes.

Finally, I am thankful to all the staff and students of the School of Geosciences, University of the Witwatersrand, Johannesburg, South Africa, for making my stay throughout the period of this research a resourceful, serene and memorable episode. I also want to thank the examiners and reviewers for improving the quality of the thesis and manuscript, respectively.

Table of Contents

1.0 General introduction....1
1.1. Application of geophysical methods to near-surface site characterisation ……...4
1.2. Brief outline of the geology of South Africa....6
1.3. Research motivation 8
1.4. Research questions....8
1.5. Aim and objectives 9
1.6. Reference....10
2.0 Literature review of the geophysical methods....13
2.1. Seismic equation, elasticity and velocities....13
2.2. Seismic waves 16
2.3. Types of seismic waves....17
2.3.1. Body waves 17
2.3.1.1. Primary waves....17
2.3.1.2. Secondary waves 18
2.3.2. Surface waves....18
2.4. Seismic methods....20
2.4.1. Reflection seismic method 22
2.4.1.1. Acquisition of active seismic data....24
2.4.2. Refraction seismic method....26
2.4.3. Multichannel Analysis of Surface Waves (MASW) 28
2.4.4. Horizontal-to-Vertical Spectral Ratio (HVSR) techniques....29
2.4.5. Seismic resolution and reflectivity 32
2.4.6. Seismic wave scattering and attenuation 35
2.4.7. Seismic attributes....37
2.5. Sources of noise in the seismic data and their filtering mechanism....39
2.6. Resistivity method 41
2.7. Magnetic potential field method....44
2.8. References 46

3.0 High-resolution shallow reflection seismic integrated with other geophysical methods for hydrogeological prospecting in the Nylsvley Nature Reserve, South Africa 56
3.1. Introduction 57
3.2. Study location and geology 59
3.3. Data acquisition 61
3.4. Data processing and analysis 64
3.4.1. Seismic data processing and analysis 64
3.4.2. Seismic refraction processing 66
3.4.3. Reflection seismic processing 68
3.4.4. Multi-channel analysis of surface waves (MASW) and resistivity tomography inversion 75
3.5. Integration 77
3.5.1. Reflection seismic 78
3.5.2. MASW, refraction and resistivity tomography 79
3.6. Conclusions 83
3.7. Reference 85
4.0 High-resolution integrated geophysical investigation at the Lancaster Gold Mine, Krugersdorp, South Africa 89
4.1. Introduction 90
4.2. Site location and geology and borehole information 92
4.3. Physical property measurement and synthetic modelling 98
4.4. Geophysical methods 102
4.4.1. Seismic methods 102
4.4.1.1. Survey design and acquisition 102
4.4.1.2. Raw data analysis 104
4.4.1.3. Data processing and results 107
4.4.1.3.1. Refraction seismic 107
4.4.1.3.2. Reflection seismic 108
4.4.2. Electrical resistivity method 114
4.4.2.1. Data acquisition 114

4.4.2.2. Data processing and results 114
4.5. Interpretation 116
4.5.1. 2D reflection seismic 116
4.5.2. Refraction and resistivity tomography 117
4.6. Discussion 123
4.7. Conclusion and recommendation 126
4.8. Reference 128
5.0 Geophysical site investigation of the Archaean-Palaeoproterozoic Transvaal Basin architecture near Boons-Magaliesburg-Hekpoort and its implication for hydrogeological prospecting and engineering 136
5.1. Introduction 137
5.2. Site location and geology 139
5.3. Tectonic and structural impact on the sedimentation in the Transvaal Basin 143
5.4. Hydrogeological potential and its structural implications 144
5.5. Engineering implications and mineral potential of Transvaal Basin 146
5.6. Methodology 147
5.6.1. Reflection seismics 147
5.6.1.1. Data acquisition, processing and analysis 147
5.6.2. Magnetic 150
5.7. Results 150
5.7.1. Seismic reflection denoising 150
5.7.2. Tilt and gradient of the magnetic field 154
5.8. Interpretations 155
5.8.1. Magnetic 155
5.8.2. 2D seismic reflection interpretation 157
5.8.2.1. Delineated geological features 159
5.9. Discussion 165
5.10. Implications for hydrogeology and engineering 171
5.11. Conclusion 174
5.12. Reference 176

6.0 Assessment of the site effect at South African National Seismograph Network stations using the HVSR technique 184
6.1. Introduction 185
6.2. Methodology 189
6.3. Data acquisition 192
6.4. Surface geological characteristics of the seismic stations 195
6.5. Data processing and analysis 196
6.6. Influence of parameters involved in signal processing 201
6.6.1. Window length (WL) variation 201
6.6.2. Variation in percentage of overlap 203
6.6.3. Varying the percentage of cosine taper width along with the smoothing function 204
6.6.4. Variation of smoothing constant (b) 205
6.7. Results and interpretation 206
6.8. Discussion and conclusion 212
6.9. References 215
7.0 General conclusions and recommendations 219
7.1. Reference 223

List of Figures

Figure 1.1: Geology of South Africa showing the locations of the investigated area and the seismological station positions (Council of Geoscience Geological map, 2008). (Copyright© Council for Geoscience, South Africa, All Right Reserved. First published by the Government printer, 1978). Index top right shows the outline of the cratons in Southern Africa (https://en.wikipedia.org/wiki/Kapvaal/Limpopo_Belt/Zimbabwe_Craton) 8
Figure 2.1: Stress components acting on an infinitesimally small volume encircle a point within an elastic material. 14
Figure 2.2: P-wave propagation (modified after Shearer, 2009). 17
Figure 2.3: S-wave propagation (Modified after Shearer, 2009). 18
Figure 2.4: Rayleigh wave propagation (modified after Shearer, 1999). 20
Figure 2.5: Seismic acquisition testing. (a) A laptop displaying recorded signal and geophone array, (b) is showing the Geode seismograph and trigger cable. ... 22
Figure 2.6: Seismic reflection in a single flat layer. Where V, Z and ρ is velocity, horizon thickness and density, respectively. 24
Figure 2.7: Simplified diagram showing Common-midpoint (CMP) gather and Common-depth-point (CDP) of a seismic signal. 25
Figure 2.8: Different types of seismic acquisition techniques. (a) forward end-on shot roll-along acquisition type, (b) centre-shot roll-along acquisition type, (c) fixed receiver asymmetric acquisition type. 26
Figure 2.9: Seismic events in a single flat layer, where V, Z and ρ is velocity, horizon thickness and density, respectively. 27
Figure 2.10: Surface wave propagation in an inhomogeneous media and multi-channel record (modified after Park et al., 1999). λ_1 and λ_2 represent the change in the wavelengths of the seismic wave as it propagates away from the point source. 29
Figure 2.11: A typical geological structure used by Nakamura (2000) to explain the HVSR technique. Note SSR – standard spectral ratio technique, $H_r(f)$ and $V_r(f)$ are the horizontal and vertical spectra components recorded on exposed bedrock rock, $H_b(f)$ and $V_b(f)$ are the horizontal and vertical spectra components on the

basement covered by sediments, $S_{Hs}(f)$ and $S_{Vs}(f)$ are the spectra components recorded on the surface above the sediments. 32
Figure 2.12: Geometrical spreading of seismic energy from a known source 37
Figure 2.13: Instantaneous seismic attributes; amplitude A(t), phase $\phi(t)$ and frequency $\omega(t)$ 38
Figure 2.14: (a) Schematic diagram illustrating the basic principle of the electrical resistivity method (b) Flow of electric current along a known conductor length. 43
Figure 2.15: Electrical current distribution in a hemispherical shell. 44
Figure 3.1: Geology map of the study area (modified from the Republic of South Africa Nylstroom Geological Survey map 2428). The index on the top left is the South Africa boundary map outline (Copyright© Council for Geoscience, South Africa, All Right Reserved. First published by the Government printer, 1978). .. 60
Figure 3.2: Base map of the study area from the Google Earth Image showing the location of the boreholes (B1, B2, B3) (the enlarged block on the bottom right shows the position of the profile lines). At the bottom is the stratigraphy of the boreholes, showing the depth to the bedrock near the study area (image@2017DigitalGlobe) 61
Figure 3.3: Data acquisition field setup. Line 1 is shown in the picture. On the right is 94 m seismic profile with 2 m geophone spacing; on the left, about 3 m away from seismic profile, is the 120 m resistivity profile with 3 m electrode spacing. The source is a 30 x 30 x 2.5 cm aluminum metal plate with a 9 kg sledgehammer. 63
Figure 3.4: (a) and (b) Raw seismic shot gathers recorded along lines 1 and 2, respectively. (c and e) Power spectrum of the raw shot gathers along lines 1 and 2, respectively. (d and f) Amplitude decay curve of the raw shot gathers along lines 1 and 2, respectively. Various seismic events are interpreted as follows: D – direct wave; R1 – first refracted P-wave; R2 – second refracted P-wave; Refl – possible P-wave reflections from bedrock and S – surface waves. 66
Figure 3.5: (a) and (b) Refraction tomography results along lines 1 and 2. (c) and (d) Raytracing of the traveling waves and waveform inversion embedded on the tomography images on the respective profiles. The contour lines represent the velocity isolines with a starting velocity of 300 m/s and 100 m/s intervals 68

Figure 3.6: Typical shot gathers from lines 1 and 2 showing the key steps in reflection seismic processing. (a) and (b) After trace editing and amplitude scaling. (c) and (d) After spiking deconvolution and bandpass frequency filtering. (e) and (f) After trace equalization (AGC), top muting (direct and refracted arrival muting) and time cut. (g) and (h) Amplitude decay-frequency curves of the shot gathers after deconvolution, bandpass frequency and F-K filtering. Notice the broadening of the reflected signal spectrum after deconvolution. The red arrows show the enhanced bedrock reflector and the yellow arrows point to the attenuated surface waves after frequency bandpass and F-K filtering. 71
Figure 3.7: Sample of CMP-gather velocity analysis. (a) CMP ensemble, (b) NMO corrected ensemble, (c) adjacent CMP gathers, (d) stacked traces and (e) velocity model at the selected CMP along line 1, respectively. Similarly, for line 2 (f – j) 72
Figure 3.8: The final stacked time seismic section after subsequent bandpass frequency filtering. (a) and (c) represents seismic time sections of lines 1 and 2, respectively, while (b) and (d) are the respective depth sections. The red arrows point to the bedrock (Refl), the fresh bedrock reflectors (FB) and the low-velocity layer (LVL)..... 74
Figure 3.9: Multichannel analysis of surface wave. (a) and (c) Dispersion spectrum of the offset shots along lines 1 and 2, respectively (show in it is the extracted dispersion curve used for Vs velocity inversion). (b) and (d) 10-layer Vs velocity model for (a) and (c), respectively. 76
Figure 3.10: Resistivity profile along lines 1 and 2. 77
Figure 3.11: Integrated interpretation of line 1 and 2. (a) and (b) Refraction tomography. (c) and (d) Resistivity tomography. (e) and (f) Reflection seismic section. (g) and (h) 1-D profile of MASW. LVL probably represents the base of the low velocity layer, Refl the bedrock reflector, FB the fresh bedrock reflector and WZ probably represents a highly weathered/fractured zone. 81
Figure 3.12 Schematic diagram showing downstream changes in the sediment transported by tributaries, and sediment underlying the Nyl River floodplain/floodout (Tooth et al., 2002 based on the borehole data in Timmerman,

1984). The depth of alluvium underlying the floodplain reaches a maximum of ~35m (Tooth et al., 2002 www.tandfonline.com). 82
Figure 3.13: A geological model along the profile lines. (a) Line 1 and (b) Line 2. Different stratigraphic units are delineated with solid coloured lines and interpreted faults are shown as black dashed lines. 82
Figure 4.1: (a) Satellite image and photographs showing residential encroachment towards mining area. (b) and (c) show the environmental degradation caused by mining activities in the area..... 92
Figure 4.2: (a) Geology of the Witwatersrand Basin indicating the location of the study area. (b) Geological cross-section across the study area indicating the dipping conglomerate reefs of Central Rand Group (c) South Africa map outline showing the position of the Witwatersrand Basin, respectively (modified from Dankert and Hein, 2010). 95
Figure 4.3: Dipping reefs exposed on the sidewall of an open cast pit, waste dump in the background..... 96
Figure 4.4: The borehole information from the Lancaster Gold Mine used to correlate the lithology of the study area. Borehole locations are shown in Figure 4.7. 97
Figure 4.5: Borehole logs with the respective reflection coefficient and synthetic seismogram. Note that the multiple traces are repetitions of the zero-offset trace at the borehole position. 100
Figure 4.6: A schematic diagram illustrating the low-velocity or hidden layer problem in the conventional seismic refraction method. (a) Showing water-filled layer; (b) Showing air-filled cavity/tunnel. The respective velocity and density values on the top of the respective models were used to calculate and construct the reflectivity and synthetic seismogram superimposed on the model. Note: the diagram was not drawn to match scale and the thickness of the hidden layer does not reflect the actual thickness of the mine stopes which is about 5 m. 101
Figure 4.7: (a) Photograph showing a collapsed mine entrance. (b) South Africa map outline showing the location of the survey area and (c) Google Earth map indicating the survey profiles, borehole locations and possible tunnel positions in the research site..... 103

Figure 4.8: Data acquisition setup showing some mine trenches alone the profiles. (a) and (b) are along L01, (c) and (d) are along L02 while (e) and (d) are along L03. 104
Figure 4.9: Seismic raw data indicating different seismic events. (a), (b) and (c) represent a single shot gather along L01, L02 and L03, respectively. (d), (e) and (f) shows the frequency spectrum of the respective shot gathers. Note, D – direct wave, r1 – first refracted wave, r2 – second refracted wave, R1 – probably the first reflected wave, R2 – probably the second reflected wave, A – air wave, S – surface wave, M – multiple reflection arrival of R2 and Mo – probably a monochromatic noise. 105
Figure 4.10: Refraction tomography results. (a), (b) and (c) represent velocity model along L01, L02 and L03, respectively. Note, the contour lines represent velocity isoline of different velocity values shown in different colour band, and LVL is low velocity layer, while BV is bedrock velocity..... 108
Figure 4.11: Reflection processing steps along L01, L02 and L03. (a), (b) and (c) illustrate after trace editing and amplitude scale. (d), (e), and (f) illustrate after deconvolution and bandpass frequency filtering. (g), (h) and (i) illustrate after velocity bandpass filtering, top muting and time cut. (j), (k) and (l) represent the frequency spectrum obtained after subsequent filtering along the respective lines. Note, the arrow SA indicates the surface wave moveout, R1 – probable first reflector and R2 – probable second reflector. 111
Figure 4.12: Stacked reflection seismic along L01, L02 and L03. (a), (c) and (e) represent the final stacked time sections. (b), (d), and (f) represent time-depth migrated sections after post-stack processing and static correction. R1 and R2 are the first and second reflectors, respectively. 113
Figure 4.13: Colour-coded electrical resistivity tomography results along L01, L02 and L03. (a), (c) and (e) are the Dipole-dipole array measurement in each respective line. Subfigures (b), (d) and (f) are the Schlumberger array measurement along each respective line. 115
Figure 4.14: (a) Interpreted reflection seismic section along L01 showing the delineated interfaces; (b) interpreted refraction tomogram superimposed on the stretched-scale reflection seismic section, indicating some structural boundaries;

(c) interpreted electrical resistivity tomogram superimposed on the stretched-scale reflection seismic section, indicating the mined-out zones. Note, R1 and R2 are the first and second reflectors, respectively, CB – indicates the conglomerate band reflector. 118
Figure 4.15: (a) Interpreted reflection seismic section along L02 showing the delineated interfaces; (b) interpreted refraction tomogram superimposed on the stretched-scale reflection seismic section, indicating some structural boundaries; (c) interpreted electrical resistivity tomogram superimposed on the stretched-scale reflection seismic section, indicating the mined-out zones. Note, R1 and R2 are the first and second reflectors, respectively, CB – indicates the conglomerate band reflector, UM- unmined surface block. 120
Figure 4.16: (a) Interpreted reflection seismic section along L03 showing the delineated interfaces. (b) Interpreted refraction tomogram superimposed on the stretched-scale reflection seismic section, indicating some structural boundaries. (c) Interpreted electrical resistivity tomogram superimposed on the stretched-scale reflection seismic section, indicating the mine-out zones. Note, R1 and R2 are the first and second reflectors, respectively, CB – indicates the conglomerate band reflector, SS – slump structure. 122
Figure 4.17: Borehole logs correlated and superimposed on the interpreted reflection seismic section indicating the mined-out Boulder Reef and material interfaces. Note, R1 and R2 are the first and second reflectors, respectively, CB – indicates the conglomerate band reflector. Note the jointing, fracturing and layering pattern of the Central Rand Group sandstone on the exposed sidewall of an open cast pit on the photograph. Borehole and synthetic seismogram superimposed on the seismic section (oriented west-east) indicate the bedrock-overburden contact and mined-out regions. The blue and white dotted lines indicate linear fractures/jointed pattern. 124
Figure 4.18: 3D correlation of the reflection seismic sections along L01, L02 and L03. The photographs indicate the profile directions. the dipping and strike direction of the layers. KPR-Kimberly Reef Package and UM-unmined region. 125
Figure 5.1: Geology of the study area with seismic lines. Index on the left is the formation stratigraphy at the Bh1-X_1 location. Insert shows the location of the

Transvaal Basin (the borehole and geology information were sourced and modified from the South Africa geological map from the Council for Geosciences (CGS)) (Eriksson and Reczko, 1995 and 1998; Eriksson et al., 1995). The dashed red line section of the RF shows probable extension of the fault at depth..... 140
Figure 5.2: The average formation stratigraphy of the Transvaal Supergroup (modified from Erikson et al., 1995; Amstrong et al., 1991). 142
Figure 5.3: A map showing the dolostone formation of the Chuniespoort Group, and compartments created by dyke intrusions and the study area location (modified from Barnard, 2000). 146
Figure 5.4: Total magnetic intensity (TMI) map and superimposed position of the seismic lines..... 150
Figure 5.5: Application of post-processing filters to seismic line AA' (a) Undenoised migrated data and (b) Denoised data after application of curvelet transformation and (c) Denoised data after application of structurally-oriented dip filter. Note 1000 ms TWT ~ 3000 m, using an average bedrock velocity of 6000 m/s..... 152
Figure 5.6: Application of post-processing filters to seismic line FF' (a) Undenoised migrated data and (b) Denoised data after application of curvelet transformation and (c) Denoised data after application of structurally-oriented dip filter. Note 1000 ms TWT ~ 3000 m, using an average bedrock velocity of 6000 m/s..... 153
Figure 5.7: Magnetic field after calculating (a) Vertical and (b) Tilt derivative Seismic lines are superimposed on the maps. 154
Figure 5.8: Interpreted first vertical derivative of the magnetic field anomalies map and superimposed seismic lines and geological map of the study area. FCF – fractured contact features, PKF – possible karst features, ECCG – Erosional contact along CG boundaries (in this map the weathered/fracture interface is with Black Reef formation and Archaean granite), AGB – Archaean Granite Basement. The dashed white lines show the west–east dyke lineaments. The dashed red line section of the RF shows probable extension of the fault at depth. 156

Figure 5.9: Uninterpreted 3D visualization of the 2D seismic section looking 30^0 northeast, plunging southwest for better orientation view. The faded black lines are XY grid in UTM coordinate system..... 158
Figure 5.10: (a) interpreted 3D visualization of the 2D seismic section looking 30° northwest, plunging southwest for better orientation view, showing the imaged geological structures and mapped Rustenburg fault plane. (b) imbedded geological map that was used to constrain the interpretations. The faded black lines are XY grid in UTM coordinate system. The dashed red line section of the RF shows probable extension of the fault. This figure is vertically exaggerated. 159
Figure 5.11: Structural interpretations across profile AA', CC' and FF' highlighting some geological features on the downthrow block of the Rustenburg fault (RF). (a) Interpreted 3D view of the three seismic sections, looking 30^0 northeast, plunging southeast for adequate orientation view (b) 2D presentation of interpreted profile FF' for better clarity of the mapped structures. Note: Sf – sigmoidal listric fault and MS – monoclinal structure. The dashed red line section of the RF shows probable extension of the fault at depth. 160
Figure 5.12: Reflection seismic section across line EE' showing the unreflective, scattering and dispersive characteristic of a seismic survey on the dolostone formation of the Chuniespoort Group. 161
Figure 5.13: Interpreted seismic sections across profile AA', CC', DD' and FF' highlighting structural features on the upthrown block of the RF. (a) presentation of the interpreted 3D view of the seismic section trending-north, plunging southward. (b) 2D presentation of the interpreted profile AA' for better clarity. Note: CFf – listric fault feature cutting across line CC' and FF', PKF – possible karst feature. The dashed red line section of the RF shows probable extension of the fault at depth. 163
Figure 5.14: Interpreted seismic sections across profile BB' CC', DD', GG' and FF' highlighting the extensional faults and palaeo-slope features. (a) presentation of the interpreted 3D view of the seismic sections looking 90° east, plunging southwest. (b) 2D presentation of the interpreted profile CC' and DD' for better clarity. Note: CFf – listric fault cutting across line CC' and FF', PKF – possible

karst feature. The dashed red line section of the RF shows probable extension of the fault at depth. The index map on the top-right is the geology of the study area. 165
Figure 5.15: 3D modelling of the Rustenburg fault (RF) to demonstrate the normal displacement and strike-slip surface appearance (a) Assumed initial sediment deposits (b) Development of the NNW-trending normal displacement (c) Eventual surface peneplanation within the fault zone. 168
Figure 5.16: Magnetic intensity profiles and surface elevations across the seismic sections showing uneven topography due to erosion (a) Line AA' (b) BB' (c) CC (d) DD' (e) GG' and (f) FF' (The elevation information was sourced from Google Earth Pro @ 2018 Google Image Landsat/Copernicus). 169
Figure 5.17: 3D visualization of the seismic sections indicating the position of some of the mapped features on the TMI map (a) approximate Timeball Hill/Rooihoogte (H1) horizon and (b) approximate Strubenkop (H5) horizon. The index on the center right is the interpreted first vertical derivative of the TMI map. ECCG indicate the erosional contact with Chuniespoort Group, PNGW the possible near-surface groundwater and the dashed white lines indicate the intrusive lineaments. 173
Figure 5.18: Total magnetic intensity map superimposed on the Google Earth map to show the relationship of the delineated structural zones and their surface structures (such as flood channels and deformed regions). The red arrows point to the delineated fault zones and observed surface features. 174
Figure 6.1: (a) Seismicity of Southern Africa. Note > 95% are mining related seismicity (Ogasarawa et al., 2009). (b) Map of current seismic hazard for South Africa. Expected peak ground acceleration (PGA, in g) with a 10% probability of being exceeded at least once in a 50 years period (Esterhuyse et al., 2014, modified by Kijko et al., 2016). 188
Figure 6.2: A typical geological structure used by Nakamura (2000) to explain the horizontal to vertical spectral ratio (HVSR) technique. Note SSR – standard spectral ratio technique, $H_r(f)$ and $V_r(f)$ are the horizontal and vertical spectral components recorded on exposed bedrock rock, $H_b(f)$ and $V_b(f)$ are the horizontal and vertical spectral components on the basement that is covered by sediments,

S_{Hs}(f) and S_{Vs}(f) are the spectral components recorded on the surface over the sedimentary column. 191
Figure 6.3: Geological map of South Africa and location of seismological stations. (Copyright© Council for Geoscience, South Africa, All Right Reserved. First published by the Government printer, 1978)..... 193
Figure 6.4: Example of seismometer used in the seismological stations. 193
Figure 6.5: Microtremor signal processing. (a) Automatic window selection on the 3-component seismometer noise record, (b) Example of HVSR result (H/V curve) with 79 noise windows for MOPA station. 197
Figure 6.6: Variation of window length. (a) WL = 10s; (b) WL =40s; (c) WL =60s; (d) WL =120. 95 different noise windows were selected and averaged. The hatched area shows the underrepresented frequency spectrum. 202
Figure 6.7: Variation of percentage overlaps between windows. (a) 0% overlaps (b) 10% overlap (c) for 20% overlap (d) 50% overlap (36 different noise windows were calculated in each the following analysis using the WDLM station). 203
Figure 6.8: Varying the percentage of Cosine taper width. (a) 0% taper width; (b) 0.5% taper width; (c) 5% taper width; (d) 50% taper width (30 different noise windows were calculated in each analysis for PRYS station)..... 204
Figure 6.9: Variation of smoothing constant (b). (a) No smoothing; (b) b = 10; (c) b = 20 (d) b = 40 (79 different noise windows were calculated in each analysis using MOPA station). 206
Figure 6.10: Amplitudes of H/V ratio as a function of predominant frequencies. (a) Stations with clear H/V curves, (b) station with double H/V peaks, (c) stations with broad peak/plateau-like curve and (d) stations with flat H/V curves. 209
Figure 6.11: Examples of spurious peaks due to non-stationary transients on the microtremor signals. (a), (b) and (c) are the H/V curve for MATJ, MSNA and SEK stations, respectively; (d), (e) and (f) are the respective frequency spectra of the three components of the seismometer (each curve represent E, N or Z component); and (g), (h) and (i) are the respective azimuth versus frequency of the power spectral density (note the transient spike on the frequency spectrum of all the three components occur at the same frequency value). 210

Figure 6.12: Site characteristics of the seismological stations placed on the map of current seismic hazard for South Africa. Expected peak ground acceleration (PGA, in g) with a 10% probability of being exceeded at least once in a 50-year period (Esterhuyse et al. 2014, modified by Kijko et al. 2016)..... 214

List of Tables

Table 2.1: Site classification scheme defined in Building Seismic Safety Council (BSSC, 1994)..... 29
Table 3.1: Seismic acquisition parameters for line 1 and 2. 64
Table 3.2: Processing sequence and parameters..... 69
Table 4.1: Physical property measurement of boreholes 1 and 2. Z is the acoustic impedance, ρ is the density, V_I is the interval velocity and Rc is the reflection coefficient. Abbreviations ws - weathered sandstone, s - sandstone, cl - conglomerate lenses, cb - conglomerate bands, and q – quartzite..... 99
Table 4.2: Seismic acquisition parameters for line 1, 2 and 3..... 103
Table 4.3: Reflection seismic data processing sequence and parameters. 110
Table 5.1: Seismic data acquisition parameters..... 148
Table 6.1: Network station coordinates and instruments..... 194
Table 6.2: Brief explanation of the surface geology and location of the stations 195
Table 6.3: Criteria for a reliable H/V curve and clear H/V peak (SESAME, 2004). 200
Table 6.4: Tabular display of the stability analysis of the H/V parameters of the seismological stations. Broadband - BB, Short period - SP and Extended short period - ESP seismometer. Note: empty cells show unavailability of data. 201
Table 6.5: Reliability of the predominant frequency as defined by SESAME (2004) guidelines (N_w-number of windows, WL-window length, n_c-number of significant cycles and σ_A-standard deviation error for amplification)..... 211
Table 6.6: Approximate sediment thickness and vulnerability index (K_g)..... 211

CHAPTER 1

1.0 General introduction

In this study I integrated the use of geophysical methods to characterize near-surface geological structures for environmental and engineering investigation, hydrogeological prospecting and subsurface geological mapping in South Africa. The geophysical methods used in this study are non-invasive geophysical investigations consistent with the goal of minimizing the use of invasive characterization methods (such as drilling, trenching, and/or exploratory excavation). These invasive geotechnical approaches are more expensive and sometime manually strenuous to operate, and only sample a relatively small part of the volume of interest. However, invasive methods typically provide "ground truth" information that reduces the inherent ambiguities associated with geophysical datasets. These ambiguities can be further reduced with the use of integrated geophysical methods. Characterization of any proposed site requires geological and geophysical information, and hydrogeological properties, subsurface geologic architecture, and geologic integrity for purposes such as earthquake hazard assessment and structural stability. Application of different geophysical techniques provides significant information related to these components of site characteristics. Regional/localised geophysical site investigation can be integrated with surface geologic mapping for a comprehensive site characterisation of the geological architecture in a candidate area.

In this series of case studies, reflection seismics, first-arrival traveltime tomography, multichannel analysis of surface waves (MASW), electrical resistivity tomography (ERT), the magnetic method and microtremor horizontal-to-vertical spectral ratio (HVSR) method have been used to characterise the subsurface architecture of the candidate sites. Each technique has its own disadvantages and advantages in resolving subsurface structures and their physical properties. Thus, the reflection seismic is efficient in resolving deep-seated geological structure due to its high penetration depth and resolution, while refraction seismic and MASW are good for imaging the near-surface (shallow

than 50 m). The ERT and magnetic field methods are good at resolving conductive and magnetic materials, respectively, and their data acquisition is efficient, fast and cost effective. HVSR analysis of the microtremor signal provides a cheap, fast and easy passive seismic geophysical techniques used to estimate site effect characteristics (such as predominant frequency and horizontal to vertical spectral ratio (H/V)) for seismic hazard assessment and microzonation studies. The resolution and penetration of these aforementioned geophysical techniques depend on the geological and topographic conditions and the acquisition geometry (e.g. station spacing and profile length etc). Hence, a combination of these methods integrates their advantages to constrain interpretation ambiguities and improve resolution. These integrated non-invasive approaches were adopted in four case studies, each with a different objective presented in different chapters of this thesis.

The thesis is structured in seven chapters. **Chapter 1** contains the introductory content, research motivation, aim and objectives, as well as a brief review of the application of geophysical method to site characterisation and brief outline of South African geology.

To avoid unnecessary repetition, **Chapter 2** explains the basic principles of the adopted geophysical technique used in this study. In particular, elements of active seismic and data acquisition, seismic attenuation and resolution as well as sources of seismic noise and its attenuation were also discussed in this chapter.

Chapter 3 shows the integration of high-resolution reflection seismic with RT, MASW and ERT for hydrogeological prospecting in Nylsvley Nature Reserve South Africa. The study estimated the depth to the top of the aquifer layer and revealed the geological structural mechanism responsible for underground water migration and storage in the area. The content of this chapter has been published in the Journal of Geophysics and Engineering (https://doi.org/10.1088/1742-2140/aadbe3) (Onyebueke et al., 2018), which is on the list of NRF-approved journals

Chapter 4 presents another use of integrated geophysical method for an environmental investigation. In this chapter, high-resolution reflection seismic, refraction tomography and ERT were combined to investigate the near-surface structure in a historic shallow narrow-reef and prospective bulk open-pit mine, the Lancaster gold mine, near Krugersdorp, South Africa. The geophysical datasets were further constrained with ground-truth borehole information. A detailed near-surface (20 – 100 m) image reveals the geometry of the subsurface structures such as fluid migration path, mined-out reef and weak zones. The content of this chapter is under revision with the Journal of Pure and Applied Geophysics.

In **Chapter 5**, I used legacy 2D reflection seismic and magnetic field datasets, constrained by boreholes and surface geological field mapping information, to characterise and delineate the subsurface features within the Transvaal Basin. Insights to hydrogeological prospecting and engineering applications were emphasized. The study shows the subsurface image of paleo-structures, fluid migration path and storage regions. The datasets also reveal the role of dykes/sills in structural deformation and the implication for hydrogeological characteristics of the area, as well as the associated risk to infrastructural development. The content of this chapter is under review with the Journal of Applied Geophysics.

Chapter 6 discusses the analysis of the microtremor signals in site-effects assessment at the South Africa seismological network stations using the Nakamura (1989) HVSR technique. The stability and reliability analysis show that the technique can be used to estimate various site effect characteristics such as the predominant frequency and H/V amplitude of vibration using the spectral ratio of the ambient noise. The study reveals some stations with high predominat frequency and H/V amplitude that could be susceptible to earthquake ground-motion amplification. The content of this chapter is also under review in the Journal of Africa Earth Sciences and has been publish as an extended abstract in the proceedings of the SAGA 2017 biannual conference in Cape Town.

Chapter 7 is the final summary and conclusion of the thesis and provides recommendation for future studies.

1.1. Application of geophysical methods to near-surface site characterisation

Geophysicists and geotechnical engineers define the "near-surface" as the uppermost few tens of meters of the Earth's crust (Butler, 2005; Stokoe et al., 2004). Essential services necessary for modern life such as agriculture, dwellings, schools, hospitals, factories, power stations, reservoirs, and transport infrastructure rely on the stability of the shallow subsurface. Geophysics is a science that uses the methods of physics to characterise the Earth and has proven very useful in many near-surface investigations. For example, geophysical techniques have been used to search for groundwater, map pollution plumes, identify voids such as natural cavities and abandoned mines, design excavations and foundations, and for seismic microzonation (Miller et al., 1999; Park et al.,1999; Yilmaz et al., 2006, Onyebueke et al., 2018, Isiaka et al., 2018). To characterise the near-surface, site investigations are needed. This involves several different studies by geologists, seismologists, geotechnical and earthquake engineers (Yilmaz, 2015). These investigations also include mapping of the site geology (using geophysical instruments and geological field mappings), geotechnical studies and laboratory test measurements. Knowledge about seismic wave velocities (both P- and S-wave) of the soil column, the geometry of the layers within the soil column and the soil-bedrock interface is required for comprehensive seismic site characterization (Kramer, 1996; Yilmaz, 2015).

Seismic characterization and ground motion investigation play an important role in geotechnical and earthquake engineering. This is because, it provides parameters that are related to the mechanical behaviour of the geomaterials at small strains for large subsurface volumes in the undisturbed conditions and provides the fundamental resonance frequency of the soil column (Yilmaz et al., 2006; Park et al., 1999). The soil column response during an earthquake depends on the resonance frequency of the ground motion, the soil properties and the geometry of the soil column overlying the bedrock (Nakamura, 1989; Nogoshi and Igarashi, 1970). This information is of paramount importance, particularly for

dynamic studies related to seismic risk assessment (Semblat et al., 2005; Yilmaz et al., 2006) and vibration propagation (Comina and Foti, 2007).

The integration of various seismic methods such as reflection, refraction, the spectral ratio method, and Multichannel Analysis of Surface Waves (MASW) provide additional knowledge for comprehensive site characterization such as soil parameters (shear stiffness, Young's modulus and Poisson's ratio) and earthquake engineering parameters (soil amplification and fundamental resonance frequency), which cannot be derived using a single technique (Miller et al., 1999; Park et al., 1999). The integration of seismics with other geophysical methods (such as ERT, GPR, gravity and magnetic field methods) provides additional information for a more constrained regional/localised site characterization (Chaiprakaikeow Susit., 2012, Malehmir et al., 2016; Brodic, B. 2017, Wang, 2017), as well as the detection of subsurface features such as voids, subsidence and sinkhole formation that may cause significant environmental and engineering problems (Foti et al., 2011; Park, 1995).

A site characterization study prior to the commencement of any construction work will provide geotechnical, and earthquake engineers with the data necessary to design an appropriate foundation for any engineering structure. It also provides valuable information for hydrogeological prospecting in targeting high yield underground water boreholes (Foti, 2000; Yilmaz, 2015). Knowledge about seismic wave velocities (P-wave and S-wave) of the soil column is useful also for seismic microzonation and seismic risk assessment. The lithologic column based on borehole datasets and surface geological mapping are used to constrain and reduce the ambiguities associated with geophysical datasets interpretation since a single set of field measurements often cannot provide unique model of subsurface conditions.

1.2. Brief outline of the geology of South Africa

South Africa has one of the best preserved ancient geological landscape in the world (Zegers et al., 1998; Anhaeusser, 2019). The Greenstone belt of the Barberton Supergroup is one of the oldest known rock formations on Earth, formed between 4000 – 3500 Ma (Zegers et al., 1998; McCarthy and Rubidge, 2005; de Wit et al., 2018; Anhaeusser, 2019). The Kaapvaal Craton, is one of the world oldest craton that stabilized ca. 3100 Ma(Zegers et al., 1998; de Wit et al., 2018; Anhaeusser, 2019).

Immemorially, the rifting and subsequent thinning of the crust at ca. 3074 Ma resulted in depostion of sedimentary and volcanic rocks of Dominion Group and the lower Pongola Supergroup (McCarthy and Rubidge, 2005). The subsidence of the crust caused by cooling at ca. 2970 Ma started the deposition of the upper Pongola Supergroup and lower Witwatersrand Supergroup (WS) (West Rand Group). Between ca. 2714 – 2650 Ma, the Zimbabwe Craton collided with the Kaapvaal Craton causing vast amount of volcanic lava to erupt, forming the Ventersdorp Supergroup (McCarthy and Rubidge, 2005). Another phase of continental rifting occured ca. 2650 Ma, resulting in the formation of the Wolkberg Group, Black Reef Fomation, and Chuniespoort Group (CG) and Ghaap Group (GG) of theTraasvaal Supergroup (TS) (McCarthy and Rubidge, 2005).

Renewed rifting and subsidence initiated the deposition of the Pretoria Group from the sediment being derived due to partial erosion of the CG and GG between ca. 2061 – 2049 Ma. An extensive volume of volcanic eruption occured across the central part of the Kaapvaal Craton resulting in the formation of the Bushveld Complex (ca. 2050 Ma). A massive meteorite struck the Kaapvaal Craton at ca. 2023 Ma. The deformation caused by this impact formed a dome-like structure known today as the Vredefort Dome impact structure. The Olifantshoek Supergroup formed under shallow water condition ca. 2000 Ma towards the western margin of the Kaapvaal-Zimbabwe Craton (McCarthy and Rubidge, 2005).

The geology of South Africa cannot be completely explained without discussing the formation (ca. 550 Ma) and break apart (ca. 200-180 Ma) of the great Gondwana Supercontinent into the present day continent of Africa, Antarctica and South American (McCarthy and Rubidge, 2005; Seton et al., 2012; Mortimer et al., 2019).The rifting of Gondwana resulted in the deposition of sediments into the Agulhas Sea that were lithified to form the rock of the Cape Supergroup. The reverse movement of the Falkland Plateau (i.e. closure of the rift valley) during the Carboniferous to early Permian periods, caused subduction of the South-Atlantic plate beneath the African plate and the folding of the Cape Supergroup sedimentary rocks into the mountains known as the Cape Fold Belt (Table Mountain is a mountain near Cape Town where the strata are not folded owing to the foundation of Cape granite.) (McCarthy and Rubidge, 2005; Seton et al., 2012; Mortimer et al., 2019). The rifting and uplifting of the southern Africa subcontinent, resulted in deposition of the Karoo Supergroup sediments, during Palaeozoic to Mesozoic periods, which was as a result of pressure and weight of the Falkland plateau exerted on the African plate (McCarthy and Rubidge, 2005) (Figure 1.1). The Karoo Supergroup (KS) Era was marked by many volcanic eruptions and kimberlite intrusions. The KS covers approximately two-third of the South African ground surface. It overlies the Cape Supergroup towards the north and east of South Africa.

The Vanrhynsdorp and Nama Group, and the Cape Supergroup are exposed in the south and west section of South Africa (Council of Geoscience Geological map, 2008). Cenozoic deposits and the wind-blown sands of the Kalahari group are also exposed in some areas of the south west and south east, while in the north east, the Archaean age Dominion Group, the Ventersdorp, Witwatersrand, Pongola and Barberton Supergroups, and the Murchison and Limpopo mobile belt are exposed. Proterozoic age of the Transvaal Supergroup, Bushveld and Alkaline complexes, were all exposed on the central and western part of South Africa. The Namaqua and Natal metamorphic province, and sand deposits of the Kalahari Group covered the northwestern part of South Africa (Figure 1.1).

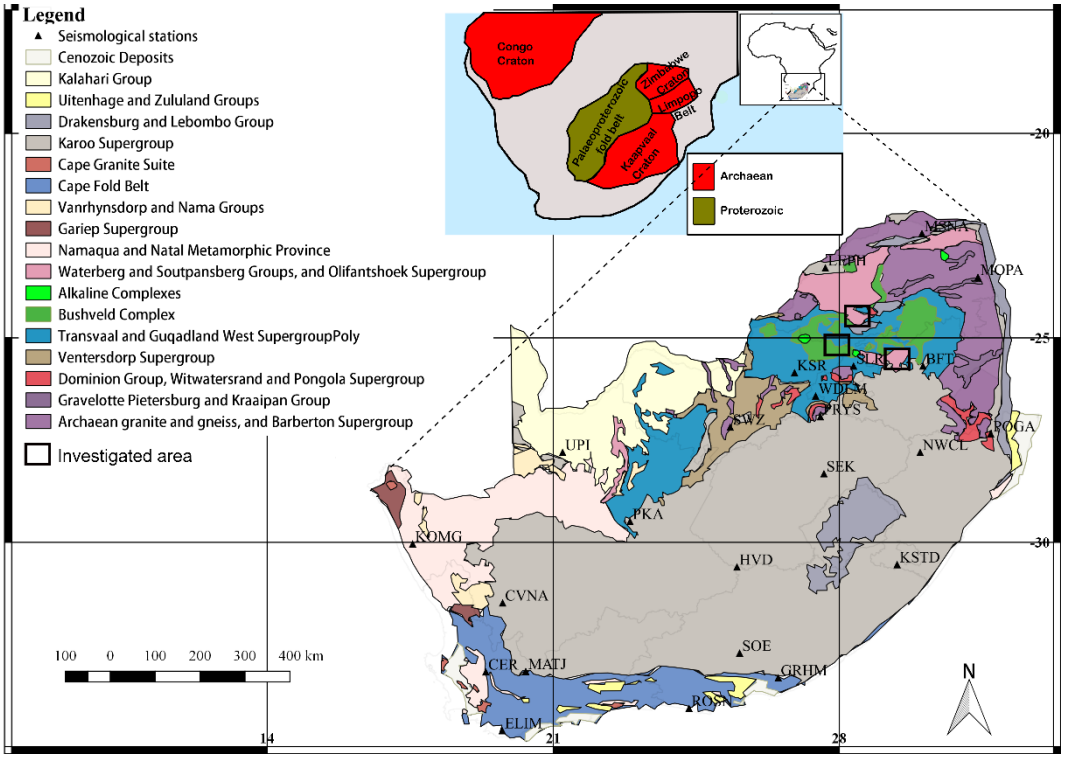


Figure 1.1: Geology of South Africa showing the locations of the investigated area and the seismological station positions (Council of Geoscience Geological map, 2008). (Copyright© Council for Geoscience, South Africa, All Right Reserved. First published by the Government printer, 1978). Index top right shows the outline of the cratons in Southern Africa (https://en.wikipedia.org/wiki/Kapvaal/Limpopo_Belt/Zimbabwe_Craton)

1.3. Research motivation

This study of geophysical methods to characterise the near-surface is motivated by the need to mitigate environmental and engineering infrastructural risks and help to sustainably manage groundwater reserves in South Africa.

1.4. Research questions

The research project will seek to answer the following important questions:

I. What are the benefits of near-surface site characterization for South African national building planning programs and hydrogeological investigations?

II. Why is it important to carry out near-surface seismic characterization before structural design and planning by engineers/geotechnical earthquake engineers?

III. What improvements to acquisition, processing and interpretation will benefit future site characterization studies in South Africa?

1.5. Aim and objectives

The aim of this research is to integrate different geophysical methods to provide more reliable and detailed subsurface models for comprehensive site characterization.

The objectives of the research are:

- To obtain images of the subsurface architecture.
- To determine the P- and S-wave velocities of different near-surface layers using seismic methods.
- To determine the depth to the bedrock and thickness of the soil column in the study areas.
- To detect and image possible near-surface anomalies such as voids, sinkholes, subsidence and tunnels.
- To provide significant information for hydrogeological prospecting.
- To determine some earthquake engineering parameters such as soil amplification and fundamental resonance frequency of the soil column.
- To correlate geophysical, geotechnical and earthquake engineering parameters.
- To evaluate the advantages and disadvantages of different seismic methods and acquisition techniques deployed in the field.

1.6. Reference

Anhaeusser, C.R., 2019. The geology and tectonic evolution of the northwest part of the Barberton Greenstone Belt, South Africa: A review. *South African Journal of Geology*, *122*(4), pp. 421-454.

Brodic, B. 2017. Three-component Digital-based Seismic Landstreamer and Methodologies for Infrastructure Planning Applications. Digital Comprehensive Summaries of Uppsala Dissertations from the Faculty of Science and Technology Uppsala 1610. 80 pp: Acta Universitatis Upsaliensis, ISBN 978-91-513-0186-0.

Butler, D.K, eds., 2005. Near-surface Geophysics: Investigations in Geophysics, *Society of Exploration Geophysicists. 13, Tulsa*.

Chaiprakaikeow Susit., 2012. Site Characterization using Reflection and Surface Wave Seismic Surveys, PhD Thesis, Utah State University: All Graduate Thesis and Dissertation paper 1273, pp. 25-119.

Comina, C.S. and Foti, S., 2007. Surface wave tests for vibration mitigation study, *Journal of Geotechnical and Geoenvironmental Engineering*, *13*, pp. 1320-1324.

de Wit, M., Furnes, H., MacLennan, S., Doucouré, M., Schoene, B., Weckmann, U., Martinez, U. and Bowring, S., 2018. Palaeoarchaean bedrock lithologies across the Makhonjwa Mountains of South Africa and Swaziland linked to geochemical, magnetic and tectonic data reveal early plate tectonic genes flanking subduction margins. *Geoscience Frontiers*, *9*(3), pp. 603-665.

Foti, S., 2000. Multistation Methods for Geotechnical Characterization using Surface Waves, Ph.D. Thesis: Politecnico di Torino, Turin, Italy, pp. 10-156.

Foti, S., Parolai, S., Albarello, D. and Picozzi M., 2011. Application of surface-wave methods for seismic site characterization, *Surveys in Geophysics*, *32*, pp. 777-825.

Isiaka, A.I., Durrheim, R.J. and Manzi, M.S., 2018. High-resolution seismic reflection investigation of subsidence and sinkholes at an abandoned coal mine site in South Africa. *Pure and Applied Geophysics*, *176*(4), pp. 1531-1548.

Kramer, S. L., 1996. Geotechnical Earthquake Engineering. *Prentice Hall*, Upper Saddle River, New Jersey.

Malehmir, A., Andersson, M., Mehta, S., Brodic, B., Munier, R., Place, J., Maries, G., Smith, C., Kamm, J., Bastani, M. and Mikko, H., 2016. Post-glacial reactivation of the Bollnas fault, central Sweden: A multidisciplinary geophysical investigation. *Solid Earth*, *7*(2), pp. 509-527.

McCarthy, T. and Rubidge, B., 2005. The Story of Earth and Life. *Struik Publishers*, Cape Town, pp. 159-161, 182, 187-195, 202-207, 267-269, 302.

Miller, R.D., Xia, J., Park, C.B. and Ivanov, J., 1999. Multichannel analysis of surface waves to map bedrock. *The Leading Edge*, *18*, pp. 1392-1396.

Mortimer, N., van den Bogaard, P., Hoernle, K., Timm, C., Gans, P.B., Werner, R. and Riefstahl, F., 2019. Late Cretaceous oceanic plate reorganization and the breakup of Zealandia and Gondwana. *Gondwana Research*, *65*, pp. 31-42.

Nakamura, Y., 1989. A method for dynamic characteristics estimation of subsurface using microtremor on the ground surface: Quarterly Report of Railway Technical Research Institute, Japan, 30, pp. 25-33.

Nogoshi, M. and Igarashi, T., 1970. On the propagation characteristics of microtremor. *Journal of the Seismological Society of Japan*, *23*, pp. 264–280.

Onyebueke, E.O., Manzi, M.S.D. and Durrheim, R.J., 2018. High-resolution shallow reflection seismic integrated with other geophysical methods for hydrogeological prospecting in the Nylsvley Nature Reserve, South Africa. *Journal of Geophysics and Engineering*, *15*(6), pp. 2658 - 2673.

Park, C. B., 1995. Characterization of geotechnical sites by multi-channel analysis of surface waves (MCASW): KGS Fall '95 National Conference, Seoul, pp. 141-148.

Park, C.B., Miller, R.D. and Xia, J., 1999. Multichannel analysis of surface waves (MASW). *Geophysics*, *64*, pp. 800-808.

Semblat, J.F., Kham, M., Parara, E., Bard, P.Y., Pitilakis, K., Makra, K. and Raptakis, D., 2005. Seismic wave amplification, basin geometry vs. soil layering. *Soil Dynamic and Earthquake Engineering*, *25*, pp. 529-538.

Seton, M., Müller, R.D., Zahirovic, S., Gaina, C., Torsvik, T., Shephard, G., Talsma, A., Gurnis, M., Turner, M., Maus, S. and Chandler, M., 2012. Global continental and ocean basin reconstructions since 200 Ma. *Earth-Science Reviews*, *113*(3-4), pp. 212-270.

Stokoe, K.H, II., Sung, H.J. and Richard, D.W., 2004. Some contributions of in situ geophysical measurements to solving geotechnical engineering problems: International Conference on Site Characterization (ISC-2), Porto, Portugal, pp. 15-50.

Stokoe, K.H, II., Wright, S.G., Bay, J.A. and Roesset, J.M., 1994. Characterization of geotechnical sites by SASW method: Geophysical characteristics of sites, ISSMFE, Technical Committee 10 for XIII ICSMFE. *International Science Publishers*, New York, pp. 15-25.

Wang, S. 2017. Joint inversion and integration of multiple geophysical data for improved models of near-surface structures. Digital Comprehensive Summaries of Uppsala Dissertations from the Faculty of Science and Technology 1536. 65 pp. Uppsala: Acta Universitatis Upsaliensis. ISBN 978-91-513-0018-4.

Yilmaz, Ö., Eser, M. and Berilgen, M., 2006. A case study of seismic zonation in municipal areas. *The Leading Edge*, *25*, pp. 319–330.

Yilmaz, Ö., 2015. Engineering Seismology with Application to Geotechnical Engineering. Investigations in Geophysics, *Society of Exploration Geophysics, 17*, pp. 162-512.

Zegers, T.E., de Wit, M.J., Dann, J. and White, S.H., 1998. Vaalbara, Earth's oldest assembled continent? A combined structural, geochronological, and palaeomagnetic test. *Terra Nova*, *10*(5), pp. 250-259.

CHAPTER 2

2.0 Literature review of the geophysical methods

2.1. Seismic equation, elasticity and velocities

Hooke's law of elasticity describes the linear relationship that exists between the induced stresses and the resultant temporary strain due to seismic wave propagation (called elastic deformation). It holds only when the produced strains are infinitesimally small. The term elastic refers to the type of strain that suddenly disappears because of removal of the stress that has caused it. The response of different subsurface media to the wave-induced strains is governed by the elastic constant that regulates the propagation of the seismic wave velocities. The strains due to the passage of seismic waves are usually small and mostly less than magnitude of 10^{-8} (Sheriff and Geldert, 1995), thereby, validating the application of Hooke's law in seismic wave propagation from one medium to another (Figure 2.1).

According to the Hooke's law of linear elasticity, the strain (ε_{ii}) is directly proportional to the stress (σ_{ii}), and the ratio of the stress to the strain gives the elastic constant (C_{ii}) (or an elastic modulus). Therefore, the elastic moduli of different types of deformation such as Young's modulus, rigidity modulus, and the bulk modulus can be estimated using the stress/strain relationship. Moreover, since the relationship is a fourth-order tensor, it can be expressed as shown in equation 2.1a (Kearey et al., 2002):

$$\begin{bmatrix}\sigma_{xx}\\ \sigma_{yy}\\ \sigma_{zz}\\ \sigma_{xy}\\ \sigma_{yz}\\ \sigma_{zx}\end{bmatrix} = \begin{bmatrix}C_{11} & C_{12} & C_{13} & C_{14} & C_{15} & C_{16}\\ C_{21} & C_{22} & C_{23} & C_{24} & C_{25} & C_{26}\\ C_{31} & C_{32} & C_{33} & C_{24} & C_{35} & C_{36}\\ C_{41} & C_{42} & C_{43} & C_{44} & C_{45} & C_{46}\\ C_{51} & C_{52} & C_{53} & C_{54} & C_{55} & C_{56}\\ C_{61} & C_{62} & C_{63} & C_{64} & C_{56} & C_{66}\end{bmatrix} = \begin{bmatrix}\varepsilon_{xx}\\ \varepsilon_{yy}\\ \varepsilon_{zz}\\ \varepsilon_{xy}\\ \varepsilon_{yz}\\ \varepsilon_{zx}\end{bmatrix} \qquad 2.1a$$

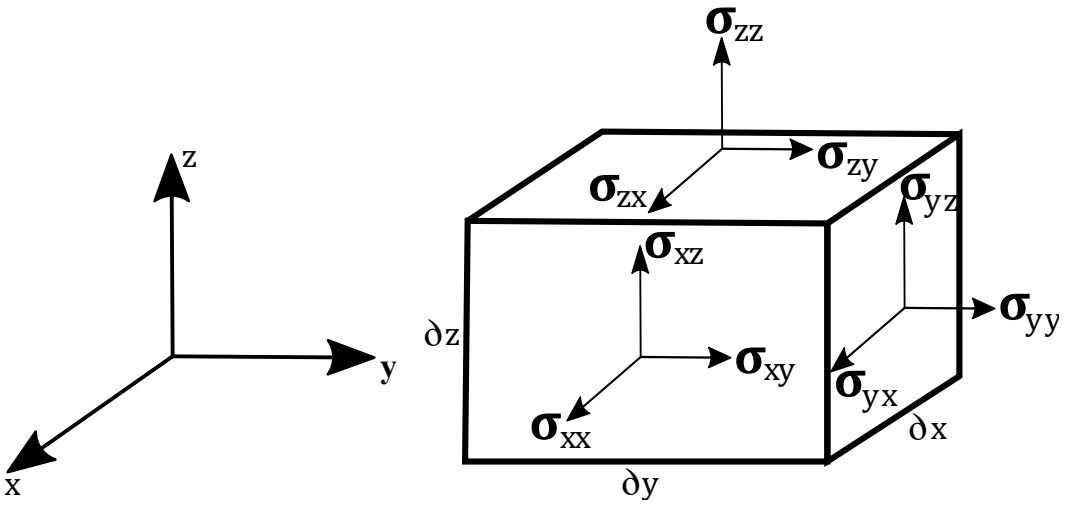


Figure 2.1: Stress components acting on an infinitesimally small volume encircle a point within an elastic material.

Hence, when the longitudinal strain component (ε_{ii}) is proportional to the corresponding longitudinal stress (σ_{ii}) components, the constant of proportionality (C_{ii}) (or elastic constant) is called the Young's modulus (E) under an extensional deformation.

Using the Einstein summation notation:

$\sigma_{xx} = E\varepsilon_{xx}$, $\sigma_{yy} = E\varepsilon_{yy}$, and $\sigma_{zz} = E\varepsilon_{zz}$, 2.1b

i.e. if the shear strain component ε_{ij} is proportional to the corresponding shear stress component σ_{ij}under a shear deformation, then the constant of proportionality is referred to as the modulus of rigidity or shear modulus (μ):

Hence, $\sigma_{xy} = \mu\varepsilon_{xy}$, $\sigma yz = \mu\varepsilon_{yz}$, and $\sigma_{zx} = \mu\varepsilon_{zx}$. 2.1c

The bulk modulus (K) under a hydrostatic pressure is defined as a ratio of pressure (p) to dilatational change in volume. In this case, the shear components are equal to zero under a hydrostatic condition:

$$K = -p/\Delta, \quad 2.1d$$

The reciprocal of the bulk modulus (K) is called the compressibility (K^{-1}).

Under an isotropic condition (i.e. when properties do not depend on the direction), the constant of proportionality as stated by Hooke's law leads to intricate stress and strain relationships that can be expressed in a simple form of equations 2.2 and 2.3 (Timoshenko and Goodier, 1951; Love, 1944):

$$\sigma_{ii} = \lambda\Delta + 2\mu\varepsilon_{ii} \qquad (i = x, y, z), \qquad 2.2$$

$$\sigma_{ij} = 2\mu\varepsilon_{ij} \qquad (i, j = x, y, z: i \neq j). \qquad 2.3$$

The proportionality **λ** and **μ** are known as Lamê's constants, where **μ** represent the measure of the resistance to shearing, also referred to the modulus of rigidity, incompressibility, or shear modulus.

If a longitudinal strain increases along the x-direction (ε_{xx}), it results in a longitudinal strain decrease in the y- and z- directions ε_{yy} and ε_{zz}, respectively. Note that these strain components are negative and proportional to ε_{xx}. The constant of proportionality (***ν***) is called the Poisson's ratio with stress – strain relationship of:

$$\varepsilon_{yy} = -\nu\varepsilon_{xx} \text{ and } \varepsilon_{zz} = -\nu\varepsilon_{xx}. \qquad 2.4$$

Thus, under an isotropic condition, P- and S-wave velocities can be estimated using the elastic constant C_{11} and C_{44}, respectively, as stated below (Thomsen, 1986 and 2002):

$$V_P = \sqrt{\frac{C_{11}}{\rho}} = \sqrt{\frac{K + 4/3\mu}{\rho}}, \qquad 2.5$$

$$V_P = \sqrt{\frac{C_{44}}{\rho}} = \sqrt{\frac{\mu}{\rho}}, \qquad 2.6$$

where ρ is the density of the media.

Hence, with shear and constrained stiffness ($M_o = K + 4/3\mu$), various other elastic parameters such as Young's modulus (E), Bulk modulus (K) and Poisson's ratio (ν) can be determined as well as their relationships with one another and Lamê's constant parameters (**λ** and **μ**):

$$E = 2\mu\,(1+\nu) \quad \text{or} \quad \frac{\mu(3\lambda+2\mu)}{\lambda+\mu}, \tag{2.7}$$

$$K = \frac{1}{3}M_0\left(\frac{1+\nu}{1-\nu}\right) \quad \text{or} \quad \frac{1}{3}(3\lambda+2\mu), \tag{2.8}$$

$$\mu = \frac{\frac{1}{2}(V_P/V_S)^2-1}{(V_P/V_S)^2-1}, \tag{2.9}$$

$$V_P = V_S\sqrt{\frac{1-\nu}{0.5-\nu}}, \tag{2.10}$$

$$\text{where } \upsilon = \frac{\lambda}{2(\lambda+\mu)} \text{ and } \lambda = \frac{E\upsilon}{(1+\sigma)(1-2\sigma)}. \tag{2.11}$$

Equation 2.5 and 2.6 shows that the P- and S-wave velocities are sensitive to various subsurface properties such as density, bulk and shear moduli. These velocities increase with increasing confining pressure (Yilmaz, 2015). The P-wave velocity is greater than S-wave velocity in any material. Integrating different velocity information and the elastic properties provide better constrained subsurface image and assist in calculating parameter such as V_P/V_S ratio which is often used as a lithological fluid indicator in oil and gas exploration. Furthermore, the elastic moduli such as shear modulus and Poisson's ratio are very significant parameters in geotechnical, geochemical and engineering site characterization.

2.2. Seismic waves

Seismic waves are elastic waves that propagate through the Earth's layers. They are caused by earthquakes, volcanic eruptions, magma movement, large landslides and man-made sources (such as dropped weight and hammer blows), mechanical vibrators (Vibroseis) and bubbles of high-pressure air injected into water. Natural and anthropogenic sources of ambient seismic noise include traffic and mechanical noise; these types of noise generate low-amplitude and low-velocity seismic waves (Kramer, 1996; Shearer, 2009). The velocity of the seismic waves depends on the density and elasticity of the medium through which it propagates. Seismic wave velocity tends to increase with depth along the path of propagation and ranges from approximately 0.1 to 8 km/s in the Earth's crust, and about

13 km/s in the lower mantle (Sammis and Henyey, 1987; Sheriff and Geldart, 1995; Shearer, 2009).

2.3. Types of seismic waves

2.3.1. Body waves

Body waves propagate through the interior of the Earth. There are two types of body waves, namely, primary and secondary waves.

2.3.1.1. Primary waves

Primary waves (P-waves) are compressional, dilatational and longitudinal waves; the movement or displacement of the particle motion is along the direction of propagation (Figure 2.2). The speed of propagation is faster than any other type of waves that travel through the Earth and first to arrive at seismograph stations. These waves propagate through any kind of materials including fluids, and travel faster than S-waves. P-waves take the form of sound wave in the air with approximate speed of 330 m/s, about 1450 m/s in water and 5000 m/s in granite (Sammis and Henyey, 1987). The velocity of the P-wave (V_P) depends on the constrained stiffness (M_o) and density (ρ) of the material as given by the equation. The P-wave velocity and the governing parameters are given by the relationship in equation (2.5).

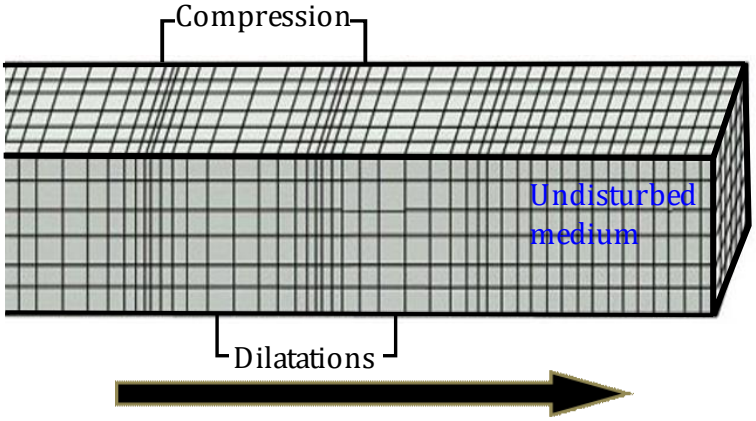


Figure 2.2: P-wave propagation (modified after Shearer, 2009).

2.3.1.2. Secondary waves

Secondary waves (S-waves) are shear waves, transverse or rotational waves in which the particle motion vibrates 90^{o} to the direction of propagation (Figure 2.3). S-waves arrive at seismic stations after the P-waves following an earthquake event (Sheriff and Geldart, 1995). The particle motion displacement can be horizontally or vertically polarized depending on the medium at which the seismic wave is propagated (Bolt, 1982). S-waves cannot propagate through fluids (liquids and gases, since fluids do not support shear stress), but can travel through solid materials. The speed of propagation (S-wave) is approximately 60% of that of P-waves in any given material (Sheriff and Geldart, 1995). The S-wave velocity (V_S) depends on the shear stiffness (μ) and density (ρ) of the material (equation 2.6).

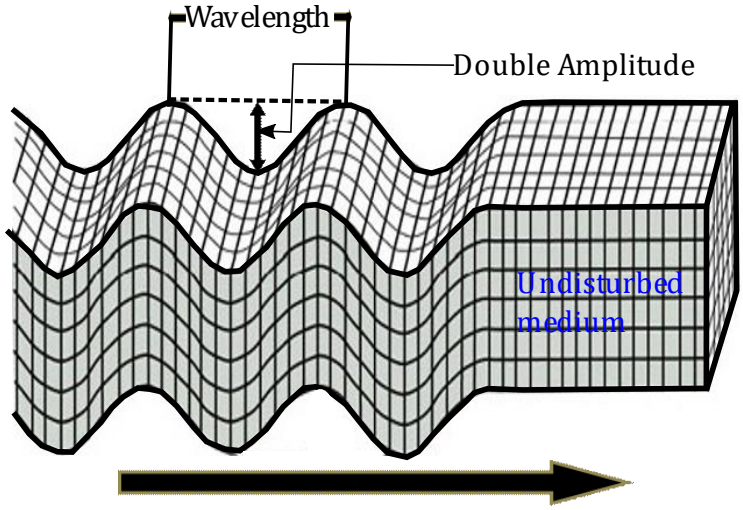


Figure 2.3: S-wave propagation (Modified after Shearer, 2009).

2.3.2. Surface waves

Surface waves are seismic signals that propagate along or near to the surface (Bolt, 1982; Sheriff, 2002). The seismic waves have both longitudinal and transverse wave's characteristics, and the direction of particle motion is both parallel and perpendicular to the direction of wave motion. Surface waves are dispersive by nature and their phase velocities are frequency dependent. The wavelength depends on both velocity and frequency. This implies that different frequency components sample different depths due to its dispersive nature. The

body and surface waves amplitude diminish away from the source (but in a different manner) with 1/r and 1/square root(r), respectively (r = radius). The speed of propagation is slower than that of the body waves (P-wave and S-wave), and the phase velocities are less than P-wave velocities and equal or less than that of S-wave velocities. The amplitude of surface wave can be up to several centimeters in large magnitude earthquakes (Bolt, 1982). There are different types of surface waves, namely Rayleigh and Love waves.

The particle motion of the Rayleigh waves (also known as ground roll) propagate near the surface and retrograde elliptical with respect to the direction of propagations similar to waves on the surface of water (Figure 2.4) (Rayleigh, 1885). Note that the restoring force for all type of seismic waves is elastic, not gravitational, which is the case for water waves. The velocity of Rayleigh wave is less and slower than that of body waves velocities, roughly about 90% of the velocity of S-waves for a typical homogeneous elastic media. In a layered medium (half-space), the Rayleigh wave velocity (V_R) depends on their frequency (f) and wavelength (λ_R), and its amplitude decreases exponentially with depth (Sheriff and Geldart, 1995). The particle motion is also confined to the vertical plane and the apparent phase velocity (V_{phase}) is given by equation (2.12):

$$V_{phase} = 2\pi f / k, \tag{2.12}$$

where k is the wavenumber (cycles/m) and f is the frequency (cycles/sec) (Park et al., 1999). A good approximation for V_R in terms of V_S and Poisson's ratio (ν) was proposed by Achenbach (1975):

$$V_R \cong \frac{0.874+1.117\nu}{1+\nu} V_S. \tag{2.13}$$

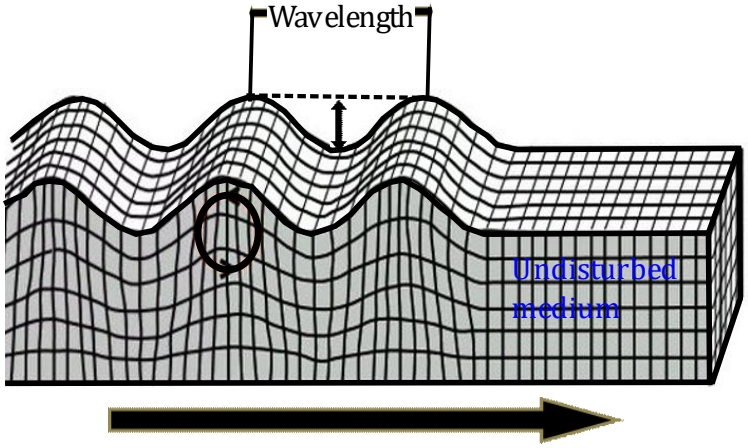


Figure 2.4: Rayleigh wave propagation (modified after Shearer, 1999).

2.4. Seismic methods

Seismic methods are based on the time interval between the commencement of a seismic (elastic) wave at the impact station/point and its arrival at the detectors. The seismic wave is detected using a geophone, accelerometer or fibre optic cables when surveying on land (Figure 2.5a) or hydrophone when surveying in water. A geophone converts a mechanical ground motion into an electrical voltage signal that can be recorded. It consists of an outer coil suspended by springs and a stable inner magnet. Once the ground motion causes coil displacement, this is in return generates a voltage signal that is proportional to the velocity of the coil-inner magnet motion. Geophone contains an electronic component (damping resistor) used to flatten amplitude responses above the coil natural frequency. The digitized voltage signals from individual channels are temporarily stored in a seismograph or seismic recorder internal memory buffer, and systematically forward to a computer or a laptop for storage and further analysis (processing and interpretation) (Figure 2.5a and b). In summary, geophones are sensitive to particle motion while hydrophones are sensitive to pressure difference (a ceramic hydrophone generates a voltage when deformed by passage of a seismic wave).

These recorded seismic wave signals are used to image the subsurface architecture through which the waves propagate. As these waves propagate through the subsurface, they tend to reflect, refract, diffract or transmit through different media due to the impeding geological discontinuities. However, some amount of

the input energy will be attenuated due to scattering, absorption and geometrical spreading (Sheriff and Geldert, 1995; Sheriff, 2002). The seismic method has been applied by members of the seismology research group at the University of the Witwatersrand in various applications, ranging from lithospheric-scale imaging (Andriampenomanana et al., 2017), mineral exploration (Durrheim, 1986; Manzi et al., 2012a, 2012b and 2013) to near-surface mapping (Onyebueke et al., 2018; Isiaka et al., 2018).



Figure 2.5: Seismic acquisition testing. (a) A laptop displaying recorded signal and geophone array, (b) is showing the Geode seismograph and trigger cable.

2.4.1. Reflection seismic method

The seismic reflection method is the most commonly used geophysical method for oil and gas, and deep mineral exploration. The theoretical background of the method is well documented in many geophysics' textbooks (Yilmaz, 2015;

Yilmaz and Doherty, 2001; Dobrin and Savit, 1988; Burger, 1992). The principle of the seismic wave propagation in seismic reflection method is shown in Figure 2.6. Generally, the body waves are generated using either vibratory sources, explosive or impact sources. The waves that reflected from geological boundaries are detected and measured by geophones (Figure 2.6). The main purpose of a reflection seismic survey is to delineate the geometry of the subsurface structures with advantage of deeper penetration depth (Yilmaz, 2015). Seismic reflection method is mostly used for oil and gas exploration. Durrheim (1986); Pretorius et al. (2007); Eaton et al. (2010) Manzi et al. (2012a and b, 2013) and Malehmir et al. (2016) have described the successful application of the seismic reflection method in mineral exploration. The technique has also been used for resource evaluation, mine planning and development (Pretorius et al., 2007; Manzi et al., 2013, Malehmir et al., 2012) and for mine safety by mapping of subsurface structures such as faults, joints, fractures and weak zones (Gibson et al., 2000; Manzi et al., 2014; Manzi et al., 2012a and 2012b).

In site characterization, the seismic reflection method is used to derive the subsurface image and geometry of the near-surface layers, and the thickness of the soil column based on the velocity of the seismic wave that travels through the medium (Onyebueke et al., 2018; Chaiprakaikeow, 2012; O'Donnell et al., 2001; Yilmaz, 2015). There are many challenges in applying the method for near surface engineering and hydrogeological investigations. This is due to the multiple reflections from near-surface acoustic impedance contrasts and misinterpretation of the ground-coupled air wave, guided wave and reverberation of refracted wave as a true reflection seismic wave (Steeples and Miller, 1995). Shallow reflections require higher frequency waves than deep reflection profiling. These high frequency waves are subjected to large attenuation within the weathered layer, and there are higher levels of environmental noise at these higher frequencies, which require high noise attenuation and signal processing (Yilmaz, 2015). Much research has been done in South Africa in the area of reflection seismic imaging as applied to mineral exploration and mining (Durrheim., 1986; Gibson et al., 2000; Trickett et al., 2006; Pretorius et al., 2007; Campbell., 2009; Manzi et al.,

2012a, 2013), but not much has previously been done in the area of site characterization.

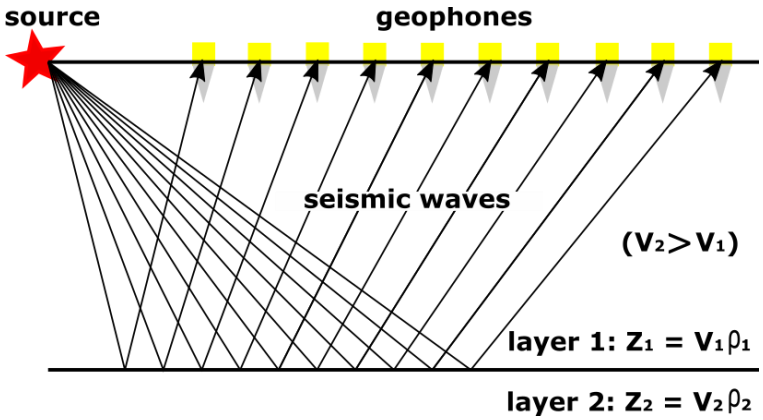


Figure 2.6: Seismic reflection in a single flat layer. Where V, Z and ρ is velocity, horizon thickness and density, respectively.

2.4.1.1. Acquisition of active seismic data

Reflection seismic acquisition commonly involves the deployment of tens to hundreds of receiver channels for shallow surveys and up to several thousand receiver arrays in the case of large-scale deep reflection seismic surveys. The recorded seismograms may be displayed and analysed in different ways, most commonly as a shot gather (display of seismic traces recorded by multiple receivers from a single source as a function of offset) and receiver gather (display of seismic traces recorded by a single receiver from different sources as a function of offset). Moreover, seismic traces can also be sorted in different domains during the data processing, such as the common midpoint (CMP) gather (plot of traces having the same midpoint between the source and the receiver) or common depth point (CDP) gather (plot of seismic traces reflecting from the same subsurface depth) (Figure 2.7) (Yilmaz, 2001).

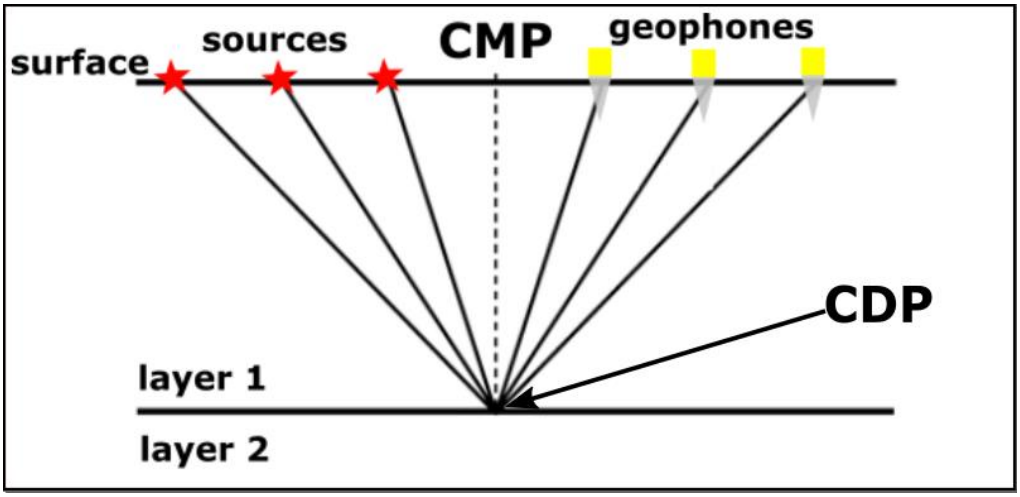


Figure 2.7: Simplified diagram showing Common-midpoint (CMP) gather and Common-depth-point (CDP) of a seismic signal.

Seismic data can be acquired in either 2D profile or 3D grid (regular, irregular, or any other pattern that provide pseudo 3D CDP coverage), depending on the arrangement of the receiver array. In 2D acquisition, the receivers and the seismic source are located along the same profile (it can be a crooked or a straight profile). The spread can either be roll-along or asymmetrical about the sources. The roll-along spread involves end-on-shot (either forward or reserve) and centre shot (Figure 2.8a and b), while an asymmetric spread involves shooting along a fixed receiver geometry as used during the data acquisition of Chapter 3 and 4 (Figure 2.8c). However, 3D acquisition technique involves arrangement of the receiver array along an XY grid (the inline and crossline) line with the source moving through the spread in a systematic manner to obtain equal fold and ensure good source-receiver offset-azimuth coverage (Ashton et al., 1994; Yilmaz and Doherty, 2001). Ultimately, reflection seismic surveys are planned to obtain a consistent multiplicity of common-midpoints within the target zone.

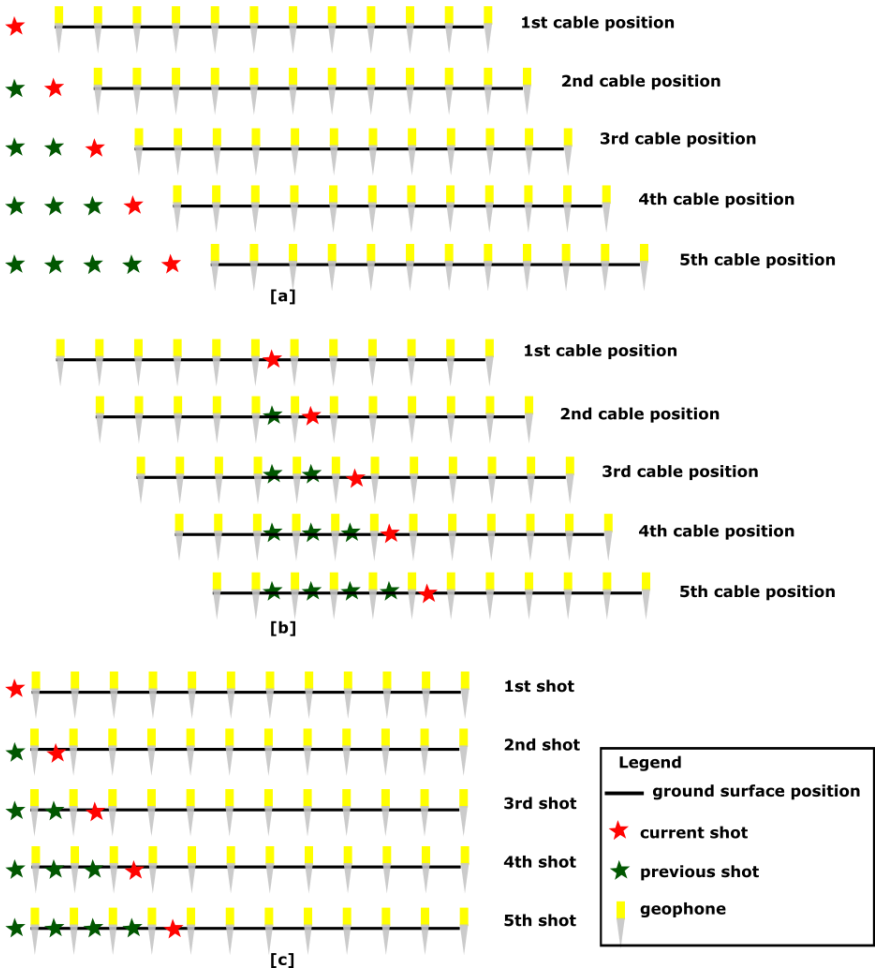


Figure 2.8: Different types of seismic acquisition techniques. (a) forward end-on shot roll-along acquisition type, (b) centre-shot roll-along acquisition type, (c) fixed receiver asymmetric acquisition type.

2.4.2. Refraction seismic method

The seismic refraction method has been deployed widely for near-surface characterization because of its simplicity in acquisition and processing (Socco and Boiero, 2008; Ivanov et al., 2005a and b). It is an established geophysical method for non-invasively mapping of the soil column velocities and soil-bedrock interfaces for geotechnical/engineering, environmental, hydrogeological and earthquake engineering problems. The method is based on the ability to detect the first arrival head waves that are critically refracted from the interface between two layers of different velocities (where velocity of the underlying layer is higher than the velocity of the upper layer) (Foti et al., 2003; Ivanov et al., 2005a and b)

(Figure 2.9). Seismic signals are generated with an active source (such as a sledgehammer impacting a metallic plate, weight drop, vibratory source or explosive charge) and the waves refracted by a higher velocity layer are detected using geophones (Figure 2.9).

The seismic refraction method has several limitations, such as the "hidden layer" problem, which is the inability to detect a low velocity layer imbedded within adjacent higher velocity layers, and arrival times that are related to unknown travel paths (Whiteley and Greenhalgh, 1979; Pant and Vijaya Raghava, 1987). Some professionals, however, have argued that the seismic refraction results can be used as a deterministic truth (Backus and Gilbert, 1967; Menke, 1989; Jaynes, 2003). In contrast, several authors have shown evidence of non-uniqueness that affects seismic refraction results, especially if no independent information is introduced to constrain travel-time interpretation. For example, Foti et al, (2003) have shown that a surface wave survey performed using the same acquisition layout as the seismic refraction survey can provide a good estimation of the velocity profile. Ivanov et al, (2005a; 2005b) have also demonstrated, using synthetic data for a simple three-layer case, that different lithologic columns could give the same P-wave travel-times in the presence of a hidden layer.

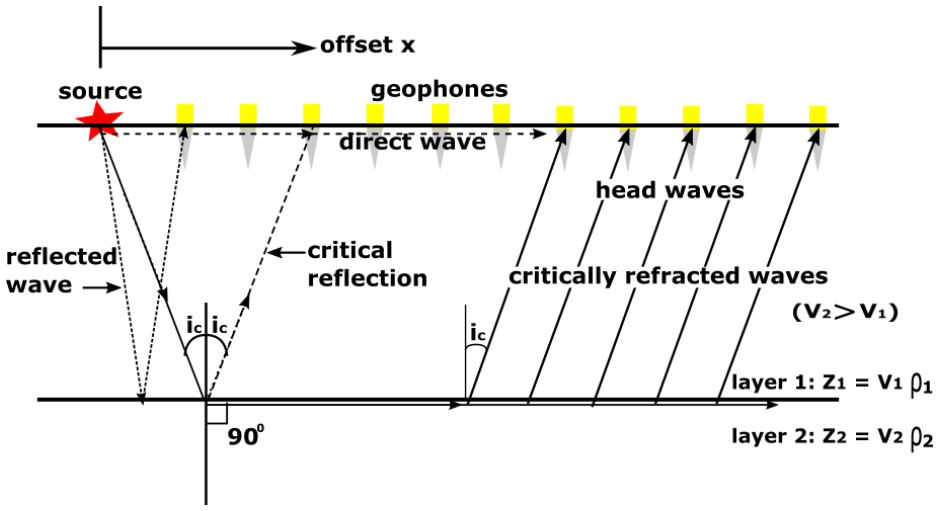


Figure 2.9: Seismic events in a single flat layer, where V, Z and ρ is velocity, horizon thickness and density, respectively.

2.4.3. Multichannel Analysis of Surface Waves (MASW)

Surface waves have been used to characterised the Earth's interior. There were major improvements in numerical analysis and instrumentation for recording seismic signals associated with earthquakes due to the advent of electronics and computers (Dziewonski and Hales, 1972; Aki and Richards, 1980; Ben-Menaham and Singh, 2000). Application of surface wave method in engineering investigation started with the steady state Rayleigh wave method (Jones, 1958). Stokoe et al. (1994) introduced the SASW (Spectral Analysis of Surface Waves) method. The next development was the multichannel analysis of surface waves (MASW) method by Park et al. (1999); Miller et al. (1999) and Xia et al. (1999) of the Kansas Geological Survey and the University of Kansas. The MASW method makes use of multi-mode surface wave energy, which improves the resolution and reliability of inversion of the shear wave velocity model. (Figure 2.10).

The MASW method has been successfully applied to various types of geotechnical and geophysical projects such as mapping of the bedrock interface and determining the shear modulus and thickness of near-surface materials (Miller et al., 1999). In addition, the MASW has also found applications in the generation of shear-wave velocity profiles (Xia et al., 2000), seismic evaluation of pavements (Ryden et al., 2001), seismic characterization of sea-bottom sediments (Park et al., 2005), as well as mapping of fault zones (Ivanov et al., 2006). MASW has also been applied to earthquake engineering design and site characterization for seismic risk assessment involving the near-surface shear wave velocity classification of top soil. According to the National Earthquake Hazard Reduction Program (NEHRP) and Eurocode 8 (EC8), the average shear wave velocity for the top 30 m of soil column (V_S^{30}) is related to the thickness (h_i) and shear wave velocity (V_i) of individual subsurface layer by the following equation 2.14 below, and can be classified according to the softness and stiffness of the subsurface material (BSSC, 1994) (Table 2.1).

$$V_S^{30} = \frac{\sum_{i=1}^{n} h_i}{\sum_{i=1}^{n}\left(\frac{h_i}{V_i}\right)}. \qquad 2.14$$

Table 2.1: Site classification scheme defined in Building Seismic Safety Council (BSSC, 1994).

Classification	**V_s^{30}(m/sec) average shear wave velocity in the upper 30 m**	**Description**
A	>1500	Hard rock material
B	760-1500	Rock
C	360-760	Very dense soil and soft rock
D	180-360	Stiff soil
E	<180	Soft soil

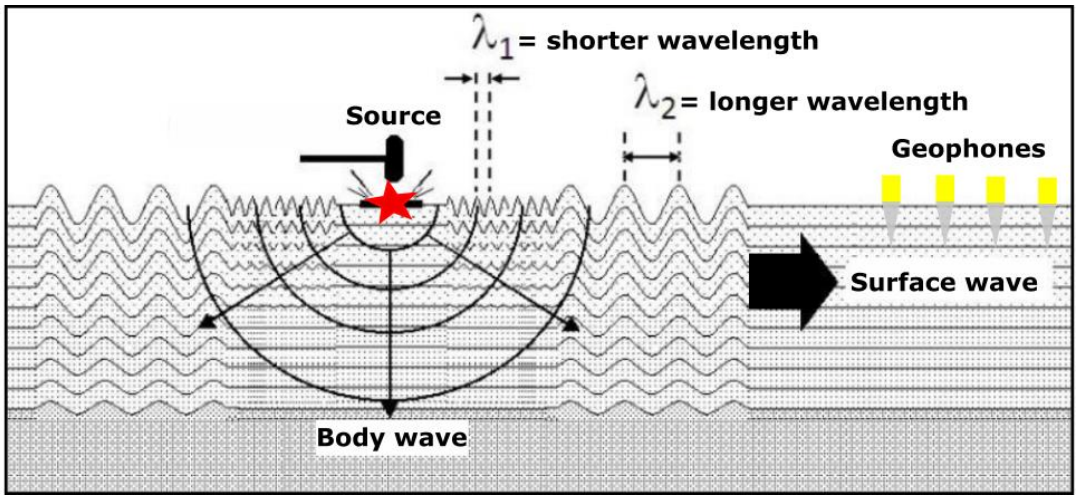


Figure 2.10: Surface wave propagation in an inhomogeneous media and multi-channel record (modified after Park et al., 1999). λ_1 and λ_2 represent the change in the wavelengths of the seismic wave as it propagates away from the point source.

2.4.4. Horizontal-to-Vertical Spectral Ratio (HVSR) techniques

Local site effects are one of the most important parts in seismic risk assessment and in the investigation of the local response of specific sites (Kramer, 1996; SESAME, 2004). Nakamura (1989) revived the Horizontal-to-Vertical spectral ratio technique (HVSR), first proposed by Nogoshi and Igarashi (1970; 1971). Since then, many studies have been published in the field of site effect estimation using both empirical and numerical methods. The numerical methods allow a detailed analysis of the parameters considered in the evaluation using available

information about the geological structure (Dravinski et al., 1996). Empirical methods are based on seismic records at sites with different geological conditions, from which the fundamental resonance frequency (natural period of the soil column) and relative amplitudes can be directly determined. For these reasons, the use of ambient seismic noise is becoming popular as an alternative to other geophysical methods in near-surface site characterization (Bard, 1998; Okada, 2003; Pratt et al., 2003; Aki, 1993).

The resonance frequencies of the ground motion have a close relationship with physical properties of the site under study, i.e., shear wave velocities, layer thicknesses and densities (Kramer, 1996). Estimation of this resonance frequency is useful for the evaluation of the physical properties at a given site (Bard, 1998; Okada, 2003; Nakamura, 1989) (Figure 2.11). The Nakamura technique (Nakamura, 1989), based on the horizontal to vertical spectral ratio (HVSR), has been commonly used to estimate the site effects. Later it was extended to both weak (Ohmachi et al, 1991; Field and Jacob, 1995) and strong ground motions (Lermo and Chavez-Garcia, 1993). Their results had showed that the HVSR can be used to estimate the fundamental resonance frequency at a site based on earthquake data and weak ground motion. Therefore, the HVSR technique is a cost effective, fast and attractive geophysical method (Field and Jacob, 1993 and 1995; Lermo and Chavez-Garcia, 1994; Bard, 1999).

Furthermore, the modification of the ground motion due to the subsurface structures in the site can be related to different factors (Kramer, 1996; Safak, 2001). The main factor is the acoustic impedance (Z) contrast between the soil column and the underlying bedrock. The impedance contrast determines how strongly the waves at particular frequencies (the fundamental resonance frequency and the higher harmonics) are multi-reflected within the upper layer. Making a simplifying assumption of vertical propagation of the S-waves, the modulus of the 1-D site amplification function A(f) is described by the following relation:

$$|A(f)| = \sqrt{\left(\frac{(1+Rc)^2}{1+2Rcos(4\pi f\tau)+Rc^2}\right)}, \qquad 2.15$$

where Rc is the reflection coefficient that is related to the acoustic impedance contrast ΔZ and τ is the travel time of the S-waves in the soil column. The peak of A(f) is obtained when $\cos(4\pi f\tau)$ is equal to -1 that is when $f = 1/(4\tau)$ (Safak, 2001). This value of f is defined as the fundamental resonance frequency (F_0).

According to the relationship by Nakamura (1989):

$$F_0 = \frac{V_{S1}}{4h_1}, \qquad 2.16$$

where V_{S1} and h_1 are the shear wave velocity and thickness of the soil column, respectively.

The amplification factor A_0 for this frequency is related to the acoustic impedance. If the densities of the basement and surface layer are the same, then:

$$A_0 = \frac{V_{S2}}{V_{S1}}, \qquad 2.17$$

and the depth to bedrock (h) is given by:

$$h = \frac{V_{S2}}{4A_0F_0}, \qquad 2.18$$

where V_{S2} is the S-wave velocity of the bedrock.

Following Arai and Tokimatsu (2000; 2004), the HVSR results determined from the field data are a combined effect of both Rayleigh and Love waves as stated below:

$$HVSR(f) = \sqrt{\frac{\alpha H_L(f) + H_R(f)}{V_R(f)}}, \qquad 2.19$$

where H_R and V_R are the Rayleigh wave contribution in terms of power spectra on the horizontal (H) and vertical (V) axes, while H_L is related to Love waves (the parameter α is an integer which can be considered as the number of waves in the background microtremor). The local site effect (represented by the shape of the Fourier spectra amplitude ratio between the surface recording and the input ground motion at the bedrock) is then determined by the S-wave velocity and the

thickness of the soil layer, which determine the frequencies that are affected by amplification, while the impedance contrast controls the amplification level.

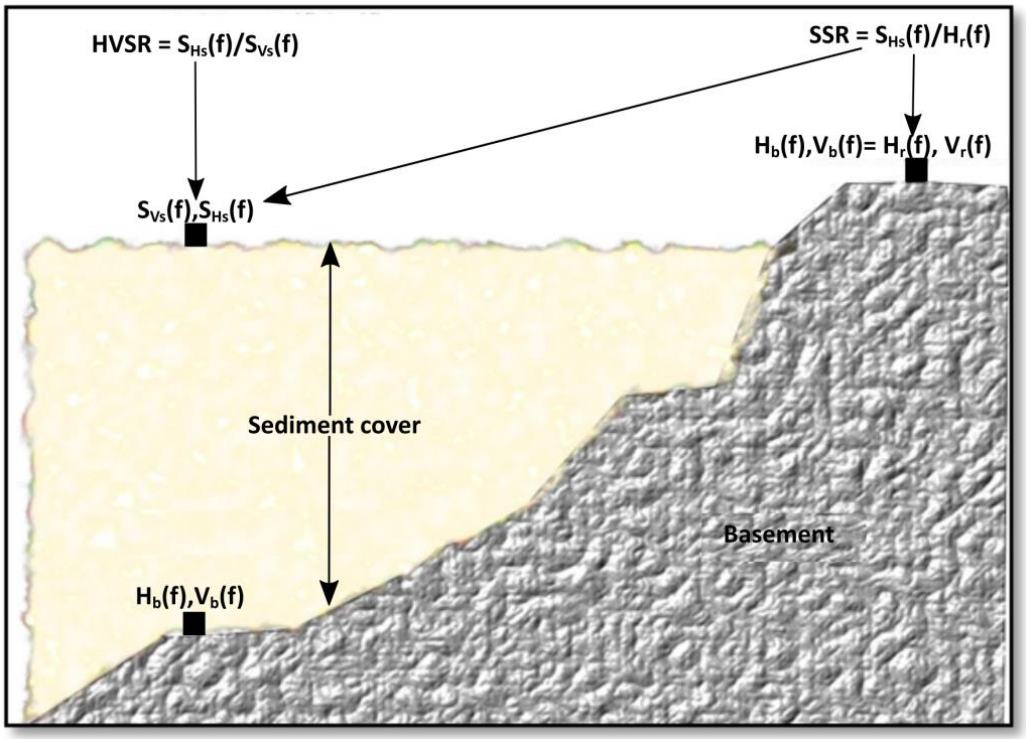


Figure 2.11: A typical geological structure used by Nakamura (2000) to explain the HVSR technique. Note SSR – standard spectral ratio technique, $H_r(f)$ and $V_r(f)$ are the horizontal and vertical spectra components recorded on exposed bedrock rock, $H_b(f)$ and $V_b(f)$ are the horizontal and vertical spectra components on the basement covered by sediments, $S_{Hs}(f)$ and $S_{Vs}(f)$ are the spectra components recorded on the surface above the sediments.

2.4.5. Seismic resolution and reflectivity

The seismic resolution limit is the minimum spatial and temporal separation between two seismic events in which they can still be resolved and distinguished separately i.e. the minimum thin bed the wavelet could image and the minimum time interval between two reflections that can still be picked without ambiguity (Chaouch and Mari, 2006). The ability to properly image the minimum resolvable subsurface geological structures depends critically on the dominant frequency and wavelength of the propagating seismic waves, as well as the acquisition geometry

(shot and receiver density) and the complexity of the geological structures (Yilmaz, 2001; Sheriff and Geldart, 1995).

Normally the depth to a reflector is measured using the two-way travel-time (i.e. the time it takes seismic wave from the source to the reflector and back to the receiver). The dominant frequency (F_D) of the seismic signal decreases with increasing depth because of attenuation, while the wavelength and the velocity of subsurface materials increases. These processes result in lower seismic resolution at deeper depth, while higher F_D gives greater resolution at the near-surface. Therefore, digital frequency filters are normally applied to remove the lower frequencies and enhance the higher frequencies to improve the resolution of near-surface data. The F_D affects both the horizontal and vertical seismic resolution. Moreover, the dominant wavelength (λ) of seismic wave is a function of the interval velocity (V_i) and F_D as given in equation 2.20:

$$\lambda_D = \frac{V_i}{F_D}. \qquad 2.20$$

Vertical seismic resolution is the ability to recognise and separate different vertical features. This limit of resolution is also called the tuning thickness (Kallweit and Wood, 1982). The vertical resolution is estimated using the seismic wavelength. Subsurface geological layer or structure can be resolved when its thickness is above $1/4$ wavelength, while layers as small as $1/32$ wavelength can still be detected depending on the impedance contrast, signal to noise ratio and acquisition geometry. However, the acceptable criterion when referring to vertical resolution is usually limited to $1/4$ wavelength (Widess, 1973; Brown, 1999; Yilmaz, 2001).

In seismics, the horizontal resolution can be described as a measure of how close two reflecting points can be and still recognized in the seismic section. The horizontal resolution is governed by the Fresnel-zone, which represents the area of a reflector covered by the seismic wavelet of a certain two-way travel-time (depth). Over a buried horizon, all discernible geological features with a lateral extent greater than the radius of the Fresnel zone will be resolvable.

The radius of the Fresnel zone (R_f) is giving by:

$$R_f = \sqrt{\frac{d_r \lambda_D}{2}} = \frac{V_i}{2}\sqrt{\frac{t_0}{F_D}}, \qquad 2.21$$

where the d_r and t_0 represent the depth to the reflector and the two-way travel time at the same depth, respectively (Kallweit and Wood, 1982; Brown, 1999; Yilmaz, 2001).

Migration of the seismic data reduces the length of "R_f" and focuses the energy spread within the Fresnel zone, thereby, repositioning the reflections and improves the horizontal resolution to about $1/4$ wavelength (Chaouch and Mari, 2006).

The seismic reflectivity depends on the change in acoustic impedance (Z) between two adjacent layers and can be referred to as reflection coefficient (R_C). R_C describes how much seismic wave is reflected at the impedance discontinuity, which is also equal to the ratio of the amplitude of the reflected wave to the incident wave as show below:

$$A_r = R_C A_i \, , \qquad 2.22$$

where A_r is the reflected wave amplitude and A_i is the incident wave amplitude and R_C can be defined as follow:

$$\mathrm{R_C} = \frac{\mathrm{Z_2 - Z_1}}{\mathrm{Z_2 - Z_1}}, \qquad 2.23$$

where Z (the acoustic impedance) is the product of density (ρ) and velocity (V) of the respective layers (Figure 2.9).

The value of R_C typically varies from -1 to +1. It becomes negative when the layer below the interface has lesser acoustic impedance than the overlaying horizon. In this case, the polarity of the reflecting seismic wave becomes opposite to that of the incident seismic wave. Generally, before any boundary discontinuity will generate a clear reflection on the seismic section, the R_C will be at least ≥ 0.06. A large R_C value between any geological interfaces indicates less energy

transmission, high reflectivity at the boundary, and high signal-to-noise ratio of the reflected seismic wave.

2.4.6. Seismic wave scattering and attenuation

Seismic wave energy decays as it travels away from the source due to geometric spreading, material absorption or scattering (Figure 2.12). This is because their energy is disseminated at every point of an expanding seismic wavefront. The attenuation of the seismic wave in rock is related to the combination of the subsurface material and proportional to its frequency. Therefore, it varies when there are changes in the material composition. Hence, the higher-frequency components of transmitting seismic waves are more attenuated compare to the lower-frequency components. The intensity (energy per unit area of the wavefront) of seismic energy decreases as the seismic wave spherically radiates away from the source (Figure 2.12). The loss of amplitude (A_0) due to geometrical spreading is inversely proportional to the spherical radius (r) at a given wavefront ($1/r_n$) in a homogeneous medium (Lowrie, 1997, Yilmaz, 2001) (Figure 2.12). Therefore, the A_0 loss at a given two different wavefront radius r_1 and r_2 can be estimated as follows (Figure 2.12):

$$A_0 = log_{10}\frac{r_1}{r_2};\ A_0 \text{ is in decibel (dB).} \qquad 2.24$$

However, the amplitude loss (A_n) because of intrinsic attenuation caused by energy absorption due to shear heating at rock material boundaries and mineral particle distribution decreases exponentially as a function of distance from the radiating source. Hence, the energy density decay is proportional to the square of the wavefront radius in a homogeneous medium ($1/r_n^2$) (Yilmaz, 2001). Therefore, the amplitude loss in this case can be expressed with the respect to the wavefront amplitude at a given radius (r_n) distance as:

$$A_2 = A_1 e^{-q(r_2 - r_1)}, \qquad 2.25$$

$$\text{The absorption loss in } (dB) = 10 log_{10} e^{-q(r_2 - r_1)}, \qquad 2.26$$

where n = 1,2,3…., A_1 and A_2 represent the wavefront amplitude at radius r_1 and r_2, respectively, and q is the absorption coefficient of the material. The parameter q represents the amount of energy due to propagation of seismic wave at a certain distance. The value normally varies from 0.25 – 0.75 $dB\lambda^{-1}$ for common subsurface materials (Kearey et al., 2002). Therefore, it can be expressed as function of velocity (V), dominant wavelength (λ) and frequency (F_D) as follows:

$$\text{Absorption loss in dB} = \frac{1.1\, F_D (r_2 - r_1)}{V}. \qquad 2.27$$

This indicates that at a fixed seismic velocity, the energy loss due to absorption depends on the frequency and the distance from the source.

Scattering attenuation is the non-uniform and diffuse dispersion of waves caused by inhomogeneities in the medium through which the energy is propagating (Sheriff, 2002). Scattering takes place due to point features reflecting, refraction or diffracting from a point source, and elastic energy conversion due to wavelength-scale irregularities in the medium. These deformities are due to intermittent or swift variations in the density and/or velocity of the medium.

Seismic wave attenuation is a useful seismic characteristic because it is very sensitive to rock properties and is extensively used to identify fluid content and zones of high permeability in hydrocarbon exploration and reservoir characterization (Winkler and Nur, 1982; Kilmentos, 1995). Note, high porosity and Vp/Vs ratio correspond to higher attenuation, while completely dry rocks reveal negligible attenuation. Amplitude equalization and the AGC algorithm can be used to recover amplitude loss due to geometrical spreading during seismic data processing based on the equation (2.27 and 2.28) (Evans, 1997).

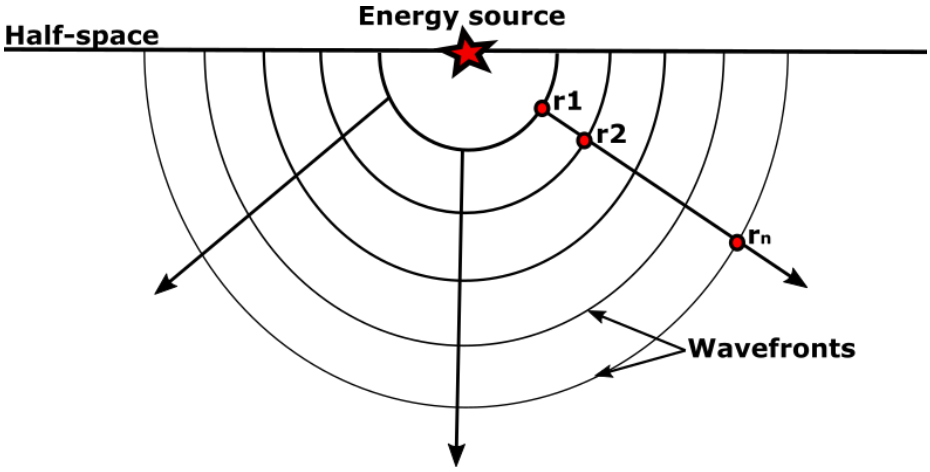


Figure 2.12: Geometrical spreading of seismic energy from a known source

2.4.7. Seismic attributes

Seismic attributes are measured and computed post-stacked reflection seismic quantities obtained from stacked and/or migrated seismic data. These attributes are an outcome of quantities derived from the complex (analytic) seismic traces. The complex seismic trace analysis concept was first introduced by Taner et al. (1979). Taner and Sheriff (1977) introduced the idea of applying the Hilbert transform to estimate the instantaneous seismic amplitude, phase and frequency. Each of these quantities are approximated at each time sample of a seismic trace, which form the basics of many amplitude, phase, and frequency seismic attribute algorithms that are used today in seismic interpretation.

The Hilbert transform converts a seismic trace *T(t)* into complex seismic trace *C(t)* by applying a 90° phase shift to every sinusoidal component of a seismic wave signal (Figure 2.13). In this context, the term "complex" is used in its mathematical perception. It means that the Hilbert transform *H(t)* refers to an imaginary seismic trace of the real seismic trace component *T*(t). Thus, the complex trace *CT(t)* can be defined as follow:

$$CT(t) = T(t) + iH(t) \qquad 2.28$$

where *H(t)* is the Hilbert transform of *T(t)*, a 90° phase shift of the real seismic trace *T(t)* and $i = \sqrt{-1}$. *T(t)* and *H(t)* represent the real and imaginary component of the seismic trace.

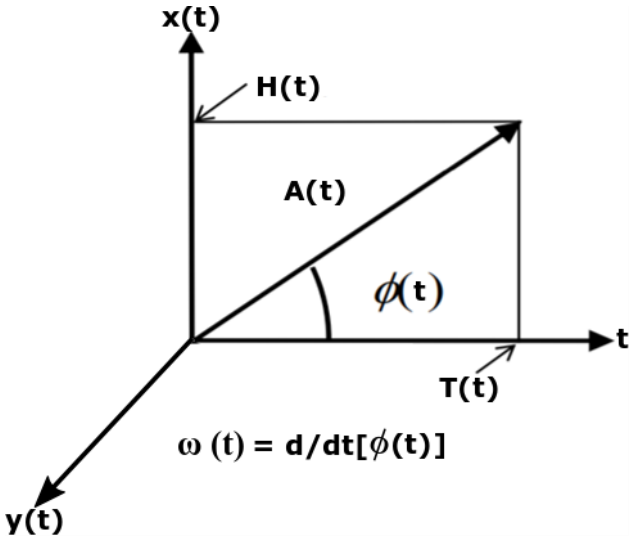


Figure 2.13: Instantaneous seismic attributes; amplitude A(t), phase ϕ(t) and frequency ω(t)

These traces are shown in a three-dimensional data space (x, y, t) (Figure 2.13), where 't' is seismic time, 'x' is the real-data plane, and 'y' is the imaginary-data plane. The actual seismic trace is confined to the real-data plane, while the Hilbert transform trace is restricted to the imaginary data plane. However, the complex trace can be transformed from a rectangular coordinate to a polar coordinate, as given below;

$$CT(t) = T(t) + iH(t) = A(t)e^{i\phi(t)} = A(t)cos\phi(t) + iA(t)sin\phi(t) \qquad 2.29$$

To calculate the instantaneous amplitude A(t), instantaneous phase ϕ(t) and instantaneous frequency $\boldsymbol{\omega}(t)$, which is the time derivative of the instantaneous phase.

$$A(t) = \sqrt{T^2(t) + H^2(t)}, \qquad 2.30$$

$$\phi(t) = tan^{-1}\left(\frac{H(t)}{T(t)}\right), \qquad 2.31$$

and $\omega(t) = \frac{d}{dt}[\phi(t)] = \frac{d\left[tan^{-1}(H(t)/T(t))\right]}{dt} = \frac{T(t)\frac{dH(t)}{dt} - H(t)\frac{dT(t)}{dt}}{A(t)^2}$. 2.32

Note that the instantaneous frequency function is periodically negative. To compute it, we need to differentiate both the seismic trace and its Hilbert transform.

Generally, seismic attributes are combinations of one or more properties derived from amplitude, period, polarity, frequency and phase component of a seismic trace. These seismic characteristics can either be classified as a single trace or multi-trace attributes. Single trace attributes include complex trace or the instantaneous attributes, while multi-trace attributes are usually obtained from the estimation of seismic coherence or semblance coefficients characteristics, which are regarded as a measure of trace to trace resemblance or discontinuity. Multi-trace attributes also include seismic attributes such as correlation, similarity, variance, and semblance. Seismic attributes such as volume rendering and texture segmentation are commonly used in digital photography and medical imaging and have been also applied in 3D seismic interpretation.

Seismic attributes, in general, are used for signal enhancement and noise attenuation without necessarily introducing any additional parameters or signal into the seismic data. They are used as lateral or horizontal indicators to map geological discontinuities, to visualize bedding configurations, detect fluid contents, fractured and permeable zones in oil and gas exploration etc.

2.5. Sources of noise in the seismic data and their filtering mechanism

Seismic noise is the unwanted component of seismic data for a particular data user. The undesired components for a reflection seismologist may be somebody else's desired signal (such as for shallow reflection purpose, refracted wave analysis, surface wave analysis and ambient noise analysis for site assessment). The actual signal for a data user is the component of the seismic wave that fits its individual conceptual model. The seismic signal is a continuous event since the earth is not in any way a quiet or steady environment. An ideal acquisition environment can only exist in a synthetic model. However, in real life, we are confronted with many possible sources of seismic noise when dealing with the reflection seismic method, from the time of data acquisition to the period of data processing and interpretation. Here, seismic noise under reflection seismic can be classified into four categories: (1) noise related to data acquisition, (2) noise related to wave propagation, (3) ambient and anthropogenic noise, and (4) processing artifacts. These noise sources create random and coherent energy on

the seismic data, which if not carefully treated could be misinterpreted as the real desired signal during data processing and interpretation, resulting in wrong interpretation of subsurface structures:

1. The data acquisition related noise includes equipment malfunctions (bad geophones or damaged take-out points etc.), recording environment and acquisition footprint (the data could be acquired along a noisy highway or mining environment etc.) and experimental error (noise due to wrong cable triggering could be counted as a stacked shot, wrong parameterization, cable noise, poor geophone planting or setting etc.). If these noises are not identified and removed, they may lead to wrong interpretation. This type of the noise appears on seismic record as linear, high frequency signals, or as dead traces in the case of bad geophone or take-out point.
2. The second category includes surface waves (ground roll), air wave, multiples (secondary reflections with interbed or intrabed wave paths), guided waves (supercritical multiple energies), reverberation (rebounding energies), and geologic noise (like point features that cause diffraction and scattering of waves). These types of noise cause coherent noise in the seismic data. Some are recognised as low-frequency and low-velocity with strong amplitude, seen sometimes as steep dipping events on the seismic data. Such events can be filtered by applying digital bandpass frequency filter, velocity bandpass (FK-filter), deconvolution, and radial/dip filters to eliminate them from the reflection data (Yilmaz, 2001). Multiples, guided waves and reverberation appears on seismic data as real events and they can be eliminated using deconvolution algorithms or effective moveout base suppressions such as CMP stack (Yilmaz, 2001).
3. Ambient or anthropogenic signals can produce erratic noise in the seismic record. These noise sources are created by wind motion, factories/mines, mammal, power line spikes (50 or 60 Hz) and subsurface biogenic activities, as well as an electrical cable noise from the recording equipment (Yilmaz, 2001). These types of noise are regarded as random noise in the seismic data. They are usually removed by isolation in the data due to its different frequency and amplitude characteristic from the true desired signals. CMP

stacks also supresses an appreciable portion of the random noise uncorrelated from trace to trace (Canales, 1984; Yilmaz, 2001). A notch frequency filter of 50 or 60 Hz can be used to remove power line frequency spikes from the seismic data.

4. The final category of the seismic noise is the processing artifact noise generated due to wrong application of processing parameters. This may occur if wrong velocities are used during normal moveout correction, which results in either over-correction or under-correction. Wrong frequency application during bandpass frequency and velocity filtering can smear the outcome of the process. Inaccurate parameterization in the reflection seismic is a serious concern if not well considered, because it can lead to a total misinterpretation and misinformation of the geological structures. Choosing an appropriate parameter in reflection seismic totally depends on the knowledge and experience of the researcher or scientist.

2.6. Resistivity method

The electrical resistivity method is an active geophysical method used to map changes in electrical properties of the subsurface material. The basic principles involve injecting current (I) into the ground with a pair of steel/copper electrodes (called the current electrodes (C)) and measuring the resultant potential difference (V) using a separate pair of electrodes (called the potential electrodes (M and N)) at the vicinity of current (Figure 2.14a) (Telford et al., 1990; Loke, 2004). The theory of electrical resistivity obeys the principles of Ohm's law, which states that a direct current with strength (I) flowing through a conductor of a known length (l) is given as (Figure 2.14b)

$$I = \frac{V}{R} = \frac{sV}{\rho l}, \qquad 2.33$$

Where R, s, ρ, and l are the resistance, cross-section, resistivity and length of the conductor, respectively.

The current flows radiate away from the current electrode so that the current distribution in the subsurface is uniform over hemispherical shells centered on the

source. Hence, the lines of equal voltage (equipotential) intersect the lines of equal current at right angles (Figure 2.15).

Therefore, the Ohm's law can now be defined as follows:

$$\frac{\partial V}{\partial l} = -\frac{\rho I}{s} = -\frac{\rho I}{2\pi l^2}. \quad 2.34$$

Thus, the potential V_l at length l is approximated by integral solution as stated in equation (2.35):

$$V_l = \int \partial V = -\int \frac{\rho I}{2\pi l^2}\partial l = \frac{\rho I}{2\pi l}. \quad 2.35$$

Then, the apparent resistivity (ρ_a) can be estimated using the measured potential difference (V) and the electrode configuration of the survey as stated below.

Potential at M:

$$V_M = \frac{\rho_a I}{2\pi}\left[\frac{1}{AM} - \frac{1}{MB}\right], \quad 2.36$$

Potential at N:

$$V_N = \frac{\rho_a I}{2\pi}\left[\frac{1}{AN} - \frac{1}{NB}\right]. \quad 2.37$$

The potential different between M and N:

$$\Delta V_{MN} = \frac{\rho_a I}{2\pi}\left\{\left[\frac{1}{AM} - \frac{1}{MB}\right] - \left[\frac{1}{AN} - \frac{1}{NB}\right]\right\}. \quad 2.38$$

The geometric factor (k) is:

$$k = 2\pi\left[\frac{1}{AM} - \frac{1}{MB} - \frac{1}{AN} + \frac{1}{NB}\right]^{-1}, \quad 2.39$$

$$\text{where } \rho = \frac{\Delta V_{MN} k}{I} \ (\Omega\text{m}). \quad 2.40$$

Note, in a homogeneous subsurface, the resistivity becomes constant and independent of both electrodes spacing and surface location; while it varies with respect to the position of electrode in inhomogeneous situations, as found in the Earth's subsurface. The resistivity of rocks depends on porosity, salinity, degrees of saturation, mineralogy, texture, content of clay and fluid content of the pore

spaces (Telford et al., 1990; Loke, 2004). The apparent resistivity depends on the geometry of the electrode configuration employed in an inhomogeneous medium.

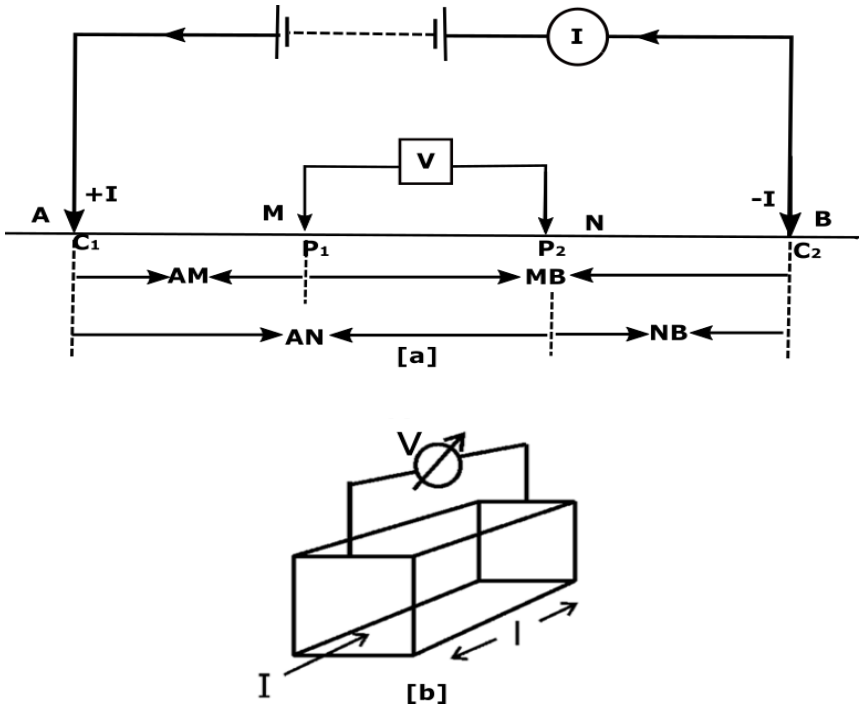


Figure 2.14: (a) Schematic diagram illustrating the basic principle of the electrical resistivity method (b) Flow of electric current along a known conductor length.

Two main ways electrode configurations are used, depending on the primary purpose of the survey. (1) Geoelectric mapping and (2) Geoelectric sounding. In geoelectric mapping, the current and potential electrodes are kept at a fixed separation and progressively moved along a profile, while in geoelectric sounding the current and potential electrodes are maintained at the same relative interval and the entire array is progressively increased about a fixed central point. However, the approach is very time consuming. Therefore, multielectrode systems can be employed with about 25 to 100 electrodes connected via a multi-core cable to a switching box and resistivity meter. Different electrode configurations such as the Schlumberger, Wenner, Wenner-Schlumberger of Gradient array, Dipole-dipole or Pole-dipole array can be used depending on the project objective. This method is employed in mineral and hydrogeological prospecting, geotechnical/engineering and environmental applications.

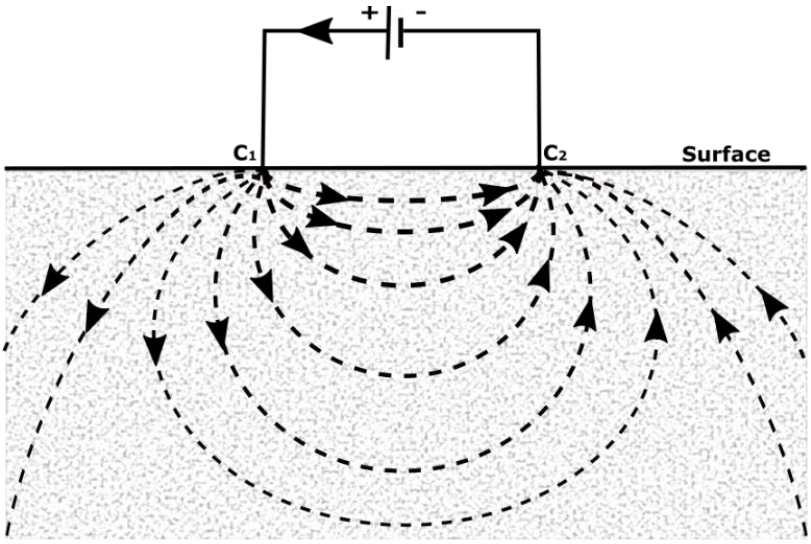


Figure 2.15: Electrical current distribution in a hemispherical shell.

2.7. Magnetic potential field method

The aim of a magnetic survey is to measure small and localised variations in the Earth's magnetic field resulting from the magnetic properties of the subsurface geologic materials and features. The magnetic properties of naturally occurring materials, such as basic igneous rocks and magnetic ore bodies, enable them to be distinguished and mapped by magnetic surveys. Generally, the magnetic susceptibility (a dimensionless physical property) of subsurface materials varies, depending on the type of rock and the surrounding environment. A common geological structure that causes magnetic anomalies includes dykes, faults and lava flows. Rocks with high magnetic susceptibility tend to have strong local magnetic field, while low magnetic susceptibility materials show weaker magnetic fields. Hence, the rock formations with higher magnetic susceptibility will appear on the magnetic map as regions of high magnetic field strength, and vice versa for the low susceptibility's material. The major magnetic mineral found in a typical rock material is usually magnetite (Fe_3O_4), distributed through most rocks in differing concentrations. The magnetisation of a rock depends on the remnant magnetisation (related to the amount of magnetic minerals it contains) and physical properties such as grain sizes and pore spaces (porosity).

The penetration depth of magnetic survey is uninfluenced by high electrical ground conductivities associated with saline groundwater, which makes it useful on sites with saline groundwater, clay or high levels of contamination (such as hydrocarbon pollution), where electrical, GPR and electromagnetic (EM) methods battle. However, the magnetic method can be integrated with other geophysical methods in order to properly constrain the geological ambiguities in geophysical interpretation. It can be used with gravity and/or seismic method to infer heat sources for geothermal exploration and mapping of intrusive structures for mine planning and safety (Coey and Sun, 1990; Scheiber-Enslin et al., 2018). Measurements of the Earth's total magnetic field or of any of its various components can be made with magnetic compass, magnetic balances, fluxgate magnetometers, proton-precession and optical-pumping magnetometers etc. Moreover, the magnetic gradient anomalies give better image of a shallow buried features such as buried artifacts, pipes and drums, but are less useful for investigating large geological features. However, the total magnetic field intensity (TMI) gives a regional overview of large-scale geological features. Note, rocks cannot retain magnetism when the temperature is above the Curie point ($\geq 500^{o}$C for most magnetic materials) and this restricts magnetic rocks to the upper 40 kilometres of the Earth's interior (Arrott, 1957; Coey and Sun, 1990).

The tilt angle θ of a magnetic anomaly A is equivalent to local phase and is given as:

$$\theta = tan^{-1}\left(\frac{\partial A/\partial z}{\partial A/\partial h}\right), \tag{2.41}$$

where the numerator and denominator are vertical and horizontal derivatives of the anomaly, respectively. The horizontal derivatives are given as (Blakely et al., 2016):

$$\frac{\partial A}{\partial h} = \sqrt{(\partial A/\partial x)^2 + (\partial A/\partial y)^2}. \tag{2.42}$$

The tilt derivative offers several advantages in the magnetic anomalies' interpretation and the dependence of θ on magnetization is the same in both the horizontal and vertical derivatives (Verduzco et al., 2004; Blakely et al., 2016).

2.8. References

Achenbach, J.D., 1975. Wave Propagation in Elastic Solids. *North Holland Publication Company*.

Aki, K., 1993. Local site effects on weak and strong ground motion. *Tectonophysics*, *218*, pp. 93-111.

Aki, K. and Richards, P.G., 1980. Quantitative Seismology: Theory and Methods. *W.H. Freeman and Company*, San Francisco California.

Andriampenomanana, F., Nyblade, A.A., Wysession, M.E., Durrheim, R.J., Tilmann, F., Julià, J., Pratt, M.J., Rambolamanana, G., Aleqabi, G., Shore, P.J. and Rakotondraibe, T., 2017. The structure of the crust and uppermost mantle beneath Madagascar. *Geophysical Journal International*, *210*(3), pp. 1525-1544.

Arai, H. and Tokimatsu, K., 2000. Effects of Rayleigh and Love waves on microtremor H/V spectra: Proceeding of the 12th World Conference on Earthquake Engineering. *New Zealannd Society for Earthquake Engineering*, Auckland, New Zealand, pp. 3-5.

Arai, H. and Tokimatsu, K., 2004. S-wave velocity profiling by inversion of microtremor H/V spectrum. *Bulletin Seismological Society America*, *94*, pp. 53–63.

Arrott, A., 1957. Criterion for ferromagnetism from observations of magnetic isotherms. *Physical Review*, *108*(6), p. 1394.

Ashton, P., Bacon, B., Deplante, C., Sinclair, D.T. and Redekop, G., 1994. 3D Seismic Survey and Design. *Oilfield Review, 6*(2), pp. 19‑32.

Backus, G.E. and Gilbert, J.F., 1967. Numerical applications of formalism for geophysical inverse problem. *Geophysical Journal of the Royal Astronomical Society*, *13*, pp. 247–276.

Bard, P.Y., 1998. Microtremor measurements, a tool for site effect estimation: Proceedings of the 2nd International Symposium on the Effect of Surface Geology on Seismic Motion, Yokohama, Japan, pp. 1-3.

Bard, P.Y., 1999. Microtremor measurements, a tool for site effect estimation? In Irikura, K., Kudo, K., Okada, H. and Sasatani, T. (Eds.) (1999), The Effects of Surface Geology on Seismic Motion: Proceedings of the 2nd International Symposium on the Effect of Surface Geology on Seismic Motion, Yokohama, Japan, 1-3 Dec. 1998, A. A. Balkema, Rotterdam, ISBN 90 5809 030 *2*, pp. 1251-1279.

Ben-Menahem, A. and Singh, S.J., 2000. Seismic Waves and Sources. *Dover Publications Inc., New York*, pp. 1102.

Blakely, R.J., Connard, G.G. and Curto, J.B., 2016. Tilt derivative made easy. *Geosoft Technical Publications, 4*, pp.30-34.

Bolt, B.A., 1982. Inside the Earth, San Francisco, W.H. Freeman: Reynolds International. *Technical Summary Sheet*. *13*, pp. 1-2.

Brown, A.R., 1999. Interpretation of three-dimensional seismic data, 5th eds. *AAPG Memoir 42,* Tulsa, Oklahoma, pp. 514 - 516.

BSSC., 1994. NEHRP Recommended Provisions for the Development of Seismic Regulations for New Buildings, Part I: Provisions, Building Seismic Safety Council, Federal Emergency Management Agency, Washington D.C.

Burger, H.R., 1992. Exploration Geophysics of the Shallow Subsurface: *Prentice Hall, Inc*.

Butler, D.K, eds., 2005. Near-surface Geophysics: Investigations in geophysics *13*. *Society of Exploration Geophysicists*, Tulsa, Okla.

Campbell, G., 2009. 2-D Seismic reflection surveys and structural mapping: Faults, dips and domes: SAGA 11th Biennial Technical Meeting and Exhibition, Swaziland, pp. 2-5.

Chaiprakaikeow Susit., 2012. Site Characterization using Reflection and Surface Wave Seismic Surveys, PhD Thesis. Utah State University: All Graduate Thesis and Dissertation Paper 1273, pp. 25-119.

Canales, L.L., 1984. Random noise reduction: In SEG Technical Program Expanded Abstracts. *Society of Exploration Geophysicists*, pp. 525-527.

Chaouch, A., and Mari, J.L., 2006. 3-D land seismic surveys: Definition of geophysical parameters. *Oil and Gas Science and Technology, 61*, pp. 611-630, doi:10.2516/ogst: 2006002.

Coey, J.M.D., and Sun, H., 1990. Improved magnetic properties by treatment of iron-based rare earth intermetallic compounds in ammonia. *Journal of Magnetism and Magnetic Materials, 87*(3), pp. L251-L254.

Dobrin, M.B. and Savit, C.H., 1988. Introduction to Geophysical Prospecting, 4th eds. *McGraw-Hill Book Company*, pp. 30-87.

Dravinski, M., Ding, G. and Wen, K.L., 1996. Analysis of spectral ratios for estimating ground motion in deep basins. *Bulletin Seismological Society of America, 86*, pp. 646–654.

Durrheim, R.J., 1986. Recent reflection seismic developments in the Witwatersrand basin. Reflection seismology: A global perspective (Barazangi, M. and Brown, L. eds). *American Geophysical Union, 13*, pp. 77-83.

Dziewonski, A.M. and Hales, A.L., 1972. Numerical Analysis of Dispersed Seismic Waves. Methods in Computational Physics: Seismology, Surface Waves and Earth Oscillations. Bolt, B.A. *Academic Press, New York, 11*, pp. 39-85.

Eaton, D.W., Adam E., Milkereit, B., Salisbury, M., Roberts, B., White, D. and Wright, J., 2010. Enhancing base-metal exploration with seismic imaging. *Canadian Journal of Earth Sciences, 47*, pp. 741-760.

Evans, B. J., 1997. A Handbook for Seismic Data Acquisition in Exploration: Geophysical monograph series. *Society of Exploration Geophysicists, 7*, pp. 272-305.

Field, E.H. and Jacob, K.H., 1993. The theoretical response of sedimentary layers to ambient seismic noise. *Geophysics Research Letters*, *20*, pp. 2925-2928.

Field, E.H. and Jacob, K.H., 1995. A comparison and test of various site response estimation techniques, including three that are non-reference site dependent. *Bulletin of the Seismological Society of America*, *86*, pp. 991–1005.

Foti, S., Sambuelli, L., Socco, L.V. and Strobbia, C., 2003. Experiments of joint acquisition of seismic refraction and surface wave data. *Near Surface Geophysics*, *1*, pp. 119-129.

Gibson, M.A.S., Jolley S.J. and Barnicoat, A.C., 2000. Interpretation of the western ultra-deep levels 3D seismic survey. *The Leading Edge*, *19*, pp. 730-735.

Isiaka, A.I., Durrheim, R.J. and Manzi, M.S., 2018. High-resolution seismic reflection investigation of subsidence and sinkholes at an abandoned coal mine site in South Africa. *Pure and Applied Geophysics*, *176*(4), pp. 1531-1548.

Ivanov, J., Miller, R.D., Xia, J., Steeples, D. and Park, C.B., 2005a. The inversion problem of refraction traveltimes, part I: Types of geophysical nonuniqueness through minimization. *Pure and Applied Geophysics*, *162*, pp. 447-459.

Ivanov, J., Miller, R.D., Xia, J. and Steeples, D., 2005b. The inversion problem of refraction traveltimes, part II: Quantifying refraction nonuniqueness using three-layer models. *Pure and Applied Geophysics*, *162*, pp. 461-477.

Ivanov, J., Miller, R.D. and Xia, J., 2006. Joint analysis of refractions with surface Waves: An inverse solution to the refraction-traveltime problem. *Geophysics*, *71*(6), pp. 131-138.

Jaynes, E. T., 2003. Probability Theory: The Logic of Science. *Cambridge University Press*, Cambridge, U.K.

Jones, R.B., 1958. In-situ measurement of the dynamic properties of soil by vibration methods. *Geotechnique*, *8*, pp. 4-21.

Kallweit, R. S., and Wood, L. C., 1982. The limits of resolution of zero-phase wavelets. *Geophysics, 47*(7), pp. 1035-1046.

Kearey, P., Brooks, M., and Hill, I., 2002. An Introduction to Geophysical Exploration, 3rd eds. *Blackwell Scientific Publisher*, Oxford, UK.

Klimentos, T., 1995. Attenuation of P- and S-waves as a method of distinguishing gas and condensate from oil and water. *Geophysics*, *60*(2), 447-458. https://doi.org/10.1190/1.1443782.

Kramer, S. L., 1996. Geotechnical Earthquake Engineering. *Prentice Hall,* Upper Saddle River, New Jersey.

Lermo, J. F. and Chavez-Garcia, F. J., 1993. Site effect evaluation using spectral ratios with only one station. *Bulletin of the Seismological Society of America, 83,* pp. 1574-1594.

Loke, M.H. 2004. Tutorial: 2-D and 3-D electrical imaging surveys.

Lowrie, W., 1997. Fundamentals of Geophysics. *Cambridge University Press*, Cambridge, U.K.

Malehmir, A., Durrheim, R.J., Bellefleur, G., Urosevic, M., Juhlin, C. and White D., 2012. Seismic methods in mineral exploration and mine planning. A general overview of past and present case histories and a look into the future. *Geophysics, 77*, pp. WC173-WC190.

Manzi, M.S.D., Gibson, M.A.S., Hein, K.A.A., King, N. and Durrheim, R.J., 2012a. Application of 3-D seismic techniques in evaluation of ore resources in the West Wits Line goldfield and portions of the West Rand goldfield, South Africa. *Geophysics, 77,* pp. WC163-WC171.

Manzi, M.S.D., Durrheim, R.J., Hein, K.A.A. and King, N., 2012b. 3-D edge detection seismic attributes used to map potential conduits for water and methane in deep gold mines in the Witwatersrand Basin, South Africa. *Geophysics, 77,* pp. WC133-WC147.

Manzi, M.S.D., Durrheim, R.J., Hein, K.A.A. and King, N., 2013. Neoarchaean tectonic history of the Witwatersrand Basin and Ventersdorp Supergroup: New constraints from high-resolution 3-D seismic reflection data. *Tectonophysics*, *590*, pp. 94-105.

Manzi, M.S., Hein, K.A., Durrheim, R.J. and King, N., 2014. The Ventersdorp Contact Reef model in the Kloof Gold Mine as derived from 3D seismics, geological mapping and exploration borehole datasets. *International Journal of Rock Mechanics and Mining Sciences*, *66*, pp. 97-113.

Menke, W., 1989. Geophysical Data Analysis: Discrete Inverse Theory. *Academic Press Inc*.

Miller, R.D., Xia, J., Park, C.B. and Ivanov, J., 1999. Multichannel analysis of surface waves to map bedrock. *The Leading Edge*, *18*, pp. 1392-1396.

Nakamura, Y., 1989. A method for dynamic characteristics estimation of subsurface using microtremor on the ground surface: Quarterly Report of Railway Technical Research Institute, Japan, 30, pp. 25-33.

Nogoshi, M. and Igarashi, T., 1970. On the propagation characteristics of microtremor. *Journal of the Seismological Society of Japan*, *23*, pp. 264–280.

Nogoshi, M. and Igarashi, T., 1971. On the amplitude characteristics of microtremor, part II. *Journal of the Seismological Society of Japan*, *24*, pp.26-40.

O'Donnell, T.M. Jr., Miller, K.C. and Witcher, J.C., 2001. A seismic and gravity study of the McGregor geothermal system, southern New Mexico. *Geophysics*, *66*, pp. 1002-1014.

Ohmachi, T., Nakamura, Y. and Toshinawa, T., 1991. Ground motion characteristics in the San Francisco Bay Area detected by microtremor measurements: Proceedings of the 2nd International Conference on Recent Advancement in Geotechnical Earthquake Engineering and Soil Dynamic, 11-15 March, St. Louis, Missouri, pp. 1643-1648.

Okada, H., 2003. The microtremor survey method: Geophysical monograph series, 12. *American Geophysical Union,* Washington.

Onyebueke, E.O., Manzi, M.S.D., and Durrheim, R.J., 2018. High-resolution shallow reflection seismic integrated with other geophysical methods for hydrogeological prospecting in the Nylsvley Nature Reserve, South Africa. *Journal of Geophysics and Engineering*, *15*(6), pp. 2658 - 2673.

Pant, P.R. and Vijaya Raghava, M.S., 1987. A simple approach to the masked-layer problem in seismic refraction work. *Geoexploration, 24*, pp. 549-556.

Park, C.B., Miller, R.D., Xia., J. And Ivanov, J., 2005. Multichannel seismic surface-wave methods for geotechnical applications (online): Available from http://www.kgs.ku.edu/Geophysics2/Pubs/Pubs PAR-00-03.pdf.

Park, C.B., Miller, R.D. and Xia, J., 1999. Multichannel analysis of surface waves (MASW). *Geophysics, 64,* pp. 800-808.

Pratt, T.L., Brocher, T.M., Weaver, C.S., Creager, K.C., Snelson, C.M., Crosson, R.S., Miller, K.C. and Trehu, A.M., 2003. Amplification of seismic waves by the Seattle basin, Washington State. *Bulletin Seismological Society of America*, *93,* pp. 533-545.

Pretorius, C.C., Chunnett, G.K., Chalke, T.W.J., and Gibson, M., 2007. 3D data integration for exploration and mine planning: Proceedings of Exploration 07, Fifth Decennial Conference on Mineral Exploration, Toronto, pp. 601-610.

Rayleigh, J.W.S., 1885. On waves propagated along the plane surface of an elastic solid: Proceedings of the London Mathematical Society, *17*, pp. 4-11.

Ryden, N., Park, C., Miller, R., Xia, J. and Ivanov, J., 2001. High frequency MASW for non-destructive testing of pavements: Proceedings of the Symposium on the Application of Geophysics to Engineering and Environmental Problems, Denver, Colorado.

Safak, E., 2001. Local site effects and dynamic soil behavior. *Soil Dynamics and Earthquake Engineering, Elsevier Science Ltd*., *21*, pp. 453-458.

Sammis, C.G. and Henyey, T.L., 1987. Geophysics Field Measurement: *Academic Press*.

Scheiber-Enslin, S.E. and Manzi, M., 2018. Integration of 3D reflection seismics and magnetic data for deep platinum mine planning and risk mitigation: A case study from Bushveld Complex, South Africa. *Exploration Geophysics*, *49*(6), pp. 928-939.

SESAME., 2004. Guidelines for the implementation of the H/V spectral ratio technique on ambient vibrations, measurements, processing and interpretation: SESAME European Research Project, WP12-Deliverable D23.12, pp. 3-62.

Shearer, P.M., 1999. Introduction to Seismology. *Cambridge University Press*, Cambridge, U.K.

Shearer, P.M., 2009. Introduction to Seismology 2nd eds. *Cambridge University Press*, Cambridge, U.K.

Sheriff R.E. and Geldart L.P., 1995. Exploration Seismology 2nd eds. *Cambridge University Press*, Cambridge, U.K.

Sheriff, R., 2002. Encyclopaedic Dictionary of Exploration Geophysics. *Society of Exploration Geophysicists*.

Socco, L. V. and Boiero, D., 2008. Improved Monte Carlo inversion of surface wave data. *Geophysical Prospecting*, *56*, pp. 357-371.

Steeples, D.W, and Miller, R.D., 1995. Seismic Reflection Methods Applied to Engineering, Environmental, and Groundwater Problems: Kansas Geological Survey, Environmental and Engineering Applications, pp. 3-28.

Stokoe, K.H, II., Wright, S.G., Bay, J.A. and Roesset, J.M., 1994. Characterization of geotechnical sites by SASW method. Geophysical characteristics of sites: ISSMFE, Technical Committee 10 for XIII ICSMFE. *International Science Publishers, New York*, pp. 15-25.

Thomsen, L., 1986. Weak elastic anisotropy. *Geophysics, 51*(10), pp. 1954-1966. https://doi.org/10.1190/1.1442051

Thomsen, L., 2002. Understanding Seismic Anisotropy in Exploration and Exploitation. *Society of Exploration Geophysicists and European Association of Geoscientists and Engineers.*

Timoshenko, S. and Goodier, J. N., 1951. Theory of Elasticity. *McGraw-Hill*, New York, USA.

Taner, M.T. and Sheriff, R.E., 1977, Application of amplitude, frequency, and other attributes to stratigraphic and hydrocarbon determination, Section 2: Application of seismic reflection configuration to stratigraphic interpretation. *AAPG, Memoir 26*, pp. 301-327.

Taner, M. T., Koehler, F. and Sheriff, R. E., 1979. Complex seismic trace analysis. *Geophysics*, *44*, pp. 1041-1063.

Telford, W.M., Telford, W.M., Geldart, L.P., Sheriff, R.E. and Sheriff, R.E., 1990. Applied Geophysics. *1, Cambridge University Press*.

Trickett, J.C., Duweke, W.A. and Kock, S., 2006. Three-dimensional reflection seismic: Worth its weight in platinum. *The Journal of the South African Institute of Mining and Metallurgy*, *105*, pp. 357–363.

Verduzco, B., Fairhead, J.D., Green, C.M. and MacKenzie, C., 2004. New insights into magnetic derivatives for structural mapping. *The Leading Edge*, *23*(2), pp. 116-119.

Whiteley, R.J. and Greenhalgh, S.A., 1979. Velocity inversion and the shallow seismic refraction method. *Geoexploration*, *17*, pp. 125-141.

Widess, M.B., 1973. How thin is a thin bed? *Geophysics*, *38*(6), pp. 1176-1180.

Winkler, K. and Nur, A., 1982. Seismic attenuation: Effects of pore fluids and frictional-sliding. *Geophysics, 47*(1), pp. 1-15. https://doi.org/10.1190/1.1441276.

Xia, J., Miller, R.D. and Park, C.B., 1999. Estimation of near-surface velocity by inversion of Rayleigh wave. *Geophysics, 64*(3), pp. 691-700.

Xia, J, Miller, R.D. and Park, C.B., 2000. Comparing shear-wave velocity profiles from MASW with borehole measurements in unconsolidated sediments: Fraser River Delta B.C, Canada. *Journal of Environmental and Engineering Geophysics*, 5, pp. 1-13.

Yilmaz Ö. and Doherty, S.M., 2001. Seismic Data Analysis, Processing, Inversion and Interpretation of Seismic Data. *Society of Exploration Geophysicists*, Investigations in Geophysics, *10*, pp. 10-62.

Yilmaz, Ö., Eser, M. and Berilgen, M., 2006. A case study of seismic zonation in municipal areas. *The Leading Edge*, *25*(3), pp. 319–330.

Yilmaz, Ö., 2015. Engineering Seismology with Application to Geotechnical Engineering. *Society of Exploration Geophysics*, Investigations in Geophysics, *17*, pp. 162-512.

CHAPTER 3

3.0 High-resolution shallow reflection seismic integrated with other geophysical methods for hydrogeological prospecting in the Nylsvley Nature Reserve, South Africa

Abstract

Two perpendicular high-resolution shallow seismic and resistivity profiles were acquired to assist in imaging the near-subsurface sedimentary architecture for hydrogeological prospecting in the Nylsvley Nature Reserve along the Nyl River floodplain in South Africa. I deployed 48 channels of 14 Hz geophones with a dense (1 - 2 m) source and geophone spacing that provided fold coverage of 24 (line 2) and 48 (line 1). The resistivity profiles were acquired with a Schlumberger electrode configuration with 2 - 3 m electrode spacing and total of 40 steel electrodes. The raw seismic shot records were characterized by low-frequency, high-amplitude source-generated noise (surface and guided waves). Reflections from bedrock were not obvious. To improve the reflected seismic signal, I employed seismic processing workflow that enhanced the seismic reflectivity on the stacked sections. The seismic reflection interpretation was constrained and integrated with seismic refraction and resistivity tomography, and the 1-D multichannel analysis of surface waves to generate the model that best represents the real subsurface geological model. The integrated results show the bedrock-overburden contact at 8 - 12 m depth, which correlates well with boreholes, drilled in the area. In addition, the reflection seismic and refraction tomography show the bedrock undulation and velocity changes associated with erosional surfaces, weathered bedrock and fracture systems. I further interpret these characteristics to be associated with groundwater movement and storage related to the fractured and weathered zones within the bedrock. The integrated data also delineate the interface between the unsaturated sand and saturated sand-gravel that represents the groundwater water table. This study demonstrates the potential of combining several surface geophysical techniques for near-surface investigations, especially for hydrogeological prospecting.

3.1. Introduction

Seismic methods are a critical component of geophysical surveys for hydrocarbons (Yilmaz 2001) and mineral exploration (Manzi et al., 2012; Malehmir et al., 2012). The depth of investigation is typically one hundred meters to a few kilometers. Shallower near-surface exploration is commonly conducted using several different methods, including magnetic, gravimetric, multichannel analysis of surface waves (MASW) and electrical resistivity tomography (ERT). These methods are often limited by poor resolution and limited depth of penetration. However, application of shallow reflection seismology for near-surface studies offers an advantage in resolution and depth of penetration (Ayers, 1989; Schmelzbach et al., 2005; Pugin et al., 2009). In the past few decades, the technique has been used successfully in hydrogeophysical, environmental and geotechnical problems for delineating shallow geological structures and locating groundwater water aquifers (Ayers 1989, Miller et al., 1989; Leucci, 2007; Pugin et al., 2009; Schreilechner and Eichkitz, 2015; Yilmaz, 2015; Dehghannejad et al., 2017).

The shallow reflection seismic method differs from the deep reflection seismic method used in hydrocarbon and mineral exploration with respect to their energy sources, source and receiver geometries, and the number of receivers deployed. For example, 1 - 5 m receiver spacing with tens to hundreds of receivers is often used for shallow reflection seismic surveys, while 5 - 25 m receiver spacing with hundreds to thousands of receivers is often deployed for deep reflection seismic surveys (Steeples, 1998). The energy source for shallow reflection surveys includes sledgehammers and mechanical weight drops, while Vibroseis and explosives are the most commonly used energy sources for deep reflection seismic surveys. Only the first arrival times of refracted head waves are used to estimate the P-wave velocity-depth model, while all the shallow reflected energy is used to obtain the near-surface seismic image (Yilmaz, 2015). Furthermore, the velocity-depth model and the seismic image can be integrated to interpret the structure of the near-surface layer and the geometry of the overburden-bedrock contact. The interpretation of the data from any single geophysical method is

often ambiguous and suffers from limitations resulting from site conditions and imaging capabilities. Therefore, integration of different geophysical methods can provide additional constraints and obtain subsurface models with higher reliability (Butler, 2005; Ahmad et al., 2009; Steelman et al., 2017).

Electrical resistivity tomography has been successfully applied in the hydrogeological investigation for lithological mapping, aquifer delineation and groundwater quality information due to the intrinsic resistivity distribution of different subsurface materials (Loke, 1994; Loke and Barker, 1996; Butler, 2005). The electrical resistivity method does not provide a direct image of the subsurface; it tends to merge layers with similar electrical resistivities and features resulting in the decrease in resolution of interfaces with increasing depths of investigation (Loke and Barker, 1996; Butler, 2005; Loke et al., 2013). However, integration of electrical resistivity techniques with other methods provides a solution for hydrogeological and engineering problems by providing different physical properties of the subsurface (Ahmad et al., 2009; Steelman et al., 2017). Furthermore, application of MASW provides the shear wave velocity of the near-surface, which is related to the modulus of rigidity, an essential parameter for geotechnical and earthquake engineers for infrastructural planning (Park et al., 1999; Yilmaz, 2015).

The study area has attracted much attention due to its environmental conservation importance and its significant groundwater potential, which is mainly utilized for agricultural purposes and municipal supply. The objectives of the study were to map the aquifer unit and delineate the structures responsible for underground water storage and bedrock-overburden contact. This study also seeks to open-up opportunities for additional shallow geophysical surveys for hydrogeophysical studies and infrastructural planning in the Nylsvley Nature Reserve. The results are compared with other previous studies in the area (Timmerman, 1984; Higgins et al., 1996; Tooth et al., 2002). To demonstrate the potential and the advantages of integrated geophysical methods for hydrogeophysical prospecting and site characterization at Nylsvley Nature Reserve, South Africa. I carried out high-resolution shallow reflection seismic survey integrated with refraction

tomography, ERT and MASW to scrutinize the data and produce a near-surface model that best represents the true geological model of the near-surface to support the siting of boreholes to exploit underground water at the area.

3.2. Study location and geology

The survey area is located within the Nylsvley Nature Reserve in the western part of the Limpopo Province, South Africa (Figure 3.1). The area is characterized by the seasonally inundated floodplain of the Nyl River, designated as a Ramser Wetland site because of its importance for nature conservation (Figure 3.2).

The surface geology is characterized by recent alluvium deposits derived from quarzitic, feldspathic and micaceous sandstones, and consists dominantly of sandy soil, grit lenses, conglomerates, clays, and silts. The accumulated sediments deposited on the flat areas such as the plateau and lower-lying plains, and valleys are flood deposits from different tributaries (such as Olifantsspruit, Middlefonteinspruit, Tobiasspruit, and Andriesspruit) (Tooth et al., 2002). Due to the mountainous and hilly nature of the area, a large portion of the soil deposit is shallow (< 15 m) (Figure 3.2). Underlying the alluvium deposit is the Nylstroom Subgroup of the Waterberg Group, which consists of feldspathic and micaceous sandstones, greywacke, grits, siltstone, shale, and conglomerates (Figure 3.1 and Figure 3.2). The Waterberg Group, deposited about 1790 million years ago, was derived from extensive weathering and erosion of the Paleo-Proterozoic Bushveld Igneous Complex and Transvaal Supergroup (McCarthy and Rubidge, 2005).

The shallow subsurface geology in the area is highly influenced by the weathering and erosion of the bedrock, viz. the Lebowa Granite Suite of the Bushveld Igneous Complex, the Rooiberg Group of the Transvaal Supergroup (Palaeo-Proterozoic in age), and the Meso-Proterozoic Waterberg Group (Higgins et al., 1996; Tooth et al., 2002). Although specific stratigraphic details are lacking, the overlying sediment consists of gravel at the base, grading upward through coarse, medium to fine sand and silt/clay near the floodplain surface (Tooth et al., 2002). The subsurface geology of the floodplain predominantly controls the movement

and storage capacity of the groundwater through the bedrock aquifer. However, the Waterberg Group sandstones in the upper sections of the floodplain are highly weathered and fractured and characterized by high porosity and infiltration rates (Higgins et al., 1996; Porszasz, 1973). These sandstones store a high volume of groundwater up to the gravel layer (aquifer) at the base of the alluvium deposit. The bedrock is overlain by approximately 10 - 15 m thick alluvium deposits along the valleys (Higgins et al., 1996) and extends up to a maximum depth of about 35 m downstream (Tooth et al., 2002) (Figure 3.2).

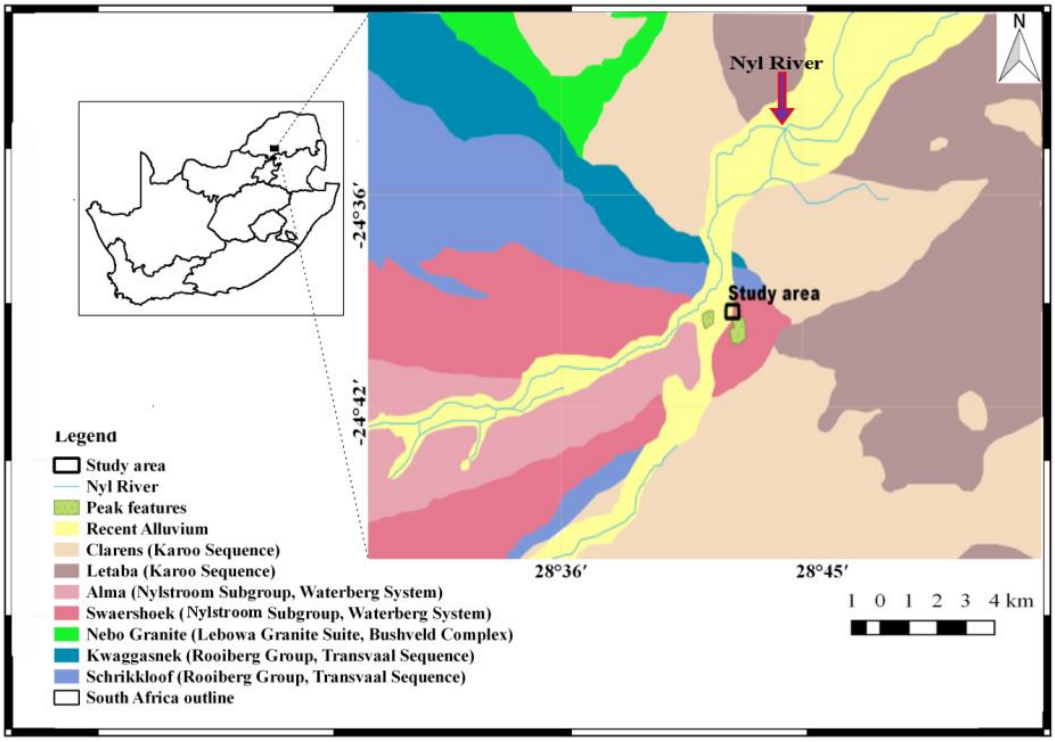


Figure 3.1: Geology map of the study area (modified from the Republic of South Africa Nylstroom Geological Survey map 2428). The index on the top left is the South Africa boundary map outline (Copyright© Council for Geoscience, South Africa, All Right Reserved. First published by the Government printer, 1978).

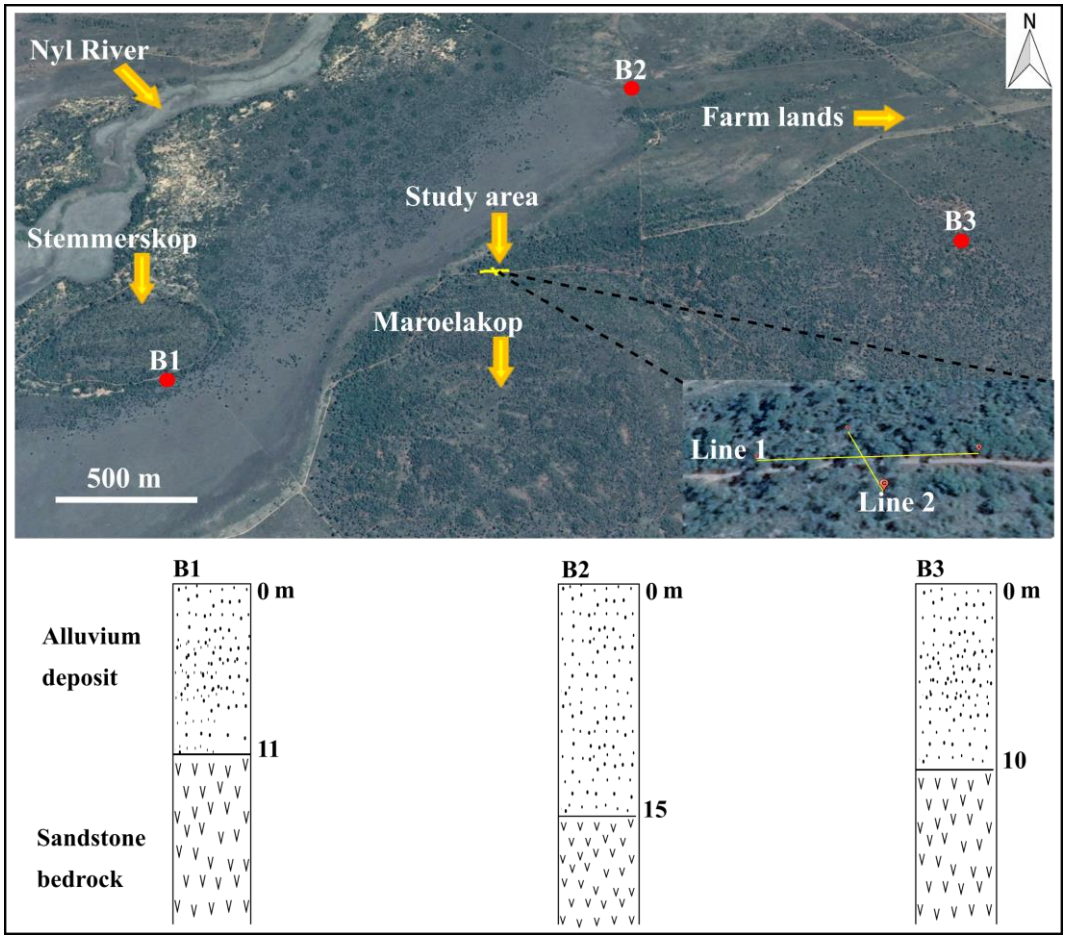


Figure 3.2: Base map of the study area from the Google Earth Image showing the location of the boreholes (B1, B2, B3) (the enlarged block on the bottom right shows the position of the profile lines). At the bottom is the stratigraphy of the boreholes, showing the depth to the bedrock near the study area (image@2017DigitalGlobe).

3.3. Data acquisition

The objective of the survey was to map the bedrock-overburden contact and hydrostratigraphic units in the area. According to the logs of existing boreholes (~ 1 km away from the survey profiles), the depth to the bedrock expected to be in the range of 10 - 15 m along the valley and up to a maximum depth of 35 m downstream (Tooth et al 2002). The seismic data acquisition parameters are summarized in Table 3.1. To minimize spatial aliasing and to obtain high-resolution images of the near-surface structure, the seismic data was acquired using high-density (1 - 2 m) shot and receiver spacing with 14-Hz geophones,

yielding a common midpoint (CMP) spacing of 0.5 to 1 m. A series of acquisition trials with different geophones (14 and 48 Hz) and geometries was done prior to the actual seismic survey. Several shallow reflections were observed in the raw shot gathers, highlighting the potential for seismic surveys in this environmental setting.

The seismic survey consists of two perpendicular profile lines (lines 1 and 2, Figure 3.2). Data was acquired along each line using asymmetrical split-spread geometry. Line 1 is oriented W-E. A total of 54 shots were recorded with 48 vertical component geophones, spaced at an interval of 2 m along the profile and 2 m shot spacing, yielding a nominal fold of 48. Line 2 is oriented in NE-SW direction and was conducted with 1 m receiver and 2 m shot spacing along 47 m profile length with 30 recorded shot positions, yielding a nominal fold of 24. Maximum source-receiver offsets of 108 m (14, 6 and 2 m to be determined offsets at each end of line 1) and 53 m (6 and 2 m offsets at each end of line 2) enabled stacking velocities to be determined up to depth of about 100 m, which is the primary target of the survey. An aluminum base metal plate (30 x 30 x 2.5 cm) with a 9 kg sledgehammer was used as an energy source. Four blows were stacked at every shot point to improve the signal-to-noise ratio (S/N). Two Geometric Geodes seismographs with 24 channels each were connected. The data were recorded at 0.25 ms sampling interval with a recording length of 300 ms for both lines. MASW data were also collected at 14 m and 6 m offset shot gathers along the same profile with the same geometry and geophone type as in the reflection seismic survey. This allowed for recording of a horizontally-traveling plane wave (Rayleigh wave) for 1-D shear wave velocity inversions.

Two electrical resistivity profiles were also surveyed with a fully-automated ARES Resistivity meter instrument with stainless steel electrodes space at 2 and 3 m along line 2 and line 1, respectively. The system is equipped with a total of 48 electrodes, with a maximum of 5 m take-out multicore cable electrode spacing. The resistivity profile conducted along the road is about 3 m away and parallel to the seismic profile along line 1. An identical geometry was used for line 2 (Figure

3.3). For optimum horizontal and vertical resolutions, a Schlumberger array was chosen along each line.



Figure 3.3: Data acquisition field setup. Line 1 is shown in the picture. On the right is 94 m seismic profile with 2 m geophone spacing; on the left, about 3 m away from seismic profile, is the 120 m resistivity profile with 3 m electrode spacing. The source is a 30 x 30 x 2.5 cm aluminum metal plate with a 9 kg sledgehammer.

Table 3.1: Seismic acquisition parameters for line 1 and 2.

Item	Parameters	
Profiles	Line 1	Line 2
Geophone type	14 Hz	14 Hz
Seismograph	Geometric Geode (32 bits)	
Source	9 kg sledgehammer	
Record length (ms)	300	300
Sampling interval (ms)	0.25	0.25
Vertical stacks	4	4
Receiver number	48	48
Receiver spacing (m)	2	1
Number of shots	54	28
Shot spacing (m)	2	2
Profile length (m)	94	47
Min/Max offset (m)	0/108	0/53
Max CMP fold	48	24

3.4. Data processing and analysis

3.4.1. Seismic data processing and analysis

The primary objective of the seismic analysis is to enhance different seismic events in the seismic shot gathers. The shot gathers shown in Figure 3.4 have been pre-processed by defining the acquisition geometry, editing the bad traces and scaling the amplitude (using the ReflexW software package), which corrects for wavefront divergence and amplitude decay caused by a geometrical spreading of seismic waves. At the near-offsets, the low-frequency, high amplitude source-generated noise (30 - 70 Hz) dominates the raw shot gathers (Figure 3.4a and b). This was attributing to: (1) the high-energy source close to the receiver; (2) poor geophone coupling with the ground; (3) a shallow water table; (4) use of low resonant frequency geophones (14 Hz) for shallow data acquisition; and (5) Coupling of the strike plate on dry sand. The raw shot gathers exhibit different seismic events such as the direct, refracted and reflected P-waves, and surface waves (Figure 3.4a and b). The normal moveout (NMO) velocities for the reflected wave are ~ 2600 - 3200 m/s and the apparent velocities of the refracted

P-waves (R1 and R2) are 1100 - 2500 m/s and 3200 - 5700 m/s, respectively. Surface waves (S) were also observed on shot records with apparent velocities of ~ 180 - 480 m/s (Figure 3.4a and b) and a dominant frequency of 45 - 65 Hz (Figure 3.4c).

The power spectra of selected shot records from line 1 and line 2 and their respective amplitude decay curves are shown in Figure 3.4c-f. The power spectra indicate that the frequency of the seismic events range from 8 to 300 Hz with a dominant frequency of 45 - 65 Hz for the surface waves. The seismic signals show rapid amplitude decay above 250 Hz (Figure 3.4d and f), where after the spectrum is dominated by coherent ambient/scattered noise. The frequency spectrum and amplitude decay curve of the recorded seismic data show higher energy content at frequencies less than 100 Hz and lower energy content at higher frequencies (~120 Hz). The high amplitude signals between 45 - 150 Hz were observed at travel times up to 100 ms (Figure 3.4a and b). This demonstrates that at the dominant frequencies, the energy of a signal decays with increasing offset and time (Sheriff, 1975; Sato et al., 2012).

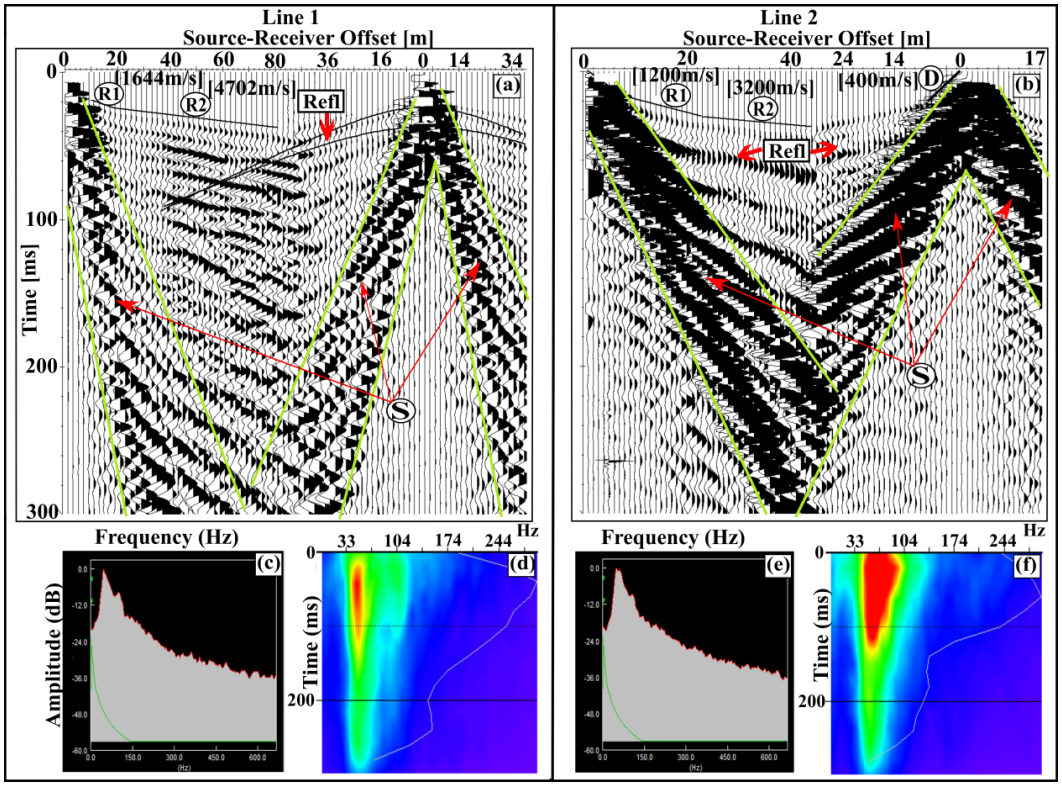


Figure 3.4: (a) and (b) Raw seismic shot gathers recorded along lines 1 and 2, respectively. **(**c and e) Power spectrum of the raw shot gathers along lines 1 and 2, respectively. (d and f) Amplitude decay curve of the raw shot gathers along lines 1 and 2, respectively. Various seismic events are interpreted as follows: D – direct wave; R1 – first refracted P-wave; R2 – second refracted P-wave; Refl – possible P-wave reflections from bedrock and S – surface waves.

3.4.2. Seismic refraction processing

The fundamental information obtained from the seismic refraction method includes the P-wave velocity and thickness of the near-surface layers. Processing of refraction seismic signals was based on picking the first arrivals (head waves) from the shot gathers. The data were processed and inverted using the ReflexW software package to generate the velocity-depth model (velocities of the direct and refracted arrivals) shown in Figure 3.5. The seismic refraction tomographic optimizes the calculated arrival times to construct a 2-D velocity model of the near-surface. As a result, this technique can be more effective at integrating spatial heterogeneities and gradational boundaries relative to conventional

interpretation methods that assume constant velocity layers (Sheehan et al., 2005; Steelman et al., 2017). The refraction tomography results (Figure 3.5a and b) clearly show variations in the near-surface velocity field from 400 to 5000 m/s, which indicate different lithologies.

The refraction tomography images (Figure 3.5a and b) were generated using a more advanced seismic refraction tomography technique (i.e., Simultaneous Iterative Reconstruction Technique (SIRT) algorithm available in the ReflexW software). The SIRT algorithm automatically adapts synthetic travel time data (calculated) to the observed data sets (Sandmeier, 1998). These synthetic travel times are automatically calculated from the picked travel time and compared with the observed data sets. Moreover, the acquisition geometry and the calculated apparent velocities from the raw datasets were used as input parameters to generate the final refraction tomographic image. The spatial limit of the starting model is 0 - 30 m for the vertical resolution with 0.5 m bin size. The minimum and maximum velocities for the starting model are 400 m/s and 6500m/s, respectively. The inversion procedure was based on 50 iterations with a defined data variance of 0.01 (misfit), permissible threshold of 0.001 and 50 % maximum defined change of the input model. The tomographic result was controlled using forward raytracing and waveform inversion (Generalized Reciprocal Method) as shown in Figure 3.5c and d. This process assisted in tracing and identifying the refractor and reflector boundaries clearly. The tomography results in Figure 3.5 show Vp velocities of different shallow subsurface materials. The velocity of the top layer is about 400-900 m/s with its base at 3 - 4 m depth; the velocity of the second layer is about 1200 - 2500 m/s, the second refractor depth varies from 5 to 12 m. The velocity of the fresh bedrock is 4500 - 5000 m/s.

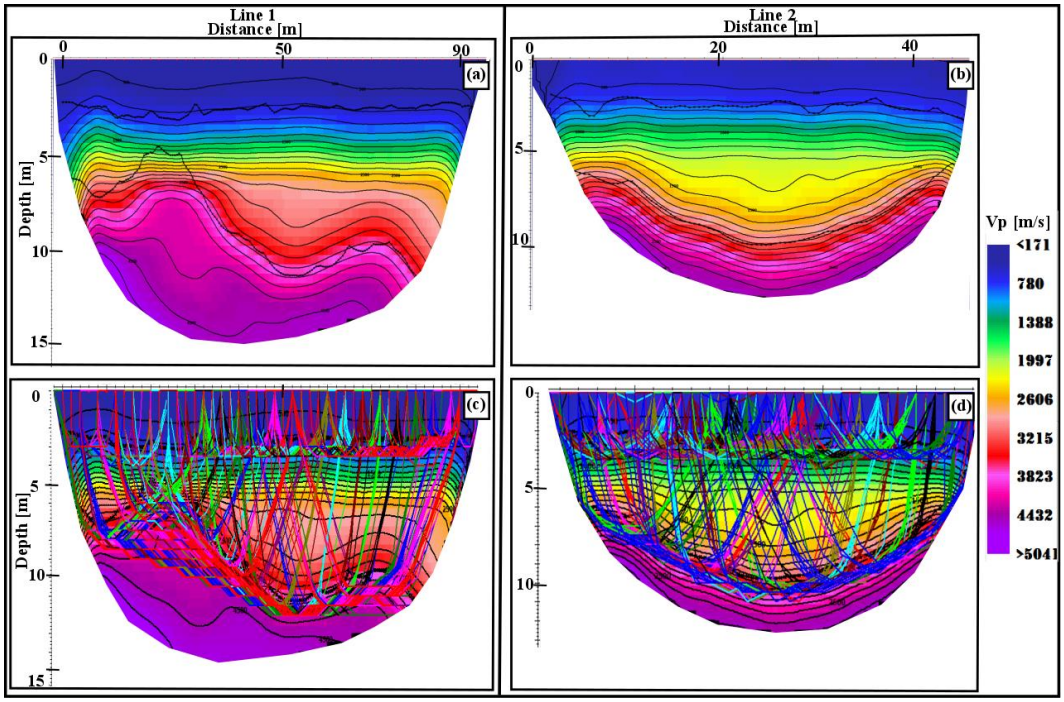


Figure 3.5: (a) and (b) Refraction tomography results along lines 1 and 2. (c) and (d) Raytracing of the traveling waves and waveform inversion embedded on the tomography images on the respective profiles. The contour lines represent the velocity isolines with a starting velocity of 300 m/s and 100 m/s intervals.

3.4.3. Reflection seismic processing

The processing of reflection seismic data aims to enhance the coherent reflections resulting from various geologic boundaries observed on the shot gathers by eliminating the undesired signals such as surface waves, direct and refracted arrivals (see Figure 3.4a and b). Table 3.2 shows the processing workflow for this study. The reflected signals identified in the seismic time section at intercept times of 20 - 30 ms were interpreted to be associated with bedrock-alluvium reflections generated from the near-surface boundary (Figure 3.4). Reflections from deeper (beyond 100 - 150 m) subsurface are not convincingly discernible on the seismic data due to the acquisition geometry and the energy source used for the seismic survey, which was designed for only shallow targets (less than 100 m in depth). Closer inspection of the shot gathers suggests that high amplitude and low-frequency source-generated noise dominates the recorded data (see Figure

3.4). Therefore, thorough processing steps were undertaken to separate the undesired signals from the useful reflected signals.

Table 3.2: Processing sequence and parameters.

Sequence	Parameter
Trace Edit	Removing dead traces
Amplitude scaling	0 - 300 ms
Spiking deconvolution	300 ms autocorrelation length, 60 ms filter length and 10% white noise
Bandpass frequency filter	100 - 250 Hz, Butterworth order of 3
Trace normalization	
F-k filter	Bandpass 400/650 - 100000 m/s velocity range, with 5 m/s taper width.
Automatic Gain Control (AGC)	150 ms
Time cut	150 ms
Top mute	Removing the direct and refraction arrivals
CMP sorting/Velocity analysis	Interactive velocity analysis
NMO correction/Stacking	Velocity range from 1200 - 2600 m/s
Bandpass frequency filtering	100 - 250 Hz, Butterworth order of 3
Static correction	Surface-consistent statics
Time-depth conversion	Using stacking velocity

Figure 3.6 shows some key processing steps involved in our reflection seismic processing workflow. Our procedures include defining the acquisition geometry, editing of noisy/bad traces, amplitude scaling of the recorded signals (Figure 3.6a and b), signal deconvolution and bandpass frequency filtering. Deconvolution sharpens the signal and removes the effect of source and receiver coupling and multiples in the data. Various deconvolution techniques were tested (spiking, predictive and zero-lag deconvolution). Spiking deconvolution with 0 - 300 ms autocorrelation window, 60 ms filter length and 10% added white noise provided the best results. This broadens the reflected signal spectrum (Figure 3.6g and h)). Subsequent bandpass frequency filtering of 100 - 250 Hz with a 3rd-order Butterworth filter provides improved resolution and attenuation of lower frequency signals (surface wave) (Figure 3.6b and c). The source-generated noise

on the upper section of the shot gathers has been well suppressed after deconvolution and bandpass frequency filtering (Figure 3.6b and c).

Surface waves sometimes appear coherent in the seismic time section and may appear as a low-velocity event with linear moveouts in the offset domain. Correcting for such low-velocity, low-frequency events requires transforming the recorded data from the space-time domain to the F-K domain, then applying a bandpass filter to remove the undesired low-velocity events within the F-K spectrum. A frequency-wavenumber (F-K) filter with high-pass velocities above 400 m/s and a squared Hanning taper were applied. In addition, automatic gain control (AGC), with 100 ms lag width was used to further improve the visibility of late arriving events, since variable coupling of the geophone and source to the ground and variations in near-surface conditions prevented the use of true-amplitude processing procedures. No reflected event was observed below 50 ms travel time. Therefore, a time cut filter was applied to remove the signals below 150 ms. To avoid misprocessing direct or refracted arrivals as reflections, a pre-stack processing strategy involved carefully hand-picked top mutes was used (Figure 3.6e and f).

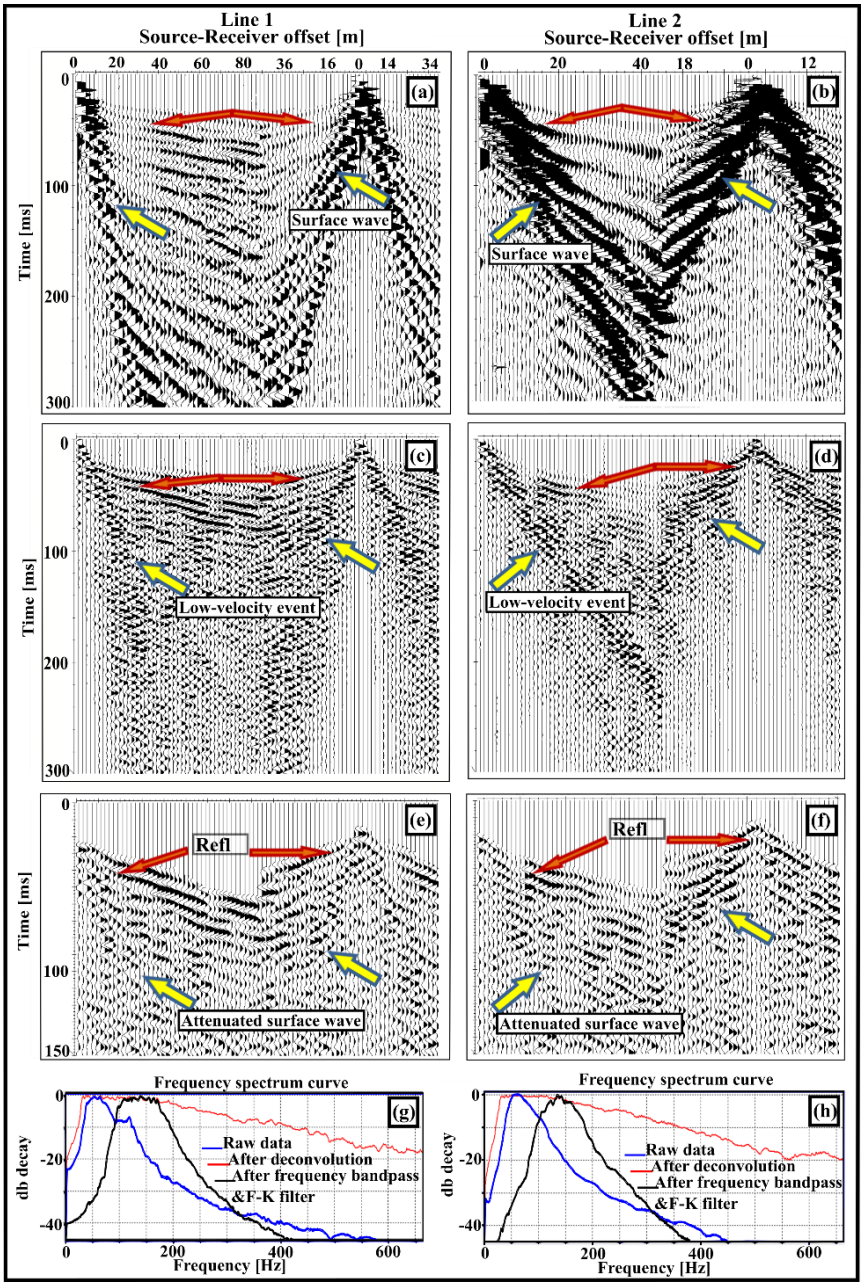


Figure 3.6: Typical shot gathers from lines 1 and 2 showing the key steps in reflection seismic processing. (a) and (b) After trace editing and amplitude scaling. (c) and (d) After spiking deconvolution and bandpass frequency filtering. (e) and (f) After trace equalization (AGC), top muting (direct and refracted arrival muting) and time cut. (g) and (h) Amplitude decay-frequency curves of the shot gathers after deconvolution, bandpass frequency and F-K filtering. Notice the broadening of the reflected signal spectrum after deconvolution. The red arrows show the enhanced bedrock reflector and the yellow arrows point to the attenuated surface waves after frequency bandpass and F-K filtering.

Furthermore, the filtered seismic shot gathers were sorted into common mid-point (CMP) gathers for velocity analysis. A reflected hyperbolic-shaped event (Refl) can be traced through the entire CMP gathers at an intercept time of 20 - 30 ms and hyperbolic velocity moveouts of 1800 - 3200 m/s. Other coherent events below 40 ms were not clearly observed in all the CMPs. Hence, further processing steps were focused on improving the visibility of reflector Refl (Figure 3.7). The velocity analyses were based on interactively picked semblances within the velocity spectrum and integrated analysis of constant velocity stacks. Figure 3.7 shows the velocity analysis performed on the CMP gathers. The final velocity model used in the NMO correction is the model that best levels the reflection hyperbola in the CMP gather and optimizes the quality of stacked data.

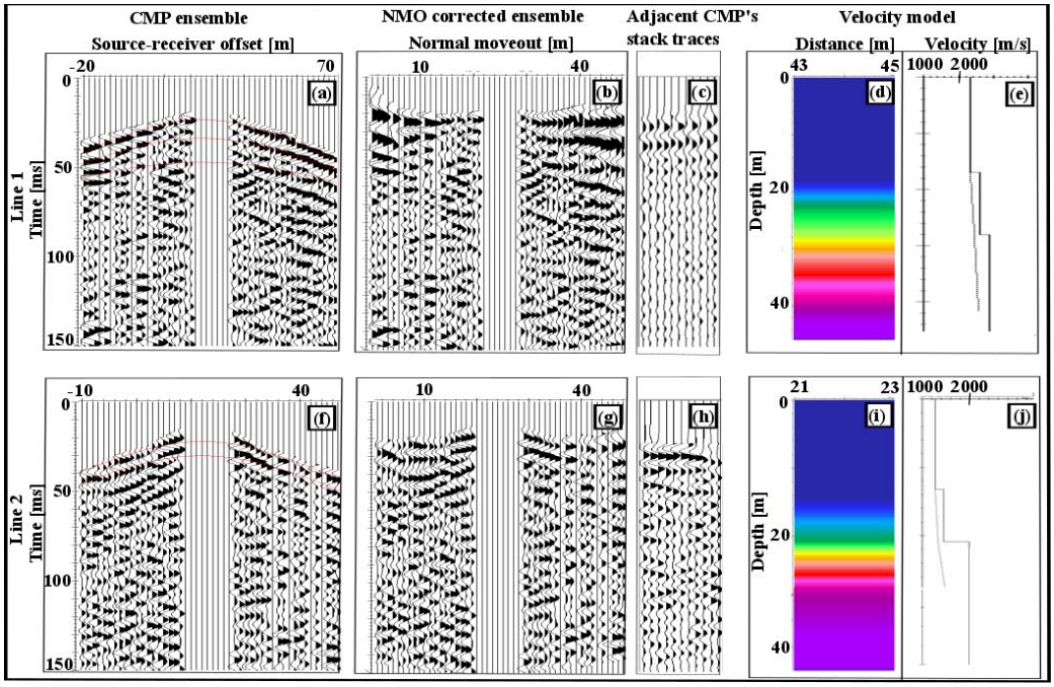


Figure 3.7: Sample of CMP-gather velocity analysis. (a) CMP ensemble, (b) NMO corrected ensemble, (c) adjacent CMP gathers, (d) stacked traces and (e) velocity model at the selected CMP along line 1, respectively. Similarly, for line 2 (f – j)

The stacked time seismic sections for line 1 and 2 with their corresponding time-to-depth converted sections are shown in Figure 3.8a - d. Surface consistence statics were used for the static correction since the profile elevation were approximately flat and the velocity of weathered layer was assumed constant

(Cox, 1999; Steeples and Baker, 1998) (Figure 3.8b and d). The CMP gathers were 45 % muted after NMO correction to prevent NMO stretch (Miller, 1998). The stacked sections were also frequency bandpass filtered (100 - 250 Hz) to remove the incoherent and coherent random noise due to wavelet deformations/stretch during NMO correction. A reflected event with a dominant frequency of 100 - 145 Hz and average velocity of 1800 - 3100 m/s can resolve about 3 - 7 m bed thickness (vertical resolution) using the one-quarter wavelet criterion (Kallweit and Wood, 1982). The width of the Fresnel zone, which is the horizontal resolution, was estimated to vary between 5 - 9 m within the overburden (Yilmaz, 2001). Finally, the seismic time sections were migrated and converted to depth sections using the stacking velocity model (see Figure 3.7). The interpretation focuses on the continuous and quasi-continuous events above 80 ms two-way travel time and the area of maximum coverage (nominal fold).

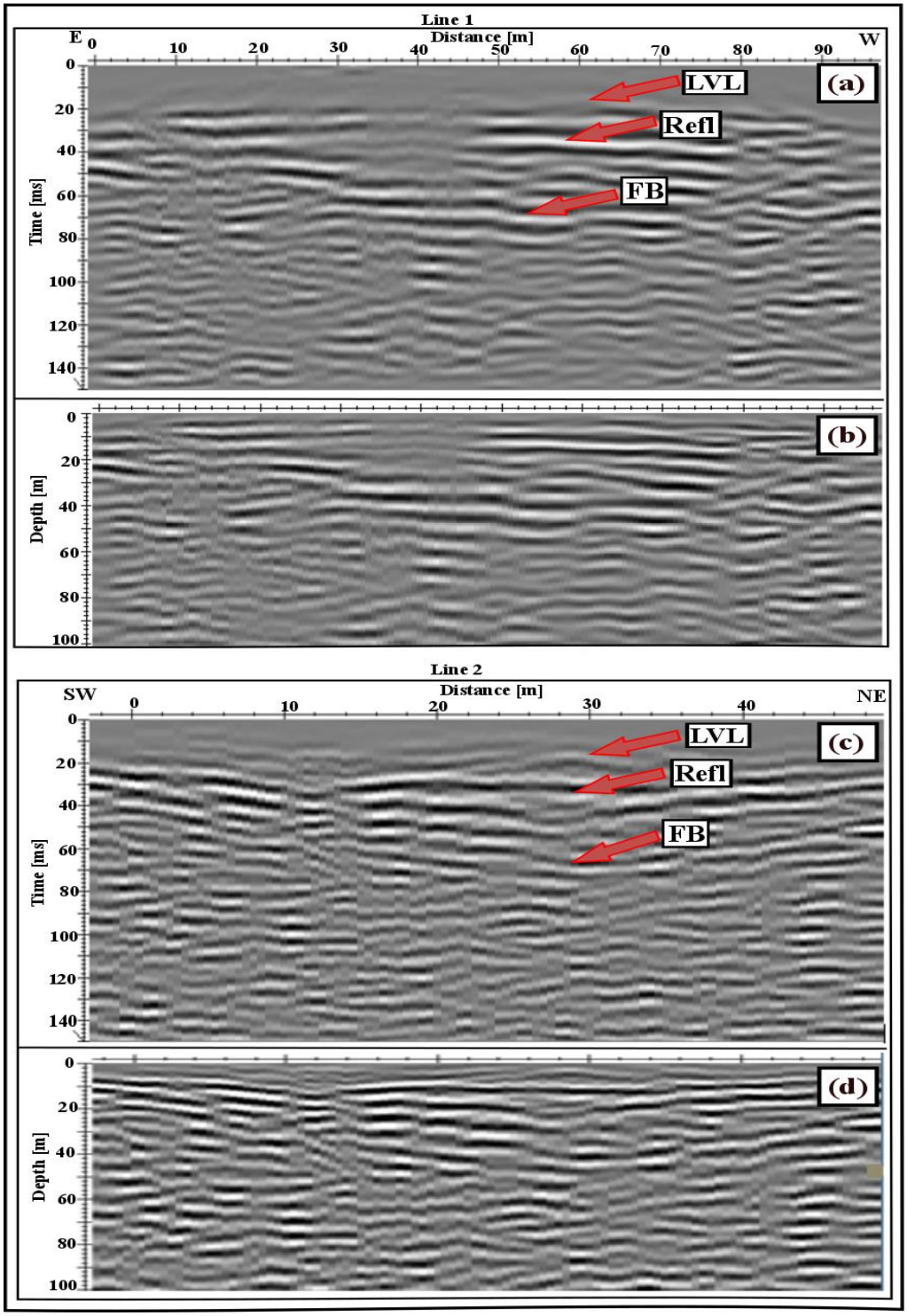


Figure 3.8: The final stacked time seismic section after subsequent bandpass frequency filtering. (a) and (c) represents seismic time sections of lines 1 and 2, respectively, while (b) and (d) are the respective depth sections. The red arrows point to the bedrock (Refl), the fresh bedrock reflectors (FB) and the low-velocity layer (LVL)

3.4.4. Multi-channel analysis of surface waves (MASW) and resistivity tomography inversion

The MASW method was used in this study to estimate the average 1-D Vs wave velocity structure of the near-surface along the active receiver spread for the offset shots (Park et al., 1999). We merged 14 m and 6 m offset shots in order to avoid the effect of near- and far-offsets on the dispersion curve. The 1-D velocity model for a shot gather is placed at the middle of the receiver spread related to that shot. We used the MASW method to constrain the interpretation of other geophysical techniques in the delineation and mapping of the water table and low-velocity layers, especially in the absence of the borehole data along the profiles. The MASW method uses the dispersive property of Rayleigh wave phase velocity (ground roll) (Figure 3.4) to estimate Vs velocities (Park et al., 1999; Xia et al., 1999; Yilmaz, 2015) (Figure 3.9). The method assumes that the subsurface is vertically heterogeneous and laterally homogeneous.

The processing of MASW data involves two main steps. The first step is to generate the dispersion curves (frequency vs. phase velocity plots) from the raw shot gather (Figure 3.9a and c) and the second step is to perform the inversion of dispersion curves to estimate Vs velocities (Figure 3.9b and d). The SurfSeis4.5 code was used in the data processing. This software involves wavefield transformation from an offset-time domain (i.e., the raw shot gathers) to an offset-frequency domain through a 1-D Fourier transform, providing a combination of amplitude and phase spectra (Park et al., 1998). Once a good quality dispersion curve was generated, an inversion scheme was applied to estimate the shear wave velocities from Rayleigh-wave phase velocities. During this process a model was specified by executing a forward solution. This model has been designed within the SurfSeis 4.5 code according to the velocity of the surface wave on the shot gather and the characteristics of the dispersion curve. Finally, the shear wave velocity model is obtained by performing the non-linear least squares method on this forward model. The results of Vs velocity were obtained after 10 iterations.

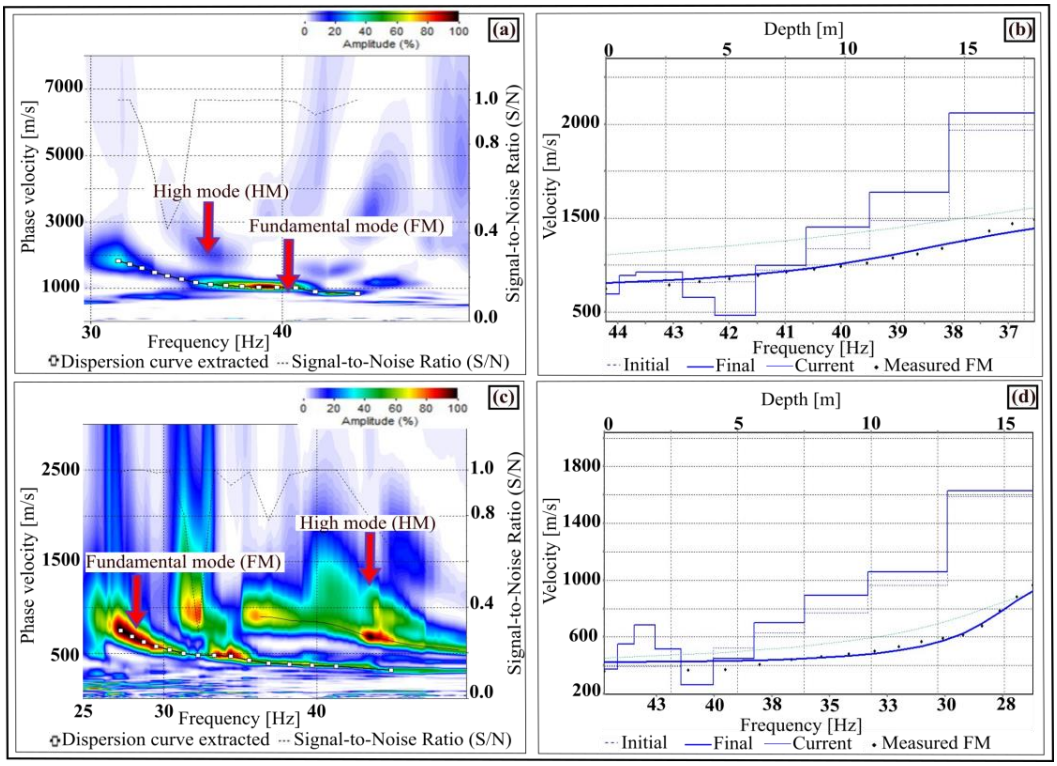


Figure 3.9: Multichannel analysis of surface wave. (a) and (c) Dispersion spectrum of the offset shots along lines 1 and 2, respectively (show in it is the extracted dispersion curve used for Vs velocity inversion). (b) and (d) 10-layer Vs velocity model for (a) and (c), respectively.

The electrical resistivity tomography (ERT) method calculates the apparent resistivity of the subsurface by injecting a direct electrical current into the ground using two electrodes and measures the potential difference across two other electrodes at various chosen spacing and distances from the current source (Keller and Frischknecht, 1996). The measured apparent resistivity data were manually filtered to remove unreasonably anomalous data points and inverted to construct 2-D resistivity pseudo-sections of the near-surface image of the subsurface materials (i.e., subsurface resistivity distribution) using the RES2DINV software package (Loke, 2008) (Figure 3.10). Since the inversion procedure is smoothness-restricted, the inversion algorithm required smoothing parameters as an input (Griffiths and Barker, 1993; Loke and Barker, 1996; Loke et al., 2013). Moderate horizontal flatness and minimum vertical flatness for the inversion was applied. The resistivity tomography was obtained after 10 iterations with a root mean square error (RMS) of 2.9 (in line 1) and 4.2 (in line 2). Although the inversions

were not constrained by any borehole measurement close to the profile lines, a reasonable agreement was achieved between the inverted models and other geophysical results (e.g., refraction tomography and MASW). An optimum investigation depth of about 24 and 16 m was achieved using a maximum offset distance of 120 m at 3 m electrode spacing along line 1, and 80 m spread length of 2 m electrode spacing along line 2, respectively (Figure 3.10a and b).

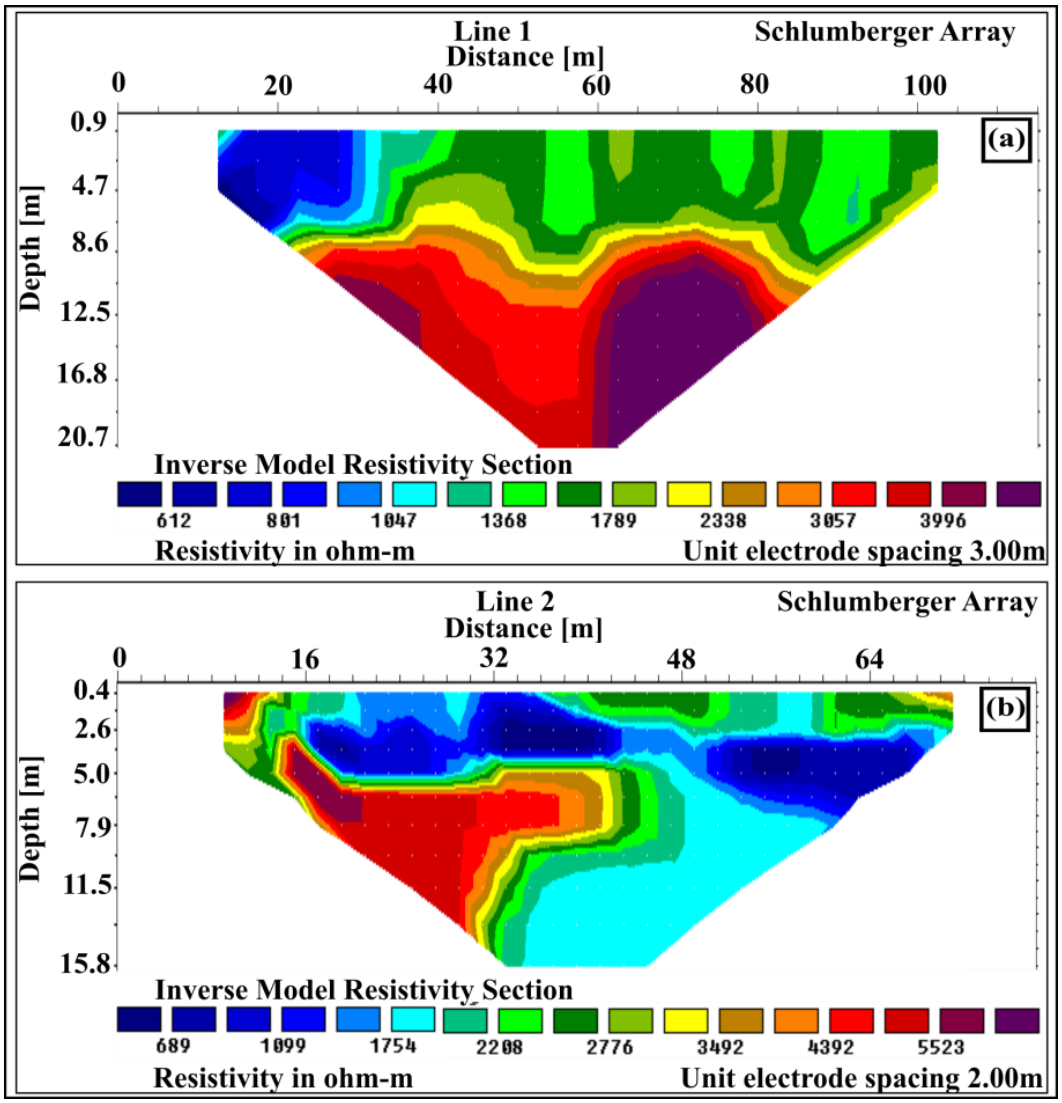


Figure 3.10: Resistivity profile along lines 1 and 2.

3.5. Integration

This study aims to delineate the shallow aquifer, map the bedrock-overburden contact that defines the groundwater storage capacity and geological structures responsible for underground water movement. Different geophysical surveys were

integrated (Figure 3.11) and compared with the bedrock information from boreholes and geological model around the vicinity of the profile lines (Figure 3.12). However, the actual position of the geological model in Figure 3.12 was not mentioned in the paper (Tooth et al., 2001). The previous studies reported two main geological formations in the area: an alluvium deposit with gravel at the base and sandstone bedrock with highly weathered surface (Timmerman, 1985; Higgins et al., 1996; Tooth et al., 2001). Due to inadequate information concerning the lithology of the study area along the survey lines, the interpretation results were more subjective. Nevertheless, the integration of different geophysical techniques (seismic reflection, refraction, MASW and resistivity measurements) provides complementary constraints in generating the final subsurface geological model. Our integrated results reveal characteristics of different geological units and structures (Figure 3.11).

3.5.1. Reflection seismic

The seismic reflection sections (Figure 3.11e and f) reveal different geological units (top sand, saturated sand/gravel, weathered and competent bedrock) and structures (faults). This is discussed in terms of reflection characteristics and comparison to other geophysical methods, as noted in Figure 3.11. The seismic event (FB) between 20 - 42 m depth (Figure 3.11e and f) was interpreted as seismic reflections emanating from competent sandstone bedrock. This was not observed on the refraction tomography (see Figure 3.11a and b) and the resistivity tomography (Figure 3.11c and d), probably due to their shallow depths of investigation. The rough topography and uneven reflectivity along the surface could be associated with different degrees of weathering and fracturing and could also be associated with the effect of 3-D structures within the layer. However, the lack of ground truth along the profiles and the 3-D view does not permit for a more definite interpretation. The seismic section also shows the mapping of a thrust fault centred across line 1 at 29 m and three normal faults along line 2 centred at distances of 8 m, 11 m and 15 m (Figure 3.11e and f). I interpret these as faults due to breaks in reflection coherency along the horizon. I also observe a shallow undulating seismic reflection (Refl) between 6 - 12 m depth, dipping

westward, which defines the base of the alluvium deposit (Figure 3.11 and Figure 3.12). From the correlation of the borehole data and the geological model (see Figure 3.3 and Figure 3.12), I correlated the prominent reflection with the interface between the alluvium gravel base and the underlying Waterberg sandstone. The shallow bedrock unit exhibits velocities of 2600 - 3200 m/s (as determined from first break, refraction tomography and stacking velocity analyses), whereas the velocity of the fresh bedrock is characterized by the velocities above 4000 m/s. This reflective boundary is truncated or interrupted (loss of reflection coherency) across line 1 at 25 - 50 m (Figure 3.11c). This feature is interpreted to be a highly weathered or fractured zone. At 5 - 10 m distance on the seismic section we also note a linear structure that cross-cuts the boundary. This is interpreted as a fault zone. In line 2, at a distance between 5 m and 10 m, the seismic section also shows the mapping of two faults that cross-cut the reflector. The discontinuous character of the reflection noticed at the edges of the seismic sections could be associated with poor S/N or data coverage.

3.5.2. MASW, refraction and resistivity tomography

When comparing the seismic refraction and electrical tomography, we notice that the reflector near the top of the seismic sections matches with (1) the second refracted arrival head waves (R2 in Figure 3.4) with Vp of ~2500 - 4500 m/s; and (2) the undulating bedrock surface observed on the resistivity tomogram with a resistivity value of about 2000-5000 ohm•m (Figure 3.11). Thus, we interpret these bedrock undulations to represent an erosional surface or weathered/fractured region near the bedrock surface.

Furthermore, the ~ 3 m thick uppermost low-velocity-layer (LVL) in the refraction tomogram corresponds to the change in velocity contrast within the intra-alluvium deposits between the top dry sand and saturated sand/gravel, although this layer is not visible on the seismic reflection section. However, its evidence in the first arrival time and refraction tomography cannot be repudiated. From direct correlations between refraction data (Figure 3.4) and MASW results (Figure 3.9), we observe the geophysical signatures of a saturated interface between depth of 3 and 5 m, which corresponds to a sharp Vp increase from the

low-velocity layer (400 - 800 m/s) to a higher-Vp layer (1200 - 2600 m/s) and a decrease in average Vs velocity from 600 to 300 m/s within this interface. These Vp velocities correspond well with the velocities obtained from CMP velocity analysis (1000 - 2100 m/s). In comparison with the resistivity tomogram (Figure 3.11c and d) the low-Vp, high-Vs layer seems to correspond with a high resistivity layer at depth of 0 - 3 m (Figure 3.11d), while the high-Vp low-Vs layer correlates with a low resistivity layer (600 - 1300 ohm•m) at depth of 2-8 m. A fault zone across line 1 between 6-12 m along the profile is also observed and this may explain the low resistivity values observed on the resistivity tomogram, possibly due to the presence of water in the shear/fractured zone. In line 2 at distances of 12 - 36 m, the resistivity tomogram indicates a low-resistivity zone that could represent a fractured or weathered region where water tends to saturate or flow. Consequently, from the observed results (MASW, refraction and resistivity tomography), the interface between the intra-alluvium materials (top sand/saturated sand-gravel) could be interpreted as the groundwater table. However, this will need to be confirmed with the borehole information when it becomes available. Based on high-resolution shallow reflection seismic data complemented with first-break travel time refraction and resistivity tomography results and 1-D MASW analysis, we compare the geological model obtained in the area by the geologist/environmentalist with the derived geological model along two perpendicular profiles within Nyl River floodplain in the Nylsvley Nature Reserve as shown in Figure 3.12 and Figure 3.13, respectively.

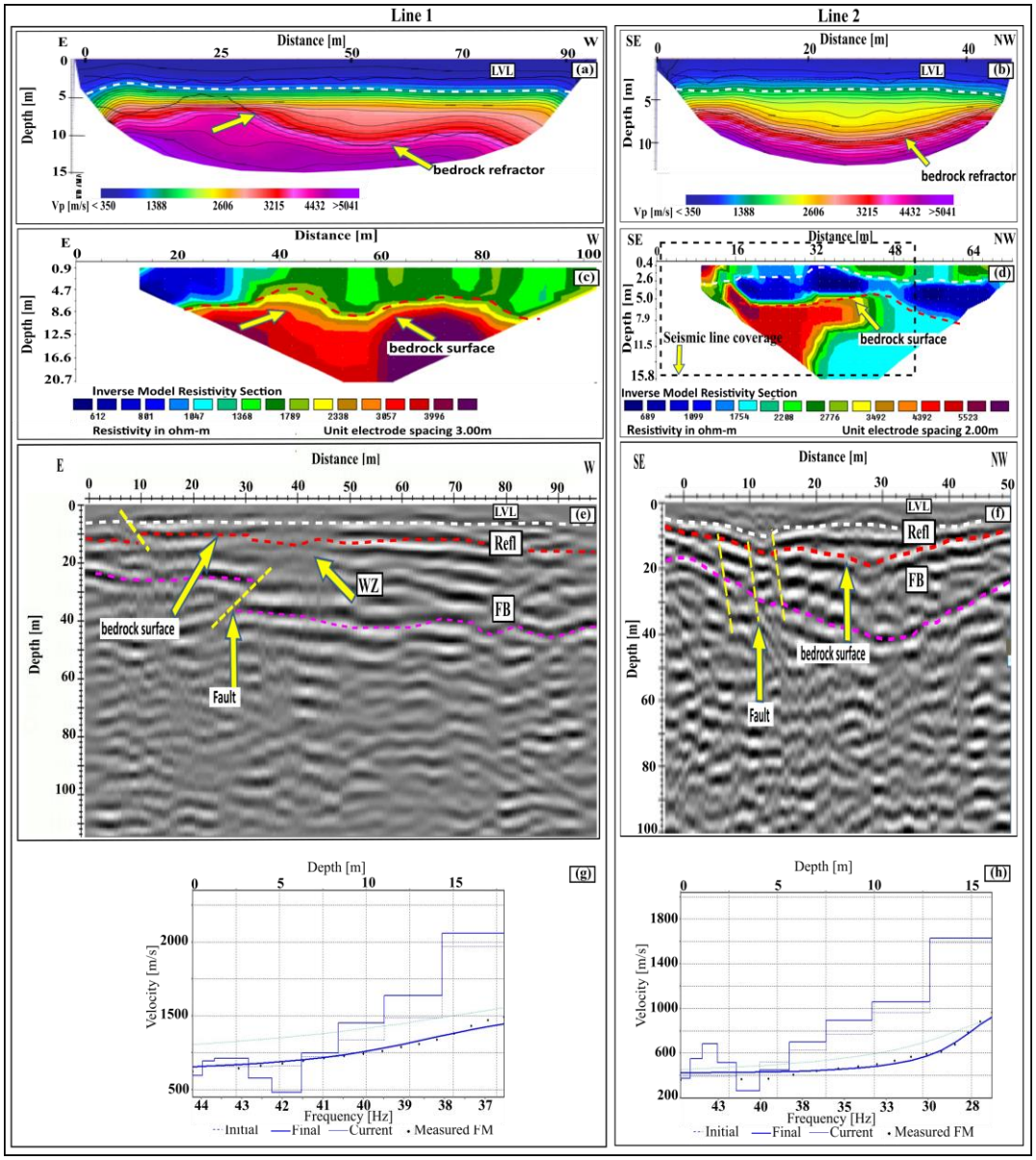


Figure 3.11: Integrated interpretation of line 1 and 2. (a) and (b) Refraction tomography. (c) and (d) Resistivity tomography. (e) and (f) Reflection seismic section. (g) and (h) 1-D profile of MASW. LVL probably represents the base of the low velocity layer, Refl the bedrock reflector, FB the fresh bedrock reflector and WZ probably represents a highly weathered/fractured zone.

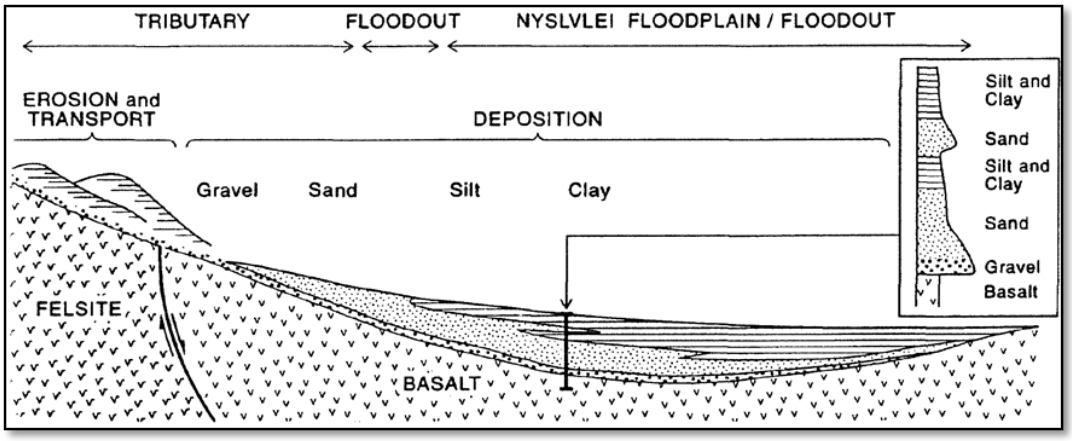


Figure 3.12 Schematic diagram showing downstream changes in the sediment transported by tributaries, and sediment underlying the Nyl River floodplain/floodout (Tooth et al., 2002 based on the borehole data in Timmerman, 1984). The depth of alluvium underlying the floodplain reaches a maximum of ~35m (Tooth et al., 2002 www.tandfonline.com).

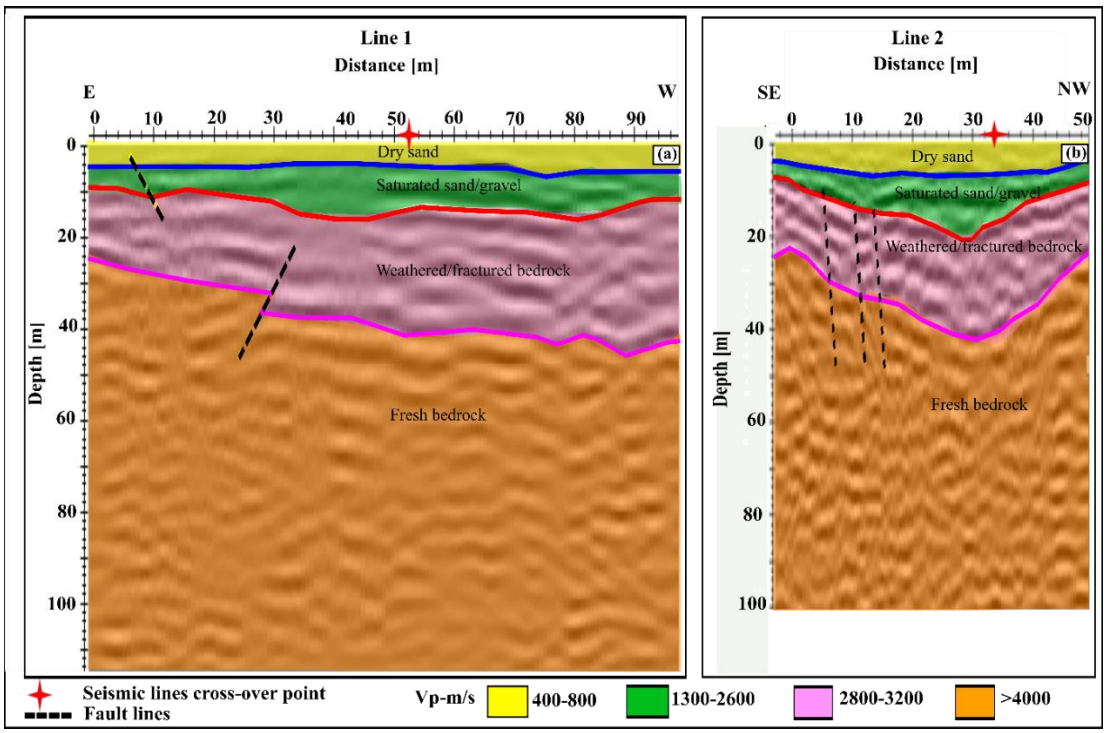


Figure 3.13: A geological model along the profile lines. (a) Line 1 and (b) Line 2. Different stratigraphic units are delineated with solid coloured lines and interpreted faults are shown as black dashed lines.

3.6. Conclusions

The seismic data analysis revealed that high–amplitude low-frequency source-generated noise dominated the raw shot gathers, making it difficult to see the reflected events clearly. However, the first arrival time was carefully picked and used to generate the refraction tomographic images and waveform inversions of the near-subsurface. Two refractor events R1 (~ 3 - 5 m depth) and R2 (~ 8 - 12 m depth) were observed with P-wave velocities of approximately 1200 - 2500 m/s and 2800 - 6000 m/s, respectively.

Subsequent reflection seismic data processing enhanced the reflectors Refl and FB in the final stacked seismic section. These reflectors are interpreted as reflections arising from the alluvium-weathered bedrock interface and the contact between weathered/fractured-competent bedrock. The seismic reflector (Refl) correlates with seismic refractor (R2) and an undulating bedrock surface observed in the resistivity tomogram. The depth of bedrock varies from 8 to 12 m. The physical property contrast observed within the alluvium deposit on refraction and resistivity tomograms were also confirmed by the MASW 1-D model, which exhibited high- to low-Vs layers. The low-Vp layer (400 - 800 m/s) in refraction tomograms correlates with the average Vs velocity of 600 m/s at 0 - 3 m depth, while the low average Vs value (~ 300 m/s) shown in the MASW 1-D model between 3 and 7 m depth corresponds to the sharp increase in Vp (1200 - 1800 m/s) and low resistivity values (600 - 1300 ohm•m) observed in refraction and resistivity tomogram, respectively. This also correlates with a poorly image reflector (LVL) on the stacked seismic section.

Moreover, the physical property contrast observed within the alluvium deposit at 3 - 5 m depth is interpreted as a transition from an unsaturated sand layer to a saturated sand/gravel layer. Thus, I interpret tthis interface within the intra-alluvium layer as the groundwater table along the profile lines at depths of 3 - 5 m. The data also shows the mapping of the bedrock undulation that is associated with the fractured/weathered zone; this is important for storage and migration of underground water in the surveyed area. In addition, the saturated alluvium deposit base (sand/gravel) combined with the weathered/fractured bedrock surface

represent the hydrostratigraphic units in the area with thicknesses of 18 - 38 m. The thickest undulated weathered/fractured zone along the profile lines is a good location for future groundwater boreholes. In support of our assertions, the previous geological and environmental research conducted in the area suggested that the fractured/weathered zone within the bedrock surface is responsible for underground water movement and storage in the area (Higgins et al., 1996; Tooth et al., 2002). Therefore, I demonstrated that shallow reflection seismic method, when combined with other geophysical techniques (such as refraction and resistivity tomography, and MASW), is a powerful tool for imaging near-subsurface architectures and hydrogeological prospecting.

Acknowledgments

All the equipment used in this study was provided by the Seismic Research Centre, School of Geosciences, University of the Witwatersrand. I thank Lebogang Sehoole, Wesley Harrison, Nkimo Moleleki and Sikelela Gomo for their assistance in the field, Dr. Steven Zhang for his immense review contribution and CSIR South Africa for granting access to ReflexW software, Council for Geosciences (CGS) South Africa for access to SurfSeis 4.5 software used in the data processing. We would like to thank Nylsvley Nature Reserve, Limpopo Province, South Africa for granting us the opportunity to conduct this survey. We also want to thank the anonymous reviewers (journal of geophysics and engineering) for their insightful recommendations, as their comments help improve the quality of the manuscript.

The authors have confirmed that any identifiable participants in this study have given their consent for publication.

3.7. Reference

Ahmad, J., Schmitt D.R., Rokosh, C.D. and Pawlowicz, J.G., 2009. High-resolution seismic and resistivity profiling of a buried Quaternary subglacial valley, Northern Alberta. *Canada Geological Society of America Bulletin, 121*, pp. 1570-1583.

Ayers, J.F., 1989. Application and comparison of shallow seismic methods in the study of an alluvial aquifer. *Groundwater, 27*, pp. 550-563.

Butler, D.K ed., 2005. Near-surface Geophysics. *Society of Exploration Geophysicists,* Investigation in Geophysics, *13,* Tulsa, Oklahoma, U.S.A.

Cox, M., 1999. Static Corrections for Seismic Reflection Surveys. *Society of Exploration Geophysicists*, Tulsa, Oklahoma, U.S.A.

Dehghannejad, M., Malehmir, A., Svensson, M., Lindén, M. and Möller, H., 2017. High-resolution reflection seismic imaging for the planning of a double-train-track tunnel in the city of Varberg, southwest Sweden. *Near Surface Geophysics, 15*, pp. 226-240.

Griffiths, D.H. and Barker R.D., 1993. Two-dimensional resistivity imaging and modelling in areas of complex geology. *Journal of Applied Geophysics, 29*, pp. 211-226.

Higgins, S.I., Coetzee, M.A.S., Marneweck, G.C. and Rogers, K.H., 1996. The Nyl River floodplain, South Africa, as a functional unit of the landscape, a review of current information. *African Journal of Ecology, 34*, pp. 131-145.

Kallweit, R.S. and Wood, L.C., 1982. The limits of resolution of zero-phase wavelets. *Geophysics, 47*, pp. 1035-1046.

Keller, G.V. and Frischknecht F C., 1996. Electrical Methods in Geophysical Prospecting. *Pergamon Press, Inc*, London.

Leucci, G., 2007. Geophysical investigations to study the physical–mechanical characteristics of the rock in a coastal environment: the cliff of Roca (Lecce, Italy). *Journal of Geophysics and Engineering*, *4*(4), pp. 462-475.

Loke, M.H., 1994. The Inversion of Two-dimensional Resistivity Data (Unpublished PhD thesis), University of Birmingham.

Loke, M.H., 2008. RES2DINV-Rapid 2D resistivity and IP inversion using the least squares method for geoelectrical imaging: 2D and 3D GEOTOMO software, Malaysia, 130p.

Loke, M.H. and Barker, R.D., 1996. Practical techniques for 3D resistivity surveys and data inversion. *Geophysical Prospecting, 44*(3), pp. 499-524.

Loke, M.H., Chambers, J.E., Rucker, D.F., Kuras, O. and Wilkinson, P.B., 2013. Recent developments in the direct-current geoelectrical imaging method. *Journal of Applied Geophysics, 95*, pp. 135-156.

Malehmir, A., Durrheim, R.J., Bellefleur, G., Urosevic, M., Juhlin, C. and White, D., 2012. Seismic methods in mineral exploration and mine planning, a general overview of past and present case histories and a look into the future. *Geophysics, 77*, pp. WC173-WC190.

Manzi, M.S.D., Gibson, M.A.S., Hein, K.A.A., King, N. and Durrheim, R.J., 2012. Application of 3-D seismic techniques in evaluation of ore resources in the West Wits Line goldfield and portions of the West Rand goldfield, South Africa. *Geophysics, 77,* pp. WC163-WC171.

McCarthy, T. and Rubidge, B., 2005. The Story of Earth and Life: A Southern Africa Perspective on a 4.6 Billion-year journey. *Struik,* South Africa.

Miller, R.D., Steeples, D.W. and Brannan, M., 1989. Mapping a bedrock surface under dry alluvium with shallow seismic reflections. *Geophysics, 54*, pp. 1528-1534.

Miller, R.D. and Xia, J., 1998. Large near-surface velocity gradients on shallow seismic reflection data. *Geophysics, 63*, pp. 1348-1356.

Park, C.B., Miller, R.D. and Xia, J., 1998. Imaging dispersion curves of surface waves: 68th Annual International Meeting, Expanded Abstracts. *Society of Exploration Geophysicists,* pp. 1377-1380.

Park, C.B., Miller, R.D. and Xia, J., 1999. Multichannel analysis of surface waves. *Geophysics, 64*, pp. 800-808

Porszasz, K., 1973. Nyl River valley: An investigation of the groundwater potential. Department of Water Affairs. Technical Report no GH 2984, Pretoria.

Pugin, A.J.M., Pullan, S.E., Hunter, J.A. and Oldenborger, G.A., 2009. Hydrogeological prospecting using P-and S-wave landstreamer seismic reflection methods. *Near Surface Geophysics, 7*, pp. 315-327.

Sandmeier, K.J., 1998. ReflexW. Program for the processing of seismic, acoustic or electromagnetic reflection, refraction and transmission data. Karlsruhe, Germany: Sandmeier Software.

Sato, H., Fehler, M.C. and Maeda, T., 2012. Seismic Wave Propagation and Scattering in the Heterogeneous Earth. *Springer Science & Business Media*.

Schmelzbach, C. Green, A.G., and Horstmeyer, H., 2005. Ultra-shallow seismic reflection imaging in a region characterized by high source-generated noise. *Near Surface Geophysics,* 3, pp. 33-46.

Schreilechner, M.G. and Eichkitz, C.G., 2015. High resolution seismic reflection in geotechnical and hydrogeological applications: In International Conference on Engineering Geophysics, Al Ain, United Arab Emirates, 15-18 November. *Society of Exploration Geophysicists.* pp. 6-9.

Sheehan, J.R., Doll, W.E. and Mandell, W.A., 2005. An evaluation of methods and available software for seismic refraction tomography analysis. *Journal of Environmental and Engineering Geophysics, 10*, pp. 21 – 34.

Sheriff, R.E., 1975. Factors affecting seismic amplitudes. *Geophysical Prospecting, 23*, pp. 125-138.

Steelman, C.M., Arnaud, E., Pehme, P. and Parker, B.L., 2017. Geophysical, geological, and hydrogeological characterization of a tributary buried bedrock valley in southern Ontario. *Canadian Journal of Earth Sciences, 18*, pp. 1-8.

Steeples, D.W., 1998. Shallow seismic reflection section: Introduction. *Geophysics, 63*, pp. 1210-1212.

Steeples, D.W. and Baker, G.S., 1998. Finding seismic static corrections. *AAPG Explorer*, *19*, pp. 20-21.

Timmerman, L.R.A., 1984. Geohydrological investigation of part of the Nyl River valley centered on the farms Olifantsklip and Brak, Technical Report no, GH 3310, Department of Water Affair and Forestry, Pretoria.

Tooth, S., McCarthy, T.S., Hancox, P.J., Brandt, D., Buckley, K., Nortje, E. and McQuade, S., 2002. The geomorphology of the Nyl River and floodplain in the semi-arid Northern Province. *South African Geographical Journal* (*www.tandfonline.com*), *84*, pp. 226–237.

Xia, J., Miller, R.D. and Park, C.B., 1999. Estimation of near-surface shear-wave velocity by inversion of Rayleigh waves. *Geophysics, 64*, pp. 691–700.

Yilmaz, Ö., 2001. Seismic Data Analysis. *Society of Exploration Geophysicists*, Tulsa, USA.

Yilmaz, Ö., 2015. Engineering Seismology with Applications to Geotechnical Engineering. *Society of Exploration Geophysicists*, Tulsa, USA.

CHAPTER 4

4.0 High-resolution integrated geophysical investigation at the Lancaster Gold Mine, Krugersdorp, South Africa

Abstract

An integrated geophysical approach using seismics and geoelectrical techniques was employed to investigate the architecture of historic narrow-reef workings and a proposed open-pit mine at Lancaster Gold Mine, near Krugersdorp, South Africa. The mining activities in the area were mainly carried out within the Kimberley Reef Package in the upper Central Rand Group of the Witwatersrand Supergroup, which hosts several gold-bearing conglomerates (locally known as reefs). The reefs are generally thin (≤ 2 m thick) and dip between 28° - 32° south. The integrated results indicate that the study area is characterised by a weathered surface layer with variable low P-wave velocity (400 – 1200 m/s) and resistivity (150 – 800) Ωm. The increase in resistivity and velocity at deeper layer characterise by lateral discontinuities are attributed to the host rock, which locally hosts weak zones, cavities or water-bearing zones due to the mining activities. The low-velocity weathered layer introduces significant static shifts in the reflection seismic data. Moreover, environmental noise from drilling and trucking, and the prominent bedrock-overburden contact that produces various wave conversions (P-S conversion), cause undesirable noise that contaminates the shot gathers as high-amplitude, source-generated and monochromatic noise. The noise was removed from the shot gathers using frequency and velocity filtering techniques. The final depth-migrated sections are characterised by high-resolution images of the subsurface from ~10 to ~150 m depth, which are constrained by the borehole information. The reflection seismic data delineate the interfaces between different rock layers and the stopes. The refraction and resistivity tomograms, on the other hand, provide more detailed images of the top 20-50 m of the subsurface and depict the approximate shallow geometry of fluid migration paths, mined-out areas, and bedrock-overburden boundaries. The combined borehole and geophysical data provide valuable information regarding the physical

characteristics of the subsurface and can be helpful for future risk management decisions, environmental and engineering studies in the area.

4.1. Introduction

Reflection seismics is a widely used geophysical exploration tool, especially for hydrocarbon and ore-body detection (Yilmaz, 2001; Malehmir et al., 2012a, Manzi et al., 2012a), and mine safety and planning (Malehmir et al., 2012b; Manzi et al., 2012b). Similarly, the technique has also been successfully used for engineering, geohydrological and environmental applications to determine the depth to the competent layer or aquifer, map contaminant plumes and features such as caves, voids, faults, mine stopes and tunnels (Steeples and Miller, 1988; Miller and Steeples, 1991; Leucci, 2004; Redhaounia et al., 2015; Isiaka et al., 2018; Onyebueke et al., 2018). The importance of imaging the near-subsurface in detail has stimulated many advances in technology to acquire data with higher frequencies (> 100 Hz) and lower background noise (for engineering, environmental and geotechnical applications) (Steeples and Miller, 1988, Miller and Steeples, 1991; Brodic et al., 2018). Integration of seismic with other geophysical methods such as geoelectric, gravimetric, GPR, magnetics, magnetotellurics that respond differently to various subsurface physical properties provide better constrained models of the subsurface (Leucci and De Giorgi, 2005; Gómez-Ortiz and Martín-Crespo, 2012; Cooper, 2014; Martinez-Moreno et al., 2014; Festa et al., 2016; Malehmir et al., 2016).

In this study, integrated high-resolution reflection/refraction seismic and electrical resistivity methods were used to investigate and image the near-subsurface architecture (mined-out zones, tunnels and fluid-migration pathways) in a shallow (< 100 m) historic gold mine located near Krugersdorp, South Africa, as a pilot project for future detailed site characterisation. Our results can also be useful to define the survey strategies for similar studies in karst and shallow mining environments. The study area is located within the Witwatersrand Supergroup of the Witwatersrand Basin, which is known to have produced 98 % of the South African gold and 45-50% of gold in the world (Handley, 2004; Anhaeusser, 2012).

The impact of these intense mining activities on the environment has left some underground voids and fissures, which are only partially remediated by backfilling and packing. Consequently, progressive dewatering of these structures could eventually lead to the formation of sinkholes and subsidence on the surface, which could pose a direct risk to infrastructural facilities (such as buildings, roads, and farmlands) and in general impede future urban development in the area (Wolmarans, 1996). Thousands of mining related seismic events such as sinkhole and subsidence have occurred in the past 60 years in the Gauteng Province of South Africa, centred on the mining district and dolomitic formations of the Transvaal Supergroup, with serious safety and socioeconomic consequences (Buttrick et al., 2011). Sinkholes occur in dolostone formations because of the progressive water ingress, which created secondary porosity through dolomitic dissolution and recrystallization, weathering, and erosion. The processes can be enhanced by the presence of carbon dioxide in groundwater (mainly from percolation through the soil, but partly derived from the atmosphere) (Whitaker and Xiao, 2010).

In addition to the formation of unstable subsurface voids, mine activities also produce considerable environmental pollution. Mine waste in the Witwatersrand Basin contains abundant pyrite, which oxidises to form insoluble ferric oxide and sulphate (Brink, 1979) (Figure 4.1); the latter further decomposes into sulfuric acid in the presence of oxygenated water (e.g., groundwater/rain water) creating acid mine drainage. Acid mine drainage permeates through any available migration path and can transport toxic elements such as uranium, lead, copper, cadmium, mercury, and zinc, all of which are available in the mine heaps, into underground water that may be used for domestic and industrial purposes. The sulfuric acid can also erode cement and concrete and result in accelerated wear and damage to infrastructures (Brink, 1979).

Hence, the inherent risk associated with shallow underground mining activities has encouraged the use of integrated geophysical methods to map potentially unstable subsurface structures (Leucci and De Giorgi, 2005; Gelis et al., 2010; Gómez-Ortiz and Martín-Crespo, 2012; Martinez-Moreno et al., 2014;

Redhaounia et al., 2015). In the past, South African scientists have attempted to develop warning devices and surface geophysical measurements that could disclose the potential unstable subsurface conditions in time to avoid such rapid and catastrophic events (Brink, 1979; Breytenbach and Bosch, 2011; Kleywegt, 2015). Since modern urban and rural developments are fast encroaching on previously mined areas, adequate use of different geophysical methods to obtain near-subsurface information in these areas is crucial (Figure 4.1)

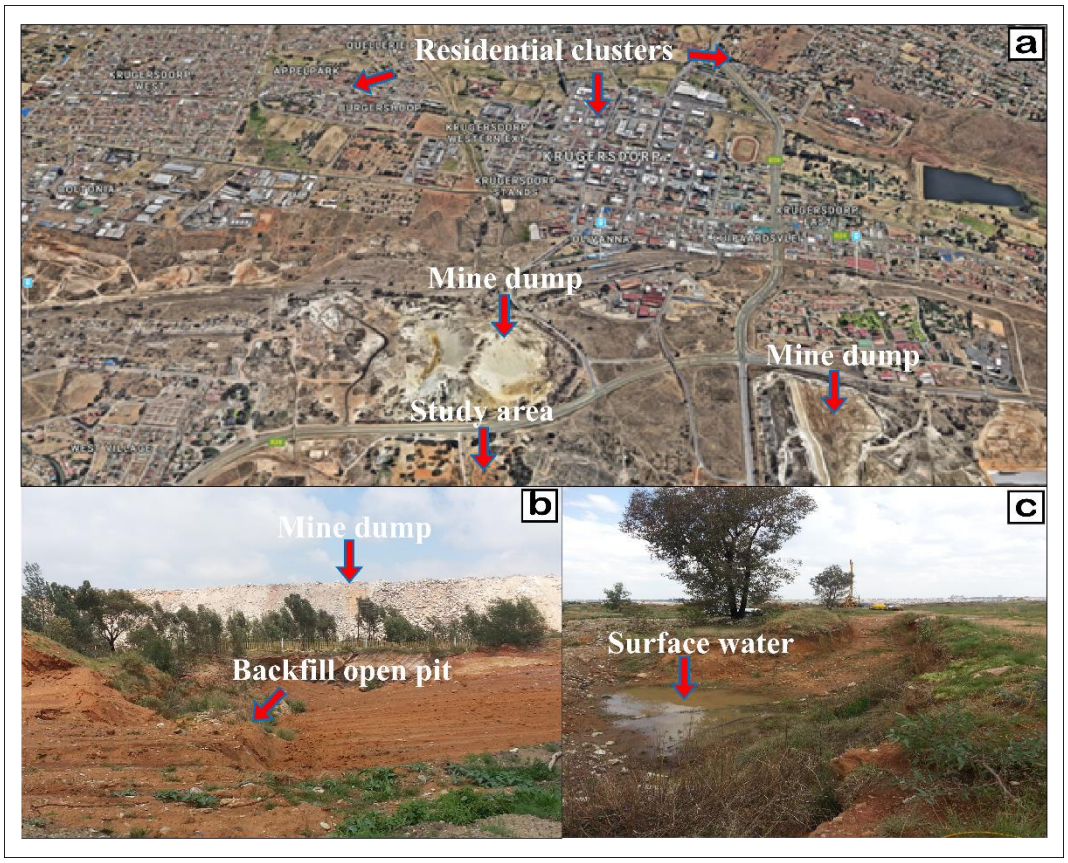


Figure 4.1: (a) Satellite image and photographs showing residential encroachment towards mining area. (b) and (c) show the environmental degradation caused by mining activities in the area.

4.2. Site location and geology and borehole information

The study area is located within the Witwatersrand Basin (WB), which lies near the centre of the Kaapvaal Craton, and has an extent of ~ 350 km NE-SW and 200 km NW-SE (Corner et al., 1990; Armstrong et al., 1991) (Figure 4.2). The WB is

approximately 84,000 km^2 in area and about 7 km deep, and is filled with terrigenous and volcanic sequences (Figure 4.2).

The WB formed over a period of ca. 800 Ma, because of sediment accumulation due to sagging, volcanism and subsequent rifting activities between ca. 3.1 and 2.3 Ga within the Kaapvaal Craton (De Wit et al., 1992; Tinker et al., 2002). The deformation process is said to be associated with the encroachment and eventual collision of Kaapvaal Craton with the Zimbabwe Craton between ca. 2.84 and 2.72 Ga (Zegers et al., 1998; Robb et al., 1991). According to Hayward et al. (2005), heavy minerals such as gold and uranium are effectively concentrated in the coarse gravels of the large fan-delta complexes seen mostly at the apices of the fans. The progressive lithification of these alluvial deposits formed the conglomerate rocks (known as reefs) that bear the gold and uranium mineral deposits. The sources of the gold and uranium mineralization within the basin are still contentious. Drennan et al. (1999) identified metamorphic/hydrothermal fluid systems as a result of the widespread preservation of detrital uraninite and gold remobilization along major fluid conduits in the WB, while Frimmel and Hallbauer (1999) attributed the gold-mobilization fluids in the Witwatersrand reefs to a meteoric source. On the other hand, Kirk et al. (2002) suggested rapid crustal growth during the Kaapvaal Craton formation as an evidence for the significant metal flux from the mantle, which corresponds to the Middle Archaean gold mineralization event. The Witwatersrand Supergroup (WS) is unconformably overlain by the sub-ordinated volcanic and sedimentary deposits of the Ventersdorp (ca. 2.7 Ga), Transvaal (ca. 2.6 Ga) and Karoo (ca. 302 - 180 Ma) Supergroups (De Wit et al., 1992). Underlying the WS is the ca. 3.1 Ga Dominion Group (DG) and greater than 3.1 Ga Archaean granite-greenstone basements. The Au-bearing reefs of the WS (Main, Bird, Kimberley (Figure 4.3), Elsburg, Basal, Carbon Leader, Steyn, Vaal, Leader, B and Composite reefs), Ventersdorp (Ventersdorp Contact Reef (VCR)) and Transvaal Supergroups (the Black Reef Formation (BRF)) have been mined for more than 100 years.

The study area is situated on the Central Rand Group (CRG) rocks known as the upper zone of the WS. It is unconformably underlain by the West Rand Group

(WRG), which is considered as the lower zone of the WS. The thickness of the CRG varies from ca. 2.8 km in the Vredefort area to ca. 1.5 km towards the East Rand area and ca. 650 m in the Evander area (NE Witwatersrand region) (Robb et al., 1991). The CRG predominantly consists of quartzites and conglomerates with minor shales. The group is further subdivided into the Johannesburg and Turffontein subgroups. A larger part of the WB was buried by enormous thickness of the Vredefort impact ejecta, preserving the CRG gold-bearing reefs over an estimated period of 2 Ga (Therriault et al., 1997). The Witwatersrand Supergroup has undergone various stages of metamorphism, structural and thermal deformation. The metamorphism and structural deformation involved progressive loading of the WB by the Ventersdorp and Transvaal sequences under extensional and rifting tectonic environments (De Waal et al., 2006; Gibson and Reimold, 2000). The thermal deformation involves the intrusion of Bushveld Igneous Complex, while Vredefort impact crater caused the exposure of deep-sitting WS to be seen as an outcrop around the vicinity of the survey area (after massive erosion of impact ejecta) and overturned strata around the centre (known as the Vredefort Dome) of the impact (Reimold and Gibson, 1996; Gibson and Reimold, 2001).

The shallow subsurface geology is made of the Johannesburg Subgroup of the Central Rand Group. It is predominantly arenaceous and argillaceous with minor rudaceous material and the lithologies were deposited in a fluvio-deltaic environment (Robb and Meyer, 1995). The payable Au-bearing reefs found in the Lancaster Gold Mine are part of the Kimberley Reef Package (KRP) of the Johannesburg Subgroup (JS) of the CRG. The KRP contains various conglomerate lenses of different economically Au grades that dip approximately 28° to 32° towards the south and strike approximately east-west, seldom extending to more than 60m depth in the area, stacked upon one another with intercalated quartzites and sandstones in between (Figure 4.2 and Figure 4.3). The Boulder Reef of the KRP is the only consistent layer in the area with moderate Au grades (2.34 – 5.08 g/t) but it is not more than 300 mm thick. Approximately 95% of the Boulder Reef has been mined-out and replaced with backfill (packed waste rock, providing roof support for stopes). The KRP is about 40 - 50 m thick in the

area, with occasionally sericitic quartzites occurring below and above the package, underlain by intercalated conglomerate bands (Figure 4.3 and Figure 4.4). The surface geology comprises friable, weathered conglomerates and sandstones/quartzites with minor rudaceous materials and disintegrated boulders. The surface materials are maroon in colour, though sometimes dark brown, with minor black and white matrices.

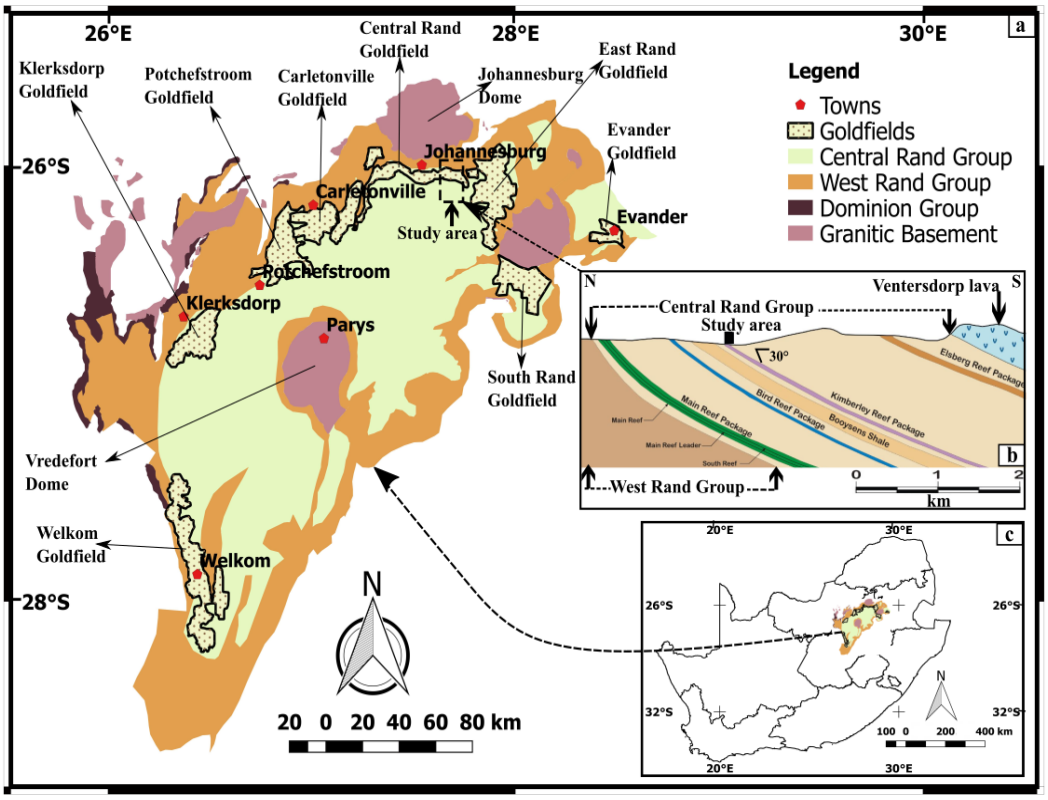


Figure 4.2: (a) Geology of the Witwatersrand Basin indicating the location of the study area. (b) Geological cross-section across the study area indicating the dipping conglomerate reefs of Central Rand Group (c) South Africa map outline showing the position of the Witwatersrand Basin, respectively (modified from Dankert and Hein, 2010).

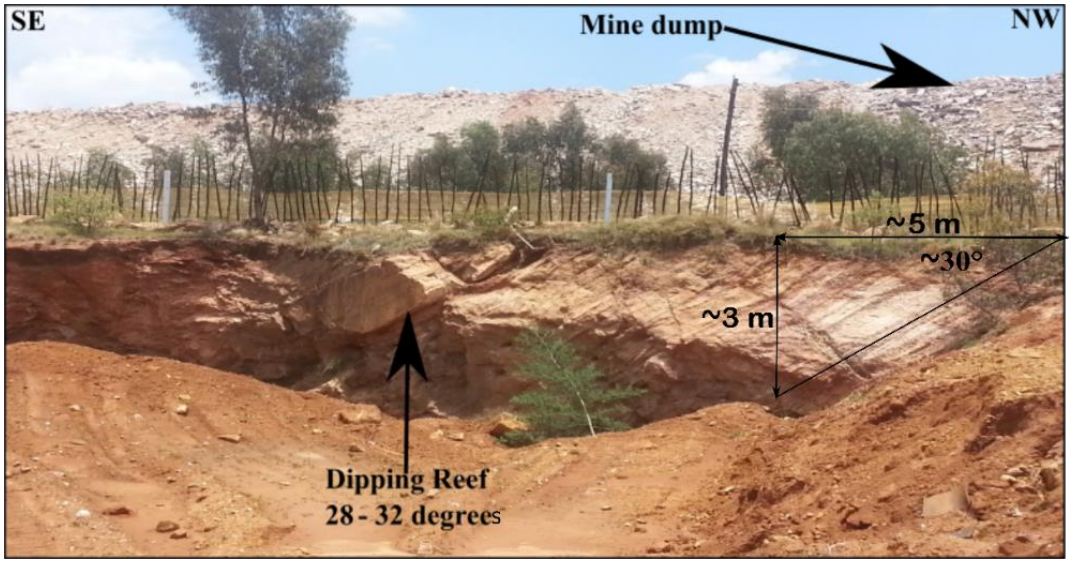


Figure 4.3: Dipping reefs exposed on the sidewall of an open cast pit, waste dump in the background.

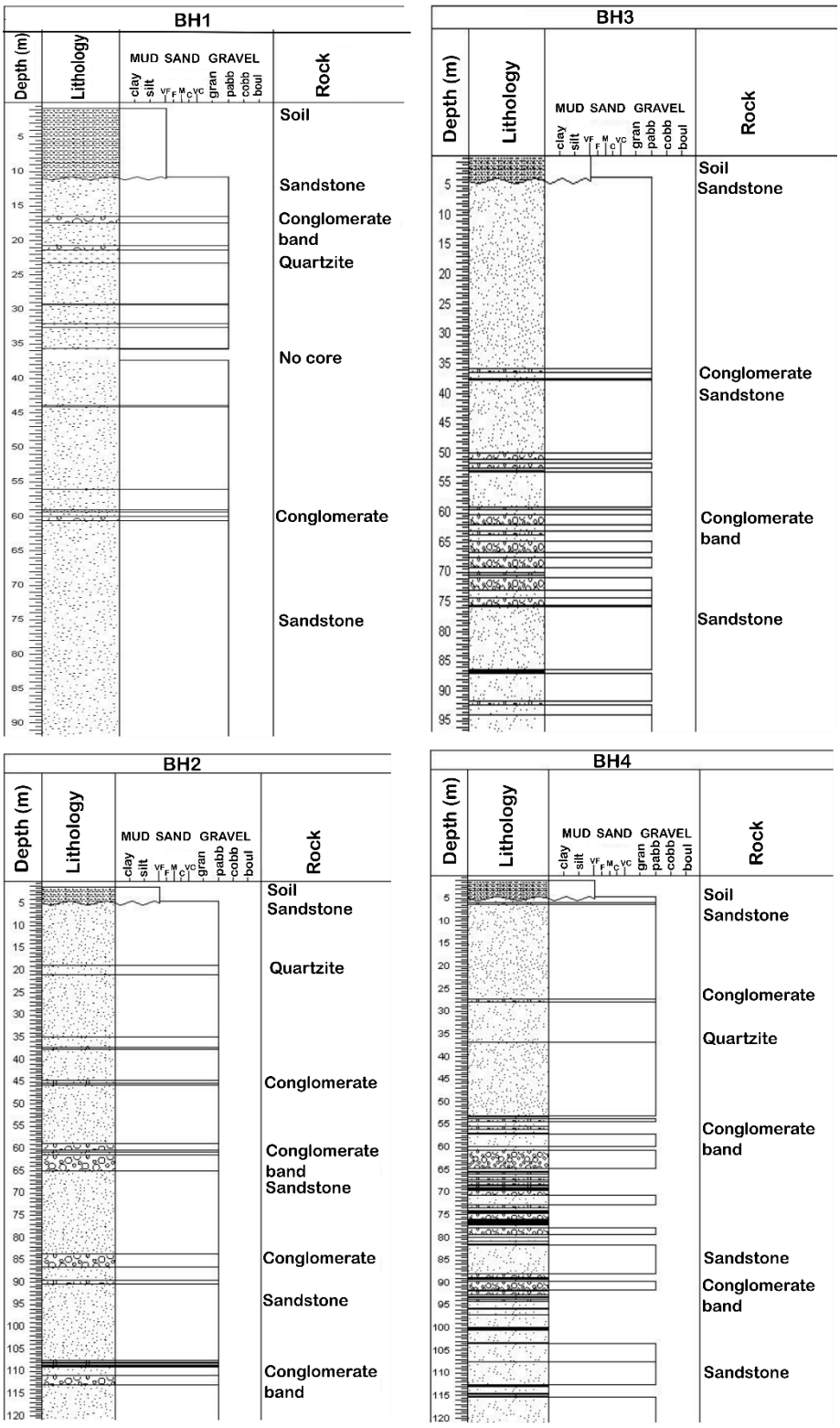


Figure 4.4: The borehole information from the Lancaster Gold Mine used to correlate the lithology of the study area. Borehole locations are shown in Figure 4.7.

4.3. Physical property measurement and synthetic modelling

Table 4.1 lists the laboratory-measured bulk densities and P-wave seismic velocities for the rock samples (each averaged over 10 readings) from two borehole close to line L01. The physical property values were used to construct synthetic seismograms and to constrain the (seismic reflection and refraction) starting model parameters. The synthetic seismogram computation assumed normal incidence waves, convolved with the first derivative of a Gaussian wavelet (minimum phase) with a dominant frequency (F_D) of 100 Hz (Figure 4.5). This analysis reveals that the interface between the weathered and fresh bedrock (reflection coefficient of 0.36 - 0.45) is anticipated to produce a noticeable reflection. The interface between the quarzitic conglomerate band (reef lenses) and underlying sandstone yielded a seismic of about 6% to 13% (0.06 to 0.126). The physical properties of the backfill zone cannot be estimated from the core measurements since the borehole was drilled before the mining took place decades ago. However, it's expected that the velocity values should be close to the velocity of dry or water-saturated sand for the backfill zone and the velocity of air for the open voids (Figure 4.6). It's expected that the voids and backfilled zones may be water-saturated as it rained for several days prior to the data acquisition. Although the physical properties of the intermediate layer cannot be estimated using conventional refraction seismic method as schematically shown in Figure 4.6 (Banerjee and Gupta, 1975; Ivanov et al., 2005 and 2006). The problem of the hidden layer can be solved using integrated geophysical methods such as multichannel analysis of surface wave (MASW), resistivity and reflection seismic methods as adopted in this study (Miller et al., 1991; Steeples et al., 1988 and 1997; Onyebueke et al., 2018).

Table 4.1: Physical property measurement of boreholes 1 and 2. Z is the acoustic impedance, ρ is the density, V_I is the interval velocity and Rc is the reflection coefficient. Abbreviations ws - weathered sandstone, s - sandstone, cl - conglomerate lenses, cb - conglomerate bands, and q – quartzite.

Borehole 1					
Depth (m)	V_I (m/s)	ρ (kg/m^3)	Z = ρV (kg/m^{2}s x 10^6)	Rc	Rock type
12	1650	2500	4.125		ws
17	3400	2600	8.840	0.364	s/cl
20	3750	2700	1.0125	0.068	s
24	4200	2800	1.1760	0.075	q/cl
29	3700	2700	9.990	-0.081	s
38	4450	2600	1.1570	0.073	s/cl
44	4600	2800	1.2880	0.054	s
45	5000	2600	1.3000	0.005	s/cl
55	5300	2800	1.4840	0.067	s/cb
59	5400	2700	1.4580	-0.01	s
61	5500	2700	1.4850	0.01	s/cb
95	5700	2800	1.5960	0.036	s
Borehole 2					
Depth (m)	V_I (m/s)	ρ (kg/m^3)	Z = ρV (kg/m^{2}s x 10^6)	Rc	Rock type
10	1400	2500	3.500		ws
20	3500	2700	9.450	0.450	s/cl
26	4000	2800	1.1200	0.085	q/s
35	3700	2700	9.990	-0.057	s
38	4400	2600	1.1440	0.068	cl
44	4200	2800	1.1760	0.014	s
45	4500	2600	1.1700	-0.003	cl
60	5200	2900	1.5080	0.126	s/cb
83	5400	2800	1.5120	0.001	s
85	5500	2900	1.5950	0.027	s/cb

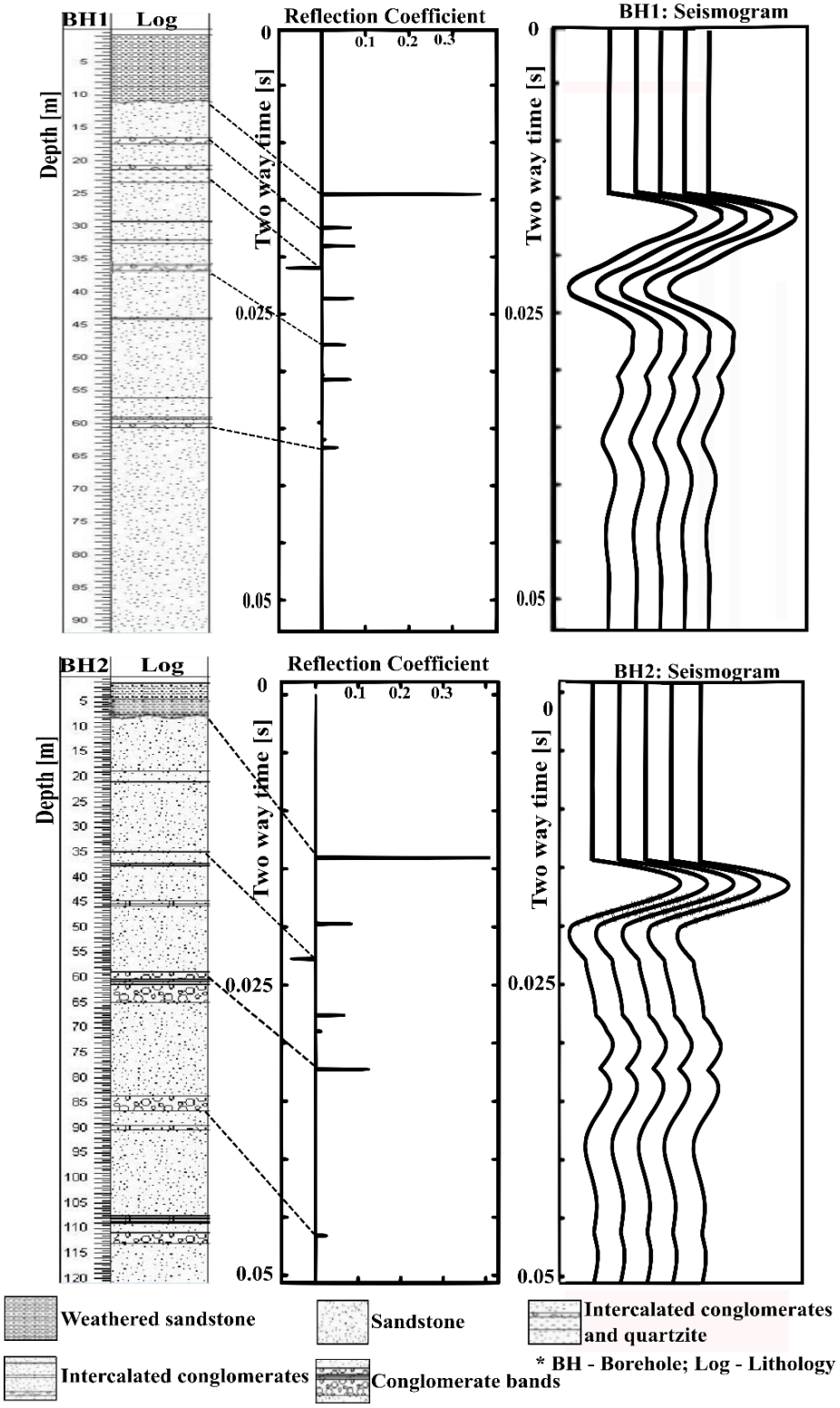


Figure 4.5: Borehole logs with the respective reflection coefficient and synthetic seismogram. Note that the multiple traces are repetitions of the zero-offset trace at the borehole position.

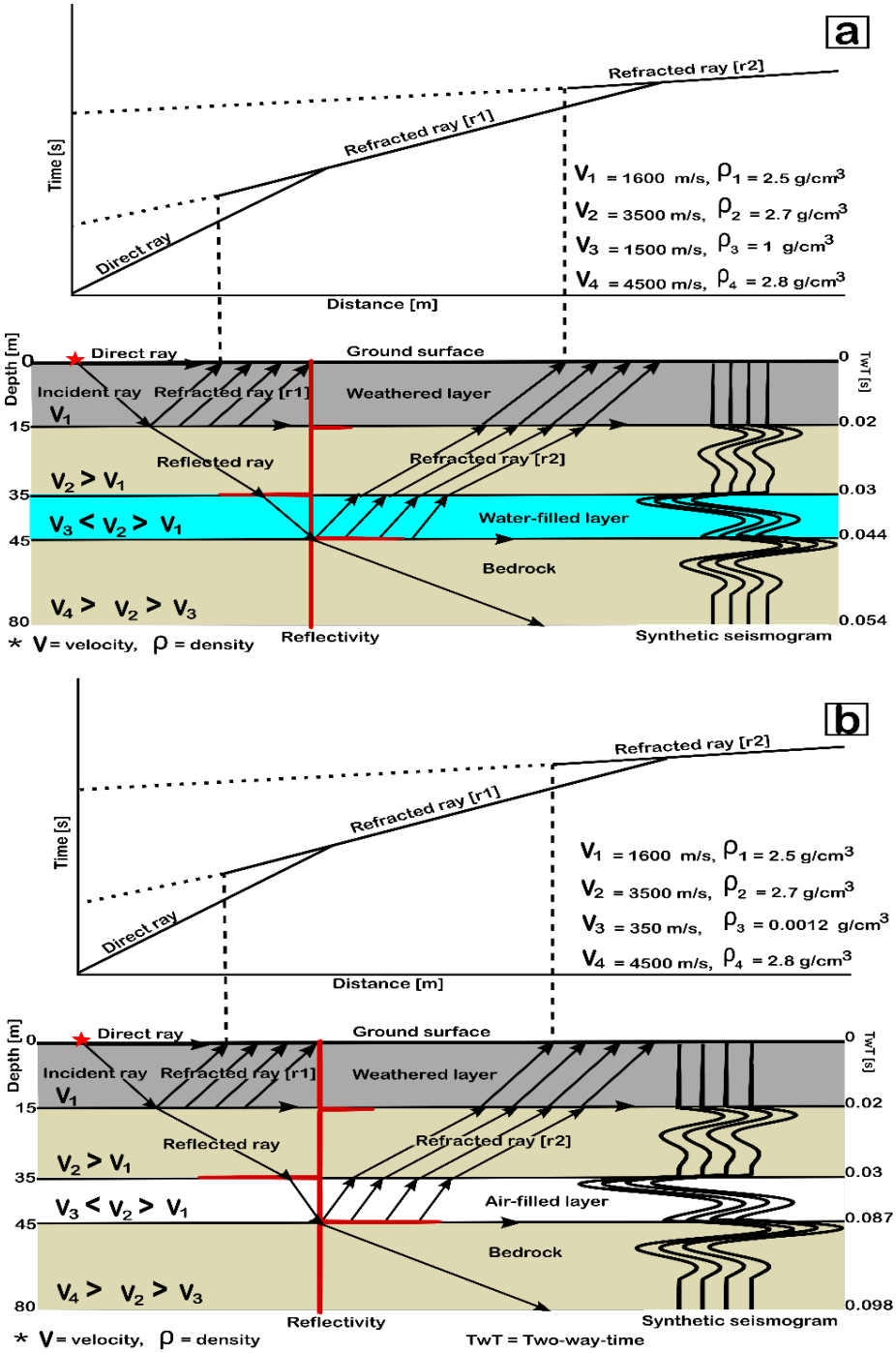


Figure 4.6: A schematic diagram illustrating the low-velocity or hidden layer problem in the conventional seismic refraction method. (a) Showing water-filled layer; (b) Showing air-filled cavity/tunnel. The respective velocity and density values on the top of the respective models were used to calculate and construct the reflectivity and synthetic seismogram superimposed on the model. Note: the diagram was not drawn to match scale and the thickness of the hidden layer does not reflect the actual thickness of the mine stopes which is about 5 m.

4.4. Geophysical methods

4.4.1. Seismic methods

4.4.1.1. Survey design and acquisition

The seismic survey included three P-wave seismic profiles (L01, L02, and L03) acquired using the asymmetric split-spread geometry at a fixed geophone position (Figure 4.7). A series of trial acquisition tests were conducted using different source and receiver offsets prior to the actual survey to fine-tune the acquisition parameters and evaluate the attenuation response of the ground. Line L01 was shot in the east-west direction parallel to the strike direction of the dipping conglomerate reefs and perpendicular to the mine-access tunnels, while L02 and L03 were shot approximately in a north-south direction parallel to the dip direction of the conglomerate reefs. Because the study area is in the mining environment, the locations of the lines were restricted along the road ways of the mine (L01 and L03) and on the covered open cast pit (L02) (Figure 4.7 and Figure 4.8). Moreover, the area has significant topographical features; the elevation along line L01 is quite flat, while the elevation along L02 and L03 varies with a highest topographic difference of about 6 m.

The equipment and parameters used in the seismic data acquisition are listed in Table 4.2. Four Geometric Geode Seismographs were connected, each having 24 14 Hz vertical component geophones. The recording of the seismic data was carefully controlled to avoid cultural noise. However, The S/N was improved by stacking five vertical shots of 9 kg sledgehammer on an aluminium plate at every shot station (Figure 4.8). The sampling interval and recording length were 0.25 ms and 250 ms, respectively. To avoid spatial aliasing and to obtain a high-resolution subsurface image, dense receiver spacing's of 1.5 – 2 m and a shot spacing of 2 m was employed, which yield a common mid-point (CMP) subsurface spacing of 0.75 – 1.0 m and nominal fold of 76 - 96. The recording of environmental noise (borehole drilling) during data acquisition was reduced by applying a low-cut and high-cut filter of 50 Hz and 800 Hz, respectively. The geophones and the energy source were firmly coupled to the ground (Figure 4.8).

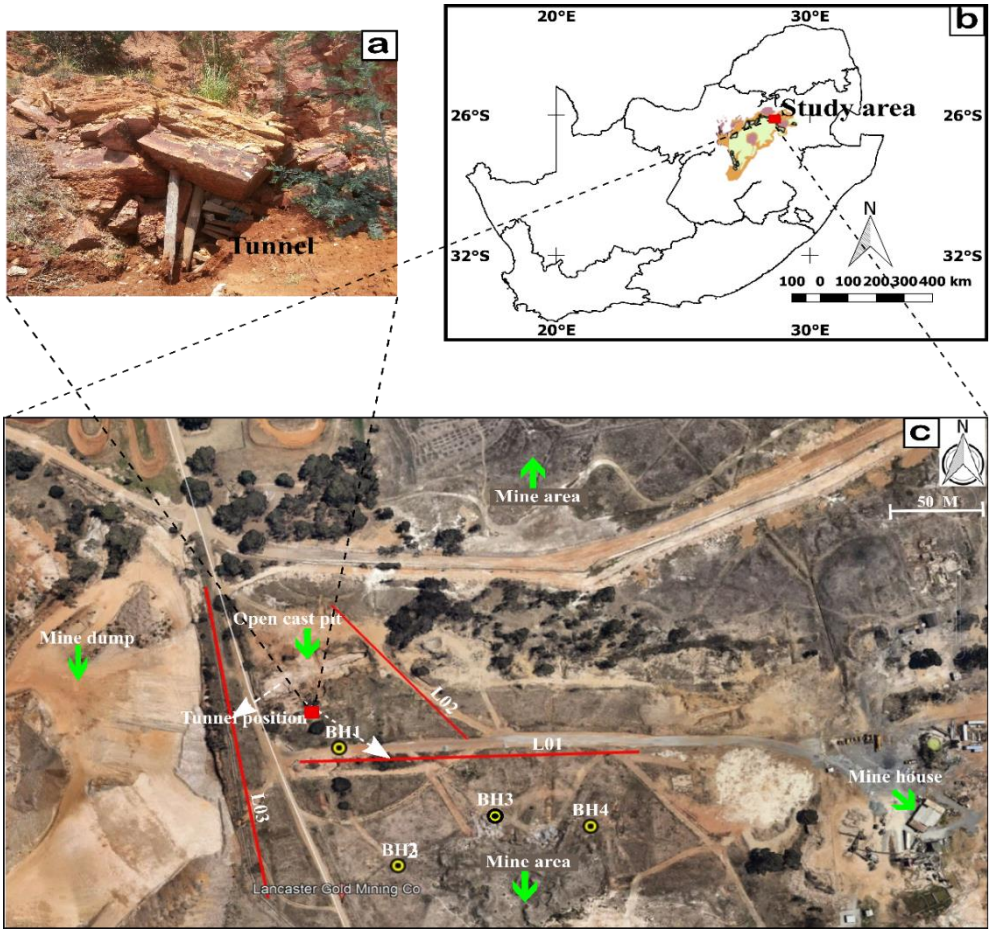


Figure 4.7: (a) Photograph showing a collapsed mine entrance. (b) South Africa map outline showing the location of the survey area and (c) Google Earth map indicating the survey profiles, borehole locations and possible tunnel positions in the research site.

Table 4.2: Seismic acquisition parameters for line 1, 2 and 3.

Item	Parameters		
Lines	L01 (E – W)	L02 (NW – SE)	L03 (NW – SE)
Profile length (m)	190	142.5	190
Geophone	14 Hz vertical		
Seismograph	Geometric Geode (32 bit)		
Source	9 kg sledgehammer		
Receiver number	96		
Receiver spacing (m)	2	1.5	2
Shot spacing (m)	2	2	2
Record length (ms)	250		
Sampling interval (ms)	0.25		
Vertical stacks	5		
Min/Max offset (m)	1/194	0.75/146.5	1/194
Max CMP fold	96	76	96



Figure 4.8: Data acquisition setup showing some mine trenches alone the profiles. (a) and (b) are along L01, (c) and (d) are along L02 while (e) and (d) are along L03.

4.4.1.2. Raw data analysis

The raw shot gathers are characterized by different seismic events: the direct (D), surface (S), refracted (r1 and r2) waves and reflected waves (R1 and R2) (Figure

4.9). Traces were normalized with respect to the maximum amplitude of the entire shot gather. The data analysis shows that the near-source traces were dominated by high amplitude surface waves, while environmental noise dominated the far-offset traces due to rapid attenuation of the source signal. Although a 50 Hz low-cut filter was applied during acquisition to suppress ground roll and other low-frequency cultural noise sources. However, a portion of the ground roll is still visible in the data dominantly within the bandwidth 45 - 55 Hz. The linear moveout velocity of the direct wave varies approximately from 300 to 550 m/s. The sudden change observed between distances 10 – 25 m in the gradient of the first arrival travel-time curve is qualitatively interpreted as a velocity variation within the weathered and low-velocity layer, while the gradual change at 30 – 50 m is interpreted to be the contrast between the weathered layer and high velocity bedrock. The velocities of r1 and r2 are about 900 – 2000 m/s and 1400 – 3000 m/s, respectively. Moreover, the coherent events at 20 - 25 ms (R1) and 35 – 50 ms (R2) on the shot gathers (Figure 4.9a, b and c)) are suspected to be reflected energy from bedrock-overburden contact and wide-angle reflections emanating from the mined-out zones. The F_D of the shot gathers varies between 60 and 140 Hz (Figure 4.9d, e and f) while the normal moveout velocity of the reflected energy varies between 800 - 1000 m/s (R1) and 1200 -1800 m/s (R2) (Figure 4.9).

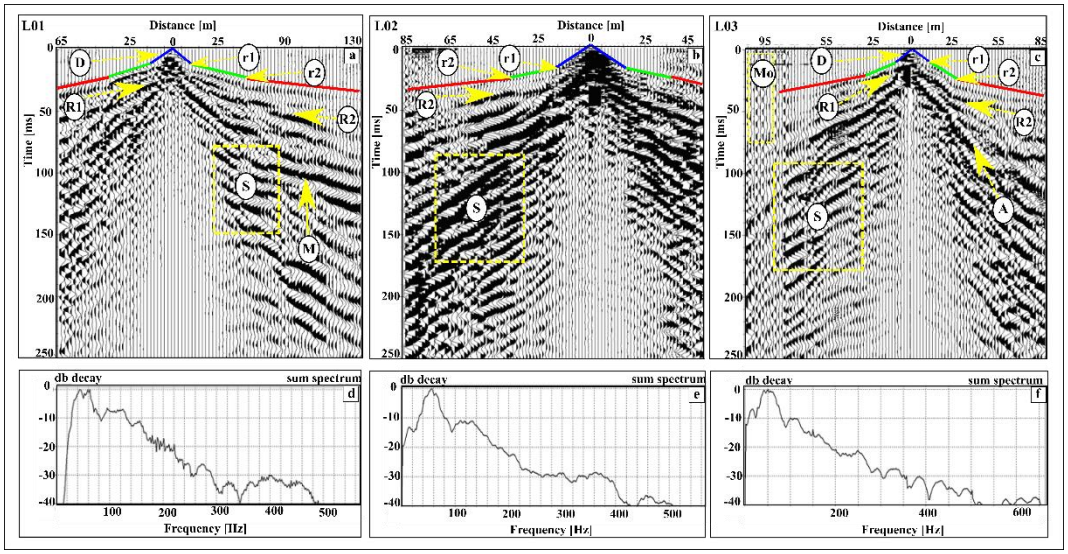


Figure 4.9: Seismic raw data indicating different seismic events. (a), (b) and (c) represent a single shot gather along L01, L02 and L03, respectively. (d), (e) and (f) shows the amplitude versus frequency spectra of the respective shot gathers.

Here, D – direct wave, r1 – first refracted wave, r2 – second refracted wave, R1 – probably the first reflected wave, R2 – probably the second reflected wave, A – air wave, S – surface wave, M – multiple reflection arrival of R2 and Mo – probably a monochromatic noise.

The seismic reflection method is governed by the Zoeppritz equation and acoustic impedance (the product of density and velocity, ρ and V, respectively) contrast that exist between two different geological boundaries $[(\rho_2V_2 - \rho_1V_1)/ [(\rho_2V_2 + \rho_1V_1)]$ (Sheriff and Geldart 1995; Yilmaz 2001). The Zoeppritz equation describes the partition of seismic wave energy at an interface of two lithological units and relates the amplitude of an incident P-wave to the reflected and refracted P- and S-wave at a given plane boundary of an incident angle (Sheriff, and Geldart 1995). The ability of a lithological boundary to produce significant reflection event depends entirely on the reflection coefficient (Rc) between two geological units, which is governed by the acoustic impedance contrast between these units. A geological interface can only generate a reflection event if the reflection coefficient at the boundary is at least 6% (0.06) (Sheriff and Geldart 1995; Yilmaz 2001; Narayan 2012).

Based on an approximated average velocity (V_a) of about 900 m/s (for R1) and 1400 m/s (for R2) with average F_D of 100 Hz, the average horizontal resolution (the radius of the Fresnel zone (Fz) = 0.5 x V_a x $(T_o/F_D)^{1/2}$) for the P-wave reflectors at 20 ms and 40 ms T_o are estimated to be 6 m and 14 m, respectively. Since the CMP sampling was 0.75 - 1 m, based on the deployed acquisition parameter (shot and receiver spacing, see Table 4.2), the horizontal sampling will be about 8 - 14 points per Fresnel zone above 40 ms two-way time. The vertical resolution of the data can be estimated using 1/4 wavelength criterion (Widess, 1973). Taking the average P-wave velocity of R1 and R2, the approximated dominant wavelength ($\lambda_D = V_a/ F_D$) of 9 m and 14 m, respectively, which indicates that the best possible vertical resolution is about 2 - 4 m. However, thinner features can still be detected in the seismic section provided there is a high enough acoustic impedance contrast (Manzi et al., 2014; Narayan, 2012).

4.4.1.3. Data processing and results

4.4.1.3.1. Refraction seismic

The basic principle in the refraction seismic method depends on the analysis of the first-arrival compressional head wave in the seismic shot gathers. In this study, I use an advanced seismic refraction analysis technique in ReflexW software (Sandmeier 2018) to analyse and generate the refraction tomogram (RT). The technique incorporates the Simultaneous Iterative Reconstruction Technique (SIRT) algorithm. The SIRT algorithm automatically adapts synthetic travel time data (the calculated travel time) to the observed data sets (the picked travel time). However, the information obtained from the acquisition geometry, the calculated apparent velocity from the raw data and physical property lab measurement of borehole core provided the initial input model for the final tomographic inversion.

The spatial limit of the starting model is 0 - 50 m for the vertical extent with a 0.5 m bin size. The minimum and maximum velocity values are set at 400 and 6500 m/s, respectively. The inversion was based on an iteration model (obtained after 50 iterations) with a defined data variance of 0.01 (misfit), permissible threshold of 0.001 and 50 % maximum defined change of the input model. Variations in shallow subsurface along all three survey lines can be seen in the tomographic results (Figure 4.10a, b and c). From the tomograms, we qualitatively observe that the velocity of the top layer (blue) is about 400-800 m/s at 0 - 10 m depth. The velocity of the second layer (green, the transition zone) is about 1200 - 2500 m/s at about 8 – 20 m depth, while the velocity of the Archaean sandstone bedrock typically varies from 3500 - 5500 m/s and can reach up to 6500 m/s (red to magenta).

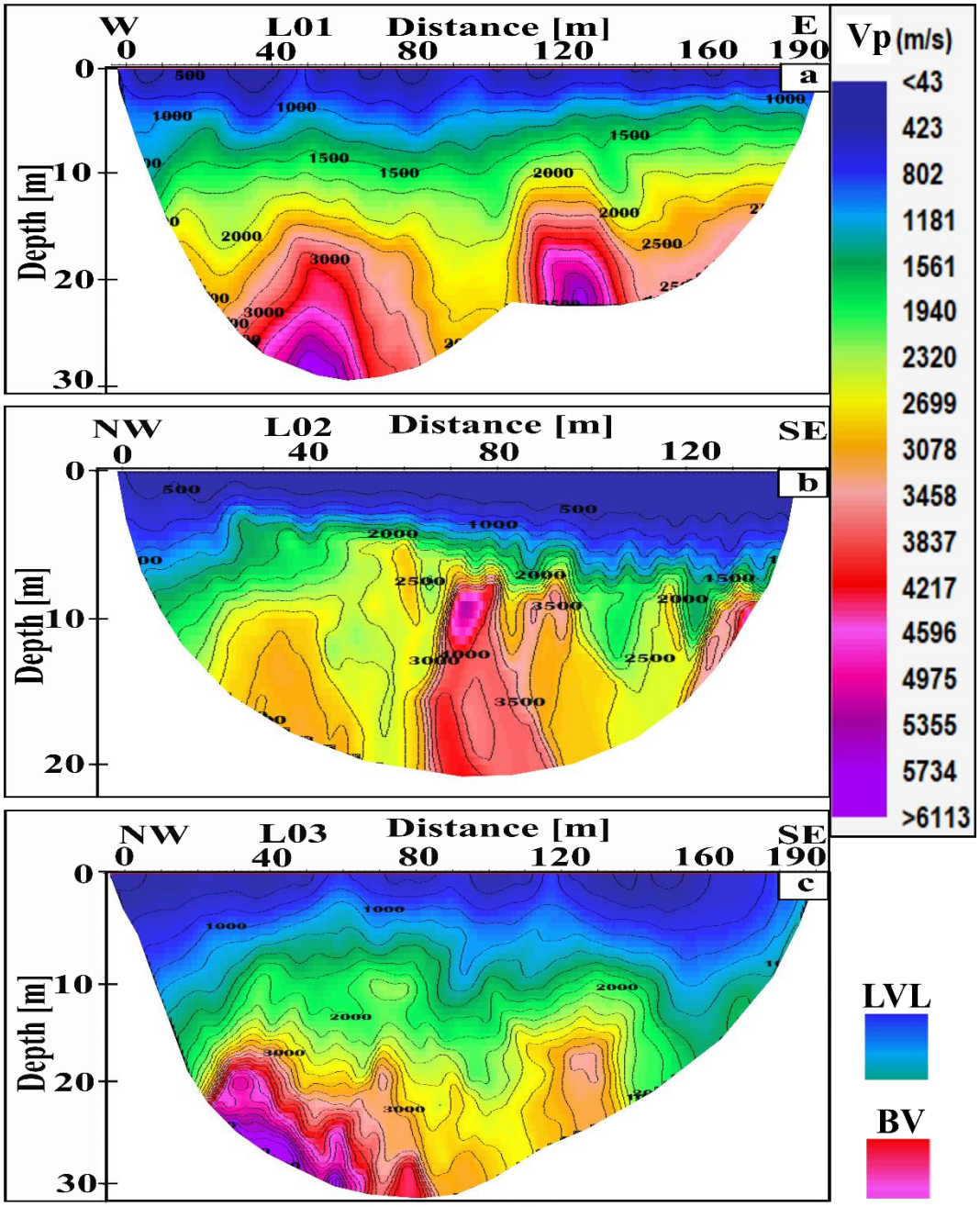


Figure 4.10: Refraction tomography results. (a), (b) and (c) represent velocity model along L01, L02 and L03, respectively. Note, the contour lines represent velocity isoline of different velocity values shown in different colour band, and LVL is low velocity layer, while BV is bedrock velocity.

4.4.1.3.2. Reflection seismic

The processing workflow (using ReflexW software package) is listed in Table 4.3. These include: geometry setup; trace edits and normalizations; frequency and velocity bandpass filtering; deconvolutions before stacking; elevation, weathering

and automatic residual statics; standard CMP analyses; careful refraction muting; stacking; migration; time-to-depth conversion and deconvolutions and time-varying bandpass filter after migration.

During geometry setup, all traces and shots were placed in their correct positions. Traces were normalized with respect to the maximum amplitude of the entire shot gather. High-amplitude noise and dead traces were removed. Traces were normalized to correct for spherical divergence effects. However, near-surface source-generated noise still affected the shot gathers. Therefore, we carefully separated direct and refracted P-waves, and surface waves from shallow reflections. Such phase recognition and separation are a difficult task in shallow 2D seismic surveys (Steeples et al. 1997; Spitzer et al. 2003). Spiking-deconvolution of 40 ms filter length with 5 % white noise provided the best results in improving the vertical resolution and compressing the signal wavelet of the seismic data; it also enhanced the frequency bandwidth (Figure 4.11) (Cary, 2006). The data were subjected to 3rd order Butterworth (95 – 250 Hz) bandpass frequency filter to eliminate the dominant surface wave (ground roll) (Figure 4.11d, e and f). The remaining steeply dipping events (such as the airwave) were further attenuated by applying 450 m/s low cut velocity filter (FK filter). Careful top muting was applied to remove direct and refracted arrivals before sorting the filtered data into CMP gathers for velocity analysis. Automatic gain control (AGC, 50 ms window length) was applied to correct for energy loss at depth with a subsequent 100 ms time cut (Figure 4.11g, h and i).

Velocity analysis was carried out on CMP gathers using interactive semblance and constant velocity stack analysis (Yilmaz 1987 and 2001). The optimal final velocity was based on the best alignment of normal-moveout (NMO) corrected velocity and quality of the stacked section with 45% automatic stretch mute. The final stacking velocity was used for NMO correction and these gathers were stacked together at the zero-offset to generate the final stacked seismic section after an automatic residual static correction (Figure 4.12a, c, and e). The random noise was suppressed with a time-varying bandpass filter (90 – 250 Hz) before and after migration.

Elevation and weathering statics were carefully applied to correct for the effect of topographic variations and near-surface velocity heterogeneity. Static correction proved to be important due to variable overburden thickness and high-velocity contrast at the base of the weathered layer with bedrock P-wave velocity reaching up to 3500-5500 m/s. Post-stack Kirchhoff time migration was applied to collapse the diffracted energy and correctly position the dipping events (Gray et al., 2001). The stacked time-migrated seismic sections shown in Figure 4.12b, d, and f were converted into depth sections using the stacking velocities, which were guided by the borehole constraints and laboratory physical property measurements.

Table 4.3: Reflection seismic data processing sequence and parameters.

Sequence	Parameter
Trace Edit	Removing dead traces
Amplitude scaling	0 - 250 ms
Spiking deconvolution	250 ms autocorrelation length, 60 ms filter length and 10% white noise
Bandpass frequency filter	95 - 250 Hz, 3rd order Butterworth
Trace normalization	with respect to the maximum amplitude of the entire shot gather
F-k filter	Bandpass 450 - 100000 m/s velocity range, with 5 m/s taper width.
Time cut	100 ms
Top mute	Removing the direct and refraction arrivals
CMP sorting/Velocity analysis	Interactive velocity analysis (semblance and constant velocity stack)
NMO correction/Stacking	Velocity ranges from 800 - 3500 m/s
Static/elevation correction	Surface-consistent statics
Bandpass frequency filtering	100 - 250 Hz, 3rd order Butterworth
Kirchoff-Migration/Time-depth conversion	Using stacking velocity
Bandpass-frequency filter/Deconvolution	90 - 250 Hz, 3rd order Butterworth
Automatic Gain Control (AGC)	100 ms (40 ms window length)

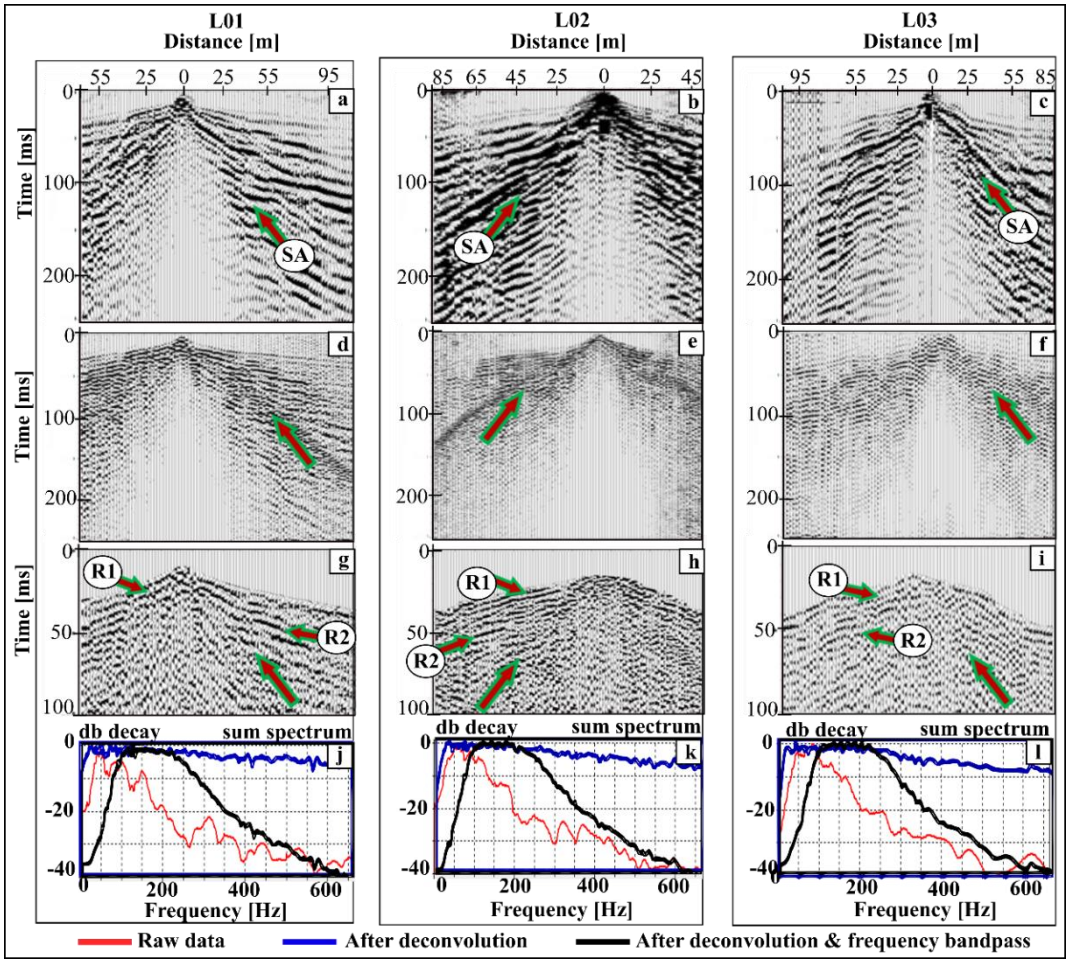


Figure 4.11: Reflection processing steps along L01, L02 and L03. (a), (b) and (c) illustrate after trace editing and amplitude scale. (d), (e), and (f) illustrate after deconvolution and bandpass frequency filtering. (g), (h) and (i) illustrate after velocity bandpass filtering, top muting and time cut. (j), (k) and (l) represent the frequency spectrum obtained after subsequent filtering along the respective lines. Note, the arrow SA indicates the surface wave moveout, R1 – probable first reflector and R2 – probable second reflector.

The processed seismic sections are shown in Figure 4.12a, c and e. The horizontal axis on the sections shows distance along the surface and the vertical axis is the two-way travel-time. The datum level for the seismic section along lines L02 and L03 varies between 1725 - 1730 m above the sea level. However, the surface topography varies with a maximum range of 4 – 5 m. The topography along line L01 was approximately flat with less than 1 m variation in elevation and the datum level was 1730 m above the sea level. The measured P-wave velocity of the

weathered layer and upper Archaean sandstone bedrock correlated with our CMP velocity analysis. These velocities range from 800-1200 m/s within the weathered layer to 1400-3000 m/s beneath the bedrock-overburden contact. The seismic sections show several reflections. A strong reflection is observed at the two-way time of about 15 – 20 ms between depth ranges of 14 –25 m (Figure 4.12a and b). A gently dipping coherent reflection was also observed between 20 – 60 ms two-way time along line L02 and L03 with intermittent reflections between 50 – 100 ms two-way time (Figure 4.12c and e). In line L01, a semi-continuous coherent reflection was observed at 40 – 50 ms two-way time at depth of 50 – 65 m. Intermittent strong reflections were also noted at depths of 75, 100 and 130 m along line L01.

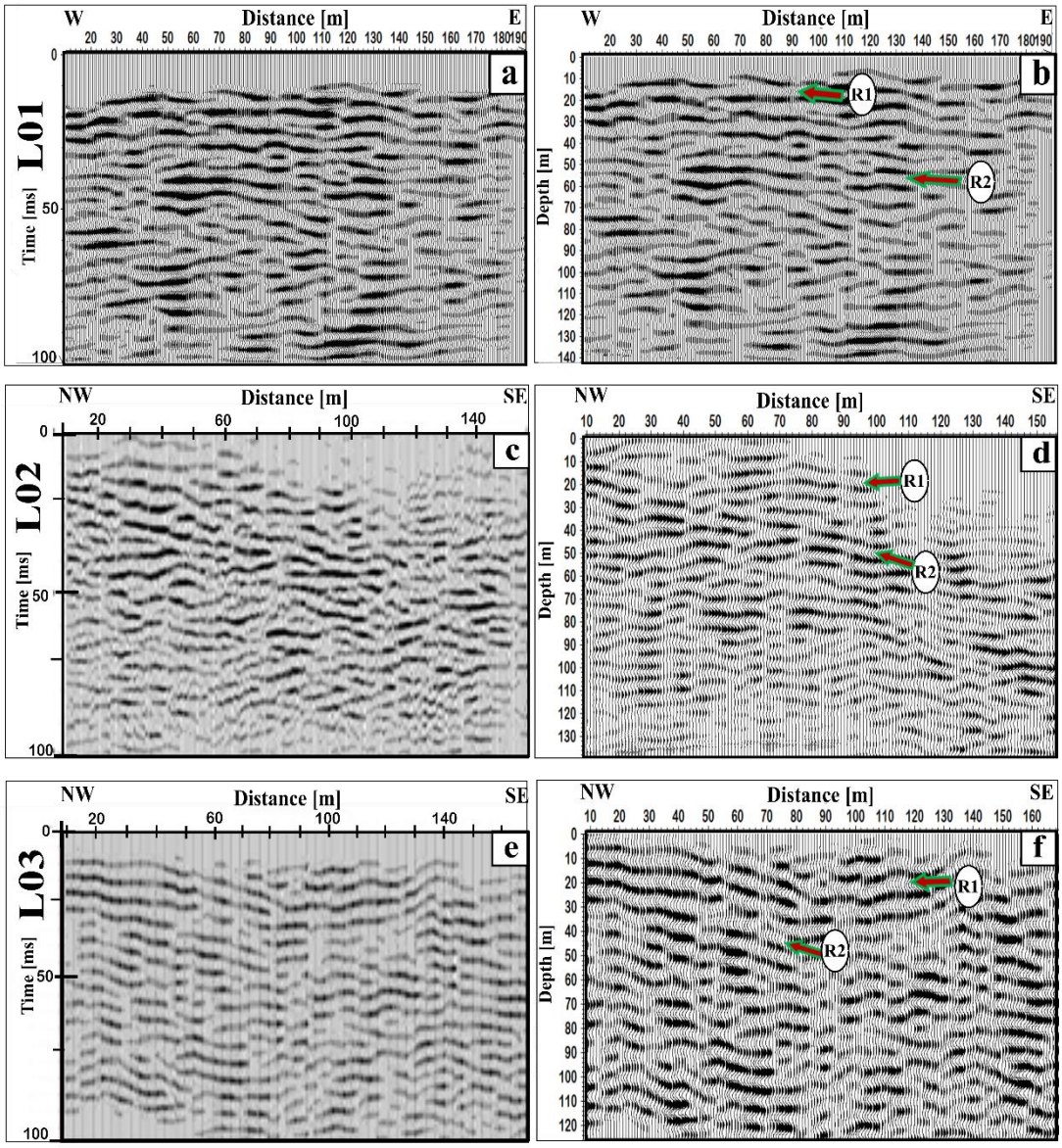


Figure 4.12: Stacked reflection seismic along L01, L02 and L03. (a), (c) and (e) represent the final stacked time sections. (b), (d), and (f) represent time-depth migrated sections after post-stack processing and static correction. R1 and R2 are the first and second reflectors, respectively.

4.4.2. Electrical resistivity method

4.4.2.1.Data acquisition

Resistivity data were acquired using the ARES Resistivity meter instrument with 48 planted steel electrodes connected to coaxial electrical cable (Figure 4.8). Three electrical resistivity profiles were collected along the seismic profiles (Figure 4.8). The electrical resistivity method measures the apparent resistivity of the subsurface by injecting a direct electrical current into the ground using two electrodes and measures the potential difference using another two electrodes at various chosen spacing and distances from the current source (Keller and Frischknecht, 1996). For optimum horizontal and vertical resolutions, Schlumberger and dipole-dipole arrays were chosen with electrode spacing of 5 m (line L01 and L03) and 3 m (line L02) L02 (Dahlin and Zhou, 2004). As a rule of thumb, the maximum depth of penetration is about the total spread-length divided by three-five depending on the ground conductivity (Keller and Frischknecht, 1996; Loke and Barker, 1996; Loke et al., 2013).

4.4.2.2. Data processing and results

The measured apparent resistivity data were pre-processed to remove outliers before running inversions. Data were inverted by means of 2D inverse modelling software (RES2DIV) that uses the Loke and Barker inversion method. The software applies a quasi-Newton technique to reduce the numerical calculations (Loke and Barker 1996) and ultimately produces a 2D resistivity model that satisfies the measured data in the form of a pseudo-section. This method is highly suitable where both strong lateral resistivity and depth variations occur, such as in karstic and mine areas (Leucci 2004; Dahlin and Zhou 2004; Martinez-Moreno et al. 2014; Festa et al. 2016) (Figure 4.13). Moderate horizontal and minimum vertical flatness inversion procedure was chosen since the inversion procedure is smoothness-restricted (Loke and Barker, 1996; Loke et al., 2013). The goodness of the fit is expressed in terms of the relative root mean square (RMS) error. The resistivity tomography models were produced after 10 iterations with an RMS error of 2.3, 1.9 and 2.9 in lines L01, L02 and L03, respectively. A maximum

investigation depth of about 49, 24 and 52 m were achieved with maximum offset distance of 235 m at 5 m electrode spacing for lines L01 and L03, and 141 m at 3 m electrode spacing along line L02.

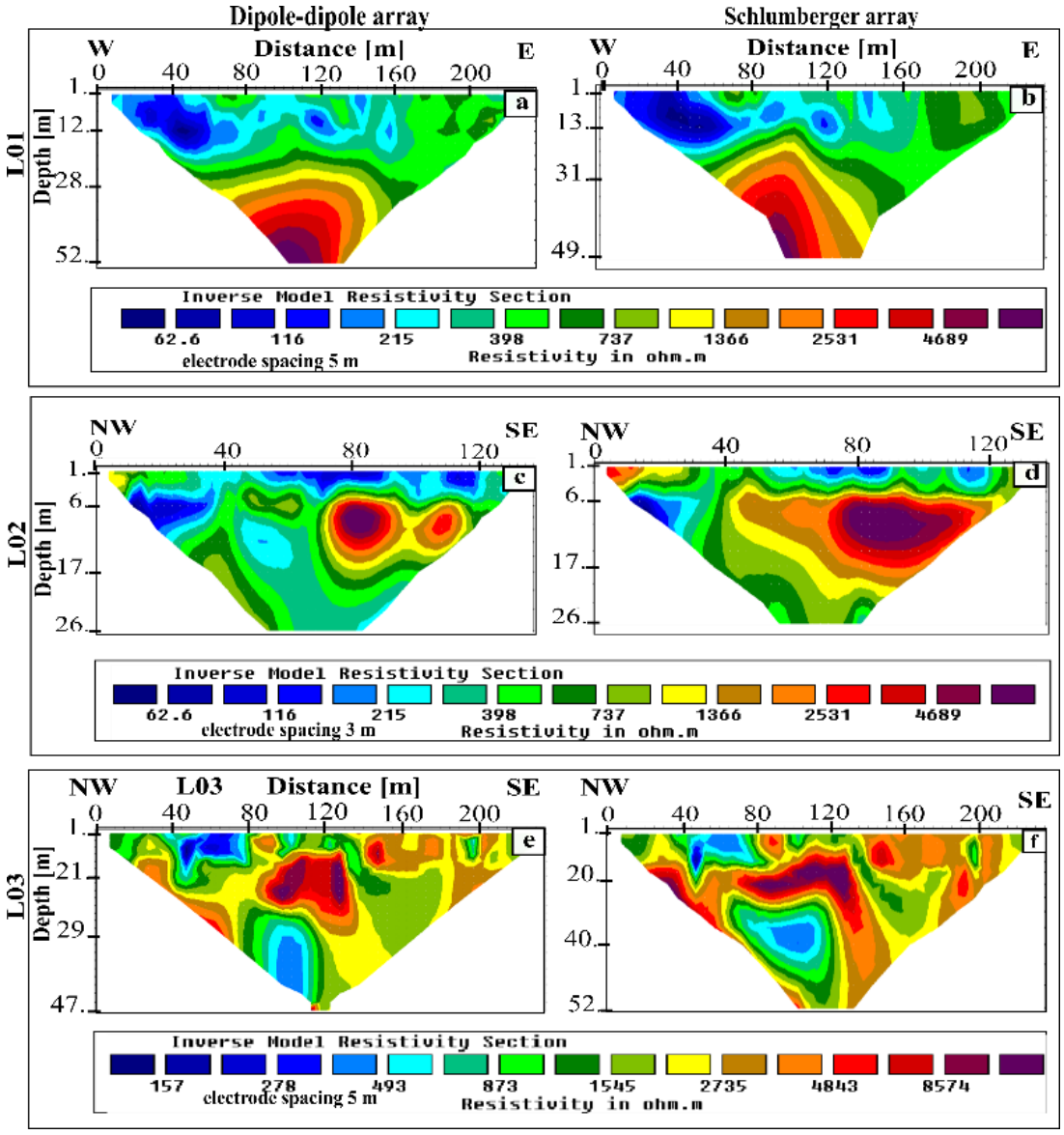


Figure 4.13: Colour-coded electrical resistivity tomography results along L01, L02 and L03. (a), (c) and (e) are the Dipole-dipole array measurement in each respective line. Subfigures (b), (d) and (f) are the Schlumberger array measurement along each respective line.

4.5. Interpretation

The interpreted reflection seismic section, refraction tomogram (RT) and electrical resistivity tomogram (ERT) are shown in Figure 4.14-16a, b and c, respectively. L02 and L03, which trend NW – SE in the investigated area, are approximately parallel to each other and perpendicular to the line L01 (trending E – W). The aim was to obtain the subsurface image of the mined area along the survey profiles. The geophysical datasets were constrained with borehole logs and experimentally-determined physical properties of borehole cores. The seismic sections were characterised by significant reflection events across the survey profiles due to the acoustic impedance contrasts at the lithological interfaces. Geological structures such as faults, joint and fractures were observed on the seismic sections (Figure 4.14-16 a) and correlated with the refraction and resistivity tomograms (Figure 4.14-16 b and c). The refraction and resistivity tomograms exhibit different colour bands which were carefully constrained and interpreted as different material responses. The dipole-dipole array of the resistivity tomogram was preferably used to compare with the refraction tomogram and reflection seismic section, as it is capable to better resolves lateral contrasts and isolated bodies (cavities and tunnels) as show in Figure 4.14-16 (Dahlin and Zhou, 2004).

4.5.1. 2D reflection seismic

Based on borehole data (BH1, BH2, BH3 and BH4 (Figure 4.4)) and synthetic seismograms (Figure 4.17), the strong reflection (R1) observed at 8 – 20 m depth was interpreted as the boundary between the weathered layer and the bedrock, which responds distinctively to different degrees of weathering and erosion. The reflection (R2), which dips at 26^{o} – 30^{o} on L02 and L03 (Figure 4.15a - Figure 4.16 a) and strikes horizontally on profile L01 (Figure 4.14a) is considered to emanates from the interface between the stope and the host Archaean sandstone. The intermittent and diffuse reflections (CB), about 40m depth most likely originate from the intercalated conglomerate bands.

The discontinuity in the amplitude of the reflection (R2) is ascribed to voids or the presence of mine pillars, or as a result of velocity artefacts due to large velocity changes in the near-subsurface. Reflection truncations were observed between distances 35 – 140 m along L03 and slump structure (SS) at distance 50 – 145 m (Figure 4.16a). This chaotic reflection exhibits a discontinuous amplitude reflection character, which could also be due to the presence of pillars and tunnels cutting across the profile. The old mine maps indicate a tunnel between distances 70 – 140 m.

4.5.2. Refraction and resistivity tomography

A low velocity (400 – 1900 m/s) and low resistivity region (150 – 800 Ωm) between distances 50 – 110 m at 12 – 30 m depth are observed along L01 (Figure 4.14b and c). Since this region is low in both resistivity and velocity, it is likely water-saturated. Hence, we interpret this region to be a backfilled and water-saturated region and a potential zone for subsurface erosion during water table fluctuation. The low resistivity values (200 – 1500 Ωm) towards the west between distances 115 – 130 m at 13 – 18 m depths along profile L01 are likely water ingress pathways from the pit and trenches seen on the surface, which is a favourable location for subsurface erosion. The high resistivity (1500 – 8000 Ωm) material at depth of about 28 m below is comparable with the strong reflection (R2) at approximately 30 – 32 m depth and unresolved depth in refraction tomography (RT) (due to poor vertical penetration and resolution).

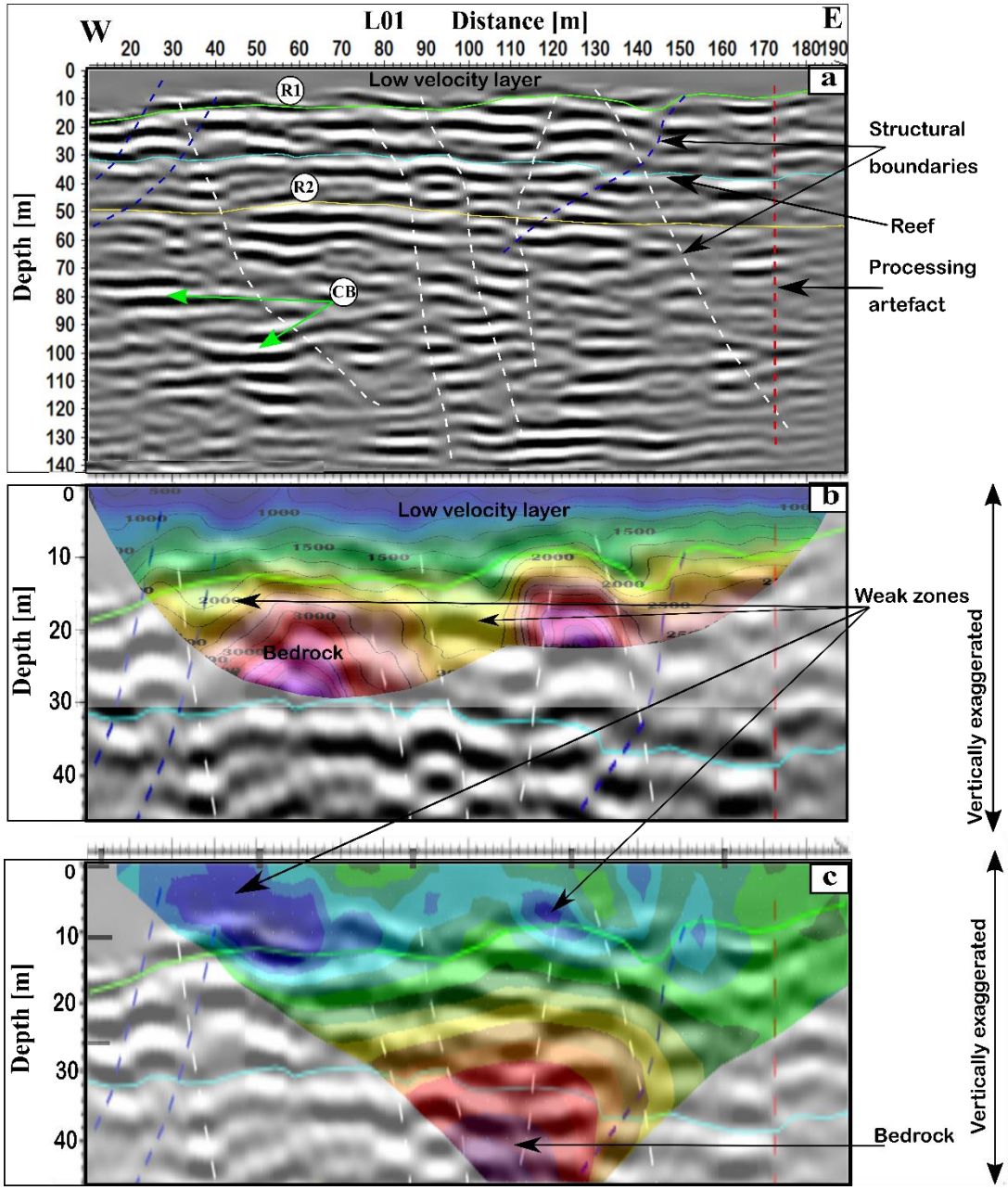


Figure 4.14: (a) Interpreted reflection seismic section along L01 showing the delineated interfaces; (b) interpreted refraction tomogram superimposed on the stretched-scale reflection seismic section, indicating some structural boundaries; (c) interpreted electrical resistivity tomogram superimposed on the stretched-scale reflection seismic section, indicating the mined-out zones. Note, R1 and R2 are the first and second reflectors, respectively, CB – indicates the conglomerate band reflector.

Comparably, on L02, the high resistivity regions (UM) between distance 80 and 130 correspond with the high-velocity zone (UM) observed on the refraction tomogram between distances 70 – 110 m and 130 – 143, respectively, at 6 – 18 m depth (Figure 4.15b and c). This area is interpreted as an unmined surface block that is currently under planning for an open cast pit mining due to its variable Au reefs grade near surface. The lower resistivity and velocity values at distance 0 – 70 m coincide with the loose material used to cover the mined stope entrances in the area. The low resistivity and velocity values across distances 35 – 55 m are likely due to water ingress from water-filled trenches located approximately at the 45 m position along the profile. This region could be a possibly fluid migration path into the mined-out regions and therefore maybe subjected to subsurface erosion.

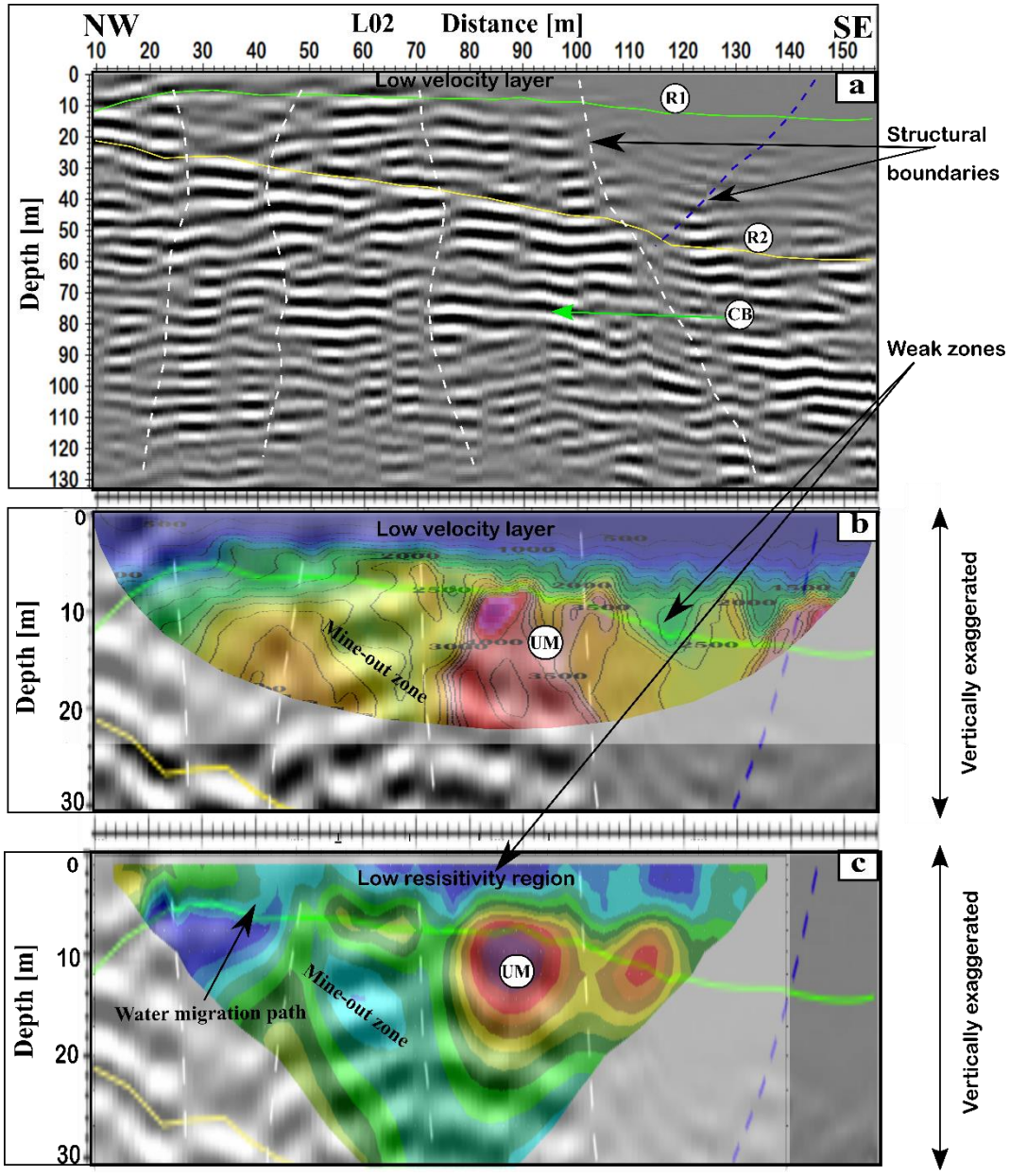


Figure 4.15: (a) Interpreted reflection seismic section along L02 showing the delineated interfaces; (b) interpreted refraction tomogram superimposed on the stretched-scale reflection seismic section, indicating some structural boundaries; (c) interpreted electrical resistivity tomogram superimposed on the stretched-scale reflection seismic section, indicating the mined-out zones. Note, R1 and R2 are the first and second reflectors, respectively, CB – indicates the conglomerate band reflector, UM- unmined surface block.

In addition, RT and ERT are comparable in resolving probably a saturated filled mine gallery/weak zone and cavity between surface distances of 30 – 110 m and

80 – 150 m, respectively on L03 (Figure 4.16b and c). The weak and saturated-filled mine-out zone revealed velocity variation between 400 – 2000 m/s, and resistivity values of 100 – 1500 Ωm. The cavity/tunnel region revealed anomalously high resistivity values of ~ 11000 Ωm, with a P-wave velocity of about 400 – 2500 m/s. This high resistivity and low velocity zone correspond at the same position of the slump structure observed on the reflection seismic section, which could also cause the zone of chaotic reflections (Figure 4.16), could also produce the chaotic reflections notice in the region. Hence, this region could be a potential hotspot for subsidence or sinkhole collapse. The low resistivity (80 – 500 Ωm) zone at distance 40 -90 m with 20 m maximum depth in the ERT section is probably a result of water inundation seen on the surface along the profile, which could also act as a fluid migration path into the underground mined gallery. Furthermore, the low-resistivity values (280 – 900 Ωm) observed at distances 120 – 170 m on ERT and RT section correspond with a low-velocity zone on the refraction tomogram at the same position. This area could be another potential fluid migration path into the stopes because of water ingress from the surface and could further enhance the erosion of cavities. From the ERT and refraction tomography results, I infer the velocity of the bedrock to be about 3500 – 5800 m/s and resistivity of about 2500 – 5000 Ωm.

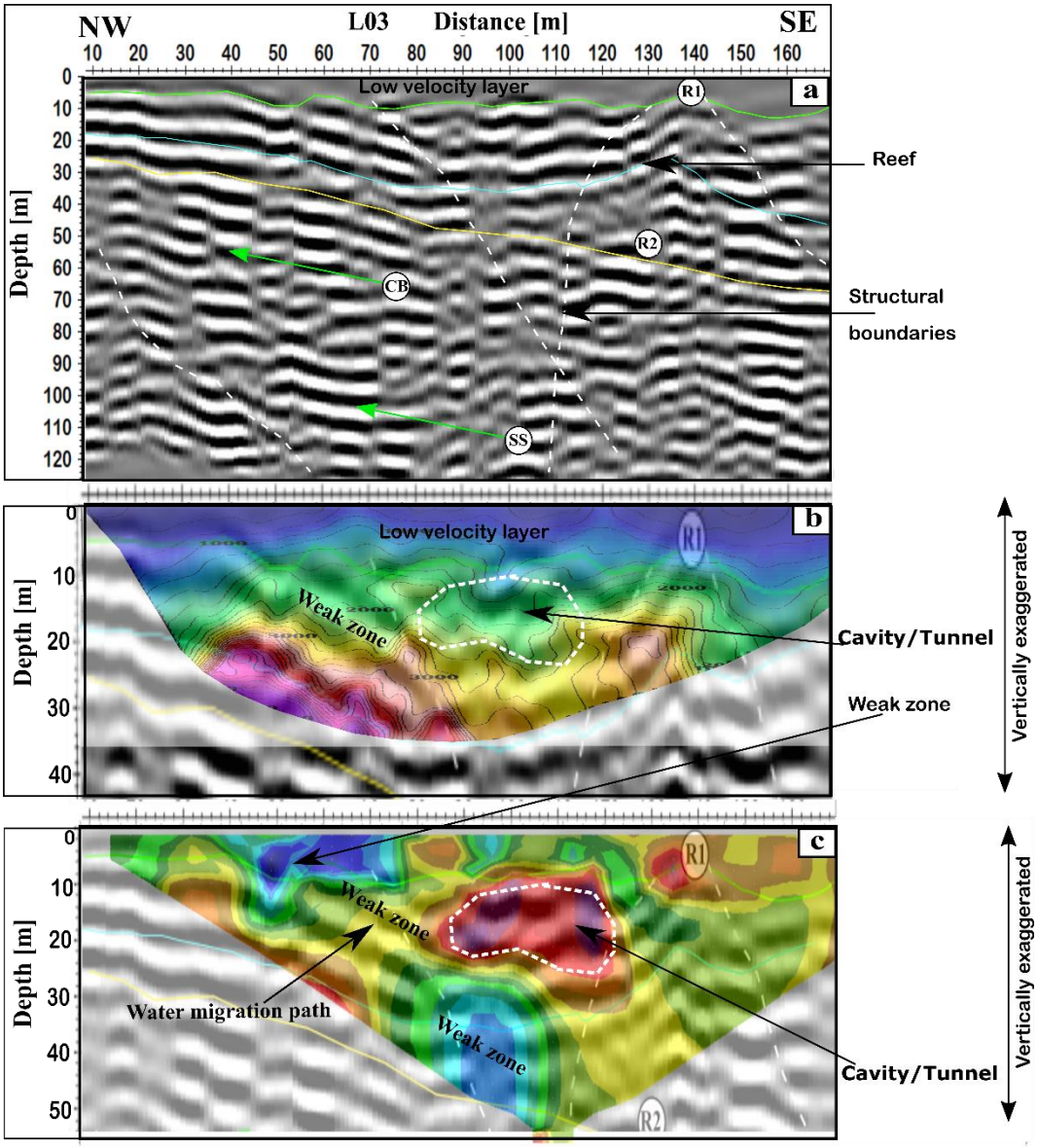


Figure 4.16: (a) Interpreted reflection seismic section along L03 showing the delineated interfaces. (b) Interpreted refraction tomogram superimposed on the stretched-scale reflection seismic section, indicating some structural boundaries. (c) Interpreted electrical resistivity tomogram superimposed on the stretched-scale reflection seismic section, indicating the mine-out zones. Note, R1 and R2 are the first and second reflectors, respectively, CB – indicates the conglomerate band reflector, SS – slump structure.

4.6. Discussion

In summary, by integrating and cross-referencing the reflection seismic with RT and ERT sections, it is possible to map the interfaces of subsurface structures such as cavities and mined-out zones. The RT and ERT provided an improved resolution of the near-subsurface image above 30 m relative to that of the reflection method alone, and allowed the detection and estimation of the geometry of isolated fissures. The ambiguity in the interpretation of seismic refraction (voids filled with air or other materials) was detected and resolved using integrated geophysical methods. Hence, it is advantageous to integrate different but complementary and highly task-appropriate geophysical techniques. The ERT sections provide the best constraint on water-saturation, cavity and water pathways, while the RT sections provide the best constraint on the subsurface material competence.

Complementary to RT and ERT, the reflection seismic sections highlight possible material interfaces and provide deeper investigation depth. The borehole logs provide ground truth evidence and correlation between different geophysical responses on the seismic section (Figure 4.17). The synthetic seismogram correlates very well with the borehole lithology and further constrains the final model (Figure 4.17). Figure 4.18 provides a 3D picture of near-surface using the reflection seismic characteristics of compressional wave arrival to map the subsurface architecture such as the mined-out zone – surrounding rock-interface and bedrock – overburden contact. The slump structure (SS) encountered across distances 30 – 120m at ~ 90 -110 m depth, dipping towards the southeast could be attributed to variations in the depositional structure or post-depositional deformation (Figure 4.16a). This feature could not be resolved by RT and ERT due to their shallow resolving depths. However, the refraction and electrical resistivity tomograms reveal probable saturated and weathered material at depths of about 5 – 20 m with velocity and resistivity value of about 400 – 2500 m/s and 100 – 2800 Ωm, respectively. The Archaean Central Rand Group (CRG) sandstone/quartzite velocity and resistivity may be as high as 6500 m/s and 5000 Ωm, respectively, as per the RT and ERT sections.

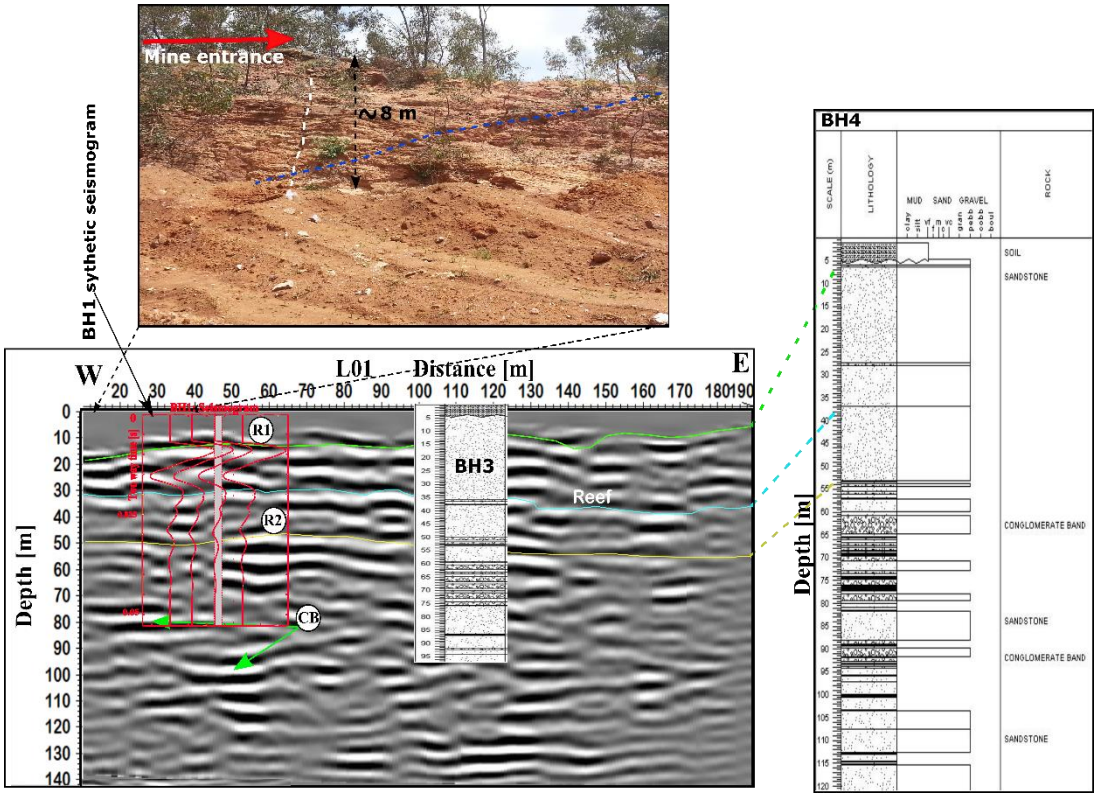


Figure 4.17: Borehole logs correlated and superimposed on the interpreted reflection seismic section indicating the mined-out Boulder Reef and material interfaces. Note, R1 and R2 are the first and second reflectors, respectively, CB – indicates the conglomerate band reflector. Note the jointing, fracturing and layering pattern of the Central Rand Group sandstone on the exposed sidewall of an open cast pit on the photograph. Borehole and synthetic seismogram superimposed on the seismic section (oriented west-east) indicate the bedrock-overburden contact and mined-out regions. The blue and white dotted lines indicate linear fractures/jointed pattern.

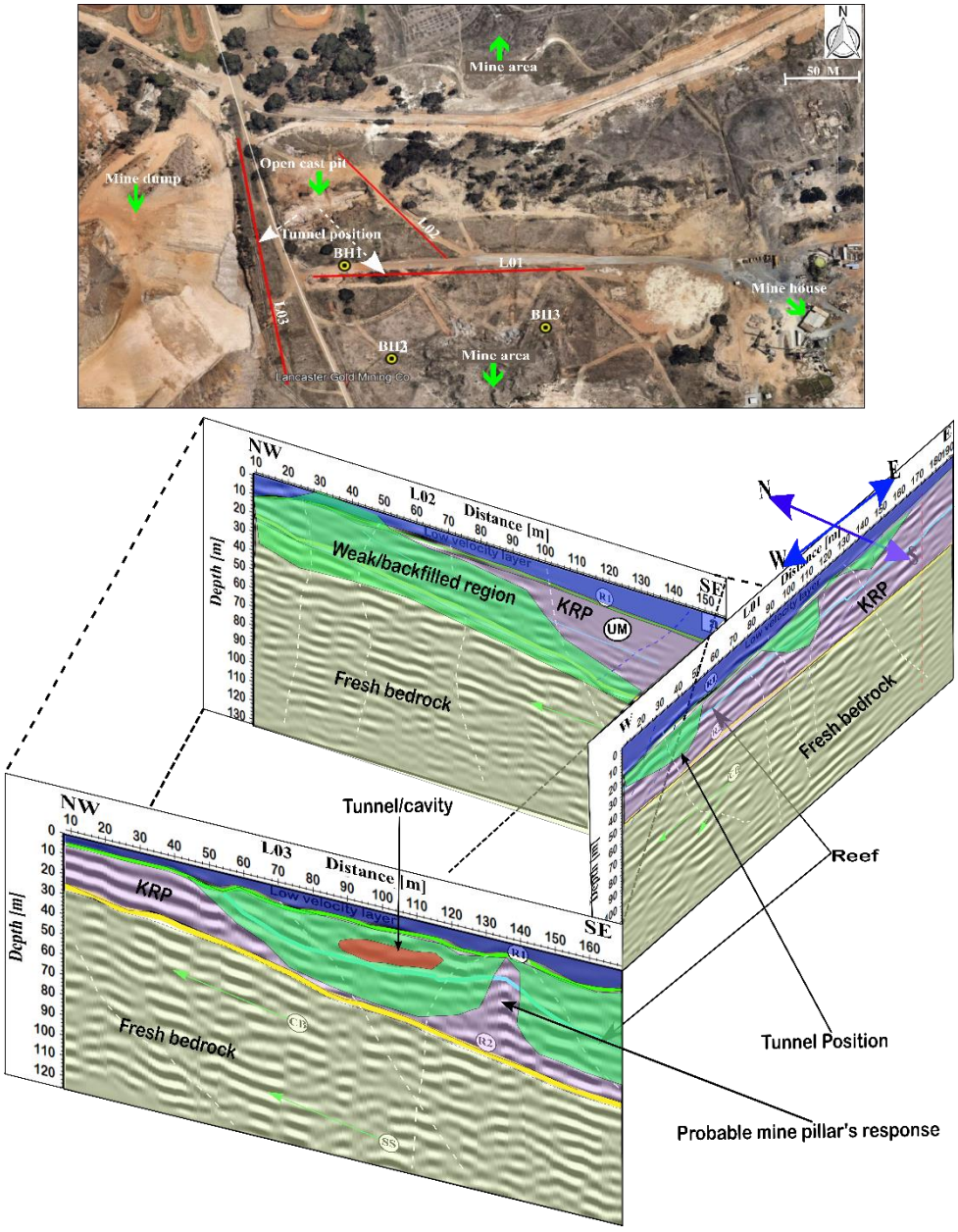


Figure 4.18: 3D correlation of the reflection seismic sections along L01, L02 and L03. The photographs indicate the profile directions. the dipping and strike direction of the layers. KPR-Kimberly Reef Package and UM-unmined region.

4.7. Conclusion and recommendation

Surface reflection/refraction seismic and electrical resistivity techniques were used to study the subsurface architectures in a historic shallow gold mine. The large material differences between the top weathered layer with that of the Witwatersrand sandstone, and the country rock with the stope cause high-amplitude coherent primary reflections induced by an active source (sledgehammer). The unwanted noise was removed using a standard reflection seismic processing procedure to generate reliable seismic sections. These sections were jointly interpreted with results of other geophysical methods (seismic refraction and electrical resistivity method) and borehole logs around the vicinity of the study area. Physical property measurements (velocity and density) were performed on the borehole cores. These values were used to generate a synthetic seismogram, which was used to constrain the final model

The refraction tomography (RT) results were compared with the electrical resistivity tomography (ERT) sections, which were acquired along the same profile. Their joint interpretation provides enhanced delineation of the shallow mined-out areas, the bedrock-overburden contact, cavity, weak zones and micro-geological structures. Moreover, the reflection seismic method supports the interpreted bedrock-overburden contact and the mined-out interface with the Archaean sandstone and quartzite rocks of the Central Rand Group. Hence, the southward dipping coherent reflection (R2) are interpreted as the stopes created to mine the high Au-grade Boulder Reef. The interrupted coherent reflections (CB) are interpreted to be the intermittent conglomerate bands.

Finally, an exact geometry (widths and thicknesses) of the subsurface structures could not be resolved due to the relatively low-frequency and low-energy source, coupled with the limited imaging capability of 2D data. However, the approximate geometries of the mined-out zones, cavities and the bedrock-overburden contact, as well as some structural boundaries in the area, were successfully obtained. The complementary RT and ERT sections provided comparably better subsurface images and resolutions than the reflection seismic sections above 30 m depth. Nonetheless, a 3D acquisition technique with a high-

energy source and denser receiver and shot spacing should be able to resolve the thicknesses of the mined-out regions adequately and provide further knowledge of the subsurface architecture in the area. Therefore, the integration of reflection seismic, refraction and electrical resistivity methods were successful in mapping potentially-hazardous shallow subsurface structures in the study area and is a viable basis for other similar subsurface characterization studies.

Acknowledgment

Appreciation goes to Dr. F. Andriampenomanana, S. Gomo, Z. Nxantsiya, A. Netsianda, P. Mlokothi, M. Hobo and M. Ntsuku and T. Nwachukwu for their assistance in the field. Thanks to Dr. Steve Zhang for his immense counseling, teaching and review. M. Westgate for his MATLAB code used to generate synthetic seismogram. We would also like to thank Prof. E. Stettler and Lancaster Gold Mine, Krugersdorp, South Africa for granting us permission to conduct our survey in the reserve. We also want to thank the reviewers and the associate editor for improving the quality of the manuscript (Pure and Applied Geophysics journal).

All the equipment used in this study was provided by the Seismic Research Centre, School of Geoscience, University of the Witwatersrand and Council for Geoscience (CGS), South Africa. R.J Durrheim acknowledges the support of the National Research Foundation of South Africa (Grant Number: 46979).

4.8. Reference

Anhaeusser, C.R., 2012. The history of mining in the Barberton greenstone belt, South Africa, with an emphasis on gold (1868–2012). *Economic Geology Research Institute, School of Geosciences, University of the Witwatersrand, Johannesburg, Google Scholar.* http://dewilde.co.za/Barberton/GoldenQuarry/THE%20HISTORY%20OF%20MINING%20%20BARBERTON%20-%20Carl%20Anhaesseur.pdf. 23/11/2018.

Armstrong, R.A., Compston, W., Retief, E.A., Williams, I.T. and Welke, H.J., 1991. Zircon ion microprobe studies bearing on the age and evolution of the Witwatersrand triad. *Precambrian Research*, *53*(3-4), pp. 243-266.

Banerjee, B. and Gupta, S.K., 1975. Hidden layer problem in seismic refraction work. *Geophysical Prospecting*, *23*(4), pp. 642-652.

Breytenbach, I.J. and Bosch, P.J.A., 2011. Application, advantages and limitations of high-density gravimetric surveys compared with three-dimensional geological modelling in dolomite stability investigations. *Journal of the South African Institution of Civil Engineering*, *53*(2), pp. 7-13.

Brink, A.B.A., 1979. Engineering Geology of Southern Africa. *Building Publications*, Pretoria, v. 1.

Brodic, B., Malehmir, A., Pugin, A. and Maries, G., 2018. Three-component seismic land streamer study of an esker architecture through S-and surface-wave imaging seismic imaging of glacial sediments. *Geophysics*, *83*(6), pp. B339-B353.

Buttrick, D.B., Trollip, N.Y., Watermeyer, R.B., Pieterse, N.D. and Gerber, A.A., 2011. A performance-based approach to dolomite risk management. *Environmental Earth Sciences*, *64*(4), pp. 1127-1138.

Cary, P., 2006. Reflections on the Deconvolution of Land Seismic Data. *CSEG Recorder*, Special Edition.

Cooper, G.R.J., 2014. The automatic determination of the location and depth of contacts and dykes from aeromagnetic data. *Pure and Applied Geophysics*, *171*(9), pp. 2417-2423.

Council for Geoscience (CGS)/South African Institute of Engineering and Environmental Geologist (SAIEG)., 2003. Guideline for Engineering-geological Characterisation and Development of Dolomitic Land.

Corner, B., Durrheim, R.J. and Nicolaysen, L.O., 1990. Relationships between the Vredefort structure and the Witwatersrand basin within the tectonic framework of the Kaapvaal craton as interpreted from regional gravity and aeromagnetic data. *Tectonophysics*, *171*(1-4), pp. 49-61.

Dahlin, T. and Zhou, B., 2004. A numerical comparison of 2D resistivity imaging with 10 electrode arrays. *Geophysical Prospecting*, *52*(5), pp. 379-398.

Dankert, B.T. and Hein, K.A.A., 2010. Evaluating the structural character and tectonic history of the Witwatersrand Basin. *Precambrian Research*, *177*, pp. 1–22, doi: 10.1016/j.precamres.2009.10.007.

De Waal, S.A., Graham, I.T. and Armstrong, R.A., 2006. The Lindeques Drift and Heidelberg Intrusions and the Roodekraal Complex, Vredefort, South Africa: Comagmatic plutonic and volcanic products of a 2055 Ma ferrobasaltic magma. *South African Journal of Geology*, *109*(3), pp. 279-300.

De Wit, M.J., Roering, C., Armstrong, R.A., Tredoux, M., de Ronde, C.E.J., Hart, R.J., Green, R., Peberdy, E. and Hart, R.A., 1992. Formation of an Archaean continent. *Nature*, *357*(6379), pp. 553-564.

Drennan, G.R., Boiron, M.C., Cathelineau, M. and Robb, L.J., 1999. Characteristics of post-depositional fluids in the Witwatersrand Basin. *Mineralogy and Petrology*, *66*(1-3), pp. 83-109.

Festa, V., Tripaldi, S., Siniscalchi, A., Acquafredda, P., Fiore, A., Mele, D. and Romano, G., 2016. Geoelectrical resistivity variations and lithological

composition in coastal gypsum rocks: A case study from the Lesina Marina area (Apulia, southern Italy). *Engineering Geology*, *202*, pp. 163-175.

Frimmel, H.E. and Hallbauer, D.K., 1999. Gold mobilizing fluids in the Witwatersrand Basin: Composition and possible sources. *Mineralogy and Petrology*, *66*(1-3), pp. 55-81.

Gélis, C., Revil, A., Cushing, M.E., Jougnot, D., Lemeille, F., Cabrera, J., De Hoyos, A. and Rocher, M., 2010. Potential of electrical resistivity tomography to detect fault zones in limestone and argillaceous formations in the experimental platform of Tournemire, France. *Pure and Applied Geophysics*, *167*(11), pp. 1405-1418.

Gibson, R.L. and Reimold, W.U., 2000. Deeply exhumed impact structures: A case study of the Vredefort structure, South Africa. In Impacts and the early Earth. *Springer*, Berlin, Heidelberg, pp. 249-277

Gibson, R.L. and Reimold, W.U., 2001. The Vredefort impact structure, South Africa: The scientific evidence and a two-day excursion guide, *92*, Council for Geoscience.

Gómez-Ortiz, D. and Martín-Crespo, T., 2012. Assessing the risk of subsidence of a sinkhole collapse using ground penetrating radar and electrical resistivity tomography. *Engineering Geology*, *149*, pp. 1-12.

Gray, S.H., Etgen, J., Dellinger, J. and Whitmore, D., 2001. Seismic migration problems and solutions. *Geophysics*, *66*(5), pp. 1622-1640.

Handley, J.R., 2004. Historic overview of the Witwatersrand goldfields: A review of the discovery, geology, geophysics, development, mining, production and future of the Witwatersrand goldfields as seen through a geological and financial association spanning 50 years. JRF Handley.

Hayward, C.L., Reimold, W.U., Gibson, R.L. and Robb, L.J., 2005. Gold mineralization within the Witwatersrand Basin, South Africa: Evidence for a

modified placer origin, and the role of the Vredefort impact event. *Geological Society, London, Special Publications*, *248*(1), pp. 31-58.

Isiaka, A.I., Durrheim, R.J. and Manzi, M.S., 2019. High-resolution seismic reflection investigation of subsidence and sinkholes at an abandoned coal mine site in South Africa. *Pure and Applied Geophysics*, *176*(4), pp. 1531-1548.

Ivanov, J., Miller, R.D., Xia, J., Steeples, D. and Park, C.B., 2005. The inverse problem of refraction travel times, Part I: Types of geophysical nonuniqueness through minimization. *Pure and Applied Geophysics*, *162*(3), pp. 447-459.

Ivanov, J., Miller, R.D., Xia, J., Steeples, D. and Park, C.B., 2006. Joint analysis of refractions with surface waves: An inverse solution to the refraction-traveltime problem. *Geophysics*, *71*(6), pp. R131-R138.

Keller, G.V. and Frischknecht, F.C., 1966. Electrical Methods in Geophysical Prospecting. *Pergamon Press, Inc*, London.

Kleywegt, R.J., 2015. Geophysics in dolomitic terrains. The History of Geophysics in Southern Africa. Johan H de Beer ed. *Sun Press,* pp. 190 - 203.

Kirk, J., Ruiz, J., Chesley, J., Walshe, J. and England, G., 2002. A major Archaean, gold-and crust-forming event in the Kaapvaal Craton, South Africa. *Science*, *297*(5588), pp. 1856-1858.

Leucci, G., 2004. Evaluation of 2D resistivity and seismic refraction methods in a complex karstic area. *Geo Acta, 3,* pp. 43-53.

Leucci, G. and De Giorgi, L., 2005. Integrated geophysical surveys to assess the structural conditions of a karstic cave of archaeological importance. *Natural Hazards and Earth System Science, 5*(1), pp. 17-22.

Loke, M.H. and Barker, R.D., 1996. Practical techniques for 3D resistivity surveys and data inversion. *Geophysical Prospecting*, *44*(3), pp. 499-523.

Loke, M.H., Chambers, J.E., Rucker, D.F., Kuras, O. and Wilkinson, P.B., 2013. Recent developments in the direct-current geoelectrical imaging method. *Journal of Applied Geophysics*, *95*, pp. 135-156.

Malehmir, A., Durrheim, R., Bellefleur, G., Urosevic, M., Juhlin, C., White, D.J., Milkereit, B. and Campbell, G., 2012a. Seismic methods in mineral exploration and mine planning: A general overview of past and present case histories and a look into the future. *Geophysics*, *77*(5), pp. WC173-WC190.

Malehmir, A., Juhlin, C., Wijns, C., Urosevic, M., Valasti, P. and Koivisto, E., 2012b. 3D reflection seismic imaging for open-pit mine planning and deep exploration in the Kevitsa Ni-Cu-PGE deposit, northern Finland. *Geophysics*, *77*(5), pp. WC95-WC108.

Malehmir, A., Andersson, M., Mehta, S., Brodic, B., Munier, R., Place, J., Maries, G., Smith, C., Kamm, J., Bastani, M. and Mikko, H., 2016. Post-glacial reactivation of the Bollnas fault, central Sweden: A multidisciplinary geophysical investigation. *Solid Earth*, *7*(2), pp. 509-527.

Manzi, M.S.D., Gibson, M.A.S., Hein, K.A.A., King, N. and Durrheim, R.J., 2012a Application of 3-D seismic techniques in evaluation of ore resources in the West Wits Line goldfield and portions of the West Rand goldfield, South Africa. *Geophysics, 77*(5), pp. WC163-WC171.

Manzi, M.S., Durrheim, R.J., Hein, K.A. and King, N. 2012b. 3D edge detection seismic attributes used to map potential conduits for water and methane in deep gold mines in the Witwatersrand basin, South Africa. *Geophysics*, *77*(5), pp. pp. WC133-WC147.

Manzi, M.S., Hein, K.A., Durrheim, R.J. and King, N. 2014. The Ventersdorp Contact Reef model in the Kloof Gold Mine as derived from 3D seismics, geological mapping and exploration borehole datasets. *International Journal of Rock Mechanics and Mining Sciences, 66*, pp. 97-113.

Martínez-Moreno, F. J., Galindo-Zaldívar, J., Pedrera, A., Teixido, T., Ruano, P., Peña, J. A., González-Castillo, L., Ruiz-Constán, A., López-Chicano, M., and

Martín-Rosales, W., 2014. Integrated geophysical methods for studying the karst system of Gruta de las Maravillas (Aracena, Southwest Spain). *Journal of Applied Geophysics*, *107*, pp. 149-162.

Miller, R.D., Steeples, D.W. and Brannan, M., 1989. Mapping a bedrock surface under dry alluvium with shallow seismic reflections. *Geophysics*, *54*(12), pp. 1528-1534.

Miller, R.D. and Steeples, D.W., 1991. Detecting voids in a 0.6 m coal seam, 7 m deep, using seismic reflection. *Geoexploration*, *28*(2), pp. 109-119.

Miller, R.D. and Xia, J., 1998. Large near-surface velocity gradients on shallow seismic reflection data. *Geophysics*, *63*(4), pp. 1348-1356.

Narayan, J.P., 2012. Effects of P-wave and S-wave impedance contrast on the characteristics of basin transduced Rayleigh waves. *Pure and Applied Geophysics*, *169*(4), pp. 693-709.

National Water Act (NWA), Act No 36 of 1998, Republic of South Africa.

Norman, N. and Whitfield, G. 2006. Geological Journeys. *Struik Publishers,* Cape Town. pp. 38-49, 60–61.

Onyebueke, E.O., Manzi, M.S.D. and Durrheim, R.J., 2018. High-resolution shallow reflection seismic integrated with other geophysical methods for hydrogeological prospecting in the Nylsvley Nature Reserve, South Africa. *Journal of Geophysics and Engineering*, *15*(6), pp. 2658 - 2669.

Redhaounia, B., Ilondo, B.O., Gabtni, H., Sami, K. and Bédir, M., 2016. Electrical Resistivity Tomography (ERT) applied to karst carbonate aquifers: Case study from Amdoun, northwestern Tunisia. *Pure and Applied Geophysics*, *173*(4), pp. 1289-1303.

Reimold, W.U. and Gibson, R.L., 1996. Geology and evolution of the Vredefort impact structure, South Africa. *Journal of African Earth Sciences, 23*(2), pp. 125-162.

Robb, L.J. and Meyer, F.M. 1995. The Witwatersrand Basin, South Africa: Geological framework and mineralization processes. *Ore Geology Reviews, 10*(2), pp. 67-94.

Robb, L.J., Davis, D.W., and Kamo, S.L., 1991. Chronological framework for the Witwatersrand Basin and environs, towards a time-constrained depositional model. *South African Journal of Geology, 94*(1), pp. 86-95.

Sandmeier, K.J., 1998. ReflexW Program for the processing of seismic, acoustic or electromagnetic reflection, refraction and transmission data. Karlsruhe, Germany: Sandmeier Software.

Sheriff, R.E., and Geldart, L.P., 1995. Exploration Seismology. *Cambridge University Press*, 2nd Eds.

Spitzer, R., Nitsche, F.O., Green, A.G. and Horstmeyer, H., 2003. Efficient acquisition, processing, and interpretation strategy for shallow 3D seismic surveying: A case study. *Geophysics*, *68*(6), pp. 1792-1806.

Steeples, D.W. and Miller, R.D., 1988. Seismic reflection methods applied to engineering, environmental, and ground-water problems: In Symposium on the Application of Geophysics to Engineering and Environmental Problems. *Society of Exploration Geophysicists,* pp. 409-461.

Steeples, D.W., Green, A.G., McEvilly, T.V., Miller, R.D., Doll, W.E. and Rector, J.W., 1997. A workshop examination of shallow seismic reflection surveying. *The Leading Edge, 16*(11), pp. 1641-1647.

Therriault, A.M., Grieve, R.A.F. and Reimold, W.U., 1997. Original size of the Vredefort structure: Implications for the geological evolution of the Witwatersrand Basin. *Meteoritics and Planetary Science, 32*(1), pp. 71-77.

Tinker, J., de Wit, M. and Grotzinger, J., 2002. Seismic stratigraphic constraints on Neoarchaean-Palaeoproterozoic evolution of the western margin of the Kaapvaal Craton, South Africa. *South African Journal of Geology, 105*(2), pp. 107-134.

Whitaker, F.F. and Xiao, Y., 2010. Reactive transport modelling of early burial dolomitization of carbonate platforms by geothermal convection. *AAPG Bulletin*, *94*(6), pp. 889-917.

Widess, M.B., 1973. How thin is a thin bed? *Geophysics, 38*(6), pp. 1176-1180.

Wolmarans, J.F., 1996. Sinkholes and subsidence on the far West Rand. Seminar on the Engineering Geology of Dolomite Areas, University of Pretoria, Pretoria, 18 January 1996.

Yilmaz, O., 1987. Seismic Data Processing. Investigations in Geophysics, *Society of Exploration Geophysicists,* Tulsa, USA.

Yılmaz, O., 2001. Seismic Data Analysis: Processing, Inversion, and Interpretation of Seismic Data. *Society of Exploration Geophysicists*, Tulsa, USA.

Youssef, A.M., El-Kaliouby, H.M. and Zabramawi, Y.A., 2012. Integration of remote sensing and electrical resistivity methods in sinkhole investigation in Saudi Arabia. *Journal of Applied Geophysics, 87*, pp. 28-39.

Zegers, T.E., De Wit, M.J., Dann, J. and White, S.H., 1998. Vaalbara, Earth's oldest assembled continent? A combined structural, geochronological, and palaeomagnetic test. *Terra Nova*, *10*(5), pp. 250-259.

CHAPTER 5

5.0 Geophysical site investigation of the Archaean-Palaeoproterozoic Transvaal Basin architecture near Boons-Magaliesburg-Hekpoort and its implication for hydrogeological prospecting and engineering

Abstract

The Transvaal basin has been well studied, both stratigraphically and structurally, using surface geological mapping and borehole logs drilled within the basin. In this study, 2D reflection seismic and aeromagnetic data were used to investigate the structure of the Transvaal Basin in the Boons-Magaliesburg-Hekpoort region, about 100 km northwest of Johannesburg. The implications for hydrogeological prospecting and engineering applications were emphasized. The geophysical datasets were constrained using geological and borehole information in the area. Several faults in the area were identified and characterised, notably the Rustenburg fault. The Rustenburg fault was modelled and interpreted as a normal planar fault. The faults were associated with subordinate antithetic and synthetic faults, and heterogeneous fracture systems. Palaeo-karst, palaeo-slope, dykes and folded features were also mapped. Intrusive lineaments (such as dykes/sills) and structures (such as faults, fractures, and slump features) were observed on the total magnetic intensity map as short and long wavelength magnetic field anomalies, respectively. Fault zones provide a path for fluid migration, fractured zones are potential aquifers, and dykes form groundwater compartments. The study provides information for hydrogeological prospecting, environmental and infrastructural planning, and further reconstruction of the subsurface geology and tectonic model in the study area.

5.1. Introduction

Geophysical methods have been used extensively to image the geological architecture of South Africa, both in 2D and 3D (Durrheim et al., 1991; Tinker et al., 2002; Manzi et al., 2012a and b; Malehmir et al., 2014; Onyebueke et al., 2018; Isiaka et al., 2018). Variations in physical properties, such as density, acoustic velocity, magnetic susceptibility, and electrical resistivity produce geophysical responses that provide an important measure of geological structure.

Joint interpretation of several geophysical datasets reduces the ambiguity that often exists when inverting a single dataset. Many researchers have integrated reflection seismic data with other datasets, such as potential field, geoelectric and ground penetrating radar (GPR) to characterise karst features (Oosthuizen and Richardson, 2011; Burberry et al., 2016), for hydrogeological prospecting and engineering investigations (Onyebueke et al., 2018; Isiaka et al., 2018; McDowell et al., 2002; Scheiber-Enslin and Manzi, 2018), and for regional survey, mineral prospecting and orebody distribution mapping (Durrheim et al., 1991; Tinker et al., 2002; Webb et al., 2004; Scheiber-Enslin et al., 2016). Moreover, legacy reflection seismic data are valuable assets because they can be interpreted and reprocessed using modern techniques to yield new insights (e.g. academic research, mining safety, and optimal resource recovery and basin model reconstruction) (Eaton et al., 2003; Malehmir et al., 2012 Manzi et al., 2012a and b; Malehmir et al., 2014; Isiaka et al., 2017, Manzi et al., 2019).

The Transvaal Basin and Supergroup have been well studied, both stratigraphically and structurally, using surface geological mapping and borehole information (Figure 5.1 and Figure 5.2) (Catuneanu and Eriksson, 1999 and 2002; Eriksson et al., 2001, 2006; Eriksson and Reczko, 1995). Barnard (2000) investigated the hydrological and hydrogeological characteristics of the Transvaal Supergroup in greater detail using borehole information.

In this study, legacy post-stack time-migrated 2D reflection seismic data were post-stack denoised and interpreted together with magnetic, borehole, and surface geological mapping data. The aim of the study is to delineate Transvaal

Supergroup structures in the Boons-Magaliesburg-Hekpoort region, about 100 km northwest of Johannesburg, and insights into hydrogeological prospecting and engineering applications. Post-stack seismic denoising and attributes such as the curvelet transform (Shukla et al., 2014) and structurally-oriented dip filter were applied to enhance the geological structures (DUG Insight software (v.4.5), 2018a). The tilt and vertical first derivatives of magnetic field were used to improve and constrain the near-surface anomalies on the aeromagnetic field map (Stettler et al., 1999). The legacy aeromagnetic data was also used to enhance the discernibility of near-surface geological structures (such as faults, dykes, sills and Archaean granitic basement) that cannot be readily observed on the 2D seismic data. Integrating these geophysical datasets for site investigation delineate the extent and geometries of structures and improves the understanding of the surface-subsurface geology.

The need to investigate these kinds of sites in detail has several objectives. One of the most pertinent is resource identification and mapping. Much of the surface of study area is occupied by agricultural lands, nature reserves, mining sites and residential facilities, all of which critically depend on the availability of fresh water resources. The demand and search for groundwater resources in the South African hard rock terrain has increased during the past decades (Onyebueke et al., 2018; Barnard, 2000), and the need for groundwater prospecting using all available datasets becomes necessary (NWA, 1998).

The study area is mostly covered by dolostone of the Malmani Subgroup of the Chuniespoort Group, and siliciclastic, shale and intrusive rocks of the Pretoria Group. The aquifer geometry in the dolostone formation usually depends on the process of dolomitization and stratigraphic architecture. The process of dolomitization increases the crystal and pore sizes, and therefore enhances the permeability and porosity of the dolomitised layer. Layer permeability and porosity are also enhanced by fracturing.

The aquifer units in the study area are thought to be compartmentalized by dykes. These create physical barriers that could limit the groundwater flow between compartments. Dykes are also of concern to engineering structures due to the

swelling characteristics of the soil produced by weathered intrusive rocks (Barnard, 2000; Altchenko et al., 2017). Currently, there is still uncertainty regarding the existence, locations and interactions of these compartments, and extent of the aquifer. The hydrogeological attributes, such as groundwater occurrence and drainage patterns, are similar in many of the geological units. For instance, the secondary permeability that is developed along faults, dyke contacts, bedding planes and lithological contacts permits groundwater movement, recharge and withdrawal in many of these geological structures.

Thus, faults, fractured and karst zones typically represent both an exploitable water resource and potential hazard for infrastructure and mining engineering. High quality information of the surface-subsurface obtained through integrated approaches are valuable resources for agriculture, environmental planning and conservation, infrastructural planning and development. In particular, the results will assist with the hydrological characterisation of geological structures (such as fault, joints, fractured and shear zones and aquifer geometry) and re-evaluation of the regional tectonic model in the area.

5.2. Site location and geology

The study area lies within the ca. 2500 Ma Transvaal Basin (Eriksson et al., 1995), northwest of the ca. 2700 Ma Witwatersrand Basin and southwest of the ca. 2050 Ma Bushveld Igneous Complex (Figure 5.1).

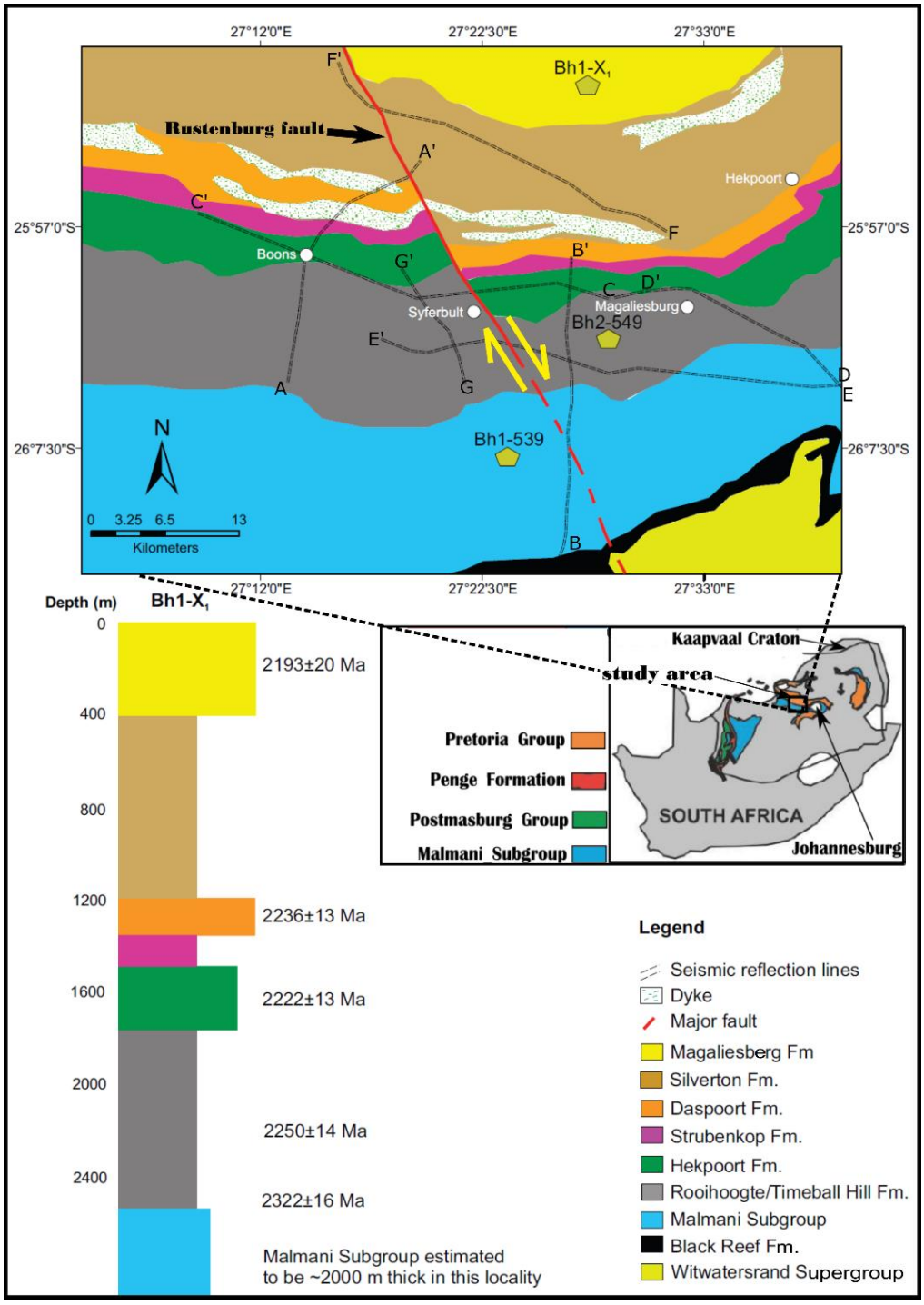


Figure 5.1: Geology of the study area with seismic lines. Index on the left is the formation stratigraphy at the Bh1-X_1 location. Insert shows the location of the Transvaal Basin (the borehole and geology information were sourced and modified from the South Africa geological map from the Council for Geosciences (CGS)) (Eriksson and Reczko, 1995 and 1998; Eriksson et al., 1995). The dashed red line section of the RF shows probable extension of the fault at depth.

The Transvaal Supergroup is preserved in two basins, *viz.* the Transvaal and Griqualand Basins, which are separated by the Vryburg arch (Cheney, 1996; Moore et al., 2001). In the study area, the Transvaal Supergroup rocks dip ~20-37° north and lie unconformably upon the ca. 2600 Ma Ventersdorp Supergroup or on Archaean basement rocks (Catuneanu and Eriksson, 1999; Basson, 2019).

Four main lithostratigraphical sequences are found in the study area:

i. The Black Reef Formation (BRF), at the base of the Transvaal Supergroup, consists predominantly of clastic sedimentary rocks (Eriksson et al., 1995).

ii. The Chuniespoort Group (CG), which is represented by dolostone and chert rocks of the Malmani Subgroup and the banded ironstones of the Penge Formation, overlies the BRF.

iii. The Pretoria Group, which overlies the CG, includes clastic sedimentary and volcanic rocks. The clastic sediments include sandstone, quartzite, mudrock, shale, carbonate, breccia, conglomerate and diamictite members of the Rooihoogte, Timeball Hill, Boshoek, Dwaalheuwel, Strubenkop, Daspoort and Silverton Formations. The main volcanic sequence is the andesite of the Hekpoort Formation. Many dykes and sills occur, especially in the Silverton Formation. The sandstone-mudrock lenses and interbedded quartzites of the Magaliesberg Formation lie at the top of the Pretoria Group (Catuneanu and Eriksson, 1999) (Figure 5.1 and Figure 5.2).

iv. The clastic sediments and volcanic rocks of the Rooiberg Group end the Transvaal Basin and marks the beginning of the Bushveld Igneous Complex (Catuneanu and Eriksson, 1999 and 2002)

The sedimentation of the Transvaal Basin was controlled by cycles of extensional rift, and thermal and mechanical subsidence, accompanied by fault-related continental sedimentary deposits, which were separated by stages of uplift, rifting

and glacio-eustatic base level fall (Catuneanu and Eriksson, 1999 and 2002; Eriksson et al., 2001 and 2006; Eriksson and Reczko, 1995). The surface geology transverses by the legacy 2D reflection seismic lines is predominantly carbonate rocks of Malmani Subgroup, clastic sedimentary rocks of Rooihoogte-Timeball Hill Formation, volcanic rocks of the Hekpoort Formation, sandstone of the Strubenkop Formation, siliciclastic rocks of the Daspoort Formation, and diabase dykes, clastic and carbonate rocks of the Silverton Formation (Figure 5.1 and Figure 5.2).

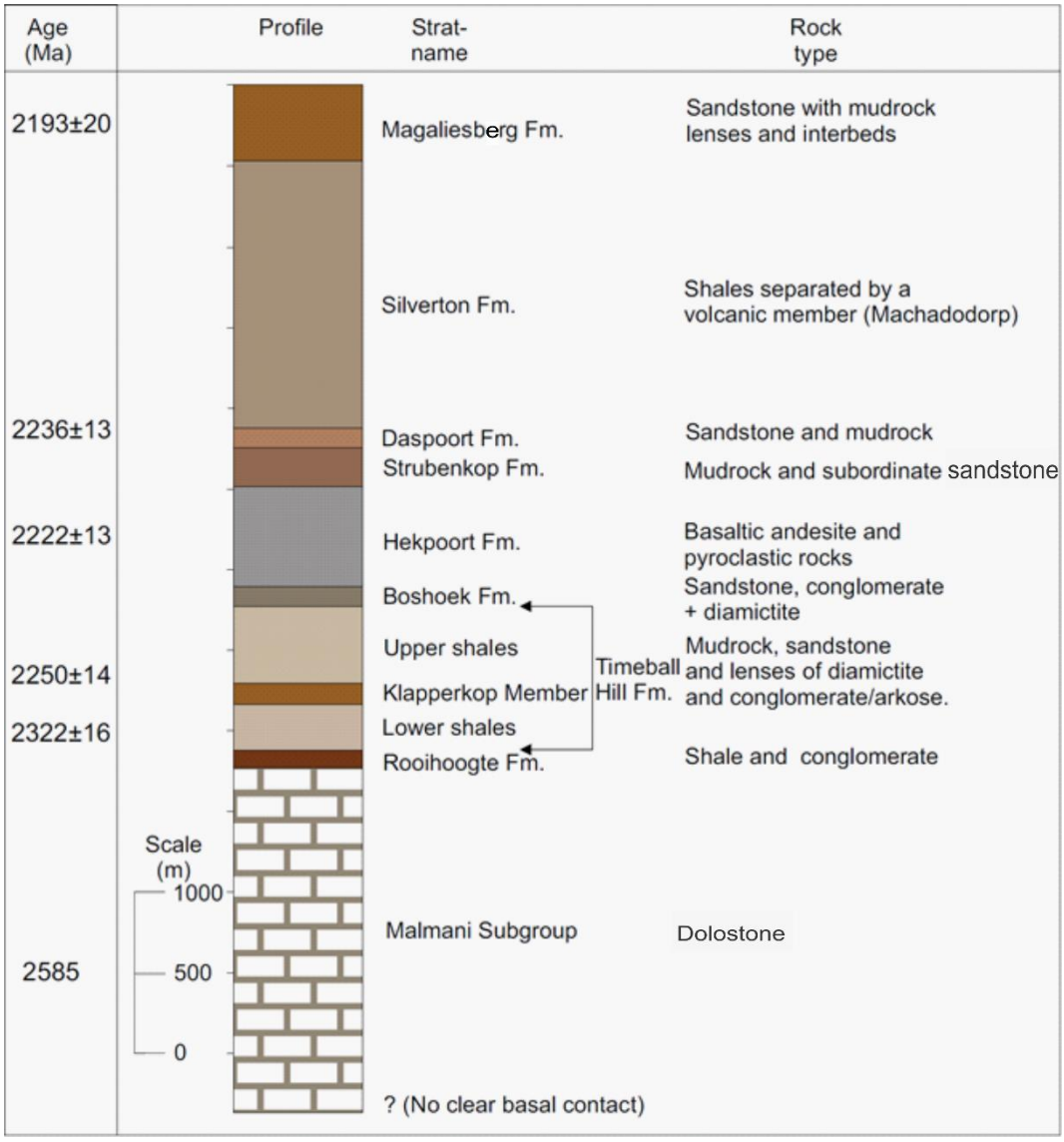


Figure 5.2: The average formation stratigraphy of the Transvaal Supergroup (modified from Erikson et al., 1995; Amstrong et al., 1991).

5.3. Tectonic and structural impact on the sedimentation in the Transvaal Basin

The activation of Archaean strike-slip faults in an extensional graben system resulted in the accumulation of bimodal volcanic rocks and fault-related alluvial-fluvial sedimentary sequences systems that characterise the basal Protobasinal rocks (Stanistreet and McCarthy, 1991; Eriksson and Reczko, 1995). Els et al. (1995) and Hilliard and McCourt (1995) argued that northward-directed compressive deformation, the Johannesburg Dome and the palaeo-drainage divide in the Klerksdorp area provide evidence of the northward tilting of the southern part of the Kaapvaal Craton. This tectonic regime caused a northerly palaeo-slope and fluvial infilling of the palaeo-floor topography and eventual deposition of Black Reef Formation (Eriksson and Reczko, 1995).

The chemical sedimentary facies that characterise the Chuniespoort Group and the absence of clastic sedimentation is further evidence of tectonic stability (Eriksson and Reczko, 1995 and 1998). Clendenin (1989) and Eriksson et al. (1995) view the Chuniespoort Group as the last stage of the late Archaean successor basins that formed on the Kaapvaal Craton due to thermal subsidence. The subsidence is caused by Ventersdorp age fault-modulated systems. The Chuniespoort Group also underwent thermal-induced flexural subsidence during this period.

Eriksson and Reczko (1995) proposed that the uplift and erosional loss of Chuniespoort rocks towards the south and southeast of the Timeball Hill Formation along the Johannesburg Dome and the Klerksdorp linear trend could be attributed to a possible zone of compressional uplift during the deposition of the Black Reef Formation, which caused the lacustrine basin deposition of the Duitschland Formation in the southeast. The preservation of the Malmani Subgroup and Penge iron Formation of the Chuniespoort Group and absence of large-scale faulting toward the south of the Transvaal Basin suggested that the Duitschland Formation was the result of a localised flexural subsidence feature rather than being a fault-related deposition, and could also be attributed to a linear uplifted zone that is preserved in the present-day Rand anticline (Eriksson and Reczko, 1995).

The tectonic process proposed to have taken place during the Pretoria Group era was dominated by thermal subsidence, followed by subordinate mechanical subsidence. This could have caused the large thick suspended mudrock deposits of the Timeball Hill and Silverton Formations (Eriksson and Reczko, 1995). Moreover, the extensive volcanic units and alluvial-fluvial sandstone deposits of the Rooihoogte, Boshoek and Dwaalheuwel Formations provide evidence of an intracratonic rift tectonic basin (Eriksson and Reczko, 1995). Allen and Allen (1990) in a general discussion of the basin evolution, postulate a continuum between intracratonic sag-basins and intracratonic rift-basins, where thermal subsidence initially predominated, followed by subordinate fault-modulated mechanical subsidence and localised rifting. Klein and Hsui (1987) and Clendenin (1989) suggest that the basin could be related to continental tectonic break-up influenced by the thermal subsidence, followed by minor mechanical subsidence.

Eriksson et al, (1995) concluded that no syn-depositional faults were thought to be related to the thickening of lava units seen in the Pretoria Group succession and no evidence of faulting was related to this volcanism. The relative absence of pyroclastic materials suggested a quiet extrusive fissure eruption supported by a dominant thermal subsidence relative to the mechanical subsidence during the deposition of the Hekpoort Formation. In addition, the Pretoria Group sedimentation was succeeded by the vast Rooiberg Group felsic lava eruption, which is suggested to have resulted in rapid uplift and tectonic instability during the immature feldspathic deposition of the post Magaliesberg units. This event was caused by rapid thermal doming of the Rooiberg magmas erupting through the crust (Eriksson et al., 1995). The Transvaal Basin was intruded by the Bushveld Igneous Complex, at about 2.06 Ga, which to a limited extent, caused classical contact metamorphism by forming hornfels in fine siliciclastic rocks (Martini et al., 1995).

5.4. Hydrogeological potential and its structural implications

The groundwater movement in the area is mostly controlled by geological structures (faults, fractures, fissures, joints and shear zones), and magmatic intrusions such as dykes and sills. The groundwater is stored in either confined or

unconfined aquifers whose storage capacity and permeability depends on the geological formation. Rainwater and significant underground water flow (demonstrated by high-yielding springs at low surface elevation) recharge the aquifers, while the geological structures control the water migration and drainage pathways. Hence, the aquifer characteristics in the Black Reef Formation are determined mainly by the direction of groundwater movement between the formation and the overlying dolostone of the Malmani Subgroup of the Chuniespoort Group (Figure 5.3). The groundwater gradient tends to be steeper in the quartzite then the dolostone, owing to the poor transmissive characteristics of the quartzite rock (Barnard, 2000).

The dolostone of the Malmani Subgroup represents one of the most significant sources of groundwater in South Africa due to the high storage capacity of the aquifer formations, which alternate between chert-rich and chert-poor (Barnard, 2000). These aquifers within the dolostone formation are named karst aquifers, compartmentalised in the region by dykes and sills (Figure 5.3). The karst systems are produced by secondary porosities that were generated during the dolomitisation process of carbonate rocks (limestone), further enhanced largely by carbonic acid or acidic rainwater infiltration and migration through planes of weakness such as bedding planes, fractures, joints and fault-related structures. These dissolved carbonate minerals are moved away in solution, resulting in the formation of cavities in the subsurface. Gradually, residual permeable deposits such as wads, silica, iron and manganese oxides filled these cavities leading to subsidence and sinkholes.

The chemical weathering and dissolution processes in the dolostone formation are known as karstification, which provides the major aquifer characteristic of the Chuniespoort Group (Barnard, 2000; Altchenko et al., 2017). The weathering, and high storage capacity and permeability of the formation aquifer is controlled lithostratigraphically. Therefore, it is composed of an extensive cover of residual debris underlain by heterogeneous karstified dolostone aquifer (Barnard, 2000). Fractures, faults and weathered shear zones and bedding planes extend to a considerable depth in non-karstified dolostone in the study area.

The Pretoria Group aquifers favour weathered shale, brecciated or jointed zones, especially the contact zone between the intrusive diabase sheets and shales. The water-bearing properties of the shale formations in Timeball Hill, Rooihoogte and Silverton formations are more favourable than those of the quartzites due to their considerable susceptibility to weathering. The aquifer in the Hekpoort Formation is associated with the weathered region of andesitic rock along the adjacent overlying and underlying shale formation contacts and in the vicinity of fractures, faults and jointed planes. Generally, intrusive dykes and sills provide low permeability and impermeable rocks that serve as barriers to the fluid migration.

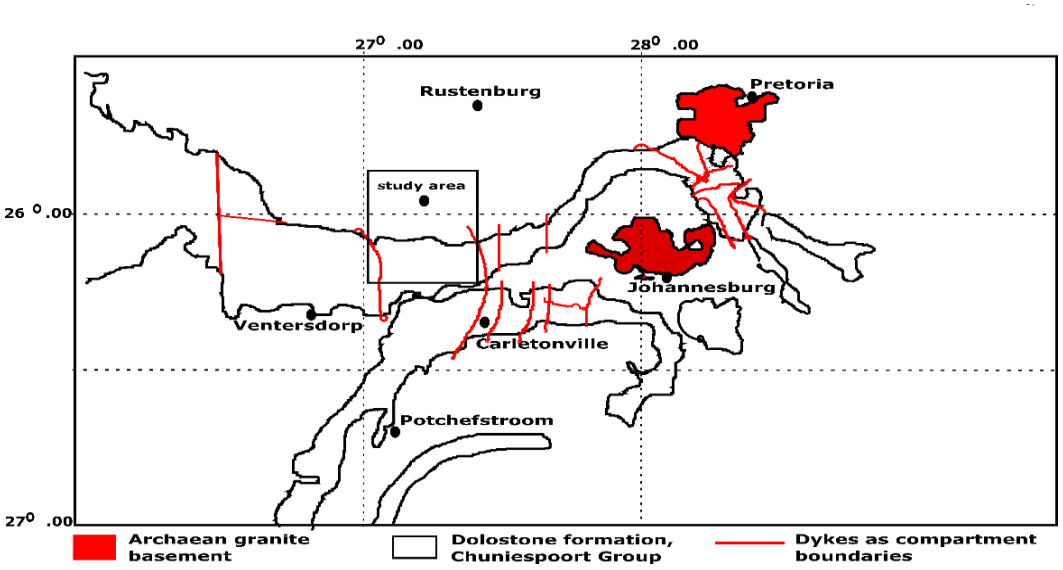


Figure 5.3: A map showing the dolostone formation of the Chuniespoort Group, and compartments created by dyke intrusions and the study area location (modified after Barnard, 2000).

5.5. Engineering implications and mineral potential of Transvaal Basin

Sinkholes and subsidence caused by the dissolution of dolostone pose a danger to infrastructures. Moreover, the expansive characteristic of Silverton shale and collapsible characteristics of residual Magaliesberg quartzites also raise a significant concern for road construction.

The economic potential of Transvaal Basin includes significant gold mineralisation in the Black Reef Formation, limestone and dolostone aggregates

of the Chuniespoort Group, and iron and manganese (80% of world reserve) in the Pretoria Group.

5.6. Methodology

5.6.1. Reflection seismics

Reflection seismic methods provide a high-resolution image of the subsurface and information about the physical properties of rocks (density and seismic velocity). Like any other geophysical methods, reflection seismics has its limitations and advantages. The ability to resolve subtle geological structures and thin layers depend on the dominant frequency and wavelength, the acquisition geometry and the signal-to-noise ratio of the field data. The acquisition and processing depend on the geological properties and target structures, and site conditions. The 2D reflection seismic data are quite challenging to interpret, especially in geologically complex terrains, and when the data were acquired along crooked lines. Furthermore, the ability of an interface to generate a clear reflection event depends on the reflection coefficient (Rc), which is governed by the acoustic impedance (Z) contrast. A general rule of thumb is that, for a geological boundary to produce a significant reflection, the reflection coefficient should be at least 6% ($Rc \geq 0.06$) (Yilmaz, 2001; Salisbury et al., 2003).

5.6.1.1. Data acquisition, processing and analysis

In the 1980s, the South Africa mining industries opened new frontiers in gold mineral exploration by using the reflection seismic to map the continuity of the gold-bearing reefs and structures of the Witwatersrand Supergroup, as well as exploring for extensions of the Witwatersrand Basin in South Africa and Botswana. The 2D reflection seismic lines used in this study were among ~ 16000 line-km of 2D reflection seismic data acquired during the project (Kostlin et al., 2015).

The reflection seismic data were acquired and processed by the Anglo American, Geophysics Department, between 1987 – 1988 (Pretorius et al., 1994; Pretorius et al., 2003). The data were collected with a SERCEL SN368-CS2502 instrument

using 120 channels of active geophones (SM4 10 Hz) with 50 m shot and receiver station interval. Table 5.1 summarises the acquisition parameters. The location of the lines is shown in the Figure 5.1a. The sampling interval of 4 ms and listening time of 6s were enough to map the entire Transvaal Supergroup overlying the older rock formations. A field pre-processing anti-aliasing filter with a low-cut frequency of 8 Hz at 12 dB/oct and 62.5 Hz at 72 dB/oct high-cut frequency resulted in a dominant frequency of 35 – 65 Hz.

Table 5.1: Seismic data acquisition parameters.

Item	Parameters						
Line	OK-200	OK-206	OK-207	OK-208	OK-209	OK-210	OK-211
Line azimuth	SW-NE	NW-NE	NW-SE	NW-SE	SE-NW	S-N	W-E
Profile length (~km)	24	34	23	33	11.5	26	39
Instrument	SERCEL SN368, CS52502						
Geophone	SM4-10 Hz						
Source	4 vibroseis truck in single file, 12.5 m spacing, 1.56 move-up						
Vertical stack	8 upsweeps, 18s long with 0.5 Cos taper (with frequency of 8 – 60 Hz)						
Numbers of channel	120						
Receiver spacing (m)	50						
Source spacing (m)	50						
Listening/Recording length(s)	6/24						
Sampling interval (ms)	4						
Max CMP fold	60						
File format	SEG-D						
Polarity	SEG						
Pre-amp gain	2^7						

All the datasets passed through the same standard processing workflow, which includes field pre-processing to post-stack time migration. The main processing steps were geometry correction, trace editing, amplitude normalization, minimum phase conversion of the data, linear denoising, first-break picking, refraction static, elevation and residual static corrections, velocity analysis, muting, Normal-Moveout Correction (NMO), Dip-Moveout Correction (DMO) and stacking. Post-stack processing steps included deconvolution, amplitude recovery, and Kirchhoff time migration (Kostlin et al., 2015; Pretorius et al., 1994; Pretorius et al., 2003).

The elevation was corrected to a 1400 m datum. A refraction seismic survey was conducted independently along each profile to obtain an adequate estimate of the depth and velocity of the overburden and weathered zone. The overburden, weathered and fresh bedrock velocities vary from 350 – 1100 m/s, 1500 – 3500 m/s and 5000 – 7000 m/s, respectively. The average overburden thickness varies between 5 and 15 m. Average velocities of ~600 m/s and ~5500 were estimated for the overburden and the refractor units, respectively and this was used to make static correction. The literature review from the History of Geophysics in South Africa reviewed by De Beer in 2015 (Durrheim, 2015, pp. 237 – 245; Kostlin et al., 2015, pp. 388 – 411 and De Wet 2015, pp. 423 - 436), Campbell (2011) and Molezzi et al. (2019) stated that the average velocities of the various bedrock units in the investigated area range from 5500 – 6800 m/s as determined using vertical seismic profiling (VSP), which correlate reasonably with the velocities obtained using refraction seismic during the data acquisition (Pretorius et al., 2003; Molezzi et al., 2019). More details on the seismic design, acquisition and processing parameters applied on these 2D seismic profiles are published by Pretorius et al. (1994) and (2003).

The vertical resolution of the data can be estimated using the 1/4 wavelength criterion (Widess, 1973). Based on the average velocity (V_a) range within the bedrock (2500 – 6800 m/s) and dominant frequency (F_D) of 40 Hz, the resolvable thickness will approximately range from 15 – 42 m (the dominant wavelength (λ_D) = V_a/ F_D). Moreover, the application of the reflection seismic method to the exploration of a hard rock environment was traditionally limited to mapping large-scale geological features with vertical and horizontal resolution greater than 25m and 100 m, respectively. However, many researchers have adopted newer and more advanced post-processing techniques and high-density acquisition geometries to improve the resolution of subtle geological structures (to less than ~10 m) (Manzi et al., 2012a and b; Manzi et al., 2014; Scheiber-Enslin and Manzi, 2018). The Transvaal rocks show small velocity changes between successive formations, owing to extensive compaction and metamorphism. Therefore, the reflections from the interfaces between various units (dolostone, shalestone, quartzite, mudstone, andesite and diabase sills) are due to density contrasts rather

than velocity contrasts (Campbell, 2011; De Beer, 2015 (Durrheim, 2015, pp. 237 – 245; Kostlin et al., 2015, pp. 388 – 411 and De Wet 2015, pp. 423 - 436); Molezzi et al., 2019).

5.6.2. Magnetic

To adequately interpret and understand the surface-subsurface geology of the study area, we combined aeromagnetic data with the reflection seismic data (Figure 5.4). The aeromagnetic data were acquired with ~1 km line spacing, 100 - 150 m flight height and a sampling interval of ~60 m by Council for Geoscience, South Africa (Campbell, 2011; Stettler et al., 1999).

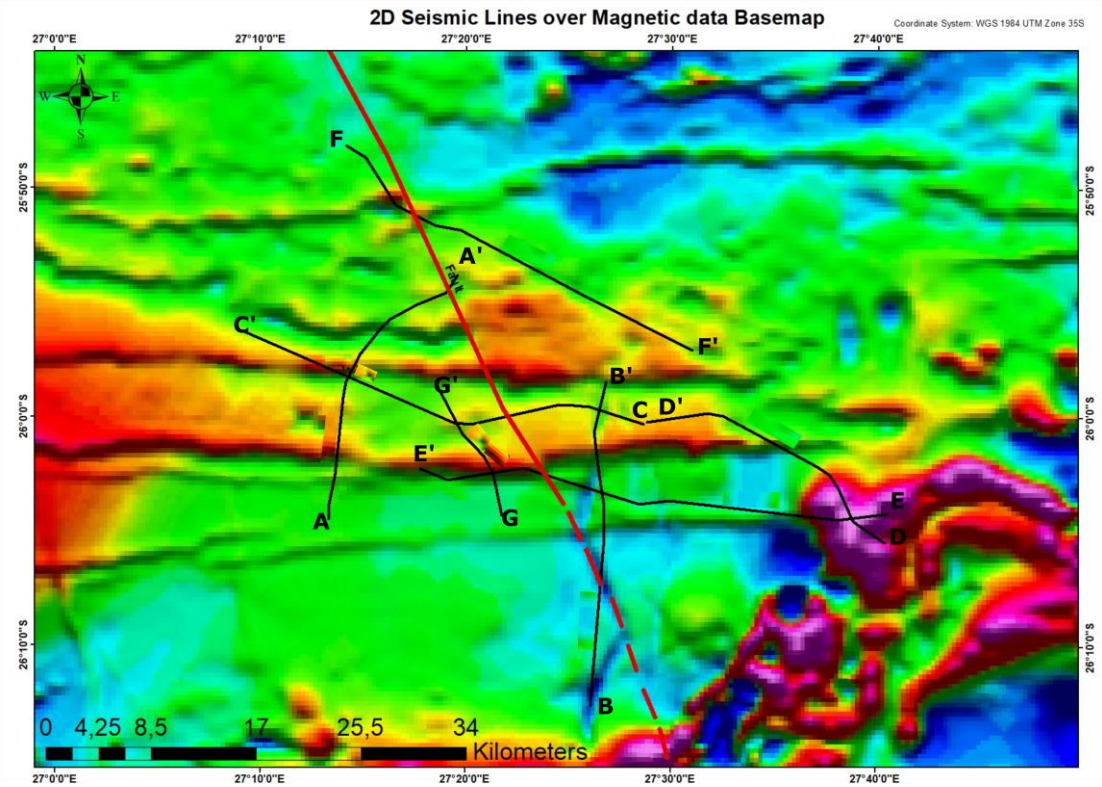


Figure 5.4: Total magnetic intensity (TMI) map and superimposed position of the seismic lines.

5.7. Results

5.7.1. Seismic reflection denoising

The reflection seismic data (Figure 5.5a and Figure 5.6a) was denoised using the post-stack curvelet transform (Shukla et al., 2014; von Ketelhodt et al., 2019) and

2D structurally-oriented dip filter (Dug-Insight-4.5, 2018b) to enhance major and subtle structures, as well as the interface boundaries.

Curvelet transformation removes noise while preserving the edges of the geological structures. It uses a multiscale and geometrical analysis of the spectrum to achieve the optimal rate of convergence by simple thresholding (Figure 5.5b and Figure 5.6b). The curvelet transformation removed the random seismic noise, but also introduced a significant coherent linear noise in the data, which could be misinterpreted as geological features if not carefully considered.

The Structurally-Oriented Filter (SOF) smooths along structural planes as defined by a dip field. It is an effective technique to remove incoherent noise and improve the continuity of the reflected events without flattening across dipping planes (Dug-Insight, 2018a) (Figure 5.5c and Figure 5.6c). The SOF also minimised the random noise in the reflection seismic section without introducing linear noise that seem like subsurface structures, and generally improved the detectability of the smaller features. In this study, the SOF provides better result of the reflection seismic image and was further used for the interpretation.

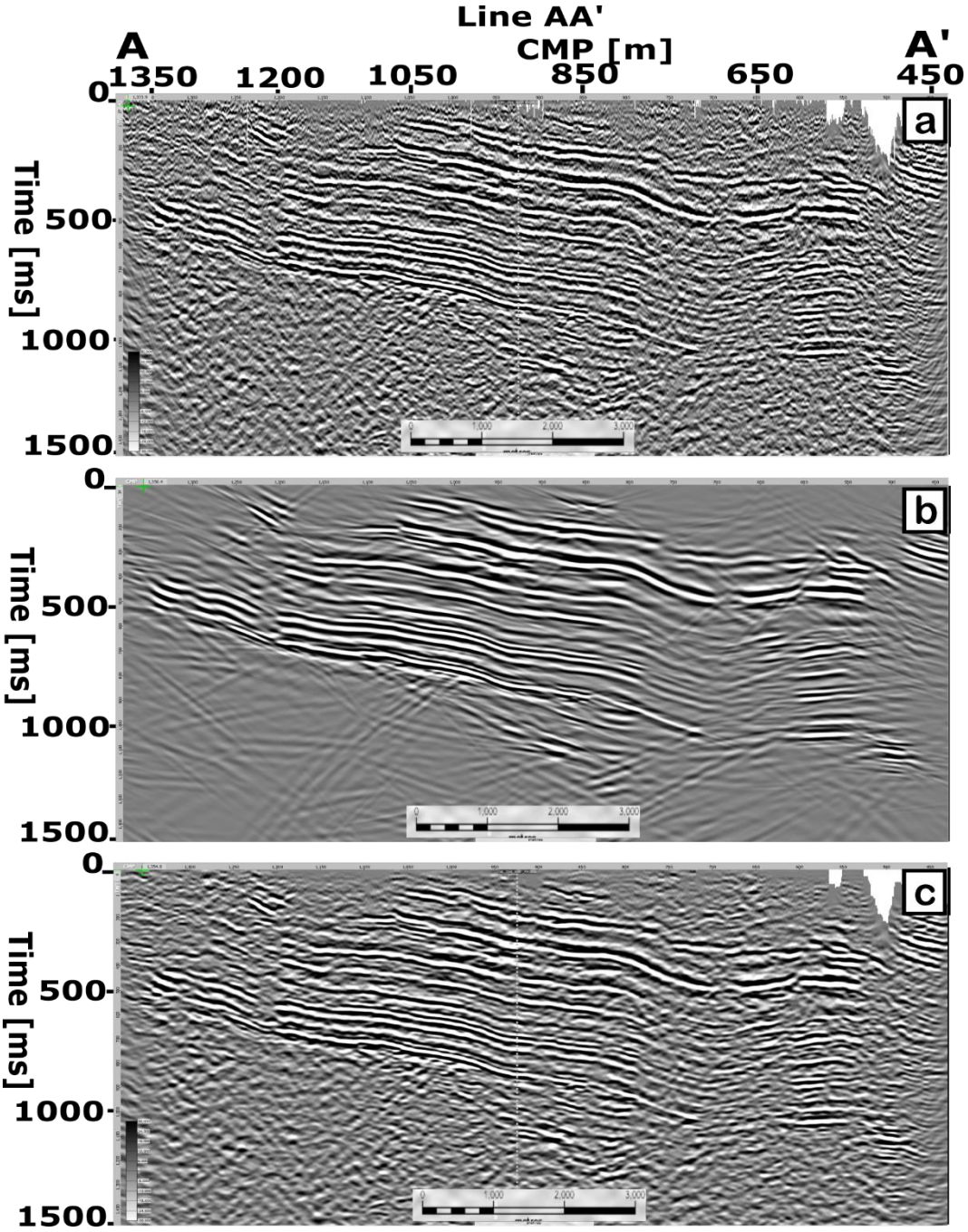


Figure 5.5: Application of post-processing filters to seismic line AA' (a) Undenoised migrated data and (b) Denoised data after application of curvelet transformation and (c) Denoised data after application of structurally-oriented dip filter. Note 1000 ms TWT ~ 3000 m, using an average bedrock velocity of 6000 m/s.

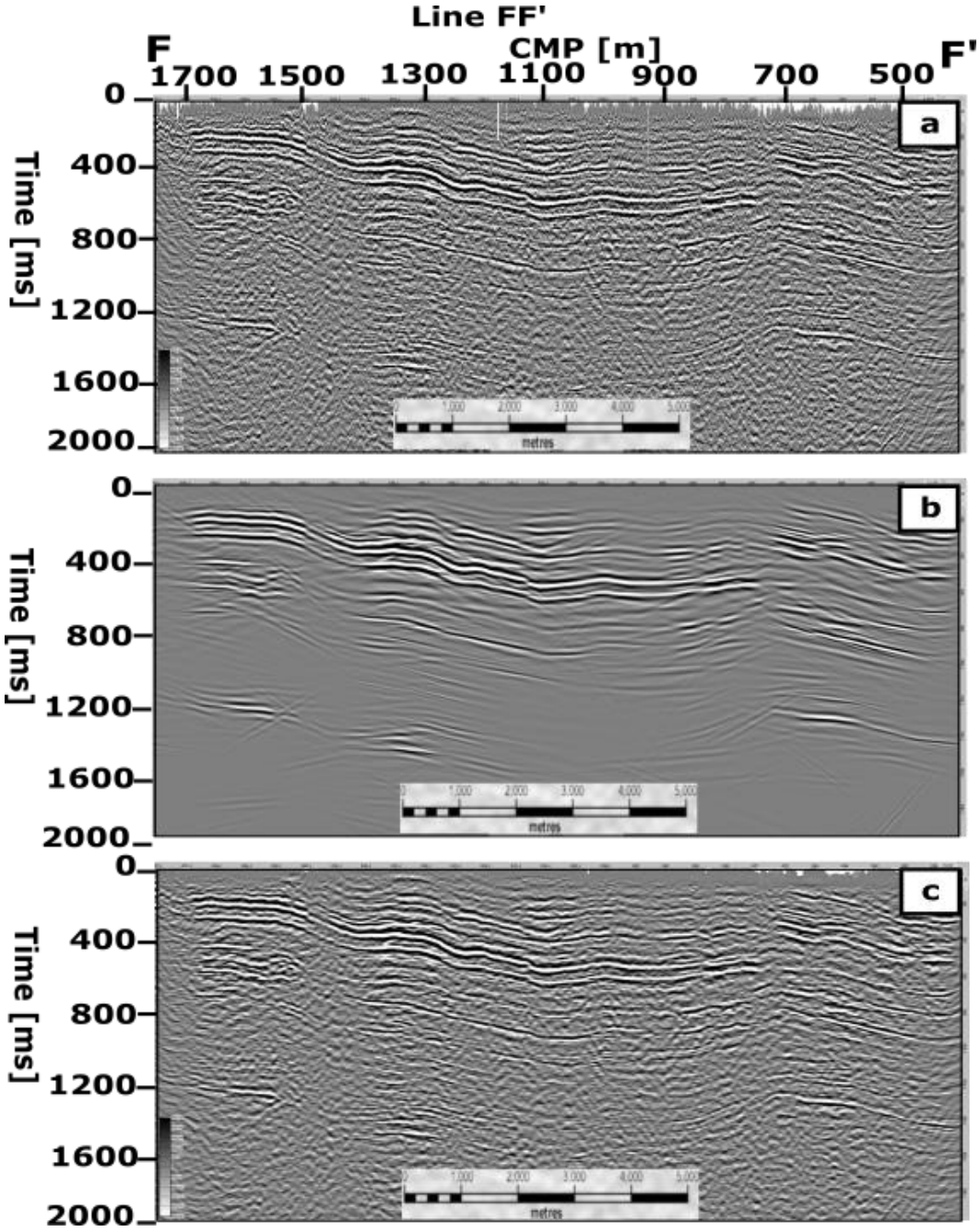


Figure 5.6: Application of post-processing filters to seismic line FF' (a) Undenoised migrated data and (b) Denoised data after application of curvelet transformation and (c) Denoised data after application of structurally-oriented dip filter. Note 1000 ms TWT ~ 3000 m, using an average bedrock velocity of 6000 m/s.

5.7.2. Tilt and gradient of the magnetic field

The tilt and first vertical derivative maps (Cooper and Cowan, 2008) were calculated from the total magnetic field data (Figure 5.7a and b). Derivatives tend to sharpen the edges of geological anomalies and enhance shallow features while tilt determines the boundary of the source anomalies, it can also resolve deep and shallow sources (Cooper and Cowan, 2008). The filtered total magnetic field intensity (TMI) data enable more detailed mapping of structural features compared to surface geological mapping.

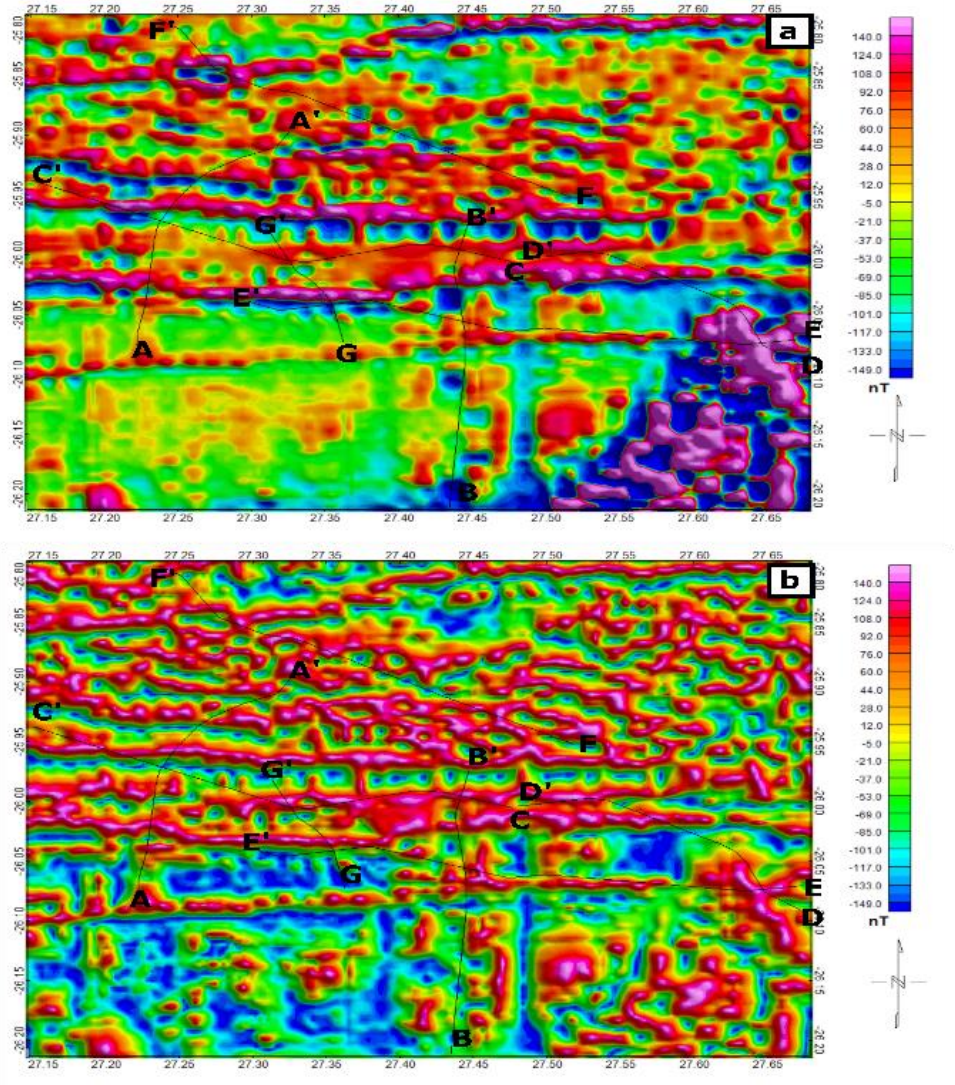


Figure 5.7: Magnetic field after calculating (a) Vertical and (b) Tilt derivative Seismic lines are superimposed on the maps.

5.8. Interpretations

5.8.1. Magnetic

The aeromagnetic data enable broad-scale geological interpretation of the survey area. Figure 5.8 shows the interpretation based on the first vertical derivative of TMI. The short-wavelength anomalies in the area towards the southeast quadrant are caused by strongly magnetic rocks in the Archaean granitic-greenstone basement (AGB) and the west-east trending lineaments are interpreted as dykes. Dykes and sills have been interpreted as pre- and syn-Bushveld intrusions (Cawthorn et al., 1981 and Campbell, 2011). The long-wavelength anomalies in the map are caused by sediment-fills, palaeo-karst system, slump-filled features (PKF), faults, fractured and weathered zones along the dyke lineaments. The feature ECCG in Figure 5.8 is interpreted as contact between the Chuniespoort Group with the AGB and Black Reef Formation, a potential water storage region.

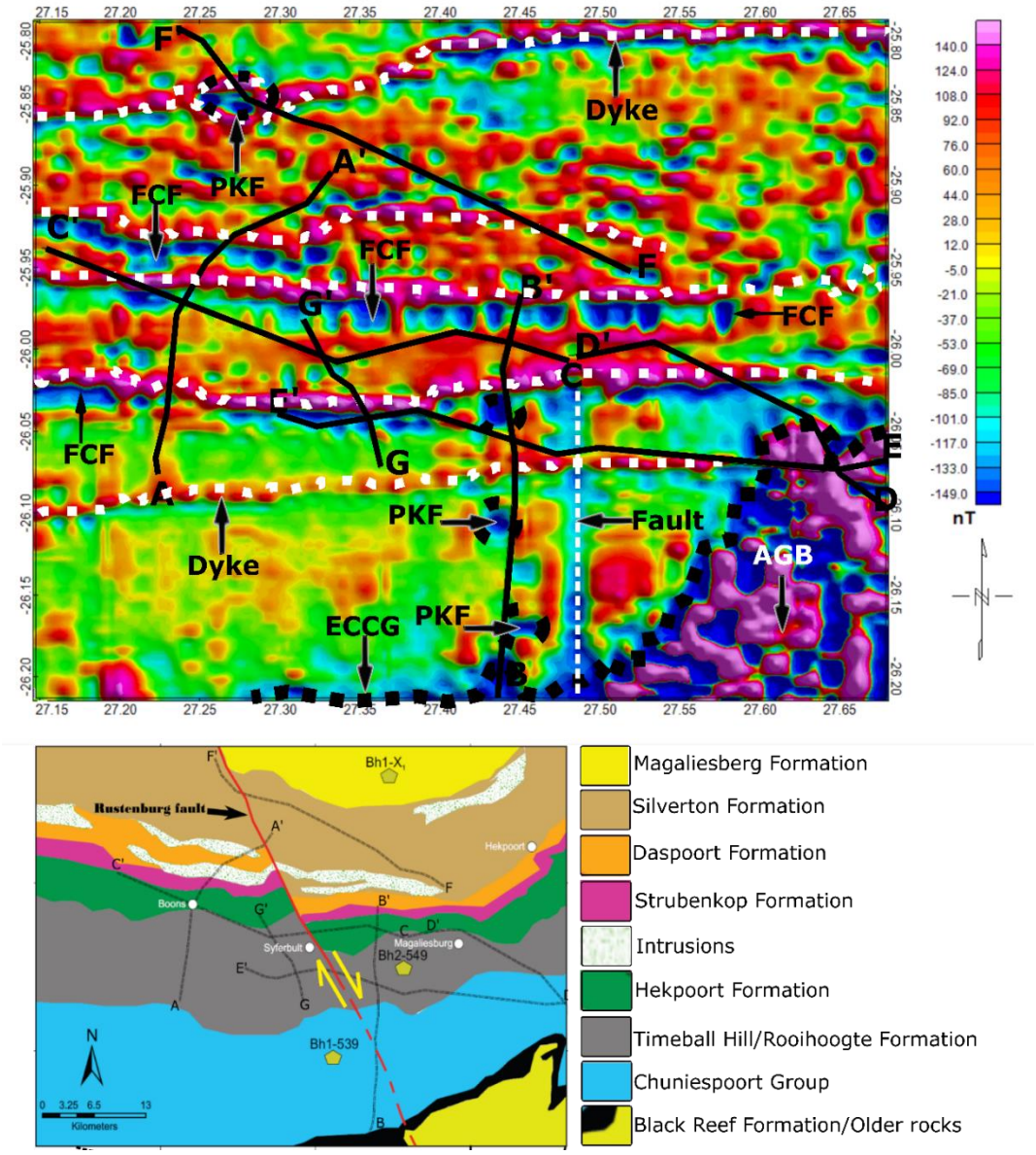


Figure 5.8: Interpreted first vertical derivative of the magnetic field anomalies map and superimposed seismic lines and geological map of the study area. FCF – fractured contact features, PKF – possible karst features, ECCG – Erosional contact along CG boundaries (in this map the weathered/fracture interface is with Black Reef formation and Archaean granite), AGB – Archaean Granite Basement. The dashed white lines show the west–east dyke lineaments. The dashed red line section of the RF shows probable extension of the fault at depth.

5.8.2. 2D seismic reflection interpretation

The interpretation was made based on the seismic reflection character seen on the seismic sections (Figure 5.9 - Figure 5.14). The main objective of using the 2D seismic section was to delineate and characterise the lithostratigraphic continuities and structural features such as faults, joint contacts and fracture zones, which are critical for hydrogeological prospecting and geotechnical planning. DUG Insight software (v.4.5, 2018) was used for seismic visualisation, interpretation and analysis. Geological structures such as faults and fractures were recognised as an offset in the reflection coherency/continuity and chaotic/diffuse reflection characteristic, respectively. The delineated geological structures were identified and interpreted based on known geology and previous research (Eriksson et al., 1995; Bumby, 1998; Basson, 2019). A combination of both the surface geology and borehole logs extracted from the Council for Geosciences, South Africa database and published research papers (Eriksson and Reczko, 1995, Catuneanu and Eriksson, 1999; Eriksson et al., 2001; Basson, 2019) were used to constrain the delineated geological horizons.

The seismic sections shown in Figure 5.9 and Figure 5.10 are characterised by strong seismic reflections from ~ 100 m to 6 km depth due to appreciable acoustic impedance contrasts at the geological boundaries. A constant velocity of 6000 m/s was used to do the time-depth conversion. The main lithostratigraphic units mapped in the seismic reflection sections are the Chuniespoort and Pretoria Groups of the Transvaal Basin. The prominent reflectors are the unconformable erosional karst interface between the Malmani dolostone formation of the Chuniespoort Group and the basal shale and conglomerate formation of the Timeball Hill/ Rooihoogte Formation of the Pretoria Group (H2), the boundary between siliciclastic rock of the Timeball Hill and Hekpoort andesite Formation (H3). Other noticeable reflection events are the interface between the Hekpoort Formation and clastic sediments of the Strubenkop Formation (H4), the Strubenkop and Daspoort interface (H5), and the Silverton shale and Daspoort sandstone formation boundary (H6). Other reflection events are interbedded shale and quartzite layers within the Timeball Hill and Silverton Formation. The

interface between the Chuniespoort and the underlying Black Reef Formation and older rock formations (H1) delineated on the seismic sections was poorly constrained due to lack of clear reflection coherency within the contact zone and ground truth evidence (Figure 5.9 and Figure 5.10).

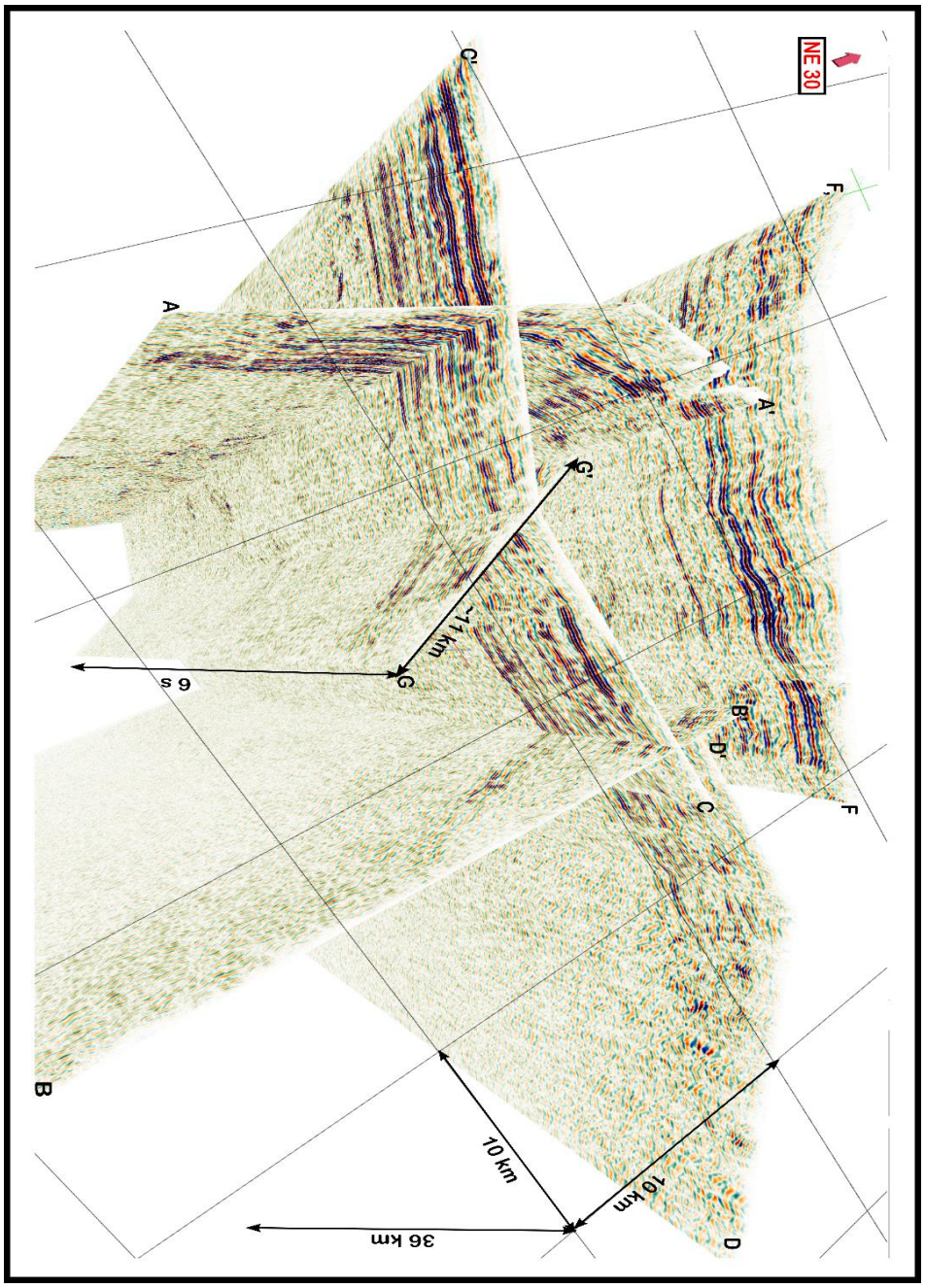


Figure 5.9: Uninterpreted 3D visualization of the 2D seismic section looking 30^0 northeast, plunging southwest for better orientation view. The faded black lines are XY grid in UTM coordinate system.

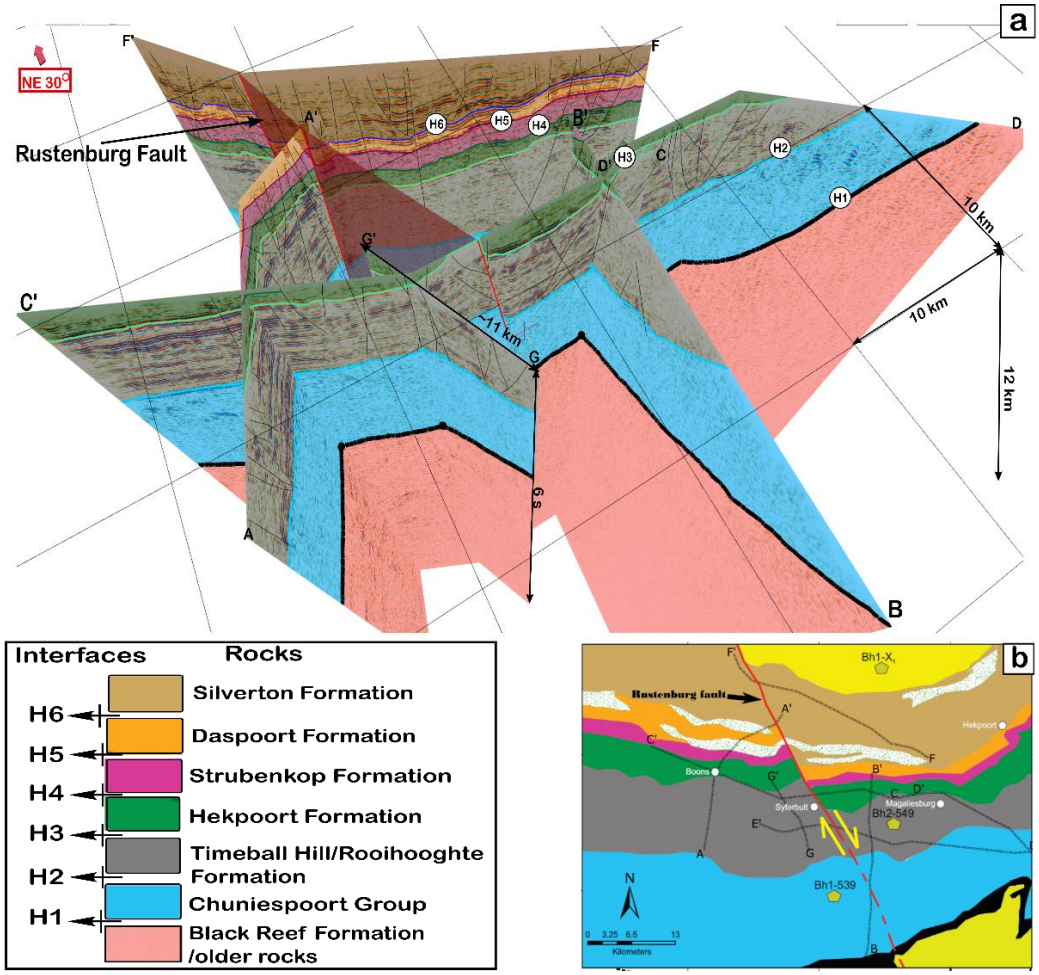


Figure 5.10: (a) interpreted 3D visualization of the 2D seismic section looking 30° northwest, plunging southwest for better orientation view, showing the imaged geological structures and mapped Rustenburg fault plane. (b) imbedded geological map that was used to constrain the interpretations. The faded black lines are XY grid in UTM coordinate system. The dashed red line section of the RF shows probable extension of the fault. This figure is vertically exaggerated.

Further interpretation of the seismic sections were given based on the structural features observed on the NW-trending upthrown block and SE-trending downthrow block of the Rustenburg Fault (RF) (Figure 5.10).

5.8.2.1. Delineated geological features

The NNW-trending Rustenburg Fault (RF) is a major fault in the area (Bumby et al., 1998; Basson, 2019). This fault was previously reported by Bumby et al. (1998) and Basson (2019) as a right-lateral fault with surface displacement of

about 10 km. In the study area, this fault intersected three seismic sections (profile AA', CC' and FF') out of seven sections used in this study (Figure 5.9 - Figure 5.14). The RF crosscuts line FF' across CMP-728; the fault plane is subvertical on this profile and dips ~ 5^0 SE. Its exhibits minor reverse dip of ~5^0 NW across profile AA' at CMP-500 and dip ~60^0 SE across CMP- 1317 – 1380 on line CC' (Figure 5.11).

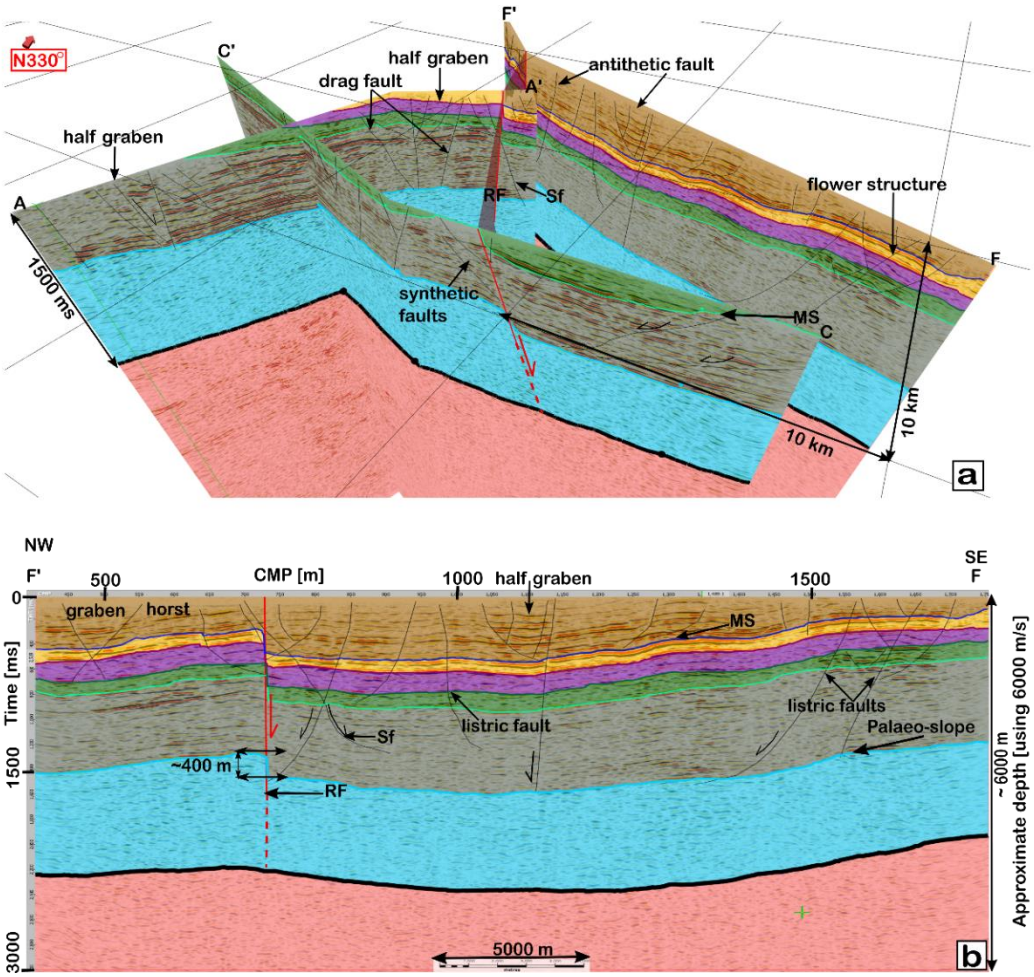


Figure 5.11: Structural interpretations across profile AA', CC' and FF' highlighting some geological features on the downthrow block of the Rustenburg fault (RF). (a) Interpreted 3D view of the three seismic sections, looking 30^0 northeast, plunging southeast for adequate orientation view (b) 2D presentation of interpreted profile FF' for better clarity of the mapped structures. Note: Sf – sigmoidal listric fault and MS – monoclinal structure. The dashed red line section of the RF shows probable extension of the fault at depth.

The seismic sections revealed new details of the RF (Figure 5.10 - Figure 5.14). The fault-throw is ~ 400 m, while the lateral displacement of contacts on the surface geological map is ~5 km, calculated across the Timeball Hill/Rooihoogte, Hekpoort, Strubenkop and Daspoort formations (Figure 5.10 and Figure 5.11). The RF clearly offsets the entire Pretoria Group, indicating that activity continued into post-Pretoria Group times. The extension of the fault into the Malmani Formation dolostones cannot be seen because of its transparent reflection character (Figure 5.12). Multiple subordinate antithetic and synthetic faults are associated with the RF. A rollover anticlinal structure is apparent on the footwall-side of the fault, and a synclinal feature (relative to the regional palaeo slope) is apparent on the hangingwall-side (Figure 5.11 and Figure 5.13). A sigmoidal-shaped fault that forms a conjugate structure with the RF is imaged on lines AA' and FF' (Figure 5.11b and Figure 5.13b).

Fractures and weathered zones can be detected within the seismic data as they result in scattering of the acoustic energy resulting diffuse portions of the reflectors. The fault zone on the seismic section exhibits a heterogenous fractured pattern and ductile-brittle shear deformation, a potential zone for hydrogeological prospecting (Gibson et al., 1999) (Figure 5.13).

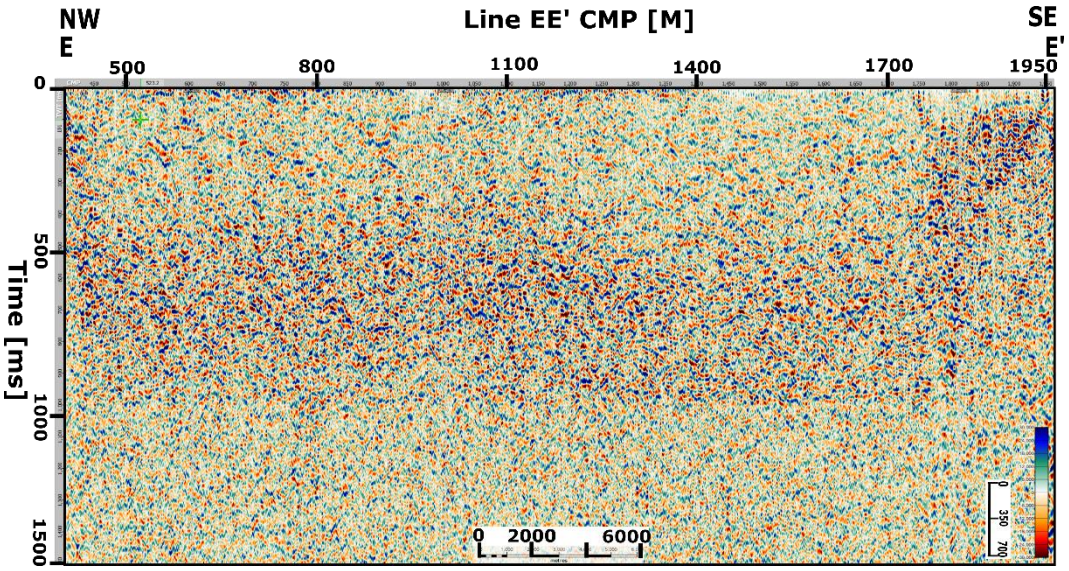


Figure 5.12: Reflection seismic section across line EE' showing the unreflective, scattering and dispersive characteristic of a seismic survey on the dolostone formation of the Chuniespoort Group.

Moreover, the downthrow block of the RF, revealed a macroscopic monoclinal structure (MS) across the Pretoria Group formations. This structure, is distinct on profile CC' and FF' (Figure 5.10 and Figure 5.11). The MS exhibits undulated, faulted, gentle NW-dipping horizons, that trend ~ 30° NW along the seismic sections (CC', DD' and FF') (Figure 5.11 and Figure 5.13). The age of the deformation could be constrained to post-Pretoria Group. The fault systems on this block consist of NW and SE-trending listric and planar normal faults, associated with minor synthetic and antithetic faults. These minor faults form a distinct flower-like structure and half grabens on the hangingwall (Figure 5.13). Across profile BB', the normal faults form a system of en-echelon faults (Figure 5.14). The unreflecting part of the Timeball Hill/ Rooihoogte formation across CMP 850 – 1300 (BB') is attributed to a combined fracture and faulted system initiated by dykes and sills emplacement as clearly shown on the magnetic map at the same position (Figure 5.8).

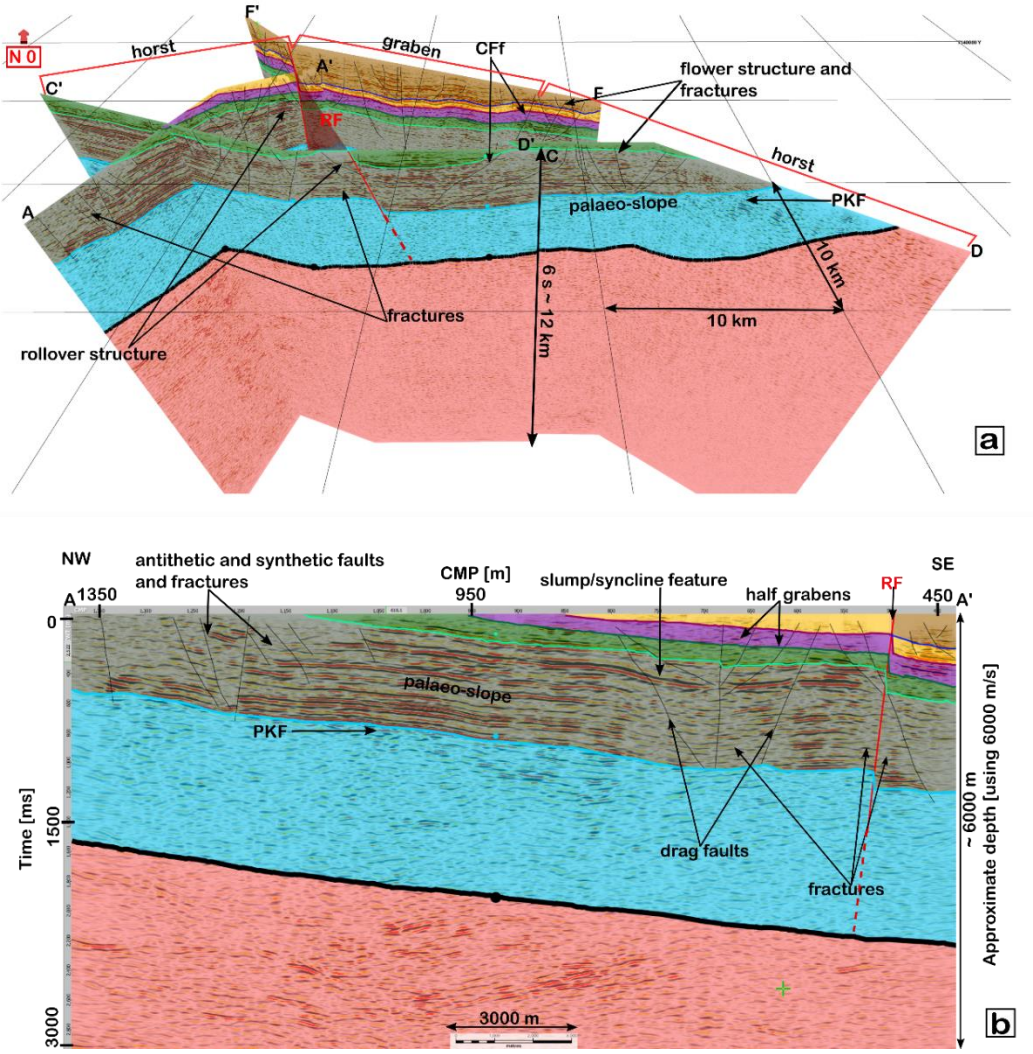


Figure 5.13: Interpreted seismic sections across profile AA', CC', DD' and FF' highlighting structural features on the upthrown block of the RF. (a) presentation of the interpreted 3D view of the seismic section trending-north, plunging southward. (b) 2D presentation of the interpreted profile AA' for better clarity. Note: CFf – listric fault feature cutting across line CC' and FF', PKF – possible karst feature. The dashed red line section of the RF shows probable extension of the fault at depth.

Furthermore, a localised depression/slump feature, is seismically imaged across line AA' and CC'. It is well defined on profile AA' on the upthrown block of the RF (Figure 5.13 and Figure 5.14). The length of this feature is ~5 km. It is bounded by drag faults and centred on a normal fault with subordinate antithetic and synthetic faults. The outer southeast section of the profile is crosscut and

offset by set of normal faults that formed half grabens across section AA' and GG' (Figure 5.13 and Figure 5.14). Several other offsets are mapped across the Pretoria Group and interpreted in the seismic sections.

When considered closely, the footwall of the RF seems like an uplifted block. However, in a regional scale view, it forms a horst and graben with the hangingwall block, bounded by RF, and CFf - towards the SE flank (Figure 5.13 and Figure 5.14). These structures exhibit an extensional tectonic deformation type, followed by fault-modulated subsidence. These structures can be interpreted as syn- to post-Pretoria Group deposition structures.

The chaotic to strong reflections observed at the unconformable interface between the chemical platform deposit of the Chuniespoort Group and the overlying siliciclastic sediments of the Pretoria Group are attributed to an erosional surface and palaeo-karst-filled sediments of the basal Rooihoogte Formation of the Pretoria Group.

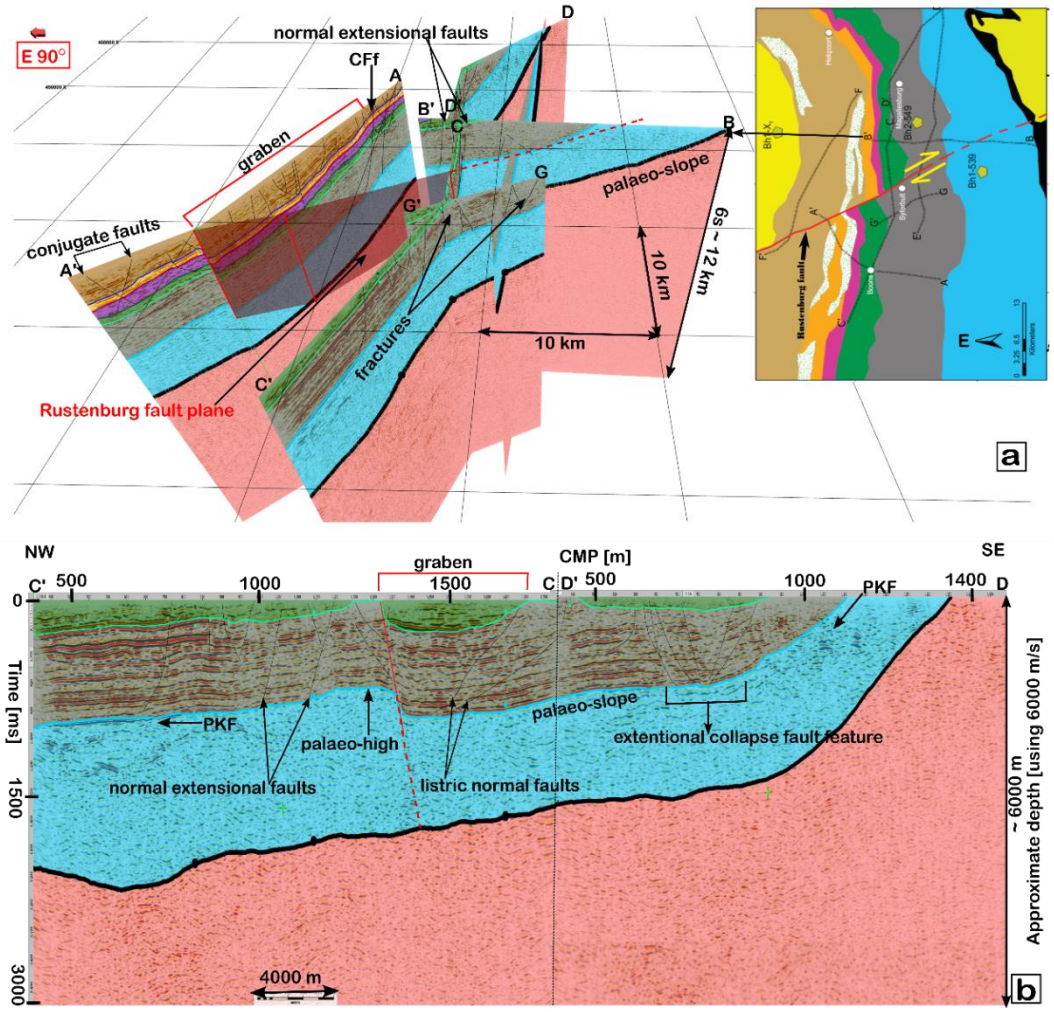


Figure 5.14: Interpreted seismic sections across profile BB' CC', DD', GG' and FF' highlighting the extensional faults and palaeo-slope features. (a) presentation of the interpreted 3D view of the seismic sections looking 90° east, plunging southwest. (b) 2D presentation of the interpreted profile CC' and DD' for better clarity. Note: CFf – listric fault cutting across line CC' and FF', PKF – possible karst feature. The dashed red line section of the RF shows probable extension of the fault at depth. The index map on the top-right is the geology of the study area.

5.9. Discussion

The Chuniespoort Group (CG) and Pretoria Group (PG) cover most of the surface in the study areas (Figure 5.1). Intrusive diabase dykes appear as east-west lineaments on the TMI map (Figure 5.4). The chemical platform deposit of the CG underlies the sedimentary succession of the PG. The deposition of the PG strata is attributed to two major rifting events (ca. 2.1 Ga) and subsequent thermal

subsidence caused by thermal cooling and densification of the lithosphere (Allen and Allen, 1990; Eriksson and Reczko, 1995; Catuneanu and Eriksson, 1999; Eriksson et al., 2006). The regional northwest-tilting of the Pretoria Group, as observed in the reflection seismic section, is attributed to the first stage of intracratonic rift-basin (Eriksson and Reczko, 1995) during the Pretoria Group deposition.

The NNW-trending Rustenburg fault (RF) is interpreted on the seismic sections as a normal planar fault, with the upthrown block to the west. The deformation mechanism of the RF and the reason for a thicker accumulation of the Magaliesberg Formation on the hangingwall side of the fault is contentious. Bumby et al. (1998) and Basson (2019) both describe the RF as a right-lateral fault. Basson (2019) attributes it to post-Bushveld Complex deformation (~1900-1700 Ma), while Bumby et al., (1998) and Bumby (1997) suggested syn-Pretoria Group and pre- to post-Bushveld deformation. Bumby et al. (1998) and Bumby (1997) propose that the faulting may have started during Pretoria Group deposition and been reactivated by NW-SE trending compressive stress field ($\boldsymbol{\sigma}_1$) (Hartzer 1995; Du Plessis and Walraven, 1995). This $\boldsymbol{\sigma}_1$ caused the NNW-trending lateral displacement of the RF. Hence, they proposed two phenomena that could have result in thicker Magaliesberg Formation towards the downthrow block; (a) creation of a second-order basin by syn-sedimentary normal faulting that formed the RF, with downthrown to east, causing deepening of the first-order sedimentary basin, or (b) thickening due to thrusting (by $\boldsymbol{\sigma}_1$), which could have cause the lateral displacement of the RF, seen on the surface geological map. Bumby et al. (1998) and Bumby (1997) later concluded that the second scenario is more feasible due to equal peak elevation of the Rustenburg Nature Reserve anticline and Olifantspoort anticline, positioned on the opposite ends of the RF. Eriksson and Reczko (1995) and Bumby et al. (1997) also reported that the Pretoria Group sediments in the vicinity of the RF were pre-susceptible to tectonic disturbance.

Seismic profiles AA', CC' and FF' reveals about 400 m vertical displacement across the RF and considerable changes in the thickness of strata (Figure 5.10,

Figure 5.13 and Figure 5.14). Simple kinematic modelling of fault movement and subsequent erosion (Figure 5.15) suggest that the displacement along the RF was not just simply strike-slip but has had a significant normal component. Peneplanation of shallowly-dipping faulted strata will create the appearance of such strike-slip movement (Figure 5.15c and Figure 5.16). Therefore, we interpret the RF to be a normal fault that was reactivated in a compressive stress field (which caused the bulk of the strike-slip displacement) (Hartzer 1995; Du Plessis and Walraven, 1995). This is in accord with the first scenario (involving syn-sedimentary normal faulting) proposed by Bumby (1997 and 1998) (Figure 5.10 and Figure 5.15).

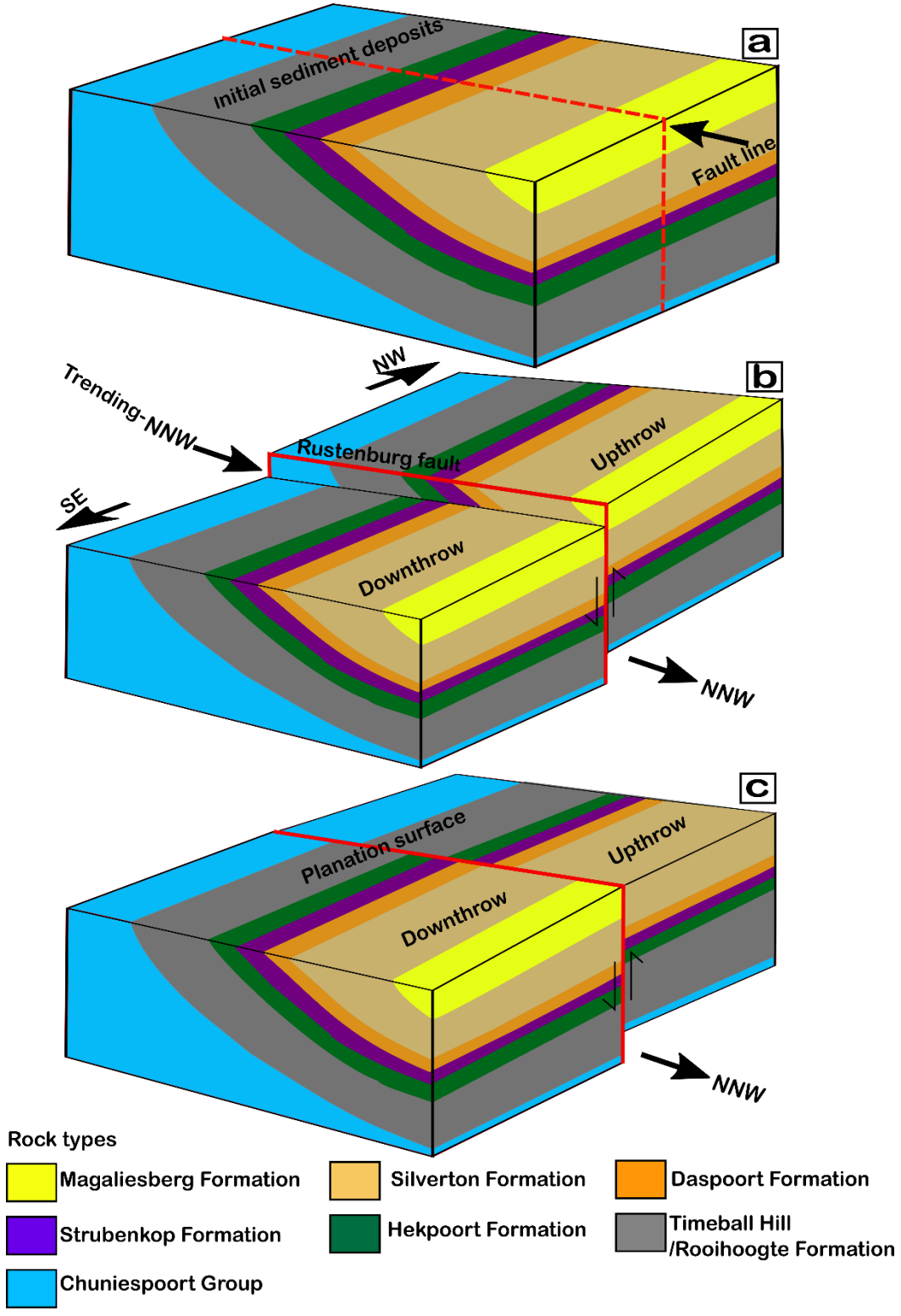


Figure 5.15: 3D modelling of the Rustenburg fault (RF) to demonstrate the normal displacement and strike-slip surface appearance (a) Assumed initial sediment deposits (b) Development of the NNW-trending normal displacement (c) Eventual surface peneplanation within the fault zone.

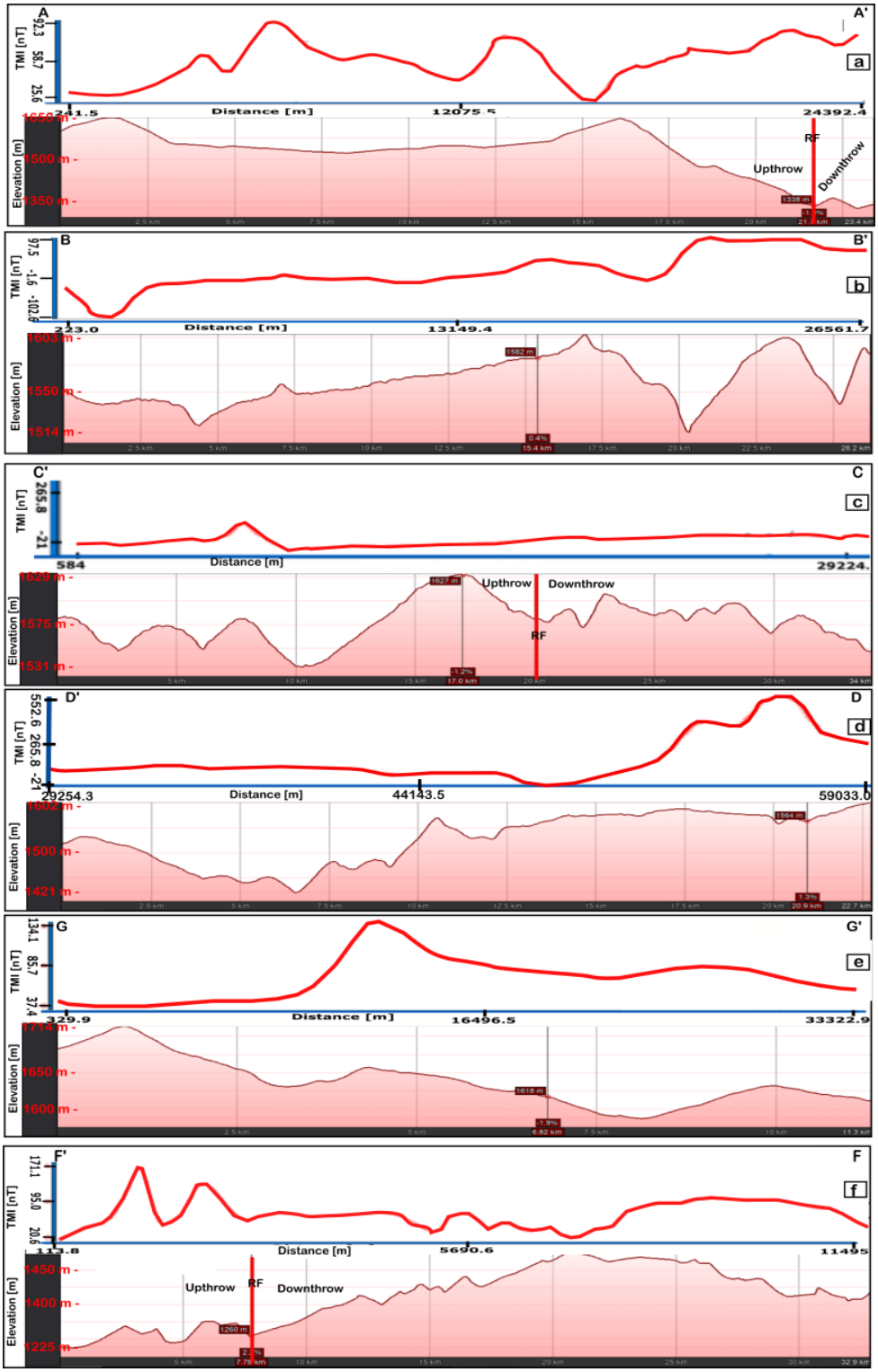


Figure 5.16: Magnetic intensity profiles and surface elevations across the seismic sections showing uneven topography due to erosion (a) Line AA' (b) BB' (c) CC (d) DD' (e) GG' and (f) FF' (The elevation information was sourced from Google Earth Pro @ 2018 Google Image Landsat/Copernicus).

Furthermore, the total thickness of the Pretoria Group formations in the downthrown and upthrown blocks were similar, about 3 km. The downthrown block has a thicker Hekpoort andesite unit. This could suggest an intracratonic sag-basin due to localised subsidence. The outcropping Silverton Formation (across profile AA', CC' and FF') about 100 m thicker on the downthrown side of the RF. This could be due to deposition on the downthrown side of the RF during the subsidence, or subsequent erosion of the upthrown block.

The units within the PG are characterised by planar normal faults that form a series of en-echelon fault, drag fault, and horst and graben structures. Smaller antithetic and synthetic fault structures were observed mainly on the Hekpoort, Strubenkop, Daspoort and Silverton formations. These complex deformation structures that formed a breakaway planar normal fault system as discerned on the seismic sections confirmed that the sediments were initially deposited under an extensional tectonic environment accompanied by fault-modulated subsidence. These assertions support the tectonic model by Eriksson and Reczko (1995), Catuneanu and Eriksson (1999) and Eriksson et al. (2001) in the area. Besides, it is apparent that some of these faults are syn- and post-depositional Pretoria Group deformations, therefore supporting the hypothesis of Bumby et al., (1998). It is possible that the brittle deformed zones associated with the mapped seismic structures could probably contain more small-scale faults and fractures that are not possible to image seismically. It is also observed that dyke intrusions contributed to the heterogeneous fractures and minor fault systems in the area. These fault systems observed in the study area are related to the same kind of structures discussed in Basson (2019), Molezzi et al. (2019) and Manzi et al. (2018).

The geometry and placement of intrusive rocks were constrained using the magnetic profile along the seismic sections and TMI map of the area (Figure 5.16 and Figure 5.17). The regional TMI provides evidence for several EW-trending dykes. These intrusions exhibit high magnetic anomaly (Figure 5.8). Moreover, the sediment-filled regions, faults, fractured zones and probably palaeo-karst regions were seen on the filtered magnetic maps as negative field anomalies, and

as a flood channel and deformed zone on the Google Earth map (Figure 5.18). These features coincide with the delineated depressed sections, faults and fractured zones on the seismic lines.

5.10. Implications for hydrogeology and engineering

The regional palaeo-slope observed on the seismic sections provides indication of groundwater flow direction and monitoring in the area. The chaotic and diffuse reflection events, suspected to be an evidence of fractured, weathered and fault related deformations, are distinct on the seismic sections across the Pretoria Group formations. These zones of chaotic and diffused reflection are possible migration pathway where underground water movement and storage can take place due to high porosity and permeability of the zone (Figure 5.10). Weathered, fractured, and karst are general targets for hydrogeological prospecting for high yield groundwater boreholes (Barnard, 2000; Onyebueke et al., 2018). Faulted zones are concern to engineering structures.

The observed zones of diffuse reflection in the Timeball Hill Formation, Hekpoort and Silverton formations (Profile AA', CC' and FF') adjacent to the RF boundary are suspected to be weathered, fractured or faulted zones. These regions are potential targets for near-surface hydrogeological prospecting (Figure 5.17). The Daspoort sandstone and Silverton shale formations and the Chuniespoort Group dolostone are the most productive aquifer horizons in the area (Barnard, 2000). The groundwater in these region favours mostly the weathered, fractured, faulted and jointed zones, and the contact between the shale, sandstone, dykes and sills. These formations are observed across profile AA' and FF', where they are crosscut and offset by several fault and dyke lineaments (Figure 5.17b). The depth range of these formations across the profiles varied from 0 – 1800 m. The delineated slump features within the horizons are bounded by faults and fractured system, which can provide pathways for groundwater migration and have high storage potential.

The intrusive features in the study area were identified on the TMI map. Dykes and sills influence groundwater flow and storage pattern by providing

impermeable rock barriers that could impede further groundwater migration and consequently store water near the contacts (Figure 5.17). Another significance of these structures in the study area is the palaeo-compartments they create within the formations. These palaeo-partitions could improve the storage capacity of groundwater water within the compartments. Therefore, understanding and delineating the appropriate geometries and positions of these features will assist in estimating the hydrogeological characteristic of the aquifer horizon, and likely will reduce the cost of groundwater exploration by constraining the appropriate locations for drilling.

However, the expansive and characteristics of the weathered intrusive rocks provides concern for infrastructural planning and design. A thorough study of the fault system in the area can aid planning for infrastructural development. The information regarding the RF geometry will also provide information for further tectonic and geological model reconstruction in the area. Hence, the importance of using geophysical methods such as seismics and magnetics to locate drilling targets and obtaining subsurface images cannot be over-emphasised.

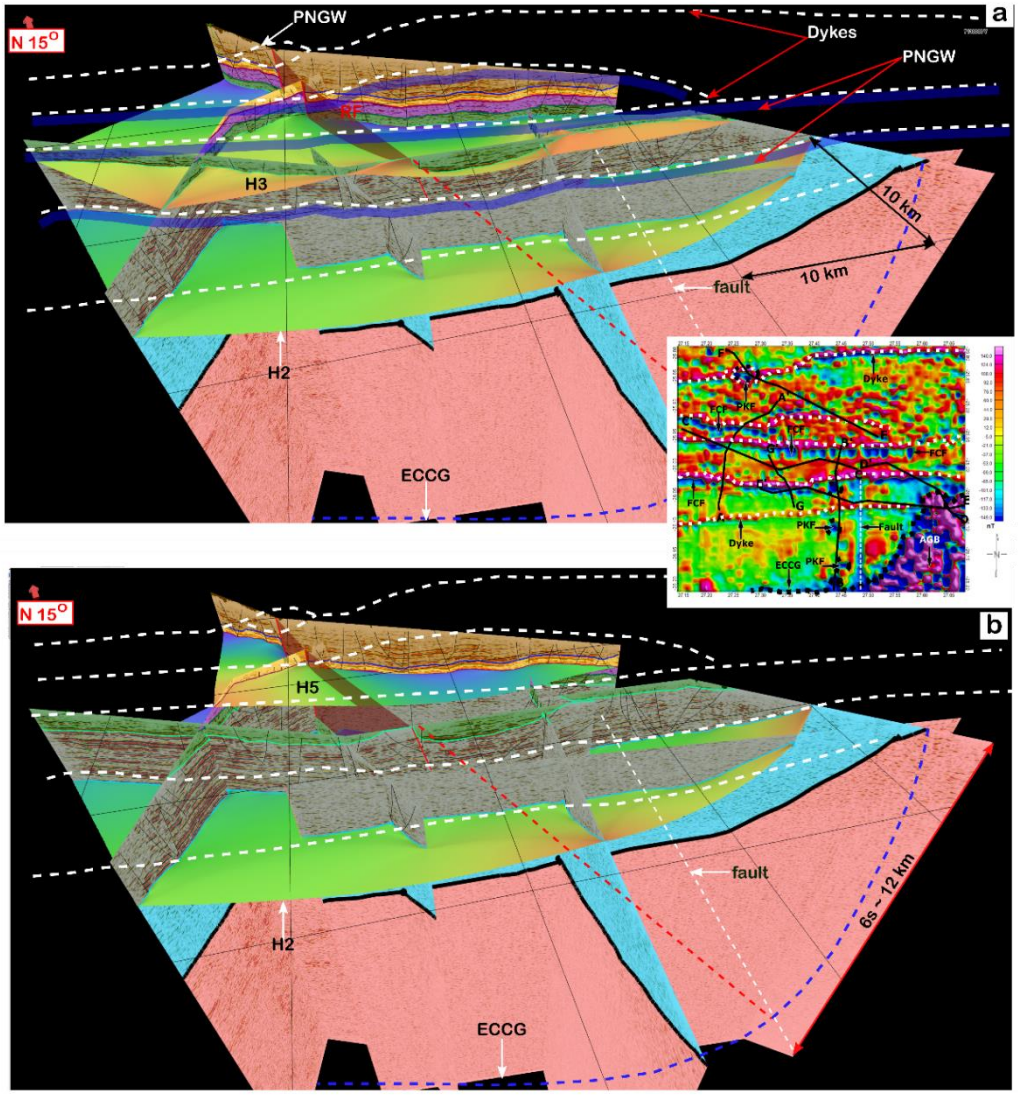


Figure 5.17: 3D visualization of the seismic sections indicating the position of some of the mapped features on the TMI map (a) approximate Timeball Hill/Rooihoogte (H1) horizon and (b) approximate Strubenkop (H5) horizon. The index on the center right is the interpreted first vertical derivative of the TMI map. ECCG indicate the erosional contact with Chuniespoort Group, PNGW the possible near-surface groundwater and the dashed white lines indicate the intrusive lineaments.

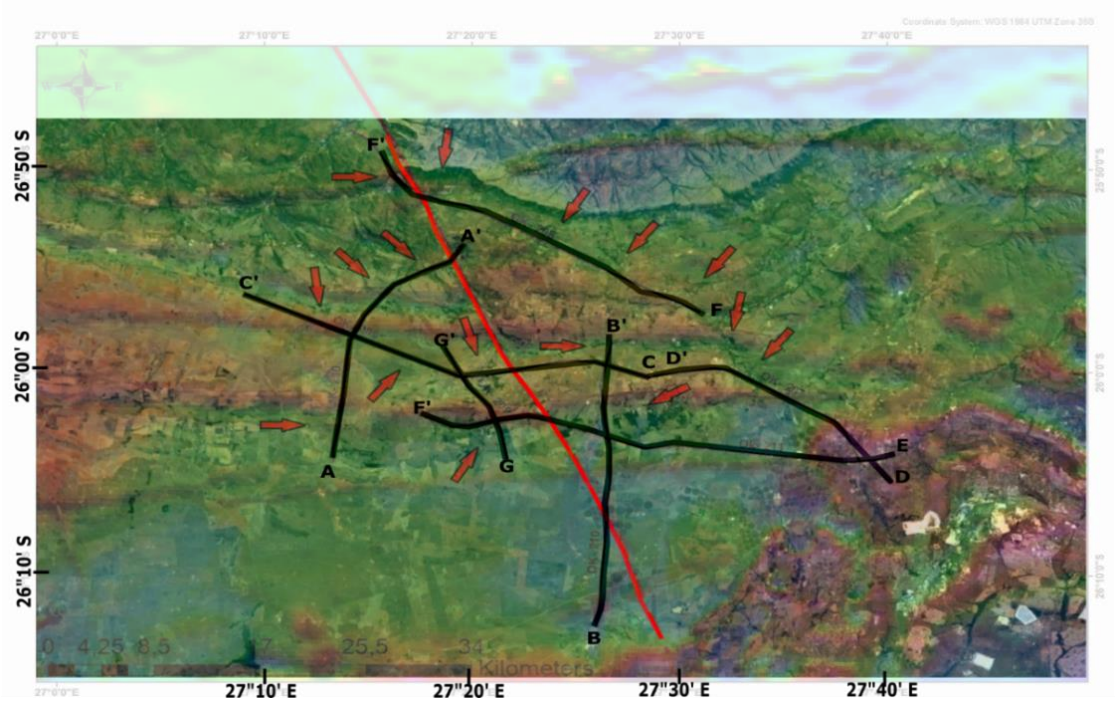


Figure 5.18: Total magnetic intensity map superimposed on the Google Earth map to show the relationship of the delineated structural zones and their surface structures (such as flood channels and deformed regions). The red arrows point to the delineated fault zones and observed surface features.

5.11. Conclusion

Legacy 2D reflection seismic and aeromagnetic data were integrated to map and characterise the subsurface architecture and discuss its implications for hydrogeological prospecting and engineering. The geophysical datasets were constrained using surface geological maps and borehole logs. In addition, post-stack denoising filters were applied to enhance geological structures and formation boundaries. Tilt and first vertical derivatives of the magnetic field were also utilised to improve the clarity of the near-surface and long wavelength magnetic field anomalies.

The Rustenburg fault was delineated and interpreted from the seismic reflection sections as a normal planar fault with vertical displacement of ~400 m. The fault systems form a series of horst-and-graben and half-graben structures. The faults are predominantly normal planar and listric faults, with associated antithetic and synthetic faults. These structures exhibit complex features and brittle-ductile

shear-type of deformation associated with a heterogenous fractured system. They are interpreted to have formed in an extensional basin-rift environment, accompanied by fault-modulated subsidence.

Folds and palaeo-karst features were also identified. The palaeo-slope observed on the seismic sections provides groundwater flow directions and monitoring in the area. The palaeo-compartment can assist in predicting successful high yield groundwater boreholes while the slump and possible karst feature will create high groundwater storage potential in the area. The faulted and fractured regions provide information regarding the secondary porosity and permeability of the zones.

Many of the interpretations presented in this study could not have been possible without the multi-disciplinary, integrated approach. Further enhancements to our approach are still very possible. For instance, our 2D seismic dataset may be replaced by a 3D seismic dataset to better compensate for crooked survey lines, allow adequate structural geometry calculation, and provide a better 3D view of the delineated structures and generally increase interpretation confidence. This shows that comprehensive analysis of the 3D seismic data will be important for detecting the geological complexity within the area and vital for tectonic model reconstruction. Further reprocessing of the legacy 2D seismic data with modern algorithms, will also provide higher quality information.

Acknowledgment

This study falls under the research initiatives of the Seismic Research Centre, University of the Witwatersrand. I would like to acknowledge the Anglo America for providing the seismic data access, DUG Insights for providing the software used for the seismic interpretation, visualisation and analysis, and Julius von Ketelhodt for his MATLAB code used for curvelet transform filter. We also thank Council for Geosciences, South Africa for providing access to magnetic potential field data, surface geological maps and borehole logs used in this study and Stephanie Enslin-Scheiber for her support in aeromagnetic data processing. I

would also like to acknowledge the funding assistance received from the Julian Baring Scholarship Fund.

5.12. Reference

Allen, P.A. and Allen, J.R. 1990. Basin Analysis: Principles and Applications, *Blackwell*, Oxford, pp. 451-495.

Altchenko, Y., Genco A., Pierce, K., Woolf R., Nijsten G.J., Ansems, N., Magombeyi, M., Ebrahim, G., Lautze, J., Villholth, K., Lefore, N., Modisha, R.C. O., Baqa, S., McGill, B. and Kenabatho P., 2017. Resilience in the Limpopo Basin: The Potential Role of the Transboundary Ramotswa Aquifer. Hydrogeology Report, Botswana.

Armstrong, R.A., Compston, W., Retief, E.A., Williams, I.T. and Welke, H.J., 1991. Zircon ion microprobe studies bearing on the age and evolution of the Witwatersrand triad. *Precambrian Research*, *53*(3-4), pp. 243-266.

Barnard, H.C., 2000. An explanation of the 1:500 000 general hydrogeological map: Johannesburg 2526. Department of Water Affairs and Forestry, South Africa.

Basson, I.J., 2019. Cumulative deformation and original geometry of the Bushveld Complex. *Tectonophysics*, *750*, pp. 177-202.

Bumby, A.J. 1997. The Geology of the Rustenburg Fault. M.Sc. thesis (unpublish), University of Pretoria, South Africa, pp. 130 - 162.

Bumby, A.J., Eriksson, P.G. and Van der Merwe, R., 1998. Compressive deformation in the floor rocks to the Bushveld Complex (South Africa): Evidence from the Rustenburg Fault Zone. *Journal of African Earth Sciences*, *27*(3-4), pp. 307-330.

Burberry, C.M., Jackson, C.A.L., and Chandler, S.R., 2016. Seismic reflection imaging of karst in the Persian Gulf: Implications for the characterisation of carbonate reservoirs. *AAPG Bulletin*, *100*(10), pp. 1561-1584.

Campbell, G., 2011. Exploration geophysics of the Bushveld Complex in South Africa. *The Leading Edge*, *30*(6), pp. 622-638.

Catuneanu, O. and Eriksson, P.G., 1999. The sequence stratigraphic concept and the Precambrian rock record: An example from the 2.7–2.1 Ga Transvaal Supergroup, Kaapvaal Craton. *Precambrian Research*, *97*(3-4), pp. 215-251.

Catuneanu, O. and Eriksson, P.G., 2002. Sequence stratigraphy of the Precambrian Rooihoogte–Timeball Hill rift succession, Transvaal Basin, South Africa. *Sedimentary Geology*, *147*(1-2), pp. 71-88.

Cawthorn, R.G., Davies, G., Clubley-Armstrong, A. and McCarthy, T.S., 1981. Sills associated with the Bushveld Complex, South Africa: An estimate of the parental magma composition. *Lithos*, *14*(1), pp. 1-16.

Cheney, E.S., 1996. Sequence stratigraphy and plate tectonic significance of the Transvaal succession of southern Africa and its equivalent in Western Australia. *Precambrian Research*, *79*(1-2), pp. 3-24.

Clendenin, C.W., 1989. Tectonic Influence on the Evolution of the Early Proterozoic Transvaal Sea, Southern Africa (Doctoral dissertation), University of the Witwatersrand, Johannesburg.

Cooper, G.R. and Cowan, D.R., 2008. Edge enhancement of potential-field data using normalised statistics. *Geophysics*, *73*(3), pp. H1-H4.

De Beer, J.H. ed., 2016. The History of Geophysics in Southern Africa. *African Sun Media*, pp. 237 – 245, 399 – 402 and 434 – 436.

De Wet, B., 2015. Geophysics in GENCO: De Beer, J.H. ed., 2015: The History of Geophysics in Southern Africa, pp. 423-436.

DUG Insight user manual (version 4.5), 2018a. Windows/Linux/Mac. Perth, Western Australia: DownUnder GeoSolutions (http://www.dug.com).

DUG Insight user manual, 2018b. DownUnder GeoSolution, http://help.dugeo.com/m/Insight4-0/l/434257-structurally-oriented-filter?id=434257-structurally-oriented-filter.

DUG Insight user manual, 2018c. DownUnder GeoSolution, http://help.dugeo.com/m/Insight4-0/l/438798-instantaneous-attributes.

Durrheim, R.J., Nicolaysen, L.O. and Corner, B., 1991. A deep seismic reflection profile across the Archaean-Proterozoic Witwatersrand Basin, South Africa. Continental lithosphere: Deep seismic reflections. *Geodynamics Series, 22*, pp. 213-224.

Durrheim, R.J., 2015. Hard rock reflection: De Beer, J.H. ed., 2015: The History of Geophysics in Southern Africa. *African Sun Media*, pp. 237-245.

Du Plessis, C.P. and Walraven, F., 1990. The tectonic setting of the Bushveld Complex in Southern Africa, Part 1. Structural deformation and distribution. *Tectonophysics*, *179*(3-4), pp. 305-319.

Eaton, D.W., Milkereit, B. and Salisbury, M.H. eds., 2003. Hardrock Seismic Exploration. *Society of Exploration Geophysicists.*

Els, B.G., Van den Berg, W.A. and Mayer, J.J., 1995. The Black Reef Quartzite Formation in the western Transvaal: Sedimentological and economic aspects, and significance for basin evolution. *Mineralium Deposita*, *30*(2), pp. 112-123.

Eriksson, P.G. and Reczko, B.F.F., 1995. The sedimentary and tectonic setting of the Transvaal Supergroup floor rocks to the Bushveld Complex. *Journal of African Earth Sciences*, *21*(4), pp. 487-504.

Eriksson, P.G. and Reczko, B.F., 1998. Contourites associated with pelagic mudrocks and distal delta-fed turbidites in the Lower Proterozoic Timeball Hill Formation epeiric basin (Transvaal Supergroup), South Africa. *Sedimentary Geology*, *120*(1-4), pp. 319-335.

Eriksson, P.G., Altermann, W., Catuneanu, O., Van der Merwe, R. and Bumby, A.J., 2001. Major influences on the evolution of the 2.67–2.1 Ga Transvaal basin, Kaapvaal Craton. *Sedimentary Geology*, *141*, pp. 205-231.

Eriksson, P.G., Hattingh, P.J. and Altermann, W., 1995. An overview of the geology of the Transvaal Sequence and Bushveld Complex, South Africa. *Mineralium Deposita*, *30*(2), pp. 98-111.

Eriksson, P.G., Mazumder, R., Catuneanu, O., Bumby, A.J. and Ilondo, B.O., 2006. Precambrian continental freeboard and geological evolution: A time perspective. *Earth-Science Reviews*, *79*(3-4), pp. 165-204.

Gibson, R.L., Courtnage, P.M. and Charlesworth, E.G., 1999. Bedding-parallel shearing and related deformation in the lower Transvaal Supergroup north of the Johannesburg Dome, South Africa. *South African Journal of Geology*, *102*(2), pp. 99-108.

Hartzer, F.J., 1995. Transvaal Supergroup inliers: Geology, tectonic development and relationship with the Bushveld Complex, South Africa. *Journal of African Earth Sciences*, *21*(4), pp. 521-547.

Hilliard, P. and McCourt, S., 1995. Bedding-parallel simple shear deformation in the West Rand Group rocks on Northcliff Promontory, Johannesburg, South Africa-insight into the Late Archaean evolution of the Kaapvaal Craton. *South African Journal of Geology*, *98*(4), pp. 349-355.

Isiaka, A.I., Durrheim, R.J. and Manzi, M.S., 2018. High-resolution seismic reflection investigation of subsidence and sinkholes at an abandoned coal mine site in South Africa. *Pure and Applied Geophysics*, *176*(4), pp. 1531-1548.

Isiaka, A.I., Durrheim, R.J., Manzi, M.S. and Andreoli, M.A., 2017. 3D seismic analysis of the AK fault, Orange Basin, South Africa: Implications for hydrocarbon leakage and offshore neotectonics. *Tectonophysics*, *721*, pp. 477-490.

Klein, G.D. and Hsui, A.T., 1987. Origin of cratonic basins. *Geology*, *15*(12), pp. 1094-1098.

Kostlin, E.O., McDowell, G.W. and De Gasparis, A.A., 2015. The history of geophysics at Anglo America and De Beers during the period 1959 to 1998: De Beer, J.H. ed., 2015: The History of Geophysics in Southern Africa. *African Sun Media*, pp. 388-411.

Malehmir, A., Durrheim, R., Bellefleur, G., Urosevic, M., Juhlin, C., White, D.J., Milkereit, B. and Campbell, G., 2012. Seismic methods in mineral exploration and mine planning: A general overview of past and present case histories and a look into the future. *Geophysics*, *77*(5), pp. WC173-WC190.

Malehmir, A., Koivisto, E., Manzi, M., Cheraghi, S., Durrheim, R.J., Bellefleur, G., Wijns, C., Hein, K.A. and King, N., 2014. A review of reflection seismic investigations in three major metallogenic regions: The Kevitsa Ni–Cu–PGE district (Finland), Witwatersrand goldfields (South Africa), and the Bathurst Mining Camp (Canada). *Ore Geology Reviews*, *56*, pp. 423-441.

Manzi, M. S., Hein, K. A., Durrheim, R. J., and King, N., 2014. The Ventersdorp Contact Reef model in the Kloof Gold Mine as derived from 3D seismics, geological mapping and exploration borehole datasets. *International Journal of Rock Mechanics and Mining Sciences*, pp. *66*, pp. 97-113.

Manzi, M., Durrheim, R., Nwaila, G., Hein, K., Frimmel, H., Gibson, R. and King, N., 2018. 3D reflection seismic data constraints on the timing of faulting in the upper crust: Implications for the origin of gold deposits in the Proterozoic Transvaal Supergroup, South Africa: In EGU General Assembly Conference Abstracts, 20, p. 16399.

Manzi, M.S., Durrheim, R.J., Hein, K.A. and King, N., 2012a. 3D edge detection seismic attributes used to map potential conduits for water and methane in deep gold mines in the Witwatersrand basin, South Africa. *Geophysics*, *77*(5), pp. WC133-WC147.

Manzi, M.S., Gibson, M.A., Hein, K.A., King, N. and Durrheim, R.J., 2012b. Application of 3D seismic techniques to evaluate ore resources in the West Wits line goldfield and portions of the West Rand goldfield, South Africa. *Geophysics*, *77*(5), pp. WC163-WC171.

Manzi, M.S., Hein, K.A., King, N. and Durrheim, R.J., 2013. Neoarchaean tectonic history of the Witwatersrand Basin and Ventersdorp Supergroup: New constraints from high-resolution 3D seismic reflection data. *Tectonophysics*, *590*, pp. 94-105.

Manzi, M., Malehmir, A. and Durrheim, R., 2019. Giving the legacy seismic data the attention, they deserve. *First Break*, *37*(8), pp.89-96.

Martini, J.E.J., Eriksson, P.G. and Snyman, C.P., 1995. The Early Proterozoic Mississippi Valley-type Pb-Zn-F deposits of the Campbellrand and Malmani Subgroups, South Africa. *Mineralium Deposita*, *30*(2), pp. 135-145.

McDowell, P.W., Barker, R.D., Butcher, A.P., Culshaw, M.G., Jackson, P.D., McCann, D.M., Skipp, B.O., Matthews, S.L. and Arthur, J.C.R., 2002. *Geophysics in engineering investigations,19*. London: Ciria.

Molezzi, M.G., Hein, K.A. and Manzi, M.S., 2019. Mesoarchaean-Palaeoproterozoic crustal-scale tectonics of the central Witwatersrand basin: Interpretation from 2D seismic data and 3D geological modelling. *Tectonophysics*, *761*, pp. 65-85.

Moore, J. M., Tsikos, H., and Polteau, S., 2001. Deconstructing the Transvaal Supergroup, South Africa: Implications for Palaeoproterozoic palaeoclimate models. *Journal of African Earth Sciences*, *33*(3-4), pp. 437-444.

NWA., 1998. Guide to the National Water Act (No. 36 of 1998) – Department of Water Affairs (DWA), Pretoria.

Onyebueke, E.O., Manzi, M.S.D. and Durrheim, R.J., 2018. High-resolution shallow reflection seismic integrated with other geophysical methods for

hydrogeological prospecting in the Nylsvley Nature Reserve, South Africa. *Journal of Geophysics and Engineering*, *15*(6), pp. 2658 - 2673.

Oosthuizen, A. C., and Richardson, S., 2011. Sinkholes and Subsidence in South Africa. Council for Geoscience Report, (2011-0010), pp. 1-31.

Philip H, James M, Daniel M and Adam W., 2003. Structural Geology of Sedimentary Basins: Sedimentary Basins in the Extension Zones. http://www.geosci.usyd.edu.au/users/prey/ACSGT/EReports/eR.2003/GroupD/Report2/web%20pages/contents.html.

Pretorius, C.C., Steenkamp, W.H. and Smith, R.G., 1994. Developments in data acquisition, processing, and interpretation over ten years of deep vibro-seismic surveying in South Africa: In Proceedings XVth CMMI Congress, pp. 249-258.

Pretorius, C.C., Muller, M.R., Larroque, M. and Wilkins, C., 2003. A review of 16 years of hardrock seismics on the Kaapvaal Craton. Hardrock Seismic Exploration, *Society of Exploration Geophysicists, pp*. 247-268.

Salisbury, M.H., Harvey, C.W., Matthews, L., Eaton, D.W. and Milkereit, B., 2003. The acoustic properties of ores and host rocks in hard-rock terranes. *Hardrock seismic exploration*, *10*, pp. 9-19.

Scheiber-Enslin, S.E. and Manzi, M., 2018. Integration of 3D reflection seismics and magnetic data for deep platinum mine planning and risk mitigation: A case study from Bushveld Complex, South Africa. *Exploration Geophysics*, *49*(6), pp. 928-939.

Scheiber-Enslin, S.E., Ebbing, J. and Webb, S.J., 2016. An isostatic study of the Karoo basin and underlying lithosphere in 3D. *Geophysical Journal International*, *206*(2), pp. 774-791.

Schreurs, G., Buiter, S.J., Boutelier, D., Corti, G., Costa, E., Cruden, A.R., Daniel, J., Hoth, S., Koyi, H.A., Kukowski, N. and Lohrmann, J., 2006. Analogue benchmarks of shortening and extension experiments. *Special Publication-Geological Society of London*, *253*, p. 1 - 27.

Shukla, M., Changlani, S. and Johari, A., 2014. Study of curvelet and wavelet image denoising by using different threshold estimators. *International Journal of Electrical, Electronics and Computer Engineering*, *3*(1), pp. 48 - 57.

Stanistreet, I.G. and McCarthy, T.S., 1991. Changing tectono-sedimentary scenarios relevant to the development of the Late Archaean Witwatersrand Basin. *Journal of African Earth Sciences (and the Middle East)*, *13*(1), pp. 65-81.

Stettler, E.H., Fourie, C.J.S., Bühmann, J.R., Hattingh, E., Cole, P., Kleywegt, R.J., Wolmarans, L.G. and Cloete, A.J., 1999. South African Geophysical Atlas, 2 (CD Rom). Council for Geoscience, South Africa

Tinker, J., de Wit, M. and Grotzinger, J., 2002. Seismic stratigraphic constraints on Neoarchaean-Palaeoproterozoic evolution of the western margin of the Kaapvaal Craton, South Africa. *South African Journal of Geology*, *105*(2), pp. 107-134.

von Ketelhodt, J.K., Manzi, M.S. and Durrheim, R.J., 2019. Post-stack denoising of legacy reflection seismic data: Implications for coalbed methane exploration, Kalahari-Karoo Basin, Botswana. *Exploration Geophysics*, *50*(6), pp. 667-682.

Webb, S.J., Cawthorn, R.G., Nguuri, T. and James, D., 2004. Gravity modelling of Bushveld Complex connectivity supported by Southern African seismic experiment results. *South African Journal of Geology*, *107*(1-2), pp. 207-218.

Widess, M. B., 1973. How thin is a thin bed? *Geophysics*, *38*(6), pp. 1176-1180.

Yılmaz, O., 2001. Seismic Data Analysis: Processing, Inversion, and Interpretation of Seismic Data. *Society of Exploration Geophysicists*, Tulsa, USA.

CHAPTER 6

6.0 Assessment of the site effect at South African National Seismograph Network stations using the HVSR technique

Abstract

The analysis of seismic noise to characterize the site response is a widely accepted geophysical tool for microzonation and seismic hazard assessment. This study determines the site effect at the stations of the South Africa National Seismograph Network using the horizontal to vertical spectral ratio (HVSR) of the ambient seismic noise. The aim was to assess the stability and reliability of the HVSR parameters and their possible application to microzonation of cities and building sites of critical infrastructure. The stability of the site response parameters was investigated by considering different times-of-day and seasons, as well as the sensitivity to the selection of the processing parameters. The results show that the fundamental natural frequency of the near-surface low-velocity-layer (LVL) was essentially the same in all the analyzed time windows, irrespective of the time-of-day or season, while the H/V amplitude varied slightly with the recording duration. The analysis was performed in accordance with the recommendations of the SESAME 2004 team. The HVSR-estimated predominant frequency was deemed to be a reliable and stable representation of the fundamental resonance frequency of the ground motion. Furthermore, the estimated values were used to approximate the thickness of the LVL and the vulnerability to liquefaction index at the stations that satisfied the criteria for a clear H/V peak. The shape of the H/V curve provides information regarding the surface geological characteristics at the seismological stations. We conclude that the HVSR technique using microtremor signals is a reliable, cheap and easy-to-use geophysical technique that can complement other geophysical methods for microzonation and seismic hazard assessment in South Africa.

6.1. Introduction

Seismological studies show that the Earth's surface is never quiet (Kanai, 1957). The constant vibration of the ground surface is caused by atmospheric disturbances, tectonics, and human activities. Such micro vibrations are called 'microtremors' or 'ambient noise' with amplitude and frequency range of 0.1 to 10 microns and 0.1 to 20 Hz, respectively (Kanai, 1957). The use of microtremor characteristics (especially the predominant frequency F_0 and amplification amplitude A_0) has become a widely used technique for site effect and microzonation studies due to their simple relationship with local geological conditions, easy data acquisition, and ability to record data without strict spatial and time constraints at a very low cost (Kwak at al., 2017; Ansary and Rahman, 2013; Bonilla, 1992; Nakamura, 1989). The predominant frequency of the microtremor signal is considered to be the natural resonance frequency of the near-surface low velocity layer (LVL) that amplifies the ground motion produced by an earthquake. This phenomenon is called the site effect.

These techniques have been used to estimate the site effect characteristics, such as numerical simulation (Lachet and Bard, 1994), Standard Spectral Ratio (SSR) (Aki, 1957) and various empirical techniques. The empirical methods use seismic noise records to estimate the site effect response of the LVL. The technique involves either relating the horizontal component of a sediment site to the horizontal component of a rock site (Reference method (Bonilla, 1992)) or relating the horizontal to the vertical component at the same site (Non-reference method (Nogoshi and Igarashi, 1971; Nakamura, 1989)). The use of the horizontal-to-vertical spectral ratio (HVSR) techniques in site response analysis attracted considerable attention after the earthquakes in Mexico (1985) (Bonilla, 1992), California (Loma Prieta earthquake 1989) and Chi-Chi, Taiwan earthquake (1999), where the ground response calculated with HVSR method correlated well with the observed earthquake strong ground motion. Although the theoretical background is still debated, the technique has proven to be reliable and credible for site effect characterization and microzonation studies (SESAME 2004; Suarez et al., 2012). The HVSR technique has been applied successfully in large cities

and highly populated areas to characterize earthquake engineering parameters such as the amplification factor and resonant frequency (e.g. Suarez et al., 2012; Talha Qadri et al., 2015).

South Africa is located on the southern intraplate region of the African plate, bounded by the southwest Indian Ocean ridge and South Atlantic Ocean ridge. Natural seismicity is mainly concentrated along branches of the active continental East African Rift System that extend through Mozambique and along the Zululand coast, and into Botswana. Clusters of seismicity are also found in the Koffiefontein area of the Free State province, and the northern and western Cape (Kijko and Cichowicz, 2006, see Figure 6.1a). The largest natural earthquakes that have been reported in South Africa are the Ceres-Tulbagh M_L6.3 earthquake that occurred on 29 September 1969 in the Western Cape, causing severe damage in the towns of Tulbagh and Wolseley (Singh et al., 2009). The M_W7.0 earthquake that occurred on 23 February 2006 in the Manica province, Mozambique caused alarm as far away as Durban (about 1700 km apart) (Fenton and Bommer, 2006) in South Africa. However, most seismicity in South Africa is due to deep gold mining activities (Figure 6.1a). These mining activities induce strain energy on the mine pillars and abutments. The accumulated pressure may be suddenly released by failure of intact rock or slip on pre-existing faults. This causes strong vibrations in the rocks, which are felt on the surface as a tremor or earthquake (Durrheim et al., 2007; Saunders et al., 2007). Mining-related earthquakes that caused damage to surface structures include (a) an M_L4.7 event that occurred near Carletonville on 7 March 1992, causing damage as far away as (~ 80 km apart) and Pretoria (~140 km apart) (Singh et al., 2009); (b) a M_L5.3 event in Klerksdorp (Stilfontein) on 9 March 2005, which damaged many buildings and mining infrastructure (Durrheim et al., 2007); and (c) a M_L5.5 event in Orkney on 5 August 2014, which caused considerable damage in the town of Khumo (~150 km apart) (Midzi et al., 2015). Both natural and mining-related earthquakes have posed a considerable hazard (Figure 6.1b), and the distribution of the damage caused by earthquakes was clearly affected by site effect phenomena.

South Africa has many large cities with high population density and giant engineering infrastructures, but with limited knowledge of the site effect characteristics. In this study, the HVSR technique using microtremor signals, recorded by the permanent seismic station that comprises the South African National Seismograph Network (SANSN), was used to determine the site effect characteristics with the aim of developing a 'reference grid' for more detailed local studies. Broadband data covering a long period of time was readily available. The Geopsy software package produced by the European SESAME research project group (http://www.geopsy.org/) was used to calculate the HVSR curves and evaluate the effect of the choices in processing parameters on the H/V values. The thickness of the near-surface LVL was calculated using the formula derived by Parolai et al. (2002) and Ibs-von Seht and Wohlenberg (1999), and the vulnerability to liquefaction index at some seismological stations was calculated using the Nakamura (2000) equation ($K_g = A_0^2 / F_0$). In summary, this is a pilot study that seeks to demonstrate how the HVSR method can be used to estimate the site effect in South Africa. A set of HVSR curves that are typical of different geological terrains has been produced and interpreted, with the aim of illustrating how they can be used for microzonation studies in major cities. This information will assist city planners, earthquake and structural engineers in planning and designing a sophisticated earthquake resistant structure.

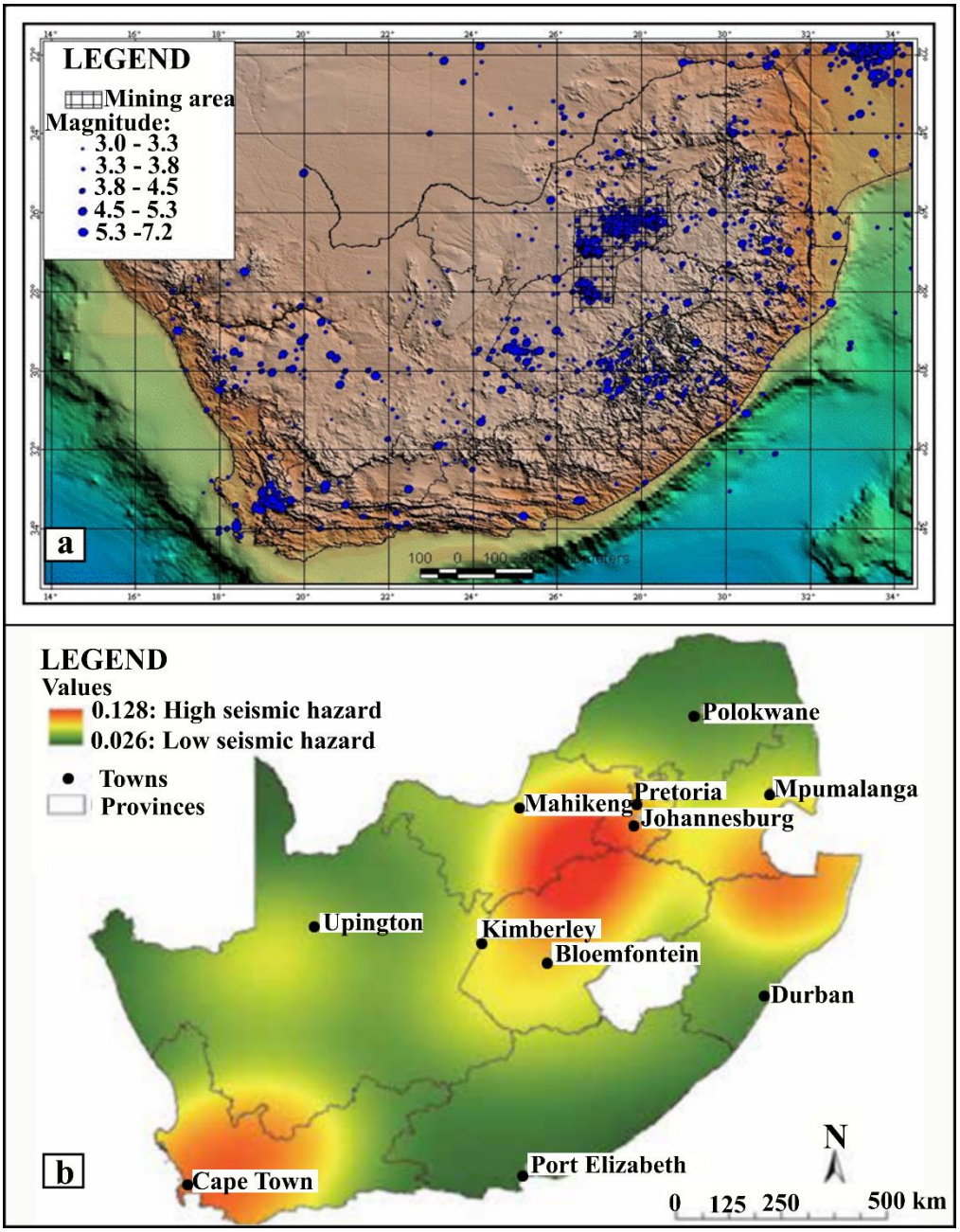


Figure 6.1: (a) Seismicity of Southern Africa. Note > 95% are mining related seismicity (Ogasarawa et al., 2009). (b) Map of current seismic hazard for South Africa. Expected peak ground acceleration (PGA, in g) with a 10% probability of being exceeded at least once in a 50 years period (Esterhuyse et al., 2014, modified by Kijko et al., 2016).

6.2. Methodology

The HVSR method, also called the Quasi-transfer spectrum (QTS) or Nakamura (1989) technique, was used to estimate the fundamental natural frequency and amplification of multiply-reflected vertically incident shear waves produced by microtremors in the near-surface low velocity layer, without considering any reference site.

According to Nakamura (2000), the amplification factor can be related to the shear wave spectra of the horizontal (S_{Hs}) and vertical (S_{Vs}) components of the ground motion recorded at the surface as follows (Figure 6.2).

$$S_{Hs}(f) = A_{hs} * H_b(f) + H_s(f) \quad (6.1a)$$

$$S_{Vs}(f) = A_{vs} * V_b(f) + V_s(f) \quad (6.1b)$$

where $H_s(f)$ and $V_s(f)$ are the horizontal and vertical spectral components of Rayleigh waves propagating along the ground surface, respectively; $H_b(f)$ and $V_b(f)$ are the recorded horizontal and vertical spectral components on the basement underlying the sedimentary basin; A_{hs} and A_{vs} are the amplification factor of the horizontal and vertical components of the vertically incident body wave registered on the soil surface, and * indicate convolutional process. The amplification factor of horizontal (A_{hb}) and vertical (A_{vb}) component of the seismic motion recorded on the basement under the basin (Figure 6.2) are as follow;

$$A_{hb} = \frac{S_{Hs}(f)}{H_b(f)} \quad (6.2a)$$

$$A_{vb} = \frac{S_{Vs}(f)}{V_b(f)} \quad (6.2b)$$

At the ground surface, where the frequency of the horizontal component received large amplification and $A_{vs} \approx 1$. Thus, $S_{Vs}(f) \cong V_b(f)$ if it is assumed that there is no Rayleigh wave contribution. Since a microtremor produces body and surface waves, the Rayleigh wave effect can be calculated using A_{vb}. Therefore, if $S_{Vs}(f)$ is greater than $V_s(f)$, it is regarded as the effect of surface waves. Then the

modified effect of the amplification on the horizontal component against the effect of Rayleigh wave can now be estimated using the compensated A_{hb}^{*}:

$$A_{hb}^{*} = \frac{A_{hb}}{A_{vb}} = \frac{\frac{S_{Hs}(f)}{S_{Vs}(f)}}{\frac{H_b(f)}{V_b(f)}} = \frac{QTS}{\frac{H_b(f)}{V_b(f)}} \quad (6.3)$$

Therefore, the Quasi-transfer spectrum (QTS) is expressed:

$$QTS = \frac{S_{Hs}(f)}{S_{Vs}(f)} \quad (6.4)$$

Following Nakamura (2000), the horizontal to vertical spectral ratio at the basement rock is approximately equal to unity ($H_b(f)/V_b(f) \approx 1$).

The thickness (h) of the sedimentary cover or weathered layer above the bedrock can now be related to the fundamental frequency (F_0) where there is a significant impedance contrast (>2.5) between the soil column and the bedrock; $F_0 = V_s/4h$ (Nakamura, 1989; Parolai et al., 2002), where V_s is the average shear wave velocity of the low-velocity layer. 'h' is related to the depth to the basement. A low F_0 is associated with deeper depth and a high F_0 is associated with shallow depth. In addition, the mathematical expressions derived by Ibs-von Seht and Wohlenberg (1999) and Parolai et al. (2002) were utilized to estimate the thickness of the column. Ibs-von Seht and Wohlenberg (1999) used the fundamental frequency of the noise measurements close to boreholes in Lower Rhine Embayment (Germany) to fit a nonlinear regression model, as stated in equation (6.5).

$$h=af_r^{b} \quad (6.5)$$

where a and b are the correlation coefficients.

They show that the resonance frequency (f_r) of a soil layer is directly associated to its thickness (h) through the nonlinear regression model in equation (6.6).

$$h=96f_r^{-1.388} \quad (6.6)$$

Parolai et al. (2002) used the same mathematical expression in equation (6.5) in the basin with a deeper depth to the bedrock in Cologne area (Germany) to emerge with equation (6.7).

$$h=108f_r^{-1.551} \quad (6.7)$$

Furthermore, the vulnerability index (K_g) is an indicator of liquefaction potential of a sedimentary deposit of a specific site. The vulnerability index values beneath the seismic stations were calculated in this study using the Nakamura (1997) equation:

$$K_g= A_0^2 / F_0 \quad (6.8)$$

where K_g is the vulnerability index, A_0 is the amplification factor and F_0 is the fundamental frequency. A high K_g value (above 10) is a sign of significant potential for liquefaction, while low K_g values (below 10) indicate no or little liquefaction potential (Nakamura, 1997).

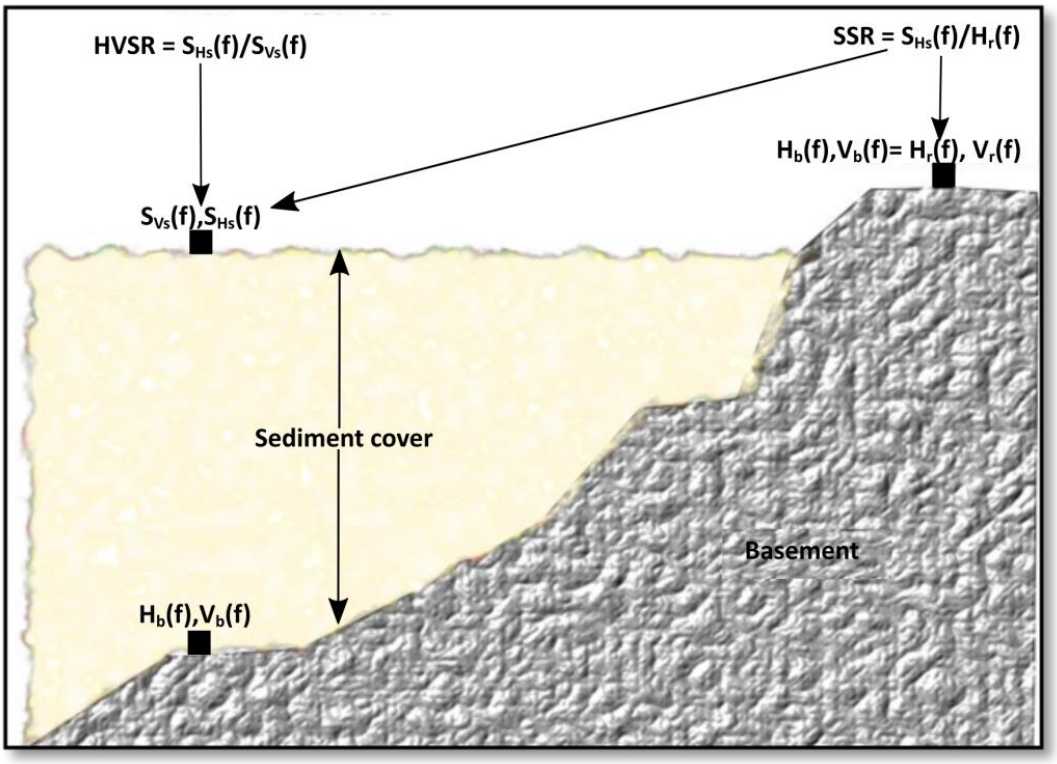


Figure 6.2: A typical geological structure used by Nakamura (2000) to explain the horizontal to vertical spectral ratio (HVSR) technique. Note SSR – standard

spectral ratio technique, $H_r(f)$ and $V_r(f)$ are the horizontal and vertical spectral components recorded on exposed bedrock rock, $H_b(f)$ and $V_b(f)$ are the horizontal and vertical spectral components on the basement that is covered by sediments, $S_{Hs}(f)$ and $S_{Vs}(f)$ are the spectral components recorded on the surface over the sedimentary column.

6.3. Data acquisition

The microtremor data used in this study was extracted from 24 South African National Seismograph Network (SANSN) and AfricaArray network stations distributed across the country (Figure 6.3). The stations were equipped with a mix of broadband, short and extended short period seismometers mounted with the Global Positioning System (GPS) for timing (Table 6.1). Figure 6.3 shows the distribution of seismological stations over geological map of the country. Figure 6.4 shows an example photo of one of the stations. The seismic stations record continuously at a sampling rate of 100 Hz. A year-long (2015) continuous record was extracted for each station through the IRIS DMC website.

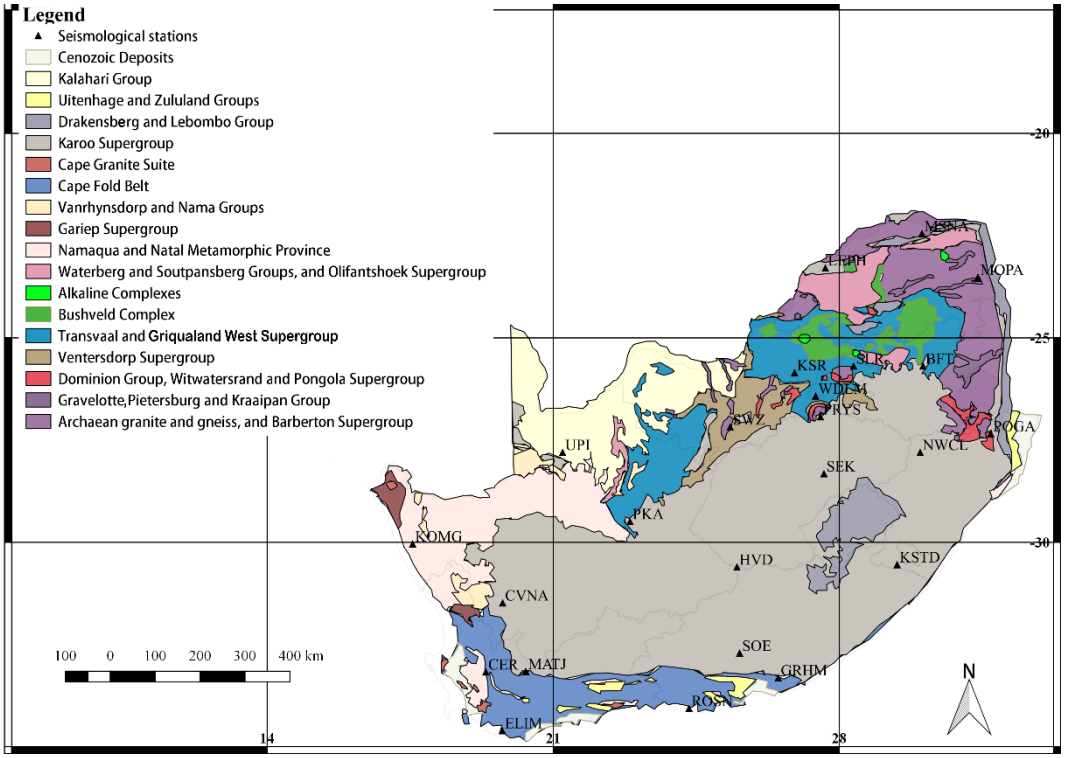


Figure 6.3: Geological map of South Africa and location of seismological stations. (Copyright© Council for Geoscience, South Africa, All Right Reserved. First published by the Government printer, 1978).



Figure 6.4: Example of seismometer used in the seismological stations.

Table 6.1: Network station coordinates and instruments

Station Town (Code)	Latitude (Deg Min)	Longitude (Deg Min)	Elevation (Meters)	Instrument
Belfast (BFT)	-25°41.20'S	30°02.60'E	1868	EARS Micro 24-bit Digital recorder with a Guralp CMG-40T extended short-period seismometer
Calvinia (CVN)	-31°27.00'S	19°45.70'E	1050	EARS Omega 24-bit Digital recorder with a Geotech Instruments KS2000 broadband seismometer.
Ceres (CER)	-33°21.70'S	19°17.60'E	472	EARS Micro 24-bit Digital recorder with a Geotech Instruments KS2000 broadband seismometer.
Elim (ELIM)	-34°35.80'S	19°44.70'E	472	EARS Micro 24-bit Digital recorder with a Guralp CMG-40T extended short-period seismometer
Grahamstown (GRM)	-33°18.80'S	26°30.50'E	610	EARS Micro 24-bit Digital recorder with a Geotech Instruments KS2000 broadband seismometer.
Gariep Dam (HVD)	-30°36.30'S	25°29.80'E	1433	EARS Micro 24-bit Digital recorder with a Guralp CMG-40T extended short-period seismometer
Komaggas (KOMG)	-24°47.94'S	17°29.02'E	299	EARS Omega 24-bit Digital recorder with a Guralp CMG-40T extended short-period seismometer
Kokstad (KSD)	-30°32.46'S	29°25.00'E	1350	EARS Micro 24-bit Digital recorder with a Geotech Instruments KS2000 broadband seismometer.
Koster (KSR)	-25°51.10'S	26°53.83'E	1623	EARS Omega 24-bit Digital recorder with a Guralp CMG-40T extended short-period seismometer
Lephalale (LEPH)	-23°38.98'S	27°44.81'E	840	Stand Alone Quake Seismometer with a Guralp CMG-40T extended short-period seismometer
Matjiesfontein (MATJ)	-33º15.84'S	20º32.87'E	1054	EARS Omega 24-bit Digital recorder with a Guralp CMG-40T extended short-period seismometer.
Mopani (MOPA)	-23º31.04'S	31º23.39'E	362	EARS Micro 24-bit Digital recorder with a Guralp CMG-40T extended short-period seismometer.
Mussina (MASN)	-22º26.92'S	30º01.42'E	600	EARS Micro 24-bit Digital recorder with a Geotech Instruments KS2000 broadband seismometer.
Newcastle (NWCL)	-27º44.15'S	29º53.51'E	1215	EARS Omega 18-bit Digital dial-up event recorder with a short-period Mark Products L4-C seismometer.
Prieska (PKA)	-29º40.20'S	22º45.40'E	960	EARS Omega 24-bit Digital recorder with a Guralp CMG-40T extended short-period seismometer
Pongola (POGA)	-27°22.19'S	31°36.70'E	290	EARS Micro 24-bit Digital recorder with a Geotech Instruments KS2000 broadband seismometer.
Parys (PRYS)	-26º55.78'S	27º27.99'E	1403	EARS Omega 24-bit Digital recorder with a Guralp CMG-40T extended short-period seismometer.
Sunshine Coast (ROSN)	-34º06.23'S	24º32.40'E	110	KS2000 Earth data low gain
Silverton (SLR)	-25°44.10'S	28°16.90'E	1348	Nanometrics Calisto Europa with a Streckeisen STS-2 broadband seismometer.
Senekal (SEK)	-28º32.30'S	27º62.50'E	1486	CMG-40T Earth data low gain

Schweizer-Reneke (SWZ)	-27°10.90'S	25°19.50'E	1342	EARS Omega 24-bit Digital recorder with a Guralp CMG-40T extended short-period seismometer.
Somerset-East (SOE)	-32°42.70'S	25°33.70'E	820	EARS Omega 18-bit Digital dial-up event recorder with a Mark Products L4-3D three-component short-period seismometer.
Upington (UPI)	-28°21.71'S	21°15.16'E	845	EARS Omega 24-bit Digital recorder with a Geotech Instruments KS2000 broadband seismometer.
Western deep levels mine (WDLM)	-26º25.38'S	27º36.49'E	1680	EARS Omega 24-bit Digital recorder with a Guralp CMG-3T extended short-period, low gain seismometer.

6.4. Surface geological characteristics of the seismic stations

The twenty-four AfricaArray and South African National Seismological Network (SANSN) stations used in this study were deployed across the nine-province of South Africa, located in different geological supergroups (Figure 6.3 and Figure 6.4). Brief explanations of the surface geology are discussed in Table 6.2 using the station codes (Truswell, 1977; Viljoen and Reimold, 1999; McCarthy and Rubidge, 2005; Fourie et al., 2007; Chinoda et al., 2009):

Table 6.2: Brief explanation of the surface geology and location of the stations

Stations Province	Surface geology
BFT Mpumalanga	The surface geology of the site is characterised by the sedimentary rock of the Ecca Group of the Karoo Supergroup, predominantly argillaceous layers of carbonaceous shales, arenaceous sandstones, and siltstones (Johnson et al., 2006).
CVNA Northern Cape	Characterised by Permian sandstone and shale of the Ecca Group, underlain by diamictite shale of the Dwyka Group of the Karoo Supergroup.
CER Western Cape	Weathered rocks of Bokkeveld Group of the Cape Supergroup consist mostly of siltstones and shale.
ELIM Western Cape	The surface geology consists of weathered rocks of the Cape Supergroup.
GRHM Eastern Cape	Consists of younger sediments and alteration deposits, underlain by sandstone, shale, gneisses and granites of the Bokkeveld Group of the Cape Supergroup.
HVD Free State	Dominated by purple and blue-gray mudstone and green shale, underlain by interbedded sandstone and siltstone of the Adelaide Subgroup of the Beaufort Group of the Karoo Supergroup.
KOMG Northern Cape	The surface geology is characterized by weathered rocks of the underlying Proterozoic crystalline basement of the Namaqua Metamorphic Province (Viljoen and Reimold, 1999).
KSTD Kwazula-Natal	The surface geology consists of mainly weathered sedimentary rocks from the underlying sandstone and mudstone of the eastern Beaufort Group of the Karoo Supergroup (Viljoen and Reimold, 1999).

KSR North West	The surface geology is made of weathered rocks from the underlying Pretoria Group of the Transvaal Supergroup consists of interbedded quartzite, andesite, shale and banded ironstone formation (Viljoen and Reimold, 1999).
LEPH Limpopo	Characterised by sediments of the Karoo Supergroup overlaying the volcanic rocks of the Kaapvaal Craton.
MATJ Western Cape	The surface geology consists of dry light brown sandstones, gravels in a sandy matrix, weathered bedded shale and mudstones underlain by the unweathered rock of the same group (Fourie et al., 2007).
MOPA Limpopo	Characterised by alluvium and superficial deposits underlain by high-grade metamorphic rocks (ortho and paragneisses) of the Kaapvaal craton.
MSNA Limpopo	The surface geology is characterized by the central zone of Limpopo Mobile Belt which is regarded as the transboundary location of supercrustal rocks, due to collision between Kaapvaal and Zimbabwe craton (Chinoda et al., 2009). Consist of Bulai gneisses.
NWCL KwaZulu-Natal	Characterised by consolidated sedimentary layers of the Ecca Group, overlying the Dwyka Group of the Karoo Supergroup (Hunter, 1991).
POGA KwaZulu-Natal	Melmoth Basement Arch which belongs to the upper sedimentary Mozaan Group of the Pongola Supergroup. The surface geology is dominated by arenaceous sediments and minor argillaceous sedimentary layers.
PKA Northern Cape	The surface geology is characterized by calcrete outcrops on the Dwyka Group of the Karoo Supergroup.
PRYS Free State	Situated on the Vredefort impact Dome (Vredefort impact crater) close to the Vaal River. The surface geology is characterized by the weathered rocks Archaean granite and gneiss.
ROSN Eastern Cape	The surface geology consists of predominantly weathered sandstones and mudstones of the Bokkeveld Group of the Palaeo-phanerozoic Cape Supergroup.
SEK Free State	The area is characterised by underlying Adelaide and Tarkastad Subgroups of the Beaufort Group of the Karoo Supergroup. The surface geology is made up of the weathered underlying rocks; consist of grey mudstone, dark-grey shale, siltstone and sandstone.
SLR Gauteng	The surface geology consists of quartzites and mudstone of the Pretoria Group sediments of the Transvaal Supergroup.
SOE Eastern Cape	Predominantly sandstone, siltstone and mudstones of the Adelaide Subgroup of the Beaufort Group of the Karoo Supergroup.
SWZ North West	The surface geology is characterised by the sequence of alluvial gravel units and colluvium of the Platberg Group of the Ventersdorp Supergroup.
UPI North west	Characterised by the windblown red-brown structureless sand of the Gordonia Subgroup of the Kalahari Group, underlain by metamorphosed sediments of the Namaqualand metamorphic province.
WDLM Gauteng	Characterised by weathered rock of the Archaean age Witwatersrand Supergroup within the Kaapvaal craton, consists of thick interbedded argillaceous and arenaceous sedimentary rocks.

6.5. Data processing and analysis

The recorded microtremor signals were transformed from binary to miniSEED format and processed using the Geopsy software (http://wwwgeopsy.org), developed by the European research project group (SESAME, 2004).

Generally, seismic noise due to industrial facilities and/or heavy traffic noise poses a serious problem in microtremor signal processing, which can result in the wrong estimation of parameters. To avoid inclusion of such transient signals into processing, the data is windowed before computing the H/V spectral ratio of the microtremor signal. An automatic window selection mode with anti-triggering on the raw data was activated within the Geopsy software package (Figure 6.5a). After the automatic window selection, the windows that still contained non-stationary noise were manually removed. The removal of these transients improved the clarity of the H/V curve, thereby lowering the standard deviation error. During the automatic window selection, a minimum of 25 and maximum of 99 windows were selected. The time length of each window varies from 30s to 120s with 10% window overlap over 3 to 5 hours of ambient noise record (Figure 6.5a).

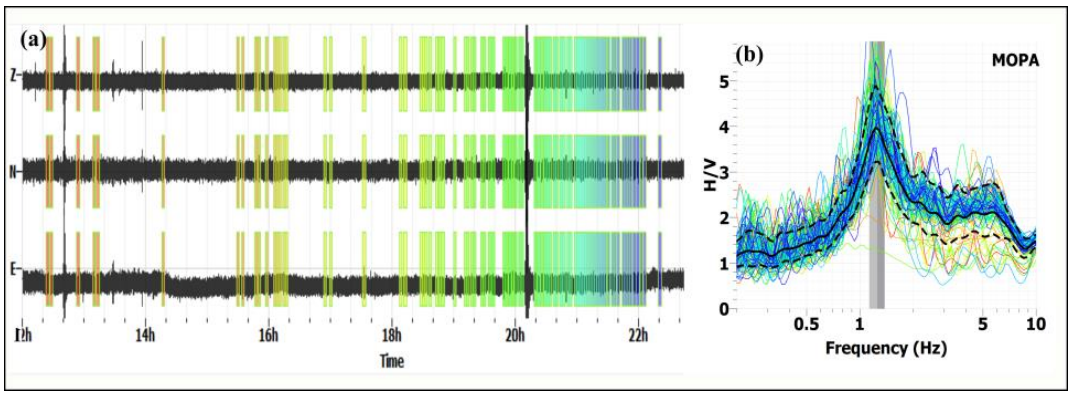


Figure 6.5: Microtremor signal processing. (a) Automatic window selection on the 3-component seismometer noise record, (b) Example of HVSR result (H/V curve) with 79 noise windows for MOPA station.

The H/V curve in Figure 6.5b shows the average H/V curve (solid black line); the dashed lines indicate the standard deviation of the H/V amplitude (A_0) curve, while the vertical gray band indicates the standard deviation of the peak frequency. The dominant frequency is the value at the H/V peak between the gray areas, and the amplification amplitude is the corresponding spectral value of the peak frequency. The coloured curves represent the individual H/V curve for each

selected noise window. The calculated output of the HVSR curve was sampled between 0.2 to 20 Hz, with 0.2 Hz high pass filter.

By means of the software the Fourier spectrum of each dataset within a time window 'w' at site 's' were calculated for both horizontal and vertical component. The frequency spectrum was tapered with 5% Cosine function before computing the average Fourier spectrum of each noise component (the horizontal (S^{s}_{Hs}) and vertical (S^{s}_{Vs})) (equation 11 and 12, respectively). This was done in order to avoid unanticipated discontinuities which may influence the Fourier spectrum result. The calculated Fourier spectra were smoothed using the Konno and Ohmachi (1998) logarithmic function with 20/40 coefficient of bandwidth along with 5% Cosine taper width in order to overcome the numerical instabilities. The instrumental effects were removed using singular DC suppression.

Computation of the horizontal to vertical spectral ratio and standard deviation was carried out as shown in the following equations:

For the horizontal Fourier spectrum:

North component: $$N^{s}(f) = \frac{1}{n}\sum^{n} {}^{w}N^{s}(f)\,, \tag{6.9}$$

East component: $$E^{s}(f) = \frac{1}{n}\sum^{n} {}^{w}E^{s}(f)\,, \tag{6.10}$$

where n is a number of the selected windows, and (${}^{w}N^{s}$), and (${}^{w}E^{s}$) are the north and east horizontal component, respectively.

The quadratic mean of the Fourier spectra of the both horizontal component at site 's' is giving by:

$$S^{s}_{Hs}(f) = \sqrt{\frac{(N^{s})^{2}(f) + (E^{s})^{2}(f)}{2}}\,. \tag{6.11}$$

The average vertical Fourier spectrum:

$$S^{s}_{Vs}(f) = \frac{1}{n}\sum {}^{n}\,{}^{w}V^{s}\,, \tag{6.12}$$

where (${}^{w}V^{s}$) is the vertical component.

Thus, the resulting spectral amplitude ratio (HVSR) at site 's' is giving by:

$$\mathrm{HVSR(f)} = \frac{S^{S}_{Hs}(f)}{S^{S}_{Vs}(f)} = \mathrm{QTS} \tag{6.13}$$

The standard deviation (σ) at site 's' is giving by:

$$\sigma^{s}(\mathrm{f}) = \sqrt{\left[\frac{1}{\mathrm{n}-1}\sum_{\mathrm{s}=1}^{\mathrm{n}}\left({}^{\mathrm{w}}\mathrm{HVSR}^{\mathrm{s}}(\mathrm{f}) - \mathrm{HVSR}\,(\mathrm{f})\right)^{2}\right]} \tag{6.14}$$

The HVSR result obtained with equation (6.13) is independent of the path and source of the seismic signal. However, the shape of the H/V curve represents the site response between the input ground motion at the base rock and the surface. The actual information extracted from the H/V curve is the predominant frequency, which is equivalent to the fundamental natural frequency (F_0) of the top low-velocity-layer. The fundamental natural frequency corresponds to the peak of the H/V curve, while the corresponding spectral value is the amplification amplitude (A_0). The H/V amplitude is considered to be an indication of the impedance contrast and lower-bound of the actual site amplification factor. Presently, there is a serious argument whether the H/V ratio amplitude represents the actual site amplification factor (Nakamura, 1989; SESAME, 2004). The sharpness of the H/V peak increases the reliability of its value. Clear high H/V peaks are associated with large velocity contrasts between the top weathered layer and the bedrock.

SESAME (2004) guidelines were considered during the processing steps in order to ascertain the reliability of the obtained results (Table 6.3). The stability of the H/V parameters was tested by analyzing different times-of-day and seasons (Table 6.4).

Table 6.3: Criteria for a reliable H/V curve and clear H/V peak (SESAME, 2004).

Criteria for a reliable H/V curve		**WL =** window length
i	$f_0 > 10/WL$	n_w = number of windows selected for the average H/V curve
	and	$n_c = I_w \times n_w \times f_0$ = number of significant cycles
ii	$n_c(f_0) > 200$	**f** = current frequency
	and	f_{sensor} = sensor cut-off frequency
iii	$\sigma_A(f) < 2$ for $0.5f_0 < f < 2f_0$ if $f_0 > 0.5Hz$	f_0 = H/V peak frequency
	or	σ_f = standard deviation of H/V peak frequency ($f_0 \pm \sigma_f$)
	$\sigma_A(f) < 3$ for $0.5f_0 < f < 2f_0$ if $f_0 > 0.5Hz$	
Criteria for a clear H/V peak (at least 5 out of 6 criteria fulfilled)		$\varepsilon(f_0)$ = threshold value for the stability condition $\sigma_f < \varepsilon(f_0)$
		A_0 = H/V peak amplitude at frequency f_0
		$A_{H/V}(f)$ = H/V curve amplitude at frequency **f**
i	$\exists f' \in [f_0/4, f_0] \mid A_{H/V}(f') < A_0/2$	f' = frequency between $f_0/4$ and f_0 for which $A_{H/V}(f') < A_0/2$
		f^+ = frequency between f_0 and $4f_0$ for which $A_{H/V}(f^+) < A_0/2$
ii	$\exists f^+ \in [f_0, 4f_0] \mid A_{H/V}(f^+) < A_0/2$	$\sigma_A(f)$ = "standard deviation" of $A_{H/V}(f)$, $\sigma_A(f)$ is the factor by which the mean $A_{H/V}(f)$ curve should be multiplied or divided
iii	$A_0 > 2$	$\sigma_{logH/V}(f)$ = standard deviation of $\log A_{H/V}(f)$, $\sigma_{logA}(f)$ is an absolute value which should be added or subtracted from the mean $\log A_{H/V}(f)$ curve
iv	$f_{peak}[A_{H/V}(f) \pm \sigma_A(f)] = f_0 \pm 5\%$	$\theta(f_0)$ =threshold value for the stability condition $\sigma_A(f) < \theta(f_0)$
v	$\sigma_f < \varepsilon(f_0)$	$V_{s,av}$ = average S-wave velocity of the total deposits
vi	$\sigma_A(f_0) < \theta(f_0)$	$V_{s,surf}$ = S-wave velocity of the surface layer
		h = depth to bedrock
		h_{min} = lower-bound estimate of **h**

Table 6.4: Tabular display of the stability analysis of the H/V parameters of the seismological stations. Broadband - BB, Short period - SP and Extended short period - ESP seismometer. Note: empty cells show unavailability of data.

Station Code (instrument)	Winter season		Summer season		Average F_0(Hz)	Winter season		Summer season		Average A_0
	Night	Day	Night	Day		Night	Day	Night	Day	
	F_0(Hz)		F_0(Hz)			A_0		A_0		
BFT (ESP)	3.74				3.74	1.22				1.22
CER (BB)	6.42	8.67	8.43	8.34	8.00	1.47	1.49	1.51	1.47	1.48
CVNA (BB)	1.85	1.94	1.93	1.99	1.93	1.16	1.30	1.25	1.28	1.23
ELIM (SP)	7.91	7.72	7.40	7.42	7.61	1.47	1.89	1.45	1.68	1.62
GRHM (BB)	1.88	2.18	2.13	2.13	2.08	0.99	1.04	1.05	1.00	1.02
HVD (ESP)	0.58	0.41	0.54	0.56	0.52	1.10	1.31	1.10	1.04	1.14
KOMG (ESP)	0.43	0.56	0.64	0.51	0.54	1.66	1.81	1.56	1.80	1.71
KSR (ESP)	0.40	0.40	0.43	0.56	0.45	1.35	1.30	1.36	1.37	1.35
KSTD (BB)	1.61	1.51	1.87	1.48	1.62	1.47	1.47	1.40	1.48	1.46
LEPH (ESP)	-	-	7.74	-	7.74	-	-	1.22	-	1.22
MATJ (BB)	18.93	18.1	18.68	16.7	18.1	1.49	1.42	1.53	2.12	1.64
MOPA(SP)	1.33	1.32	1.28	1.27	1.30	2.77	3.04	3.07	3.05	3.00
MSNA (BB)	-	-	5.49	4.44	4.97	1.33	1.32	1.33	1.35	1.33
NWCL (SP)	1.52	1.62	I.63	1.51	1.57	1.55	1.50	1.44	1.36	1.46
PKA (ESP)	-	-	-	-	-	1.27	1.20	1.40	1.40	1.32
POGA (BB)	6.20	8.41	8.30	7.57	7.62	1.32	1.25	1.34	1.20	1.28
PRYS (ESP)	1.64	2.10	1.70	1.89	1.83	1.89	2.45	2.40	2.41	2.30
ROSN (SP)	-	9.47	9.23	9.54	9.41	-	2.43	2.76	4.27	3.13
SEK (ESP)	3.88	3.85	-	-	3.87	1.56	1.82	-	-	1.69
SLR (BB)	5.85	6.47	6.13	5.75	6.05	1.44	1.61	1.57	1.62	1.56
SOE (ESP)	-	-	-	-	-	1.21	1.41	1.28	1.35	1.25
SWZ (ESP)	5.90	5.70	5.50	5.60	5.68	1,41	1.42	1.40	1.46	1.42
UPI (BB)	0.97	1.02	0.92	0.85	0.94	2.30	2.30	2.20	2.20	2.25
WDLM (BB)	1.52	1.52	1.67	1.62	1.58	1.50	1.68	2.00	2.60	2.00

6.6. Influence of parameters involved in signal processing

In this section, the influences of various parameters used in microtremor signal processing were examined.

6.6.1. Window length (WL) variation

The alteration of the window length was inspected to check the minimum window length required to obtain a reliable H/V curve. Analyses of four different window lengths were performed. Figure 6.6 shows the results obtained with 10s, 40s, 60s

and 120s window length, UPI station is presented as an example. Comparing the H/V curves, it can be observed that short window length (10s as observed in the data) could result in inadequate sampling of low frequency values within the Fourier spectra considering the hatched areas shown in the Figure 6.6a and Figure 6.6b. This could result in a wrong estimation of predominant frequency and amplification amplitude. Thus, considering the analysis performed in this study, it is recommended to use at least 30 s window lengths for adequate spectrum frequency representation.

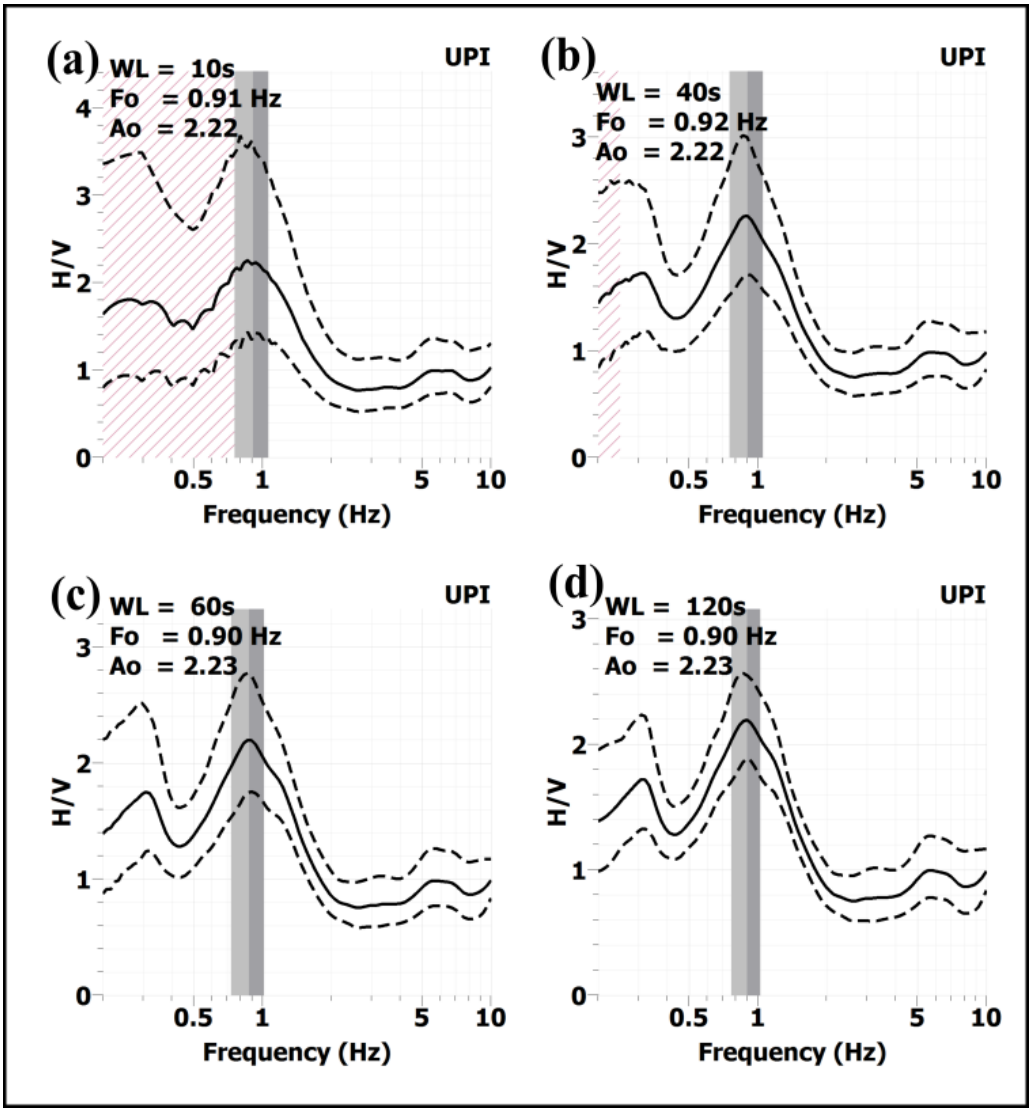


Figure 6.6: Variation of window length. (a) WL = 10s; (b) WL =40s; (c) WL =60s; (d) WL =120. 95 different noise windows were selected and averaged. The hatched area shows the underrepresented frequency spectrum.

6.6.2. Variation in percentage of overlap

The effect of varying the percentage of overlap between the selected noise windows is shown in Figure 6.7. Testing were conducted using 0, 10, 20, and 50% window length overlap, and WDLM station as an example. Comparing the H/V curves in Figure 6.7, it appears that variation in the percentage of overlap has little effect on the H/V parameters. However, it is recommended to use a certain percentage of overlap in order to obtain enough windows for adequate average (SESAME recommends at least 10 % window length overlap).

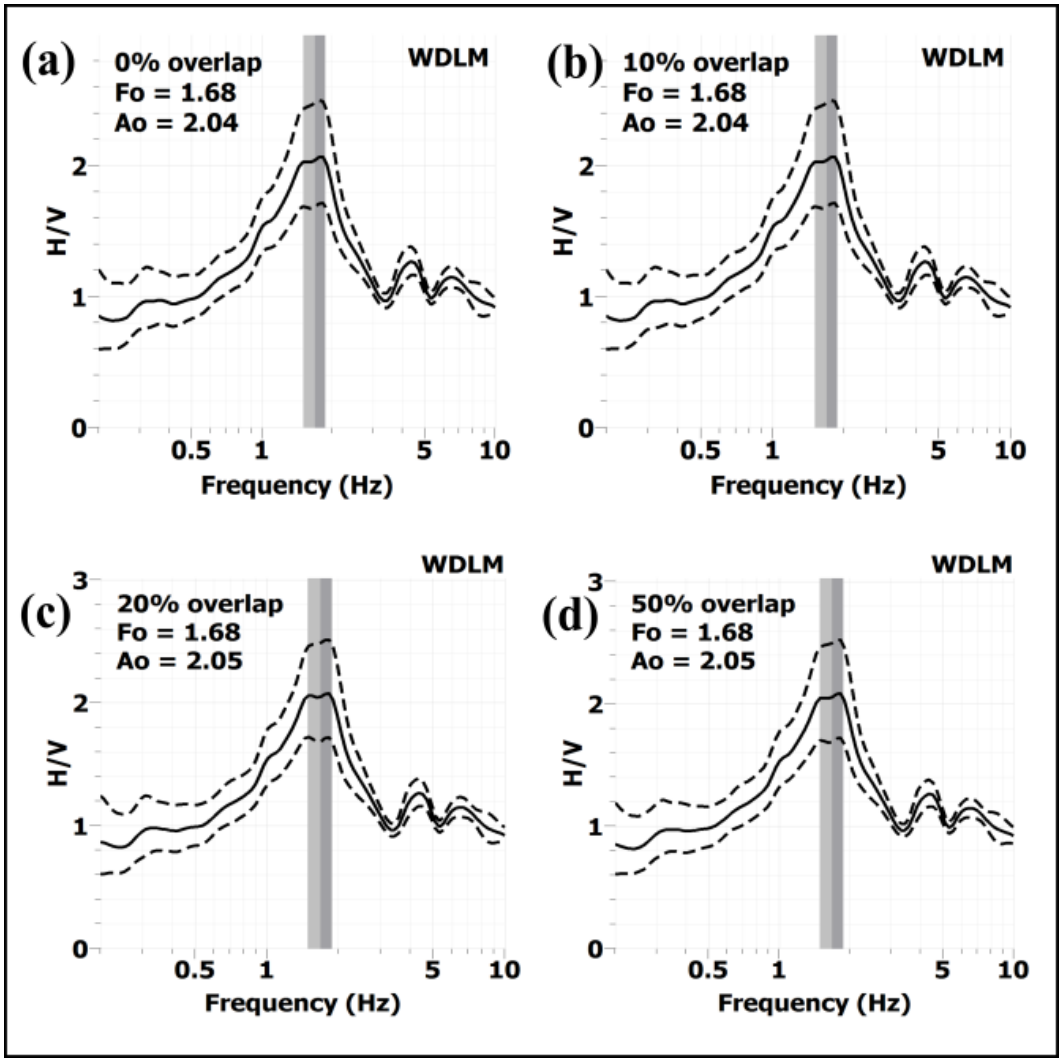


Figure 6.7: Variation of percentage overlaps between windows. (a) 0% overlaps (b) 10% overlap (c) for 20% overlap (d) 50% overlap (36 different noise windows were calculated in each the following analysis using the WDLM station).

6.6.3. Varying the percentage of cosine taper width along with the smoothing function

Here different percentages of Cosine taper were tested so as to observe its effect on the H/V parameters during signal processing. Four different percentage values (0%, 0.5%, 5% and 50%) were used. The results of the PRYS station are shown in Figure 6.8. Comparing the H/V curves in Figure 6.8, it was observed that the percentage of Cosine taper can have a significant effect on H/V parameters. Thus, one should be very careful when selecting the value to use, because applying small values can totally change the shape of the H/V curve, and cause misinterpretation of H/V parameters as shown in Figure 6.8a and b. It is advisable to use appreciable values (above 1%); since the observed results revealed that small values (less than 1%) can truncate the signal.

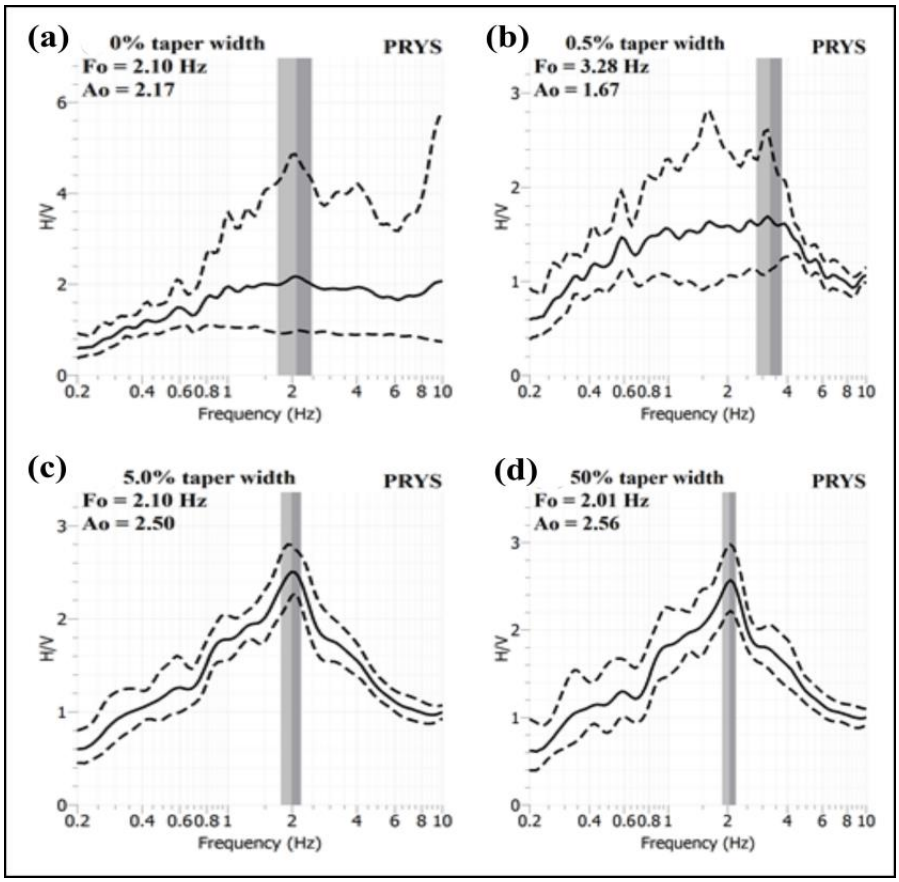


Figure 6.8: Varying the percentage of Cosine taper width. (a) 0% taper width; (b) 0.5% taper width; (c) 5% taper width; (d) 50% taper width (30 different noise windows were calculated in each analysis for PRYS station).

6.6.4. Variation of smoothing constant (b)

The variation of the coefficient (smoothing constant "b") was carried out, in order to observe its effect on the H/V characteristics as shown in Figure 8 (using MOPA station sample). Comparing the H/V curves in Figure 6.9, it shows that the smoothing constant value has a significant effect, not only on the H/V peak ratio, but also on the predominant frequency of the microtremor signal. Therefore, considering the appropriate b-value, there seems to be a balance between the two H/V parameters (A_0 and F_0); a smaller b-value is better when acquiring a linear relationship between the A_0 and velocity contrasts, while a larger b-value is preferred when reducing the shift in F_0 towards the right side of the H/V curve as revealed in the Figure 6.9 (Konno and Ohmachi., 1998). However, it is recommended to apply a reasonable value (20-40) when processing H/V spectral signals. In this study, a b-value of either 20 or 40 was applied, considering the effect of non-stationary transients on the signal. In the case where a serious transient was noticed, b = 20 was applied, while b = 40 was applied to signals free of transients.

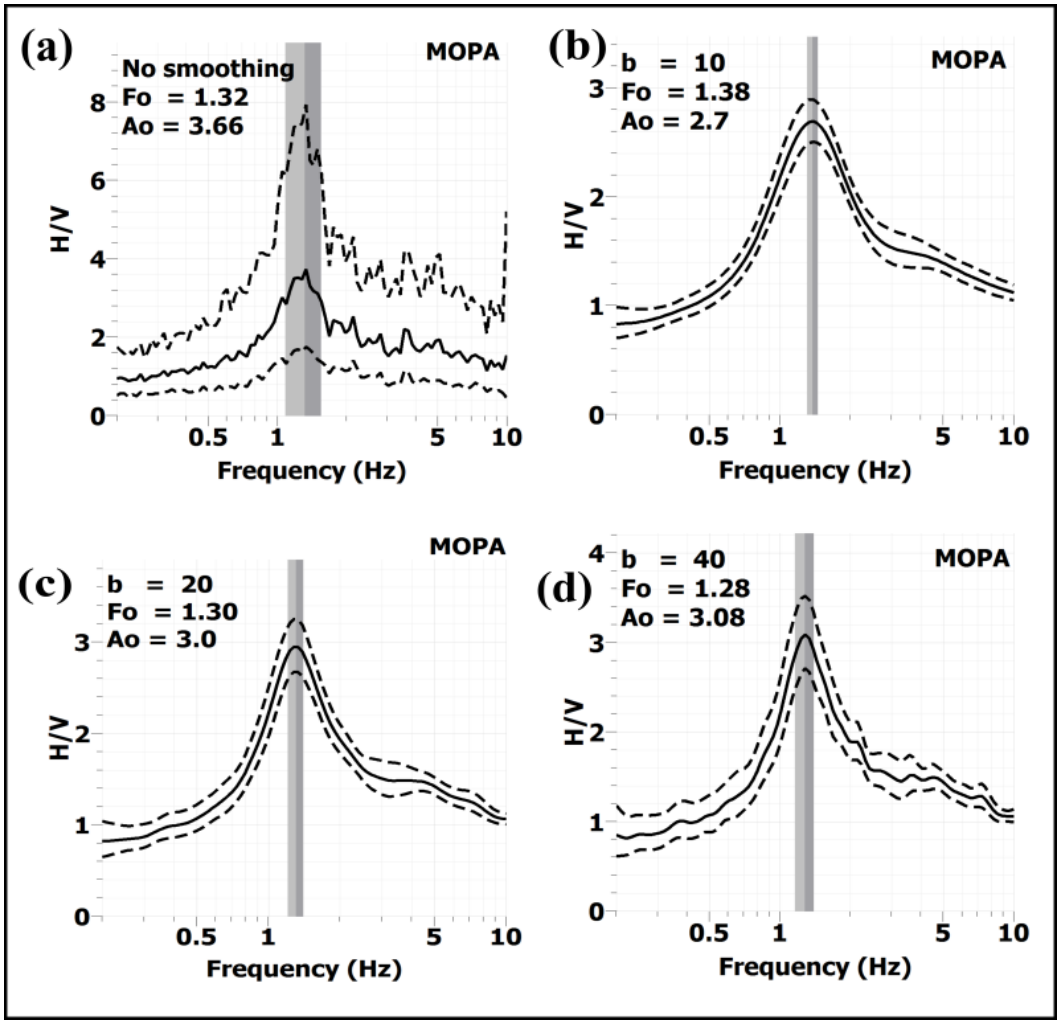


Figure 6.9: Variation of smoothing constant (b). (a) No smoothing; (b) b = 10; (c) b = 20 (d) b = 40 (79 different noise windows were calculated in each analysis using MOPA station).

6.7. Results and interpretation

The analysis of the HVSR curve at the 24 SANSN (Figure 6.10, Figure 6.11) has been computed. Table 6.4 and Table 6.5 show the results of the stability and reliability analysis of the H/V calculation, respectively. One-year microtremor noise window length was analysed. Table 6.6 shows the results of the low-velocity-layer thickness and vulnerability index for liquefaction approximated for stations that satisfied the clarity criteria of the SESAME project.

Generally, interpretation was based on the shape of the H/V curve as follows:

i. A clear H/V peak was found at seven stations (GRHM, KOMG, KSTD, MOPA, PRYS, UPI, and WDLM) (Figure 6.10a). The clarity of the peak can be interpreted as an evidence of significant velocity contrast between the top layer and the bedrock. These results also revealed that the stations that were situated on the alluvial sand, superficial deposit and highly weathered surface (MOPA, PRYS, UPI, and WDLM) were characterised by low peak frequency values ranging from 0.94 to 1.83 Hz, reflecting the effect of sediment thickness with H/V amplitude range of 2.20 to 3.13. These stations satisfied the criteria for a clear H/V peak and may likely amplify the ground motion during earthquake events.

ii. A double H/V peak was found at three stations (BFT, CVNA and NWCL) (Figure 6.10b). These stations revealed two H/V peaks with general low H/V amplitude (A_0 < 1.5) and peak frequency at 3.75, 1.95 and 1.57 Hz, respectively. The second peaks represent other natural resonance frequencies (the shallowest subsoil interface). These spectra could be interpreted as an indication of two successive hard geological formations with significant impedance contrast between the successive boundaries.

iii. A broad peak and plateau-like curve was found at four stations (HVD, LEPH, POGA and ROSN) (Figure 6.10c). These stations were placed in the mountain valley/rolling hill terrains, yielding a broad peak (LEPH and POGA) and plateau-like H/V curves (HVD and ROSN) with predominant frequency range of 6 to 10 Hz and 0.3 to 1.5 Hz, respectively. There H/V amplitudes were generally less than 1.30.

iv. A flat H/V with sign of no amplification was found at seven stations (CER, ELIM, KSR, PKA, SLR, SOE and SWZ) (Figure 6.10d). These stations were installed in a hard rock formation. They show a flat H/V curves with general low amplification amplitude range (A_0 < 1.5), which is expected from a rock site.

v. Finally, a spurious H/V peak was found at three stations (MATJ, MSNA and SEK). The evidence of spurious H/V peaks was confirmed in the Fourier

amplitude spectra of these stations (Figure 6.11). The analysis of Fourier frequency spectra provided insight into the distribution of energy over the analysed frequency range. The spurious peak could be due to a transient signal of industrial origin or other anthropogenic sources. These peaks were not considered as the true peak of the H/V curve. Note, for someone to be aware of this false peak, the transient spike should occur at the same particular peak frequency in the Fourier spectrum of all the three components.

Considering the H/V curves in Figure 6.10, the H/V characteristics from the stations that satisfied the criteria for a clear H/V peaks were further used to estimate the thickness and vulnerability index for liquefaction of the sedimentary cover. The mathematical model used in these approximations may not be the appropriate model for all the investigated sites since the background nature of the wavefield varies in different sites. However, the estimated vulnerability index was considered low when compared with the values Nakamura (1997 and 2000) estimated for the region affected by the 1989 Loma Prieta earthquake in California.

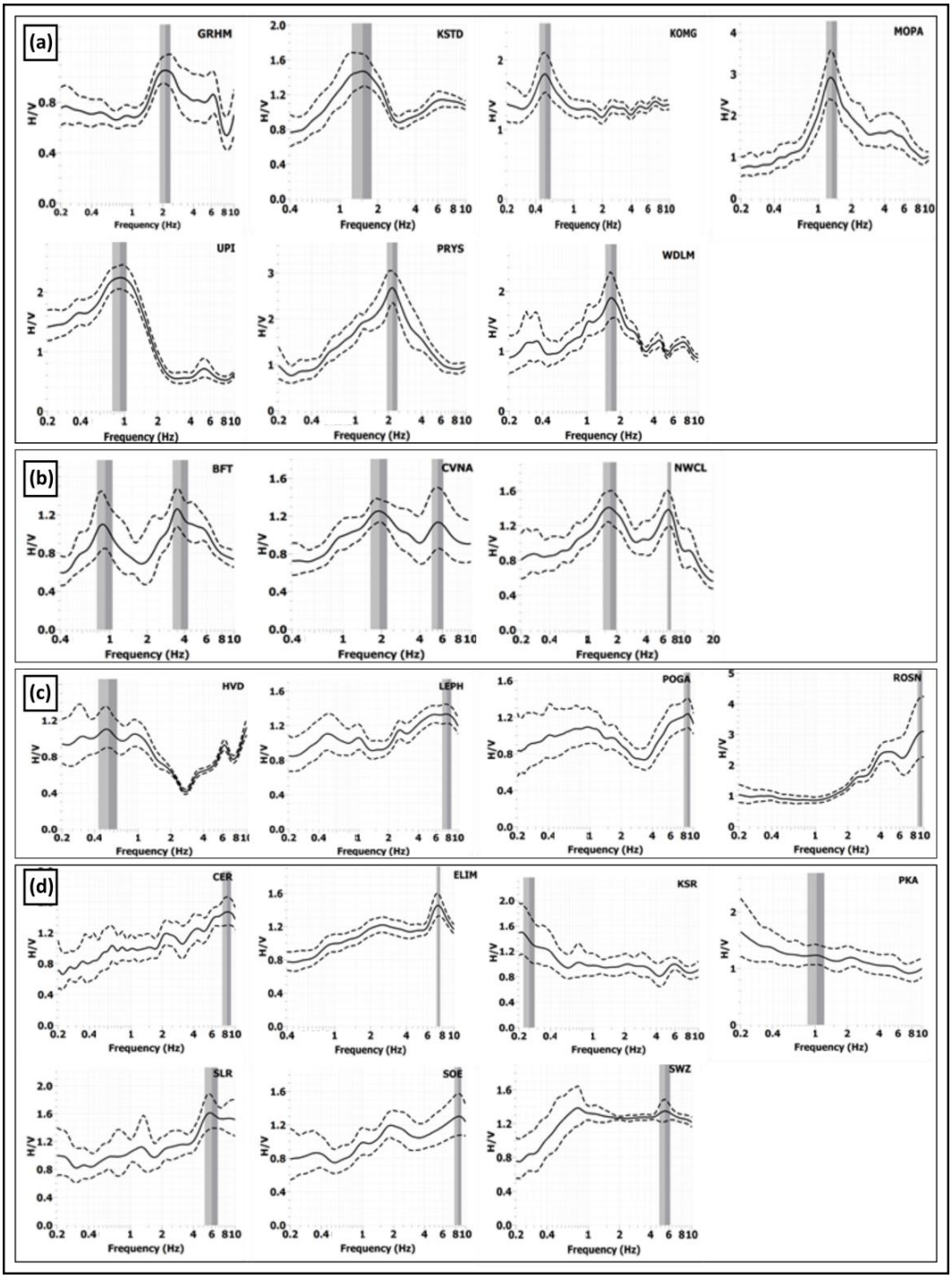


Figure 6.10: Amplitudes of H/V ratio as a function of predominant frequencies. (a) Stations with clear H/V curves, (b) station with double H/V peaks, (c) stations with broad peak/plateau-like curve and (d) stations with flat H/V curves.

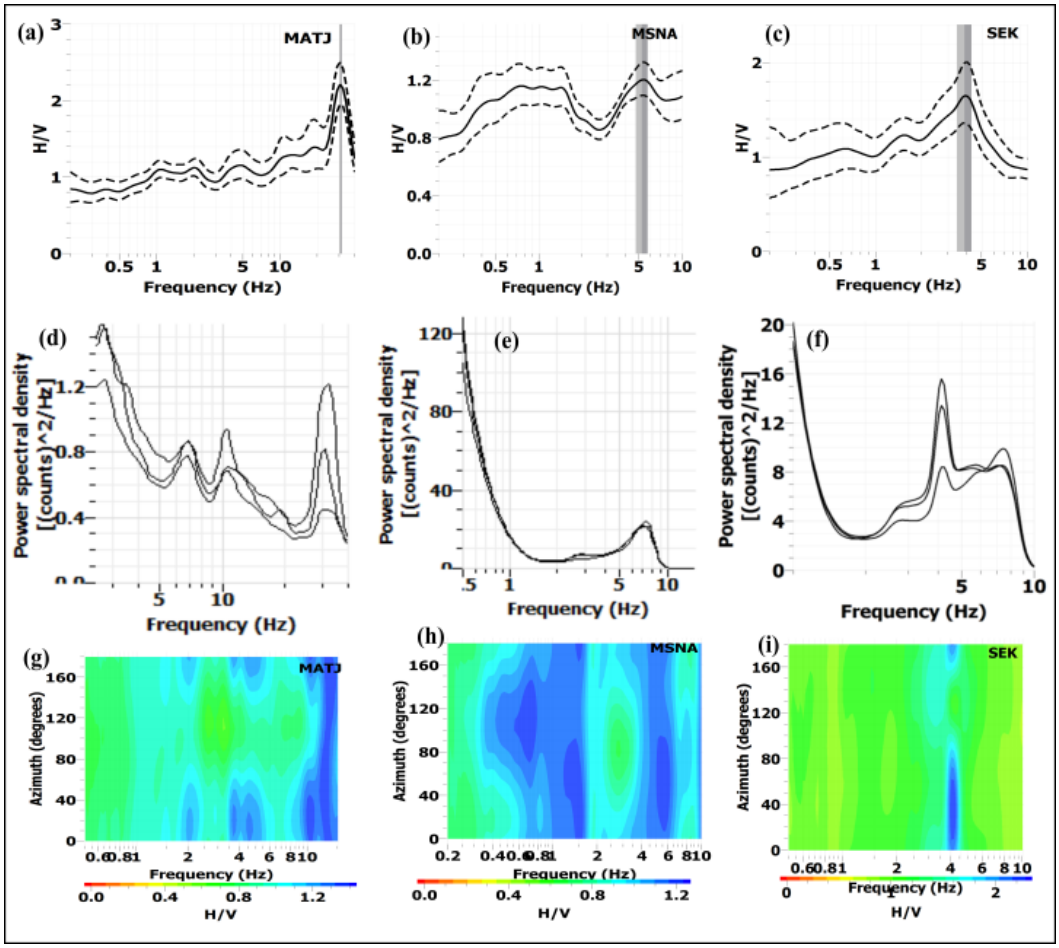


Figure 6.11: Examples of spurious peaks due to non-stationary transients on the microtremor signals. (a), (b) and (c) are the H/V curve for MATJ, MSNA and SEK stations, respectively; (d), (e) and (f) are the respective frequency spectra of the three components of the seismometer (each curve represent E, N or Z component); and (g), (h) and (i) are the respective azimuth versus frequency of the power spectral density (note the transient spike on the frequency spectrum of all the three components occur at the same frequency value).

Table 6.5: Reliability of the predominant frequency as defined by SESAME (2004) guidelines (N_w-number of windows, WL-window length, n_c-number of significant cycles and σ_A-standard deviation error for amplification)

Station Code	Average F_0(Hz)	Average A_0	N_w	WL	F_0 >10/WL	n_c> 200	$\sigma_A(f)$< 2	comment
BFT	3.74	1.22	16	35	0.29	2094	±0.19	Reliable
CER	8.00	1.48	24	60	0.17	11520	±0.17	Reliable
CVNA	1.93	1.23	53	60	0.17	6137	±0.18	Reliable
ELIM	7.61	1.62	122	120	0.08	111410	±0.35	Reliable
GRHM	2.08	1.02	77	60	0.17	9610	±0.15	Reliable
HVD	0.52	1.14	26	30	0.33	406	±0.34	Reliable
KOMG	0.54	1.71	90	120	0.08	5832	±0.26	Reliable
KSR	0.45	1.35	28	50	0.20	630	±0.31	Reliable
KSTD	1.62	1.46	24	60	0.17	2333	±0.15	Reliable
LEPH	7.74	1.22	59	60	0.17	27400	±0.10	Reliable
MATJ	18.1	1.64	99	120	0.08	215028	±0.32	Reliable
MOPA	1.30	3.00	79	100	0.10	10270	±0.45	Reliable
MSNA	4.97	1.33	95	100	0.10	47215	±0.28	Reliable
NWCL	1.57	1.46	29	60	0.17	2732	±0.15	Reliable
PKA	-	1.32	53	75	-	-	±0.26	Flat curve
POGA	7.62	1.28	40	60	0.17	18288	±0.19	Reliable
PRYS	1.83	2.30	30	40	0.25	2196	±0.57	Reliable
ROSN	9.41	3.13	40	60	0.17	2196	±0.86	Reliable
SEK	3.87	1.69	44	60	0.17	10217	±0.30	Reliable
SLR	6.05	1.56	38	50	0.20	11495	±0.22	Reliable
SOE	-	1.25	20	30	-	-	±0.16	Flat curve
SWZ	5.68	1.42	59	75	0.13	25134	±0.20	Reliable
UPI	0.94	2.25	95	120	0.08	10716	±0.41	Reliable
WDLM	1.58	2.00	36	60	0.17	3413	±0.36	Reliable

Table 6.6: Approximate sediment thickness and vulnerability index (K_g)

Station code	**F_0 (Hz)**	**A_0**	**$h=96f_r^{-1.388}$ (m)**	**$h=108f_r^{-1.551}$ (m)**	**$K_g = A_0^2 / F_0$**
MOPA	1.30	3.00	71.9	66.7	6.92
PRYS	1.82	2.30	42.7	41.8	2.9
UPI	0.94	2.25	118.9	104.6	5.4
WDLM	1.58	2.00	53.1	50.9	2.53

6.8. Discussion and conclusion

The use of horizontal to vertical spectral ratio (HVSR) technique to analyse microtremor signals has proven to be an effective tool to characterise the site effect for microzonation and seismic hazard assessment, irrespective of the debate concerning the theoretical background. In this study we aimed to estimate and investigate the stability and reliability of the local site effect characteristics at 24 permanent seismological stations in South Africa. The stability and reliability analysis of the H/V spectral ratio parameters (predominant frequency and amplification amplitude) of the recorded data shows that the estimated results were reliable and stable (Table 6.4 and Table 6.5). The results showed that the predominant frequency (F_0) was not affected by the time-of-day or season, while the H/V ratio is slightly affected by the time-of-day when the signal was recorded. Hence, the calculated predominant frequency can be used to estimate the fundamental resonance frequency value of the top low-velocity-layer (typically weathered rock or sedimentary cover), while the amplification of the H/V ratio yields the lower bound of the actual site amplification factor. Additionally, it was observed that the geological conditions were the prominent factor responsible for the variation in the H/V spectral ratio. The effect of processing parameters such as window length, smoothing constant, percentage of window overlap, and Cosine taper function were studied, while the effect due to instrumental type was not achieved in this study because only one type of instrument were used to record signals at each site.

Generally, considering the results from all the seismic stations, it was found that the fundamental resonance frequency of the top low-velocity-layer was in the range 0.4 – 18 Hz, and the H/V amplitude of the microtremor signal varied from 1 to 3 (Table 6.5). Picozzi et al. (2009) and Talha Qadri et al. (2015) have also used this technique successfully to estimate site effects in Istanbul, Turkey, and Fateh Jang, Pakistan, respectively. Moreover, the results further revealed that seven stations placed on weathered surfaces or soil columns displayed spectral peaks that satisfied the criteria for a clear H/V peak. These sites could be subjected to ground motion amplification during an earthquake. Furthermore, the stations

placed on solid bedrock revealed a flat H/V curve, while the stations located on the valley/rolling hill terrain revealed broad peak/plateau-like curves.

Table 6.6 shows the estimated sediment thickness (h) and vulnerability index (K_g) for liquefaction of those stations that satisfied the clear H/V peak criteria, although the K_g values were generally lower than 7, showing that there is no risk of liquefaction in those sites, when it is compared with Nakamura's (1997) result. However, the shape of H/V curves revealed the surface geological characteristics of the station sites. Figure 6.12 shows the site effect response characteristics of the seismological stations superimposed on the seismic hazard map of South Africa. The black circles indicate the fundamental frequency, while the red stars represent the different range of the H/V amplitude. From Figure 6.12, it is noted that some stations (UPI, MOPA, PRYS and WDLM), which could be subjected to amplification during earthquake ground motion, are located in regions with higher seismic hazard. Therefore, dense data acquisition in these regions is recommended and other geophysical techniques such as seismic refraction and multichannel analysis of surface wave (MASW) should be conducted. These complementary geophysical methods will provide an integrated approach in estimating the appropriate thickness and shear wave velocities of the sedimentary cover or weathered layers in the sites. Finally, the HVSR technique using microtremor signals can provide a fast, cheap and complementary geophysical method to determine site effect characteristic for microzonation and seismic hazard assessment of cities in South Africa.

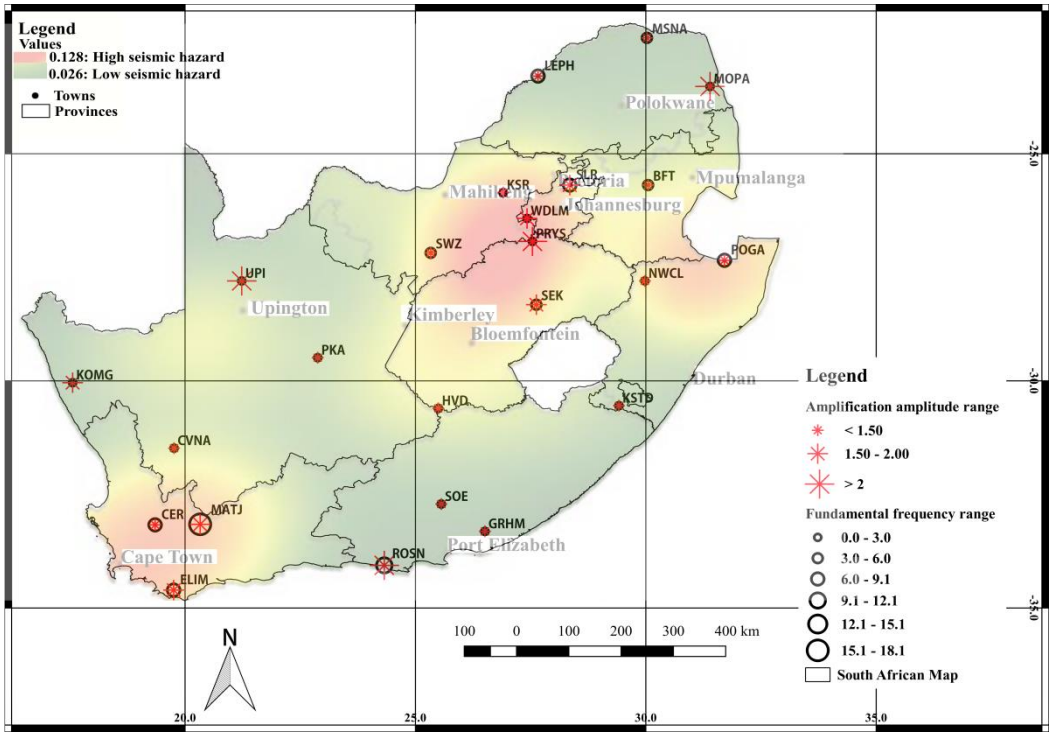


Figure 6.12: Site characteristics of the seismological stations placed on the map of current seismic hazard for South Africa. Expected peak ground acceleration (PGA, in g) with a 10% probability of being exceeded at least once in a 50-year period (Esterhuyse et al. 2014, modified by Kijko et al. 2016).

Acknowledgments

Acknowledgment goes to AfricaArray Research Group, Council for Geoscience and South African National Seismograph Network (SANSN) for giving me access to the data used in this study. We want to thank University of the Witwatersrand, Geophysics department for technical and financial support, and the SESAME Research Group for the free access software.

6.9. References

Aki, K., 1957. Space and time spectra of stationary stochastic waves, with special reference to microtremors. *Bulletin of the Earthquake Research Institute., 35,* pp .415-456.

Ansary, M.A. and Rahman, M.S., 2013. Site amplification investigation in Dhaka, Bangladesh, using H/V ratio of microtremor. *Environmental earth sciences, 70*(2), pp. 559-574.

Bonilla, M.G. and O'Rourke, T.D., 1992. Geologic and historical factors affecting earthquake damage: The Loma Prieta, California, Earthquake of October 17, 1989-Marina District, p. 215.

Chinoda, G., Matura, N., Moyce W. and Owen R., 2009. Baseline Report on the Geology of the Limpopo Basin Area: A Contribution to the Challenge Program on Water and Food Project. In 17 Integrated Water Resource Management for Improved Rural Livelihoods, Managing Risk, Mitigating Drought and Improving Water Productivity in the Water Scarce Limpopo Basin. Water-Net Working Paper 7. WaterNet, Harare. Online at: http://www.waternetonline.ihe.nl

Durrheim, R.J., Anderson, R.L., Cichowicz, A., Ebrahim-Trollope, R., Hubert, G., Kijko, A., McGarr, A., Ortlepp., W.D and van der Merwe N., 2007. Investigation into the Risks to Miners, Mines, and the Public Associated with Large Seismic Events in Gold Mining Districts, *2,* Department of Minerals and Energy, Pretoria.

Esterhuyse, S., Avenant, M., Watson, M., Redelinghuys, N., Kijko, A., Glazewski, J., Plit, LA., Kemp, M., Smit, A., Sokolic, F., Vos AT., Reynolds, D., von Maltitz, M., van Tol J., Bragg, C., van Soelen, B. and Ouzman, S., 2014. Development of an interactive vulnerability map and monitoring framework to assess the potential and environmental impact of unconventional oil and gas extraction by means of hydraulic fracturing: Seismic hazard map for South Africa, Revision 2013. University of Pretoria Natural Hazard Centre, Africa, Open File Report, June 2013. WRC Report No. 2149/1/14, 2014.

Fenton, C.H. and Bommer, J.J., 2006. The M_w7 Machaze, Mozambique's earthquake of 23 February 2006. *Seismological Research Letters*, *77*(4), pp. 426-439.

Fourie, C., Combrinck, L., Croukamp, L. and Saunders, I., 2007, October. A Proposed Space Geodesy Observatory Near Matjiesfontein: A Geotechnical Site Investigation: In Proceedings of the 5th Inkabaye Africa Workshop, Wild Coast Sun, KZN, South Africa, pp. 22-23.

Geopsy Software Manual at www.geopsy.org, 2017/10/31.

Hunter, D.R., 1991. Crustal processes during Archaean evolution of the southeastern Kaapvaal Province. *Journal of African Earth Sciences, 13* (1), pp. 13-25

Ibs-von Seht, M. and Wohlenberg, J., 1999. Microtremor measurements used to map thickness of soft sediments. *Bulletin of the Seismological Society of America*, *89*(1), pp. 250-259.

Johnson, M.R., Anhaeusser, C.R. and Thomas, R.J., 2006. The Geology of South Africa: Geological Society of South Africa, Johannesburg and the Council for Geoscience, Pretoria.

Kanai, K.,1957. The requisite conditions for predominant vibration of ground. *Bulletin of the Earthquake Research Institute, Tokyo University, 31,* p. 457- 495.

Kijko, A. and Cichowicz A., 2006. Origin, Intensity and Damage Potential of Tectonic and Mining Seismic Events. Seismological Unit, Council for Geoscience, South Africa, Seismological Report. Appendix 4.2.

Kijko, A.N.D.R.Z.E.J., Smit, A., Kahle, B. and Glazewski, J., 2016. Hydraulic Fracturing, Waste Water Pumping and Seismicity. Proposed Hydraulic Fracturing in the Karoo: Critical Perspectives. Chapter 13, pp. 263-276.

Konno, K., and Ohmachi, T., 1998. Ground motion characteristics estimated from spectral ratio between horizontal and vertical components of microtremors. *Bulletin Seismological Society of America*, *88*(1), pp. 228-241.

Kwak, D.Y., Stewart, J.P., Mandokhail, S.U.J. and Park, D., 2017. Supplementing VS^{30} with H/V spectral ratios for predicting site effects. *Bulletin of the Seismological Society of America, 107*(5), pp. 2028-2042.

Lachet, C., and Bard, P.Y., 1994. Numerical and theoretical investigations on the possibilities and limitations of Nakamura's technique. *Journal of the Physics of the Earth, 42,* pp. 377-397.

McCarthy, T. and Rubidge, B., 2005. The Story of Earth and Life. *Struik Publishers*, Cape Town, pp. 159-161, 182, 187-195, 202-207, 267-269, 302.

Midzi, V., Zulu, B., Manzunzu, B., Mulabisana, T., Pule, T., Myendeki, S. and Gubela, W., 2015. Macroseismic survey of the M_L5. 5, 2014 Orkney earthquake. *Journal of Seismology, 19,* pp. 741-751.

Nakamura, Y., 1989. A method for dynamic characteristics estimation of subsurface using microtremor on the ground surface. *Railway Technical Research Institute, Quarterly Reports, 30*(1). pp.25-33.

Nakamura, Y., 1997. Seismic vulnerability indices for ground and structures using microtremor: In World Congress on Railway Research, Florence, Italy.

Nakamura, Y., 2000. Clear identification of fundamental idea of Nakamura's technique and its applications: In Proceedings of the 12th World Conference on Earthquake Engineering, Auckland, New Zealand, paper no 2656.

Nogoshi, M. and Igarashi, T., 1971. On the amplitude characteristics of microtremor, Part II. *Journal of the seismological society of Japan, 24*, pp. 26-40.

Ogasawara, H., Durrheim, R.J., Nakatani, M., Yabe, Y., Milev, A., Cichowicz, A., Kawakata, H., Moriya, H. and the JST-JICA SA research group., 2009. A Japanese - South African Collaboration to Mitigate Seismic Risks in Deep Gold Mines: The Southern African Institute of Mining and Metallurgy Hard Rock Safe Safety Conference, pp. 115-134.

Parolai, S., Bormann, P. and Milkereit, C., 2002. New relationships between Vs, thickness of sediments, and resonance frequency calculated by the H/V ratio of

seismic noise for the Cologne area (Germany). *Bulletin of the seismological society of America*, *92*(6), pp. 2521-2527.

Picozzi, M., Strollo, A., Parolai, S., Durukal, E., Özel, O., Karabulut, S., Zschau, J. and Erdik, M., 2009. Site characterization by seismic noise in Istanbul, Turkey. *Soil Dynamics and Earthquake Engineering*, *29*(3), pp. 469-482.

Saunders, I., Brandt, M.B.C. and Kgaswane, E., 2007. Preliminary appraisal of the effect of a magnitude M_L5.3 event of 9 March 2005, Klerksdorp, South Africa: Report no 2005-0066. Council for Geoscience, Pretoria.

SESAME., 2004. Guideline for the implementation of the H/V spectral ratio technique on ambient vibrations: measurements, processing and interpretation. SESAME European research project, WP12, available online at: http://sesame-fp5.obs.ujfgrenoble. fr/index.htm., pp. 1–62.

Singh, M., Kijko, A. and Durrheim, R., 2009. Seismotectonic models for South Africa: Synthesis of geoscientific information, problems, and the way forward. *Seismological Research Letters*, *80*(1), pp. 71-80.

Suarez, L.E., Pando, M.A. and Ritta, R., 2012. Ambient vibration measurements for estimation of site fundamental period at the city of Mayaguez, Puerto Rico. USGS Grant Number: 10HQPAQ0001.

Talha Qadri, S.M., Bushra, N., Sajjad, S.H. and Sheikh, R.A., 2015. Ambient noise H/V spectral ratio in site effects estimation in Fateh Jang area, Pakistan. *Earthquake Society*, *28*(1) pp. 87–95.

Truswell, J.F., 1977. The Geological Evolution of South Africa. *Purnell*, Cape Town, pp. 93-96, 114-159.

Viljoen, M.J. and Reimold, W.U., 1999. An Introduction to South Africa's Geological and Mining Heritage. Randburg, South Africa, *Mintek Publisher*.

CHAPTER 7

7.0 General conclusions and recommendations

Integrated geophysical site investigations were employed at different locations in South Africa, to support various infrastructural and environmental development by providing necessary near-surface images and associated physical properties. The presented case studies in this thesis clearly demonstrate that an integrated geophysical approach improves the subsurface structural model when compared to an individual geophysical method. The various integrated approaches minimize the ambiguities associated with the geophysical dataset's interpretation, due to complementary capabilities and characteristics of each method. The interpretation was constrained with borehole and surface geological mapping information. I showed that the high-resolution reflection and/or refraction seismic method, when compared with other geophysical techniques (resistivity tomography, MASW, and magnetic method), are powerful tools for imaging near-subsurface architectures for hydrogeological prospecting, engineering and infrastructural development. In addition, I also demonstrated that microtremor signal characteristics (dominant frequency and spectral amplitude ratio) are stable and reliable to be used in site effect assessment for microzonation study in the area.

In **chapter 3**, high-resolution shallow reflection seismic method was integrated with refraction tomography, MASW and ERT, and constrained with borehole log information for hydrogeological prospecting in the Nylsvley Nature Reserve, South Africa. The result revealed that the depth to the bedrock and the weathered rock surface in the area were ~3 – 5 m and ~8 – 12 m, respectively, with P-wave velocities of ~1200 – 2500 m/s and 2800 – 6000 m/s, respectively. Thus, the interface within the intra-alluvium layer was interpreted as the groundwater table in the area. This study also showed that the bedrock undulation observed in the results (reflection section, refraction, and electrical resistivity tomogram) were associated with fractured/weathered zones, and was attributed to the fluid storage and migration pathways in the survey area. Hence, it was suggested that the saturated alluvium deposit base (sand/gravel) combined with the

fractured/weathered bedrock surface, constrained with MASW results, represent the hydrostratigraphic units in the area with an estimated thickness of about 18 – 38 m. The results and assertion confirmed the previous geological and environmental research conducted in the area, which suggested that the fractured/weathered zone within the bedrock surface is responsible for groundwater movement and storage in the area (Higgins et al., 1996, Tooth et al., 2002).

I recommended that the thickest undulated weathered/fractured zone in the survey area as the highest prospect location for a high yield groundwater borehole. Furthermore, I also recommend further geophysical investigation and geological (mainly drilling) investigation at the prospecting locations for underground water supply in the reserve.

A similar integrated geophysical approach was discussed in **chapter 4**. By using complementary geophysical methods approach, I was able to improve the mapping resolution of the subsurface features (mine-out, stopes, and weak zones) and estimate the geometry of the underlying features for environmental planning and site reclamation. The near-surface rocks of the Johannesburg Subgroup in the survey area revealed high-velocity and resistivity variations of about 400 – 2500 m/s and 60 – 2300 Ωm, respectively at depths 10 and 20 m. Although, some of these variations were attributed to the subsurface structure irregularities associated with mining environment. The bedrock velocities and resistivities vary from ~ 3500 to 6500 m/s and from 200 to 8000 Ωm, respectively. Moreover, the integration of high-resolution reflection seismics integrated with the refraction seismic and ERT, showed the delineation of the shallow mined-out areas and the bedrock-overburden contacts. The complementary RT and ERT sections comparatively improved near-surface images and detection resolution above 30 m in depth, while the reflection seismic provided high-resolution subsurface imaging down to about 100 m

Finally, the exact geometry of the subsurface structures could not be resolved due to the relatively low source frequency and energy, coupled with limited imaging capability of 2D data sets. Therefore, I recommend that further site

characterisations in this area should incorporate a 3D reflection seismic technique with a high-energy source, and denser receiver and shot spacing. It is hope that this will assist in resolving the thicknesses of the mined-out regions and further provide knowledge of the subsurface architecture in the area for infrastructural and environmental development.

Chapter 5 presented the results obtained from the interpretation of legacy 2D reflection seismic and magnetic field datasets for site investigation of the Archaean-Paleoproterozoic Transvaal Basin architecture, providing insights into hydrogeological prospecting and engineering application. Post-stack denoising techniques were applied to enhance and identify subsurface structures and formation boundaries. In addition, potential field processing methods, such as tilt and first vertical derivatives of the magnetic field, were also utilized to improve the quality of the magnetic data by delineating near-surface and long wavelength magnetic field anomalies. The integrated geophysical datasets were constrained with surface geological maps and borehole logs in mapping different formation boundaries. The geometry of the Rustenburg Fault (RF) previously mapped by the geologists was estimated, and the new features were observed and discussed. The RF new features were interpreted and modelled as a normal fault with the upthrown side on the NW and downthrown side on the SE. The vertical displacements were estimated at ~ 400 m and the surface lateral displacement is ~ 5 km.

The newly mapped subsurface deformation features such as faults systems formed a series of horst and graben, and half-graben structures, as well as a slump and palaeo-karst features associated with general heterogenous fractured system. The faults were predominantly normal faults with variable dips due to their association with antithetic and synthetic subtle faults. These structures exhibit complex features and a brittle shear-type of deformation, which could have occurred under extensional tectonic environment (Schreurs et al., 2002). Thus, validating Eriksson and Reczko (1995), Catuneanu and Eriksson (1999) and Eriksson et al. (2001) research report in the area. It was also observed that the dykes/sills provided palaeo-partitions within the rock formation. These compartments could

serve as a fluid storage zone in the area, coupled with the fractured and weathered undulated surface. The fault planes, erosional formation boundaries, joints and fractured zones were also observed for possible fluid migration pathways and storage.

Base on the limitations of my study, I recommended a 3D seismic interpretation and further reprocessing of the legacy 2D seismic data with modern algorithms. This will enhance structural discernibility and better understanding of the 3D geometries of these delineated geological features, as well as reconstruction of the subsurface geology and tectonic model in the survey area.

Chapter 6 showcased a study of an assessment of the site effect at the seismological network stations in South Africa using the continuous microtremor records. The research was a pilot project to assess the stability and reliability of the microtremor signal using the HVSR technique in the study area. The analysis employed the Nakamura (1989) method. The analysis confirmed that the microtremor characteristics of the network stations were stable and reliable. The technique is an inexpensive, fast, and reliable method that can be used to approximate the predominant frequency and spectral amplitude ratio of the ambient signal. The estimated microtremor characteristics were further used to assess the site effect at these network stations. This valuable information is required for any seismic hazard assessments and microzonation studies, as part of a comprehensive site characterisation of the survey area. Furthermore, the estimated dominant frequency of those stations that satisfied all the stability and reliability criteria of SESAME (2004) report was used to approximate the thickness of the low-velocity layer and the vulnerability index for liquefaction potential of those stations. It was also observed that some stations with high signal amplitudes and predominant frequencies could be subjected to ground motion amplification during seismic events.

Hence, I recommended an increase in the number of stations point around the stations that were seen to be susceptible to earthquake ground motion amplification and further microzonation study of the area.

7.1. Reference

Catuneanu, O. and Eriksson, P.G., 1999. The sequence stratigraphic concept and the Precambrian rock record: An example from the 2.7–2.1 Ga Transvaal Supergroup, Kaapvaal Craton. *Precambrian Research*, *97*(3-4), pp. 215-251.

Eriksson, P.G. and Reczko, B.F.F., 1995. The sedimentary and tectonic setting of the Transvaal Supergroup floor rocks to the Bushveld Complex. *Journal of African Earth Sciences*, *21*(4), pp. 487-504.

Eriksson, P.G., Altermann, W., Catuneanu, O., Van der Merwe, R. and Bumby, A.J., 2001. Major influences on the evolution of the 2.67–2.1 Ga Transvaal basin, Kaapvaal Craton. *Sedimentary Geology*, *141*, pp. 205-231.

Higgins, S.I., Coetzee, M.A.S., Marneweck, G.C. and Rogers, K.H., 1996. The Nyl River floodplain, South Africa, as a functional unit of the landscape: A review of current information. *African Journal of Ecology*, *34*(2), pp. 131-145.

Nakamura, Y., 1989. A method for dynamic characteristics estimations of subsurface using microtremor on the ground surface. *Railway Technical Research Institute, Quarterly Reports, 30(1).* pp. 25-33.

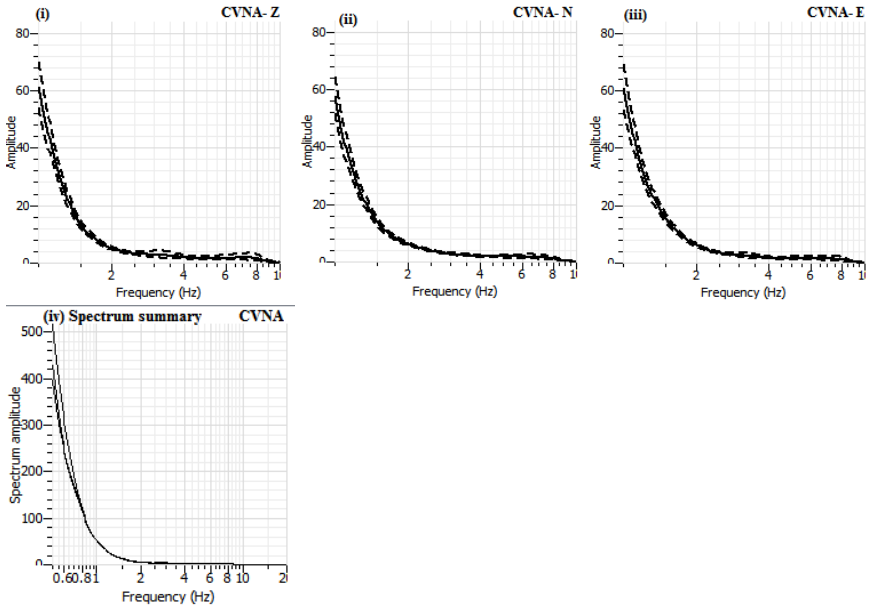
Schreurs, G., Buiter, S.J., Boutelier, D., Corti, G., Costa, E., Cruden, A.R., Daniel, J., Hoth, S., Koyi, H.A., Kukowski, N. and Lohrmann, J., 2006. Analogue benchmarks of shortening and extension experiments. *Special Publication-Geological Society of London*, *253*, pp. 1 - 27.

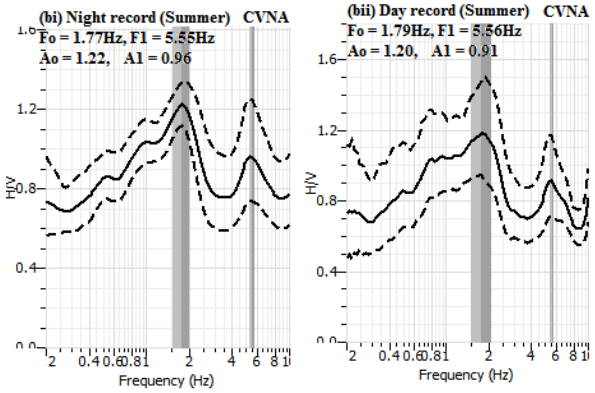
SESAME, 2004. Guideline for the implementation of the H/V spectral ratio technique on ambient vibrations: measurements, processing and interpretation. SESAME European research project, WP12, available online at: *http://sesame-fp5.obs.ujfgrenoble. fr/index.htm*, pp. 1–62.

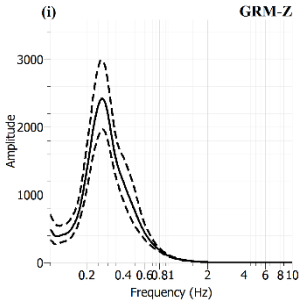
Tooth, S., McCarthy, T.S., Hancox, P.J., Brandt, D., Buckley, K., Nortje, E. and McQuade, S., 2002. The geomorphology of the Nyl River and floodplain in the semi-arid Northern Province. *South African Geographical Journal*, *84*, pp. 226–37.

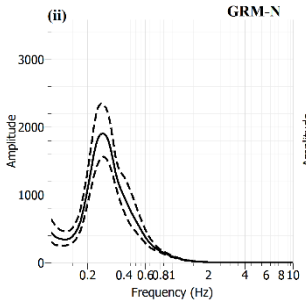
Appendix 1

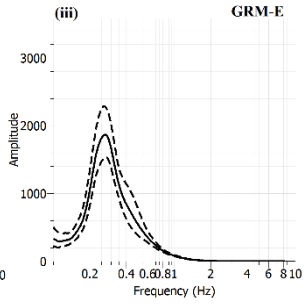
Frequency spectrum and HVSR curve of the individual stations

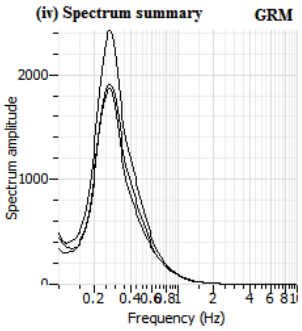


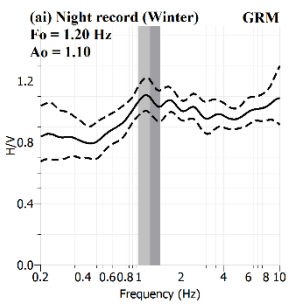


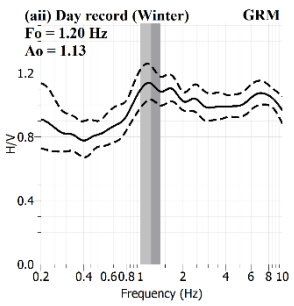

(i)
GRM-Z
Amplitude
Frequency (Hz)

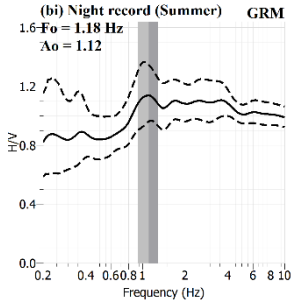

(ii)
GRM-N
Amplitude
Frequency (Hz)

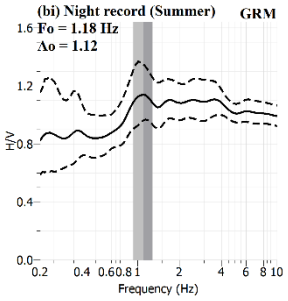

(iii)
GRM-E
Amplitude
Frequency (Hz)

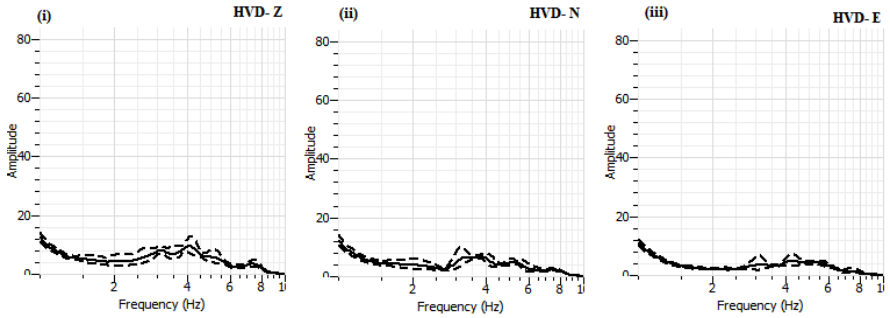

(iv) Spectrum summary
GRM
Spectrum amplitude
Frequency (Hz)

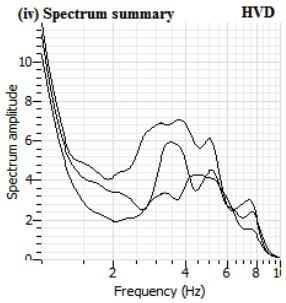

(ai) Night record (Winter)
GRM
Fo = 1.20 Hz
Ao = 1.10
H/V
Frequency (Hz)

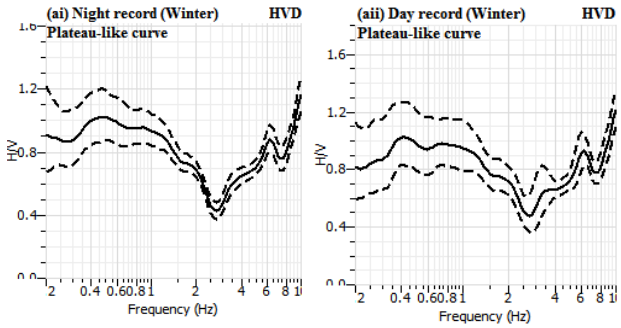

(aiii) Day record (Winter)
GRM
Fo = 1.20 Hz
Ao = 1.13
H/V
Frequency (Hz)

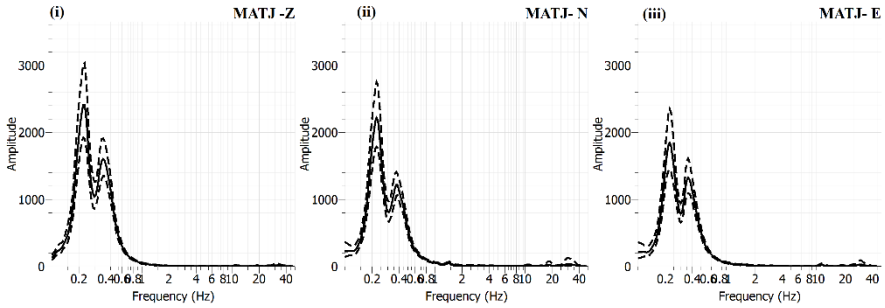

(bi) Night record (Summer)
GRM
Fo = 1.18 Hz
Ao = 1.12
H/V
Frequency (Hz)

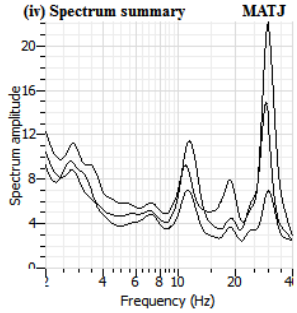

(bi) Night record (Summer)
GRM
Fo = 1.18 Hz
Ao = 1.12
H/V
Frequency (Hz)

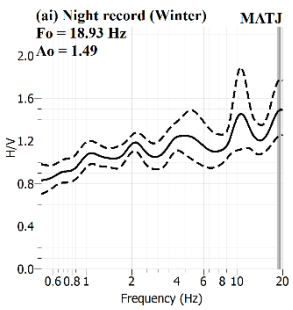

(i) HVD- Z
(ii) HVD- N
(iii) HVD- E
Amplitude
Frequency (Hz)

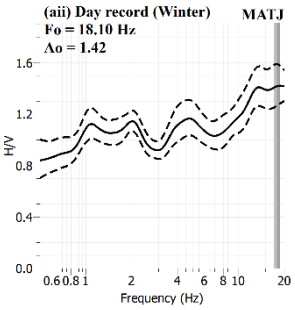

(iv) Spectrum summary HVD
Spectrum amplitude
Frequency (Hz)

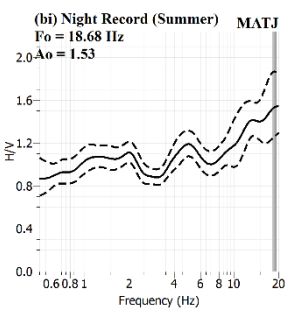

(ai) Night record (Winter) HVD
Plateau-like curve
(aii) Day record (Winter) HVD
Plateau-like curve
H/V
Frequency (Hz)

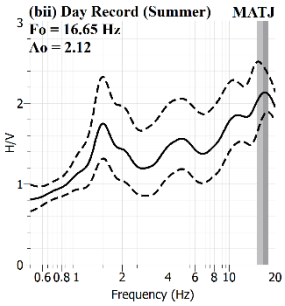

(i) MATJ -Z
(ii) MATJ- N
(iii) MATJ- E
Amplitude
Frequency (Hz)

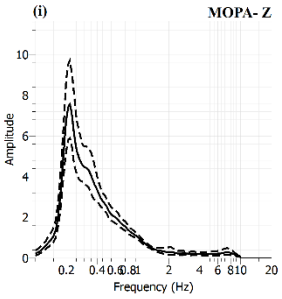

(iv) Spectrum summary MATJ
Spectrum amplitude
Frequency (Hz)

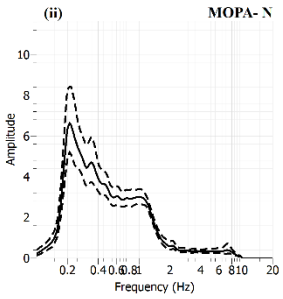

(ai) Night record (Winter)
MATJ
Fo = 18.93 Hz
Ao = 1.49
H/V
Frequency (Hz)

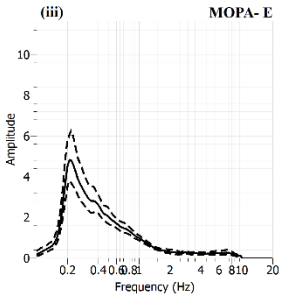

(aii) Day record (Winter)
MATJ
Fo = 18.10 Hz
Ao = 1.42
H/V
Frequency (Hz)

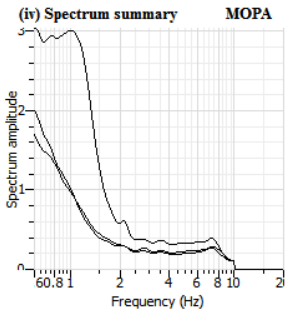

(bi) Night Record (Summer)
MATJ
Fo = 18.68 Hz
Ao = 1.53
H/V
Frequency (Hz)

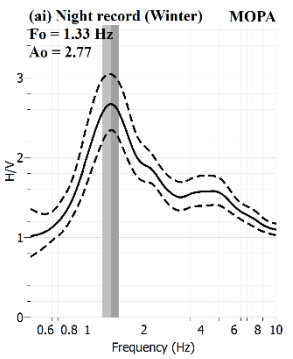

(bii) Day Record (Summer)
MATJ
Fo = 16.65 Hz
Ao = 2.12
H/V
Frequency (Hz)

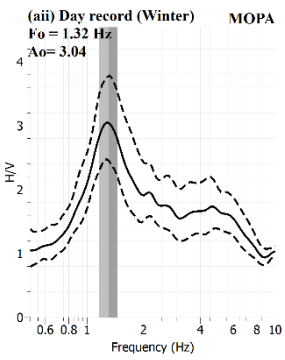

(i)
MOPA- Z
Amplitude
Frequency (Hz)

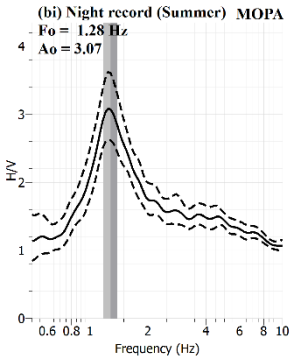

(ii)
MOPA- N
Amplitude
Frequency (Hz)

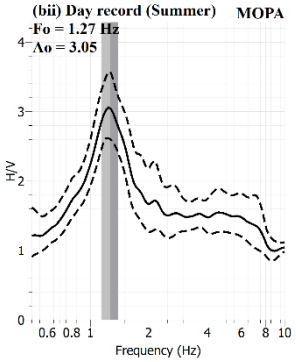

(iii)
MOPA- E
Amplitude
Frequency (Hz)

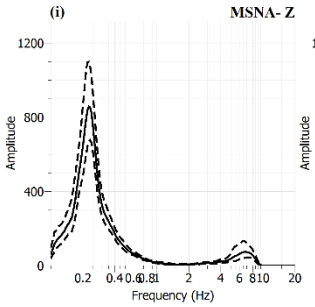

(iv) Spectrum summary
MOPA
Spectrum amplitude
Frequency (Hz)

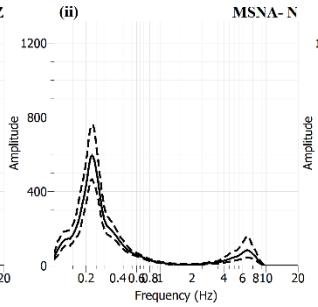

(ai) Night record (Winter) MOPA
Fo = 1.33 Hz
Ao = 2.77
H/V
Frequency (Hz)

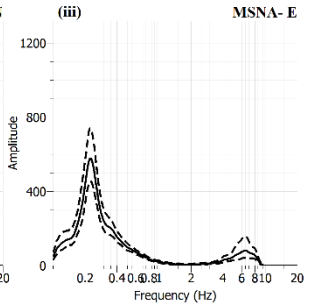

(aii) Day record (Winter) MOPA
Fo = 1.32 Hz
Ao= 3.04
H/V
Frequency (Hz)

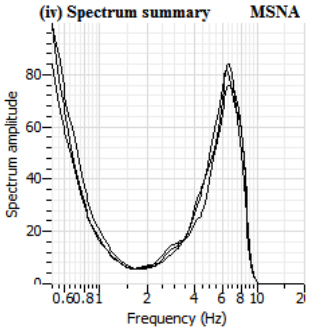

(bi) Night record (Summer) MOPA
Fo = 1.28 Hz
Ao = 3.07
H/V
Frequency (Hz)

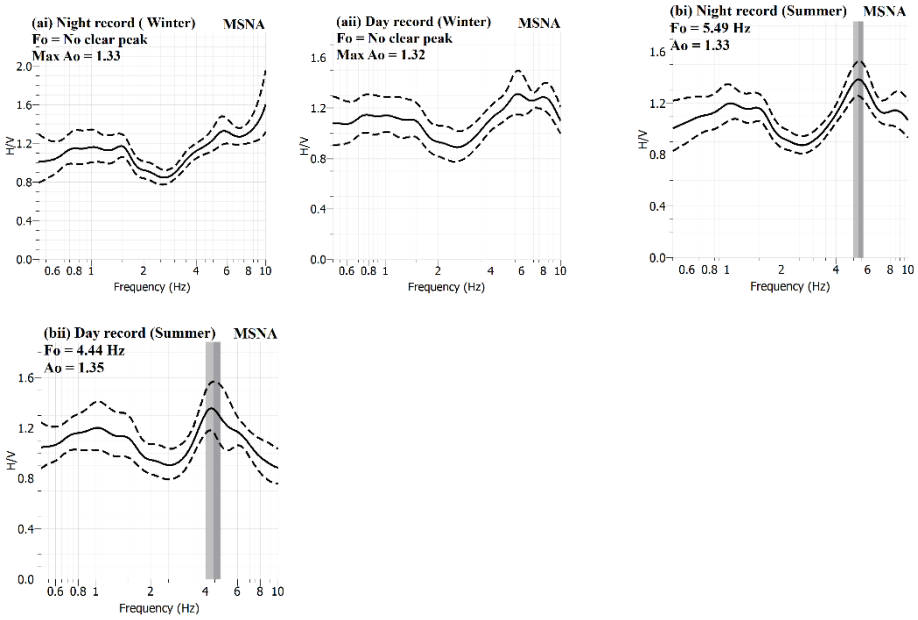

(bii) Day record (Summer) MOPA
Fo = 1.27 Hz
Ao = 3.05
H/V
Frequency (Hz)

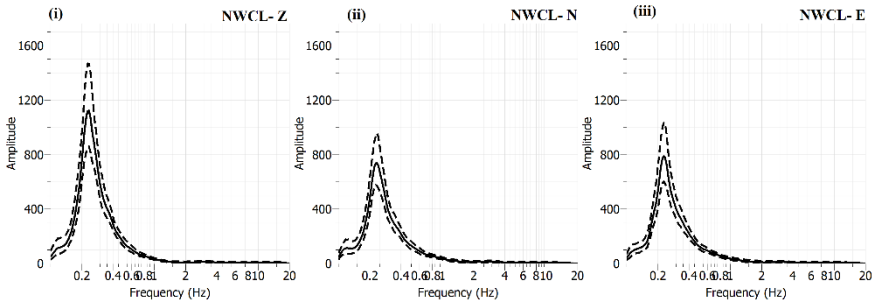

(i) MSNA- Z
Amplitude
Frequency (Hz)

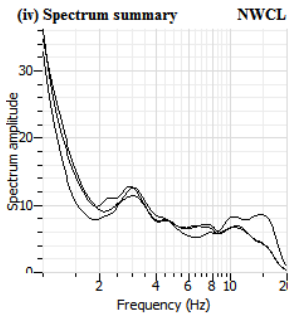

(ii) MSNA- N
Amplitude
Frequency (Hz)

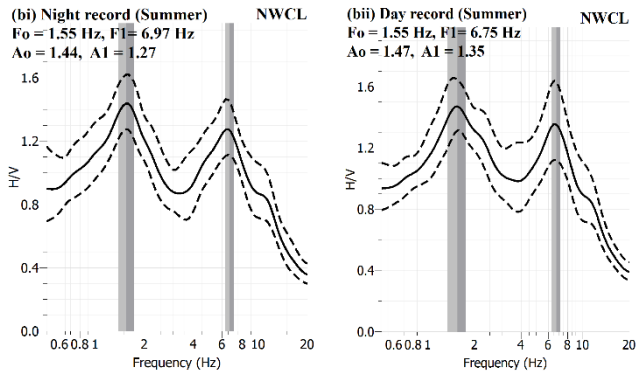

(iii) MSNA- E
Amplitude
Frequency (Hz)

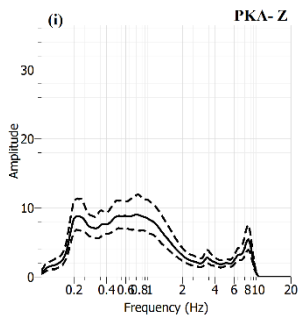

(iv) Spectrum summary MSNA
Spectrum amplitude
Frequency (Hz)

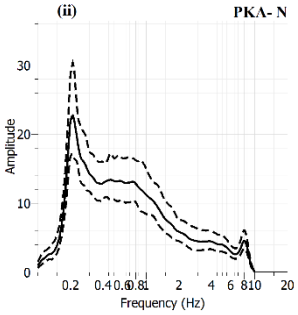

(ai) Night record (Winter) MSNA
Fo = No clear peak
Max Ao = 1.33
(aiii) Day record (Winter) MSNA
Fo = No clear peak
Max Ao = 1.32
(bi) Night record (Summer) MSNA
Fo = 5.49 Hz
Ao = 1.33
(bii) Day record (Summer) MSNA
Fo = 4.44 Hz
Ao = 1.35
H/V
Frequency (Hz)

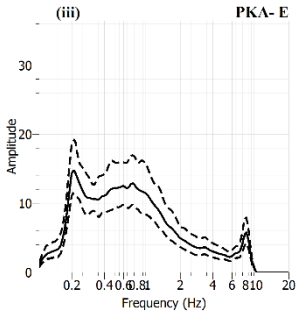

(i) NWCL- Z
(ii) NWCL- N
(iii) NWCL- E
Amplitude
Frequency (Hz)

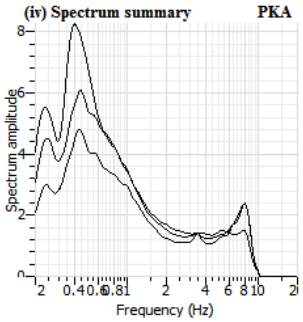

(iv) Spectrum summary NWCL
Spectrum amplitude
Frequency (Hz)

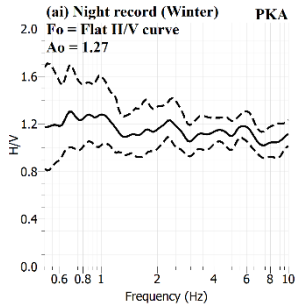

(bi) Night record (Summer) NWCL
Fo = 1.55 Hz, F1= 6.97 Hz
Ao = 1.44, A1 = 1.27
(bii) Day record (Summer) NWCL
Fo = 1.55 Hz, F1= 6.75 Hz
Ao = 1.47, A1 = 1.35
H/V
Frequency (Hz)

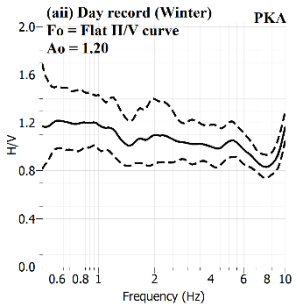

(i)
PKA- Z
Amplitude
Frequency (Hz)

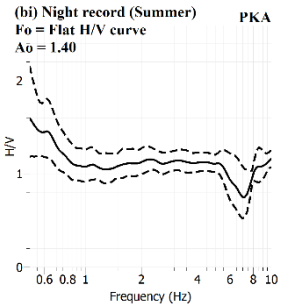

(ii)
PKA- N
Amplitude
Frequency (Hz)

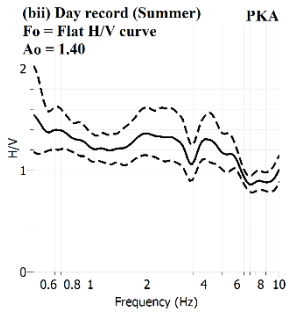

(iii)
PKA- E
Amplitude
Frequency (Hz)

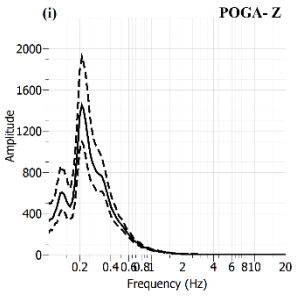

(iv) Spectrum summary
PKA
Spectrum amplitude
Frequency (Hz)

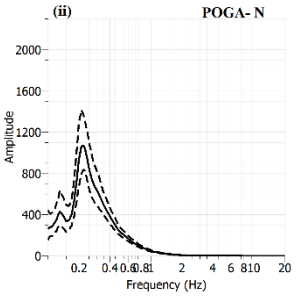

(ai) Night record (Winter)
PKA
Fo = Flat II/V curve
Ao = 1.27
H/V
Frequency (Hz)

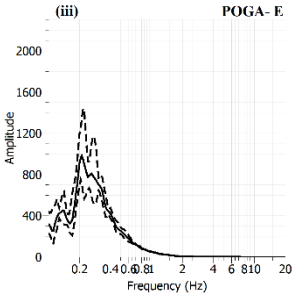

(aii) Day record (Winter)
PKA
Fo = Flat II/V curve
Ao = 1.20
H/V
Frequency (Hz)

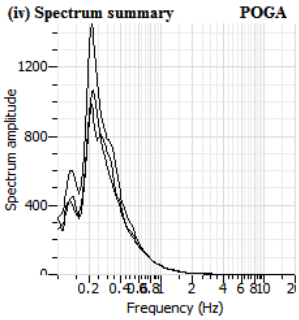

(bi) Night record (Summer)
PKA
Fo = Flat H/V curve
Ao = 1.40
H/V
Frequency (Hz)

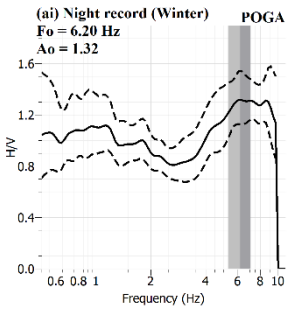

(bii) Day record (Summer)
PKA
Fo = Flat H/V curve
Ao = 1.40
H/V
Frequency (Hz)

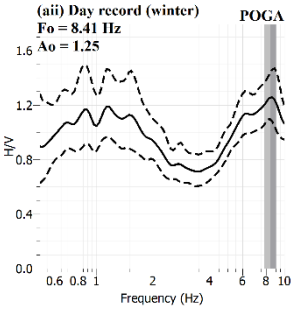

(i)
POGA- Z
Amplitude
Frequency (Hz)

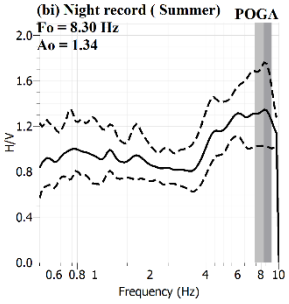

(ii)
POGA- N
Amplitude
Frequency (Hz)

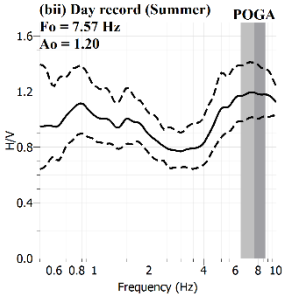

(iii)
POGA- E
Amplitude
Frequency (Hz)

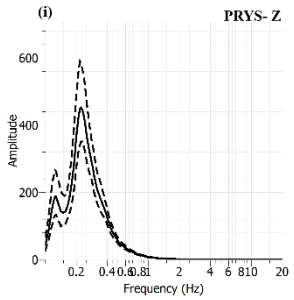

(iv) Spectrum summary
POGA
Spectrum amplitude
Frequency (Hz)

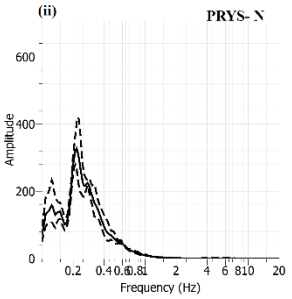

(ai) Night record (Winter)
Fo = 6.20 Hz
Ao = 1.32
POGA
H/V
Frequency (Hz)

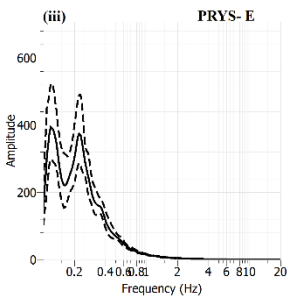

(aii) Day record (winter)
Fo = 8.41 Hz
Ao = 1.25
POGA
H/V
Frequency (Hz)

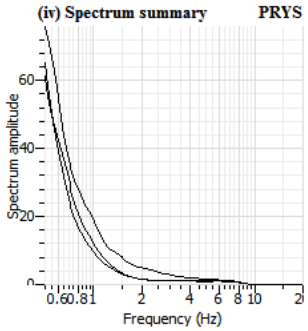

(bi) Night record (Summer)
Fo = 8.30 Hz
Ao = 1.34
POGA
H/V
Frequency (Hz)

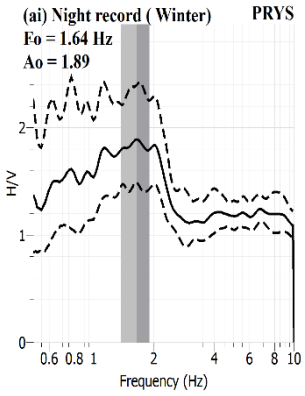

(bii) Day record (Summer)
Fo = 7.57 Hz
Ao = 1.20
POGA
H/V
Frequency (Hz)

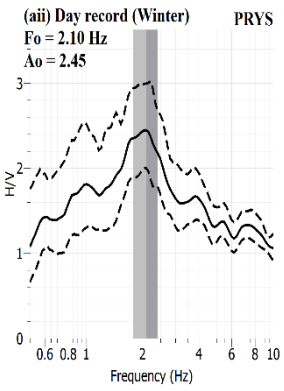

(i)
PRYS- Z
Amplitude
Frequency (Hz)

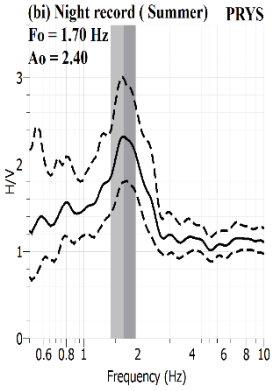

(ii)
PRYS- N
Amplitude
Frequency (Hz)

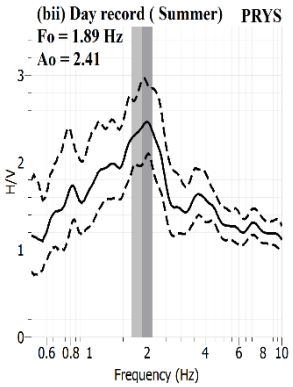

(iii)
PRYS- E
Amplitude
Frequency (Hz)

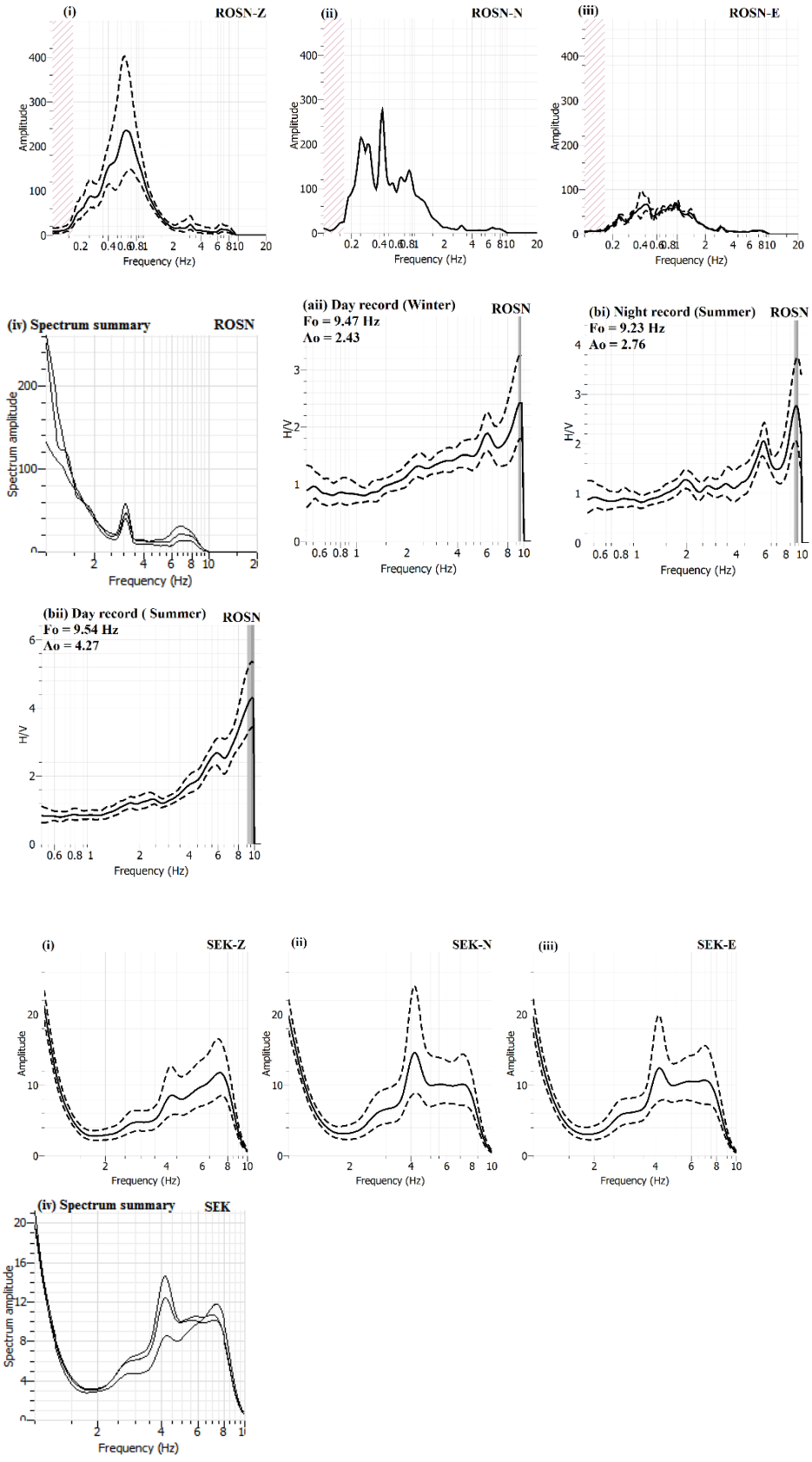

(iv) Spectrum summary
PRYS
Spectrum amplitude
Frequency (Hz)

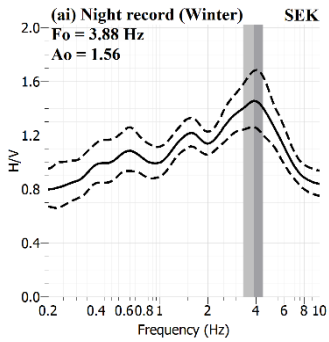

(ai) Night record (Winter)
PRYS
Fo = 1.64 Hz
Ao = 1.89
H/V
Frequency (Hz)

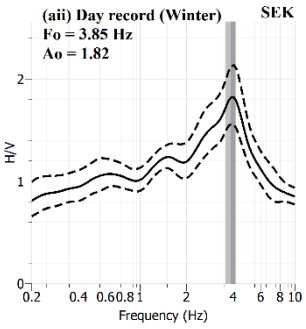

(aii) Day record (Winter)
PRYS
Fo = 2.10 Hz
Ao = 2.45
H/V
Frequency (Hz)

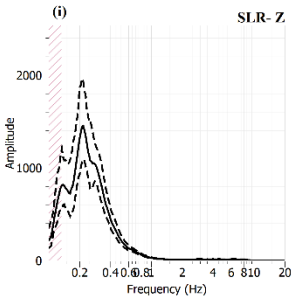

(bi) Night record (Summer)
PRYS
Fo = 1.70 Hz
Ao = 2.40
H/V
Frequency (Hz)

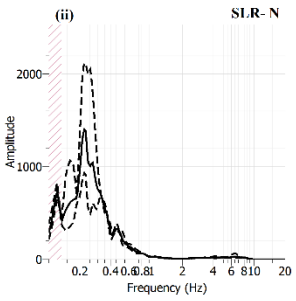

(bii) Day record (Summer)
PRYS
Fo = 1.89 Hz
Ao = 2.41
H/V
Frequency (Hz)

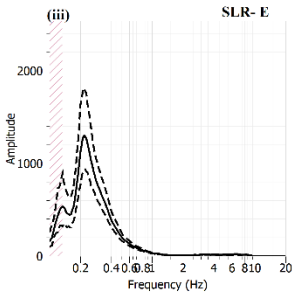

(i) ROSN-Z
(ii) ROSN-N
(iii) ROSN-E
Amplitude
Frequency (Hz)
(iv) Spectrum summary ROSN
Spectrum amplitude
(aii) Day record (Winter)
Fo = 9.47 Hz
Ao = 2.43
(bi) Night record (Summer)
Fo = 9.23 Hz
Ao = 2.76
H/V
(bii) Day record (Summer)
Fo = 9.54 Hz
Ao = 4.27
(i) SEK-Z
(ii) SEK-N
(iii) SEK-E
(iv) Spectrum summary SEK

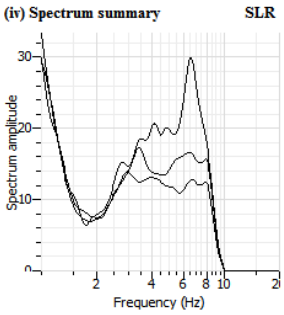

(ai) Night record (Winter)
SEK
Fo = 3.88 Hz
Ao = 1.56
H/V
Frequency (Hz)

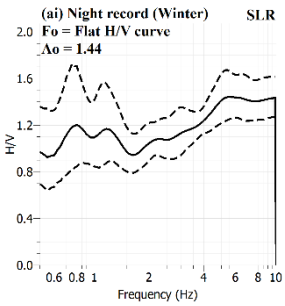

(aii) Day record (Winter)
SEK
Fo = 3.85 Hz
Ao = 1.82
H/V
Frequency (Hz)

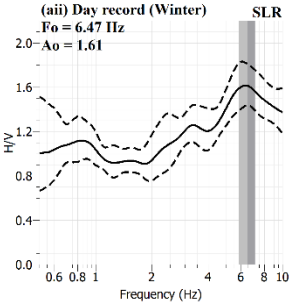

(i)
SLR- Z
Amplitude
Frequency (Hz)

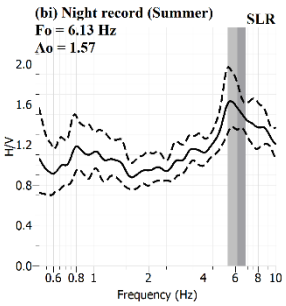

(ii)
SLR- N
Amplitude
Frequency (Hz)

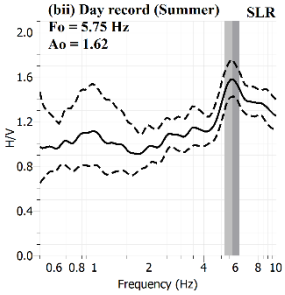

(iii)
SLR- E
Amplitude
Frequency (Hz)

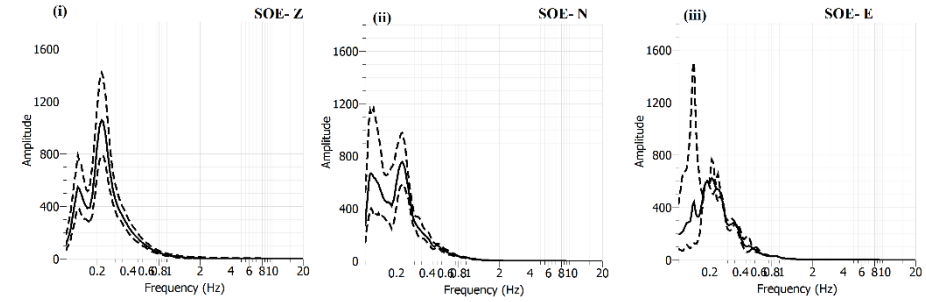

(iv) Spectrum summary
SLR
Spectrum amplitude
Frequency (Hz)

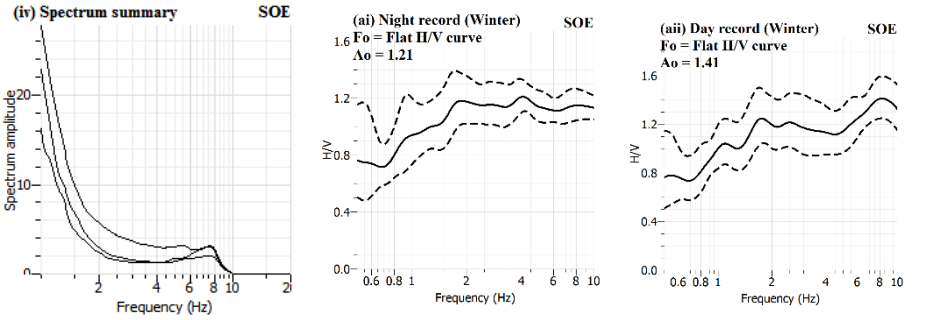

(ai) Night record (Winter)
SLR
Fo = Flat H/V curve
Ao = 1.44
H/V
Frequency (Hz)

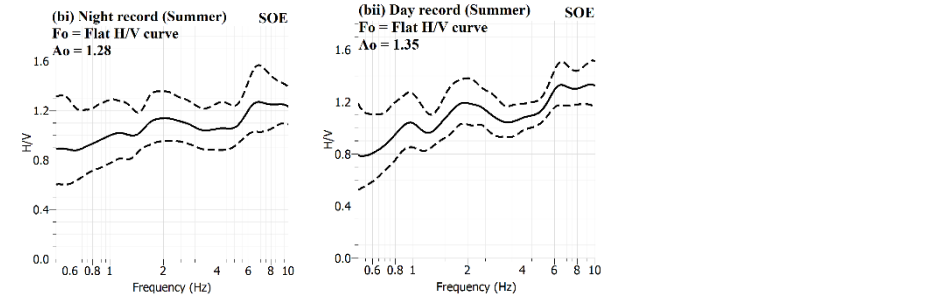

(aii) Day record (Winter)
SLR
Fo = 6.47 Hz
Ao = 1.61
H/V
Frequency (Hz)

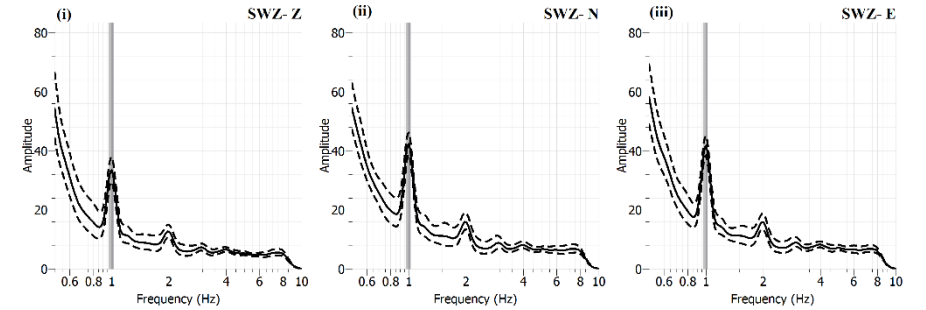

(bi) Night record (Summer)
SLR
Fo = 6.13 Hz
Ao = 1.57
H/V
Frequency (Hz)

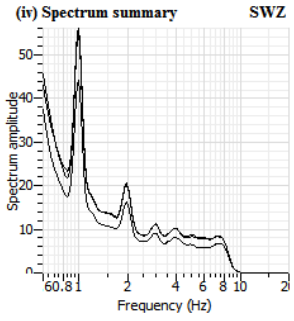

(bii) Day record (Summer)
SLR
Fo = 5.75 Hz
Ao = 1.62
H/V
Frequency (Hz)

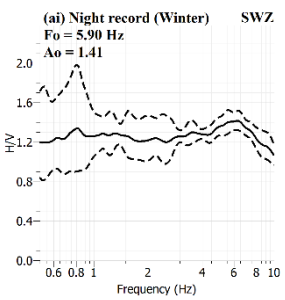

(i) SOE- Z
(ii) SOE- N
(iii) SOE- E
Amplitude
Frequency (Hz)

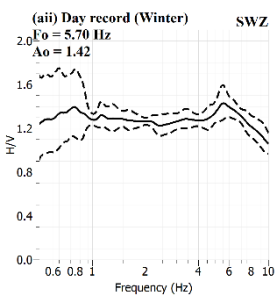

(iv) Spectrum summary SOE
Spectrum amplitude
(ai) Night record (Winter) SOE
Fo = Flat H/V curve
Ao = 1.21
(aiii) Day record (Winter) SOE
Fo = Flat H/V curve
Ao = 1.41
H/V
Frequency (Hz)

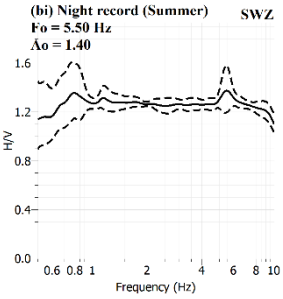

(bi) Night record (Summer) SOE
Fo = Flat H/V curve
Ao = 1.28
(bii) Day record (Summer) SOE
Fo = Flat H/V curve
Ao = 1.35
H/V
Frequency (Hz)

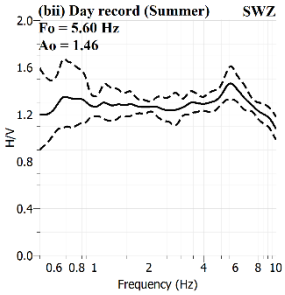

(i) SWZ- Z
(ii) SWZ- N
(iii) SWZ- E
Amplitude
Frequency (Hz)

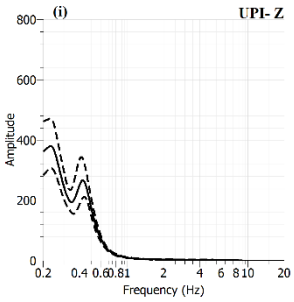

(iv) Spectrum summary SWZ
Spectrum amplitude
Frequency (Hz)

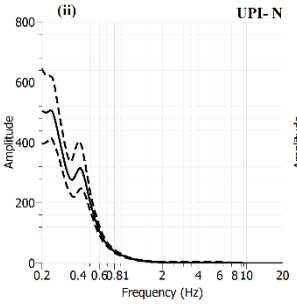

(ai) Night record (Winter)
SWZ
Fo = 5.90 Hz
Ao = 1.41
H/V
Frequency (Hz)

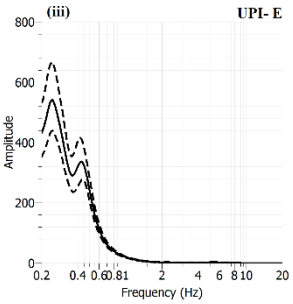

(aii) Day record (Winter)
SWZ
Fo = 5.70 Hz
Ao = 1.42
H/V
Frequency (Hz)

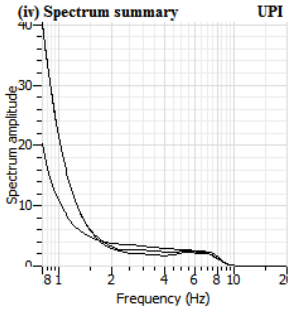

(bi) Night record (Summer)
SWZ
Fo = 5.50 Hz
Ao = 1.40
H/V
Frequency (Hz)

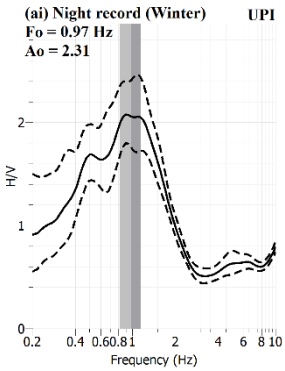

(bii) Day record (Summer)
SWZ
Fo = 5.60 Hz
Ao = 1.46
H/V
Frequency (Hz)

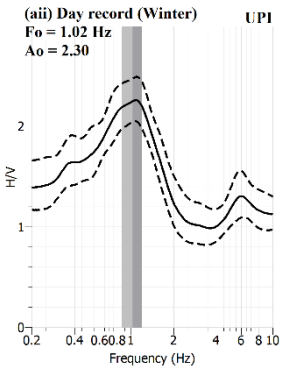

(i)
UPI- Z
Amplitude
Frequency (Hz)

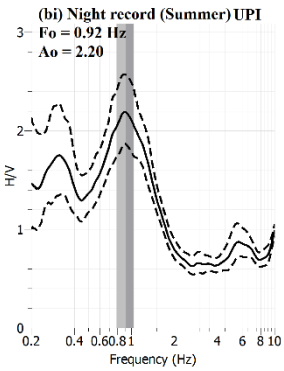

(ii)
UPI- N
Amplitude
Frequency (Hz)

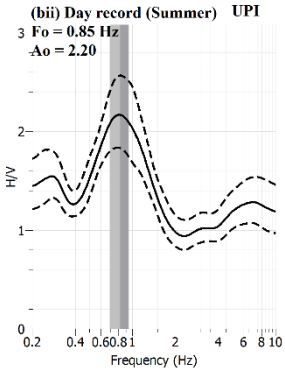

(iii)
UPI- E
Amplitude
Frequency (Hz)

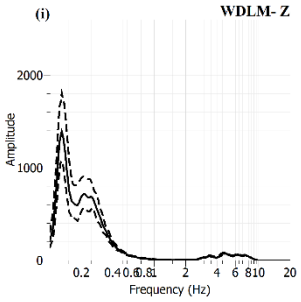

(iv) Spectrum summary
UPI
Spectrum amplitude
Frequency (Hz)

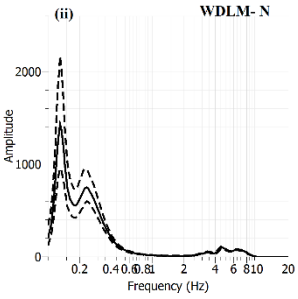

(ai) Night record (Winter)
UPI
Fo = 0.97 Hz
Ao = 2.31
H/V
Frequency (Hz)

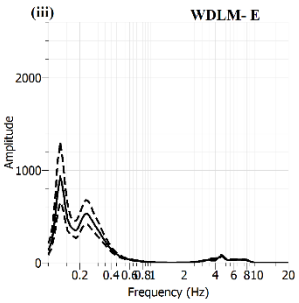

(aiii) Day record (Winter)
UPI
Fo = 1.02 Hz
Ao = 2.30
H/V
Frequency (Hz)

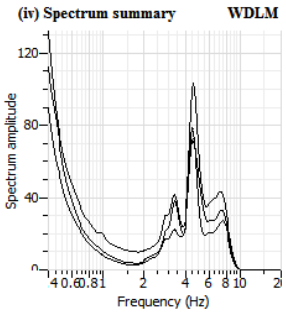

(bi) Night record (Summer)
UPI
Fo = 0.92 Hz
Ao = 2.20
H/V
Frequency (Hz)

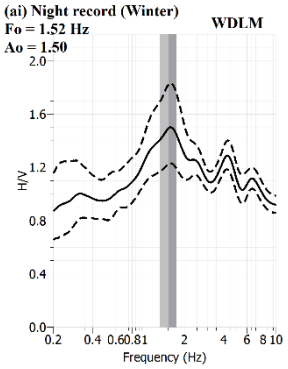

(bii) Day record (Summer)
UPI
Fo = 0.85 Hz
Ao = 2.20
H/V
Frequency (Hz)

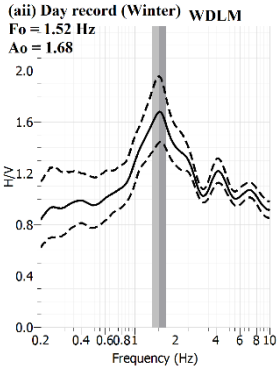

(i)
WDLM- Z
Amplitude
Frequency (Hz)

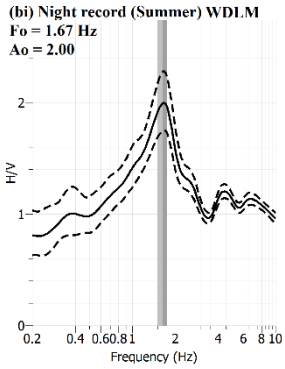

(ii)
WDLM- N
Amplitude
Frequency (Hz)

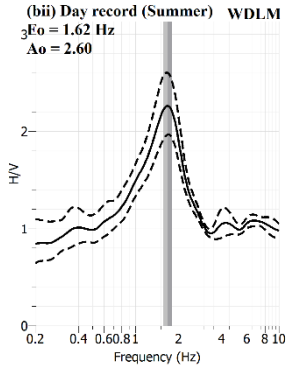

(iii)
WDLM- E
Amplitude
Frequency (Hz)


(iv) Spectrum summary
WDLM
Spectrum amplitude
Frequency (Hz)


(ai) Night record (Winter)
Fo = 1.52 Hz
Ao = 1.50
WDLM
H/V
Frequency (Hz)


(aii) Day record (Winter)
Fo = 1.52 Hz
Ao = 1.68
WDLM
H/V
Frequency (Hz)


(bi) Night record (Summer) WDLM
Fo = 1.67 Hz
Ao = 2.00
H/V
Frequency (Hz)


(bii) Day record (Summer)
Fo = 1.62 Hz
Ao = 2.60
WDLM
H/V
Frequency (Hz)